The Applications of Quantitative Scanning Transmission Electron Microscopy to the Analysis of Intracellular Elemental Distributions



Amy Alexandra Sheader

St Peter's College

University of Oxford

A thesis submitted for the degree of Doctor of Philosophy

Trinity Term 2021

Abstract

The scanning transmission electron microscope (STEM) is an extraordinarily powerful tool for materials characterisation. The wealth of signals available in the microscope mean that chemical and structural details may be probed simultaneously, and often at the atomic scale. Recent developments in quantitative STEM methods have brought about new capabilities for acquiring mass and compositional information. In particular, advances in the measurement of the high-angle annular dark-field (HAADF) signal means it is now possible to count atoms within individual nanostructures with extremely high precision. In parallel, new approaches for quantifying energy-dispersive x-ray spectroscopy (EDX) and electron energy loss spectroscopy (EELS) data afford new opportunities for the determination of elemental composition on an absolute scale.

Thus far, many of these emergent methods have seen little application outwith inorganic samples. This thesis aims to explore to what extent these advances can be applied in complex biological environments, with a particular focus on the measurement of intracellular elemental distributions. High-resolution imaging is first used to elucidate the nanoscale structure of two platinum-based chemotherapeutics. Similar methods are then used to identify single heavy atoms inside the cell bodies of dorsal root ganglia following Pt-drug administration. The use of quantitative HAADF STEM allows experimental measurements of atomic scattering cross-sections to be directly compared with those predicted from simulation. This ultimately confirms that the single atoms observed are indeed platinum, and allows the masses of small atomic clusters visualised in the cells to be measured.

In later chapters, it is further shown that quantitative STEM imaging may be combined with spectroscopy to measure EDX and EELS partial scattering cross-sections. These are acquired for several elements of biological significance, including calcium, sodium and potassium. Finally,

spectroscopic cross-sections are applied in samples of peripheral nerve to quantify aggregations of calcium in the mitochondria, and to measure changes in intra-axonal sodium and potassium levels following treatment with a chemotherapeutic agent.

Disclaimer

I hereby declare that this thesis is my own original original work, undertaken during my DPhil studies at the University of Oxford. Where research was undertaken in collaboration with others, I have clearly stated which parts of the work were done by people other than myself.

Acknowledgements

I would like to extend my thanks to a number of people at Oxford and King's for their generous contributions to this work. I am very grateful to my supervisors, Peter Nellist, Roland Fleck, and Sarah Flatters, for their invaluable support and advice during my DPhil. I would like to express my special gratitude to Pete; his encouragement, patience and mentorship has made me a better scientist. Thank you for having faith in me, even when everything went sideways.

I am indebted to Gema Vizcay-Barrena and Christina Ferguson from King's, without whose incredible technical skills and perseverance this whole project would have never got off the ground. I am also very grateful to many Nellist group members, both past and present. In particular, Lewys Jones, Gerardo Martinez and Aakash Varambhia were incredibly generous with their time and knowledge. Thank you for giving up your evenings and weekends to teach me how to not break the microscope (or at least how to put it back together!). I also thank Colum O'Leary and Juan Lozano, for the terrible jokes and the pints respectively.

Last (but very much not least) I would like to thank my family for their unwavering support, encouragement and love. Robert Moran, Alison and Andrew Sheader, Maureen Hayes and Linda and John Barraclough; thank you for always believing in me. You mean the absolute world to me, and I could not have done this without you.

Dedication

I dedicate this thesis to my grandad, Colin Hayes. I know you'd have been proud.

Contents

List of Figures **14**

List of Tables **17**

Introduction **19**

1 STEM Instrumentation and Imaging **22**

1.1 Aims & Scope 22

1.2 Microscope Development 22

1.2.1 A Brief History of the Transmission Electron Microscope 23

1.2.2 Scanning Transmission Electron Microscopy 24

1.2.3 The Resolution Revolution 25

1.3 Instrumentation 26

1.3.1 Configuration of the STEM 27

1.3.2 The Electron Gun 27

1.3.3 The Condenser System 29

1.3.4 Aberration Correction 29

1.3.5 Other Lens Systems 30

1.4 Imaging Modes 30
1.4.1 LAADF & MAADF 33
1.4.2 HAADF 33
1.4.3 HAADF Quantification 34
1.4.4 BF and Other Techniques 36
1.4.5 Other Detectors and Next Generation Microscopy 37
1.5 Summary 37

2 Spectroscopic Methods **38**

2.1 Aims & Scope 38
2.2 Inelastic Interactions 38
2.3 Energy Dispersive X-ray Spectroscopy 40
2.3.1 The EDX Detector 42
2.3.2 EDX Spectra 43
2.3.3 Quantification of EDX Spectra 46
2.4 Electron Energy Loss Spectroscopy 49
2.4.1 The EEL Spectrometer 50
2.4.2 Electron Energy Loss Spectra 51
2.4.3 EELS Quantification 53
2.5 Comparison of EDX and EELS 56
2.6 Summary 60

3 STEM in Life Science **61**

3.1 Aims & Scope 61

3.2 STEM Imaging Applications in Life Sciences 61

3.2.1 Macromolecular Mass Measurement 62

3.2.2 Structural Determination and Tomography 66

3.2.3 Localisation and Imaging 68

3.2.4 Summary 72

3.3 Applications of STEM EDX & EELS in Life Sciences 72

3.3.1 EDX 73

3.3.2 EELS 77

3.3.3 Summary 81

3.4 Outlook for ADF, EDX & EELS 81

4 Platinum Pharmaceuticals in the STEM **83**

4.1 Aims & Scope 83

4.2 Platinum-based Chemotherapeutics 84

4.2.1 Cisplatin 84

4.2.2 Oxaliplatin 84

4.2.3 Mechanisms of Action and Toxicity 85

4.3 Sample Preparation 86

4.4 Cisplatin 86

4.4.1 Low Magnification Observation 86

4.4.2 High Magnification Observations and Measurements 87

4.4.3 Discussion 92

4.5 Oxaliplatin 93

4.5.1 HAADF Observations of Oxaliplatin 93

4.5.2 Cluster Calculations 93

4.5.3 Discussion 98

4.6 Summary 99

5 Quantification of Platinum in DRG **100**

5.1 Aims & Scope 100

5.2 Oxaliplatin in Dorsal Root Ganglia 100

5.3 Sample Preparation 101

5.4 Low- and Medium-Magnification Imaging 103

5.5 Single Atom Visualisation 104

5.6 Species Identification Using Probe-Integrated Scattering Cross-Sections 108

5.6.1 Theory 108

5.6.2 Experimental PICS calculation 109

5.6.3 Simulated PICS 111

5.7 Cluster Weighing 111

5.8 Visibility of Other Species 113

5.8.1 Implications for Integration 114

5.8.2 Applications to Thin Sections 115

5.9 Limitations of EDX 118

5.10 Discussion . . . 119

5.10.1 Other Techniques for Pt Localisation . . . 120

5.10.2 Electron Microscopy for Pt Localisation . . . 122

5.11 Summary . . . 123

6 Measurement of EDX and EELS Partial Cross-Sections 125

6.1 Aims & Scope . . . 125

6.2 Partial Scattering Cross-Sections in EDX and EELS . . . 126

6.3 Sample Preparation . . . 128

6.4 Partial Cross-Sections Measured for the Oxford ARM . . . 130

6.4.1 Calculation of $\sigma_{\mathrm{Ca}}^{\mathrm{EDX}}$ and $\sigma_{\mathrm{Ca}}^{\mathrm{EELS}}$ . . . 130

6.4.2 Calculation of $\sigma_{\mathrm{Na}}^{\mathrm{EDX}}$, $\sigma_{\mathrm{Cl}}^{\mathrm{EDX}}$ and $\sigma_{\mathrm{K}}^{\mathrm{EDX}}$. . . . 140

6.5 Partial Cross-Sections Measured for the CUI F200 . . . 143

6.5.1 Calculation of $\sigma_{\mathrm{Na}}^{\mathrm{EDX}}$, $\sigma_{\mathrm{Cl}}^{\mathrm{EDX}}$ and $\sigma_{\mathrm{K}}^{\mathrm{EDX}}$. . . . 143

6.6 Error Propagation . . . 146

6.6.1 EDX Error . . . 146

6.6.2 EELS Error . . . 147

6.7 Discussion . . . 147

6.7.1 EDX . . . 147

6.7.2 EELS . . . 150

6.8 Summary . . . 151

7 Applications of EDX and EELS Partial Cross-Sections 152

7.1 Aims & Scope . . . 152

7.2 Intracellular Elemental Distributions and the Effects of Paclitaxel . . . 153

7.3 Sample Preparation . . . 153

7.3.1 Discussion . . . 156

7.4 Application 1: Mitochondrial Calcium Stores . . . 156

7.4.1 Data Acquisition . . . 156

7.4.2 Spectral Processing . . . 159

7.4.3 Measurement of N_{atoms} from EDX and EELS . . . 159

7.4.4 Discussion . . . 160

7.4.5 Summary . . . 162

7.5 Application 2: Intracellular Na and K . . . 162

7.5.1 Data Acquisition . . . 163

7.5.2 Spectral Processing: Theoretical k-factors . . . 163

7.5.3 Spectral Processing: Partial Scattering Cross-Sections . . . 165

7.5.4 Measurement of Na and K Areal Densities . . . 165

7.5.5 Comparison of Experimental and Literature k-factors . . . 167

7.5.6 Discussion . . . 170

7.5.7 Summary . . . 174

Conclusions & Outlook **174**

7.6 Summary . . . 175

7.7 Emerging Opportunities . . . 176

7.8 Wider Applications 178

Appendices **179**

Appendix A **181**

A.1 Spectroscopic Processing Parameters 181

A.1.1 $CaSO_4$ EDX Processing 181

A.1.2 $CaSO_4$ EELS Processing 182

A.1.3 BK_3O_3, NaCl and $NaCO_3$ EDX Processing 182

Appendix B **183**

B.1 CUI F200 Detector Calibration 183

B.1.1 Recording a Diffraction Pattern 183

B.1.2 Calibration of Condenser Apertures 183

B.1.3 Extension of Camera Calibration 184

B.1.4 Observation of Inner Edge of ADF Detector 184

B.1.5 ADF Detector Scans 186

B.1.6 Results 186

B.2 Probe Currents 188

Appendix C **191**

C.1 EDX Data from Peripheral Nerve 191

C.1.1 Sample Preparation 191

C.1.2 EDX Data Collection 191

C.1.3 Statistical Analysis 193

List of Figures

1.1 Diagram of STEM instrumentation 28

1.2 Schematic of detector geometries in STEM 31

2.1 Schematic of the inelastic electron-sample interaction 39

2.2 Geometry for acquisition of simultaneous EDX, EELS and ADF data 41

2.3 A typical EDX Spectrum 44

2.4 A typical EEL Spectrum 52

4.1 Chemical structure of cisplatin and oxaliplatin 85

4.2 Low magnification overview of cisplatin 87

4.3 Pt nanoparticles in cisplatin 88

4.4 Nanoparticle orientation and lattice measurement 89

4.5 Multiframe acquisition of Pt nanoparticles in cisplatin 91

4.6 Low magnification overview of oxaliplatin 94

4.7 Pt clusters in oxaliplatin 95

4.8 Oxaliplatin cluster quantification procedure 96

4.9 Pt atoms per cluster against diameter 97

5.1 Schematic of the Dorsal Root Ganglion . . . 102

5.2 Low-magnification imaging of DRG . . . 105

5.3 Intermediary-magnification imaging of DRG . . . 106

5.4 Atomic clusters in DRG . . . 107

5.5 HAADF image fractionation . . . 110

5.6 Simulated HAADF cross-sections . . . 112

5.7 Atomic cluster weighing in the DRG . . . 113

5.8 Single atom visibility limits in HAADF STEM . . . 116

5.9 Single atom measurability limits in HAADF STEM . . . 117

5.10 EDX of Pt-containing clusters in DRG . . . 119

6.1 Low-magnification overviews of $CaSO_4$, BK_3O_3, $NaCO_3$ and NaCl . . . 129

6.2 ARM200F: Data acquisition for measurement of $\sigma_{\mathrm{Ca}}^{\mathrm{EDX}}$ and $\sigma_{\mathrm{Ca}}^{\mathrm{EELS}}$ . . . 131

6.3 ARM200F: HAADF cross-sections for compound samples . . . 133

6.4 ARM200F: Measurement of $\sigma_{\mathrm{Ca}}^{\mathrm{EDX}}$ and $\sigma_{\mathrm{S}}^{\mathrm{EDX}}$ . . . 136

6.5 ARM200F: Measurement of $\sigma_{\mathrm{O}}^{\mathrm{EDX}}$ . . . 137

6.6 ARM200F: Measurement of $\sigma_{\mathrm{Ca}}^{\mathrm{EELS}}$. . . . 139

6.7 ARM200F: Measurement of $\sigma_{\mathrm{K}}^{\mathrm{EDX}}$ and $\sigma_{\mathrm{Cl}}^{\mathrm{EDX}}$ . . . 141

6.8 ARM200F: Measurement of $\sigma_{\mathrm{Na}}^{\mathrm{EDX}}$ from two standards . . . 142

6.9 F200: Measurement of $\sigma_{\mathrm{Na}}^{\mathrm{EDX}}$, $\sigma_{\mathrm{Cl}}^{\mathrm{EDX}}$ and $\sigma_{\mathrm{K}}^{\mathrm{EDX}}$ . . . 145

6.10 ARM200F: All σ^{EDX} . . . 149

7.1 Low-magnification overview images of peripheral nerve samples . . . 155

7.2 Strongly scattering clusters in axons of the peripheral nerve 157

7.3 EDX and EELS spectra recorded inside axons 158

7.4 $N_{\mathrm{Ca}}^{\mathrm{EDX}}$ against $N_{\mathrm{Ca}}^{\mathrm{EELS}}$ measured for different clusters 160

7.5 Intra-axonal wt% of Na and K measured using theoretical k-factors 164

7.6 Intra-axonal areal density of Na and K measured using partial scattering cross-sections 166

7.7 Theoretical and literature experimental values of Cliff-Lorimer k-factors $k_{x,\mathrm{Si}}$ . . 168

7.8 Schematic of action potential generation 171

7.9 Ratio data for myelinated and unmyelinated axons compared at different timepoints 173

B.1 Acquisition of diffraction patterns 184

B.2 Calibration of probe-forming apertures 185

B.3 Full angular calibration of large phosphor screen camera 185

B.4 Observation of ADF detector hole 186

B.5 ADF detector scans 187

C.1 Bright-field STEM image of peripheral axons from Technai T12 192

C.2 Example EDX data recorded from Technai T12 with EDAX detector 192

C.3 Statistical analysis of Technai T12/EDAX EDX data 193

List of Tables

1.1 Approximate criteria to categorise LAADF, MAADF and HAADF STEM imaging 33

2.1 Comparison between the key equations k-factor and ζ-factor EDX quantification. 48

2.2 Comparison between EDX and EELS for quantitative elemental measurement . . 57

6.1 Table of standards for partial cross-section quantification 128

6.2 ARM200F: Experimental parameters for measuring $\sigma_{\mathrm{Ca}}^{\mathrm{EDX}}$ and $\sigma_{\mathrm{Ca}}^{\mathrm{EELS}}$. 132

6.3 ARM200F: $\sigma_{\mathrm{Ca}}^{\mathrm{EDX}}$ and $\sigma_{\mathrm{S}}^{\mathrm{EDX}}$ 135

6.4 ARM200F: Experimental and theoretical values of $\sigma_{\mathrm{Ca}}^{\mathrm{EELS}}$ 139

6.5 ARM200F: $\sigma_{\mathrm{Cl}}^{\mathrm{EDX}}$ and $\sigma_{\mathrm{K}}^{\mathrm{EDX}}$. 140

6.6 ARM200F: $\sigma_{\mathrm{Na}}^{\mathrm{EDX}}$ 141

6.7 F200: Experimental parameters for measuring $\sigma_{\mathrm{Na}}^{\mathrm{EDX}}$, $\sigma_{\mathrm{Cl}}^{\mathrm{EDX}}$ and $\sigma_{\mathrm{K}}^{\mathrm{EDX}}$ 144

6.8 F200: Values of $\sigma_{\mathrm{Na}}^{\mathrm{EDX}}$, $\sigma_{\mathrm{Cl}}^{\mathrm{EDX}}$ and $\sigma_{\mathrm{K}}^{\mathrm{EDX}}$ 144

6.9 ARM200F: All partial EDX cross-sections 148

6.10 ARM200F: Theoretical values of σ^{EELS} 151

7.1 Experimental parameters used to acquire data in calcium-containing clusters . . 157

7.2 Number of calcium atoms in cluster measured with EDX and EELS 160

7.3 Percentage differences in Na and K areal density and their ratio 167

7.4 Comparison of theoretical and experimental $k_{\mathrm{Na,K}}$ 169

A.1 Data processing parameters for measuring $\sigma_{\mathrm{Ca}}^{\mathrm{EDX}}$ 181

A.2 Data processing parameters for measuring $\sigma_{\mathrm{Ca}}^{\mathrm{EELS}}$ 182

A.3 Data processing parameters for measuring $\sigma_{\mathrm{Na}}^{\mathrm{EDX}}$ and $\sigma_{\mathrm{K}}^{\mathrm{EDX}}$ 182

B.1 CUI F200 Condenser Aperture Semi-Convergence Angles 188

B.2 CUI F200 Condenser Aperture Semi-Convergence Angles 189

B.3 CUI F200 Probe Currents 190

Introduction

In the eighty four years which have passed since the scanning transmission electron microscope (STEM) was first realised, it has become an indispensable tool for materials characterisation. Acquisition of structural and chemical information on the atomic scale is now a routine endeavour, and affords a means of understanding the behaviour of the building blocks which make up the world around us.

In the STEM, a finely focused electron probe is scanned across the sample. The resulting electron-atom interactions generate a wealth of signals which may be collected individually or simultaneously on a pixel-by-pixel basis. While much has been done qualitatively, in recent years there have also been significant developments in the quantification of STEM data. This is particularly evident for high-angle annular dark-field (HAADF) imaging, where progress has been to such an extent it is now possible to atom-count individual nanostructures with a precision of $\pm$ a single atom. In parallel, improvements in spectrometer design and data processing methods mean energy-dispersive x-ray spectroscopy (EDX) and electron energy-loss spectroscopy (EELS) are able to offer complementary and quantitative information about composition. A well-calibrated STEM is therefore uniquely positioned to probe elemental distributions at very high spatial resolution.

The aim of this thesis is to examine to what extent some of the most recent advances in quantitative STEM - namely the measurement of elastic and inelastic partial scattering cross-sections - may be applied to investigate elemental distributions within cells. Thus far, these methods have largely been limited to applications in catalytic nanoparticles. However, as will be demonstrated in this work, the fundamental principles which underpin these measurements are not unique to heavy species, but may in fact be applied to elements of considerable biological significance. As distributions of these elements drive fundamental subcellular processes,

characterisation at very high spatial resolution and in the context of the cell ultrastructure is therefore a powerful motivation behind this work.

The structure of this thesis is as follows:

- **Chapter 1** concerns STEM instrumentation and the imaging modes accessible in the microscope. In particular, the key developments in HAADF imaging, simulation and quantification which have facilitated the work in this thesis are discussed.
- **Chapter 2** provides an overview of the spectroscopic methods available in the STEM, containing detail on the acquisition, interpretation and quantification of EDX and EELS data.
- **Chapter 3** reviews the applications of qualitative and quantitative STEM imaging and spectroscopy in life sciences to date.
- **Chapter 4** shows the results of HAADF image acquisition from clinical solutions of two platinum-based chemotherapautics, cisplatin and oxaliplatin. The former of these is demonstrated to unexpectedly form sub-2 nm metallic nanoparticles, while the latter is shown to contain disordered Pt clusters.
- **Chapter 5** presents the results of high-resolution imaging applied in tissue samples recovered following *in vivo* oxaliplatin administration. Quantitative imaging techniques are used to measure the masses of small disordered platinum clusters with subcellular context.
- **Chapter 6** builds upon existent methods for the measurement of EDX and EELS partial scattering cross-sections. Measurements are made for a number of elements with biological significance on an aberration-corrected JEOL ARM200F and an uncorrected JEOL JEM-F200.
- **Chapter 7** demonstrates the application of EDX and EELS partial cross-sections in measuring intracellular elemental distributions. These are subsequently used to atom-count concentrated calcium deposits in samples of peripheral nerve, and to measure differences in intra-axonal levels of sodium and potassium following administration of the anti-cancer drug paclitaxel.
- **Chapter 8** contains conclusions about the applications of quantitative STEM methods in

complex biological samples, and discusses future avenues which may benefit from these approaches.

This thesis also contains three appendices, relevant to the calculation of EDX and EELS partial scattering cross-sections in Chapter 6, and the measurement of intracellular sodium and potassium in Chapter 7:

- **Appendix A** details the background and integration energy windows used to process EDX and EELS data.
- **Appendix B** outlines steps for calibrating probe convergence semi-angles and ADF detector collection semi-angles on the JEOL JEM-F200.
- **Appendix C** contains unpublished pilot data recorded from peripheral nerve prior to optimisation of sample preparation procedures.

Chapter 1

STEM Instrumentation and Imaging

1.1 Aims & Scope

All data presented in this thesis have been recorded using imaging and spectroscopic methods enabled by scanning transmission electron microscopy (STEM). In this Chapter key developments which led to the "resolution revolution", and subsequently enabled single-atom imaging and characterisation, are briefly reviewed. The constituent parts of the STEM, and their role in achieving high-resolution imaging, are also discussed.

The final Section of this Chapter concerns different imaging modes and their applications, in combination with a review of methods for the quantification and simulation of high-angle annular dark field images used in this thesis.

1.2 Microscope Development

Nearly 100 years ago, Hans Busch proposed that magnetic fields could be used to deflect electrons in much the same way as photons refract through glass lenses [1]. Busch's suggestions paved the way for the development the a new field of electron microscopy, where the substantially smaller wavelength of electrons could be exploited to provide higher resolution images than attainable with light.

Transmission electron microscopy is now established as one of the most powerful and

fundamental characterisation tools available for materials research. Scanning transmission electron microscopes (STEM) and transmission electron microscopes (TEMs) are uniquely positioned to deliver structural, compositional, and chemical imaging simultaneously, on length scales ranging from hundreds of microns down to the single atom - in some cases, within a single instrument.

1.2.1 A Brief History of the Transmission Electron Microscope

The first TEM was developed in Berlin by Ernst Ruska and Max Knoll in the early 1930s. They calculated the diffraction-limited resolution for their prototype instrument to be 2.2 Å, several orders of magnitude smaller than that of a contemporary light microscope [2]. Although this resolution was not realised in practice until four decades later, the improvements afforded by imaging with electrons provided sufficient motivation to convince Ruska to continue his work (despite Knoll's departure to work on the development of the television) [3].

Around the same time, Manfred von Ardenne (also in Berlin) commenced work on the first STEM. Following his efforts to improve the performance of the early scanning electron microscope (SEM), von Ardenne sought to apply a similar approach to transmission electron microscopy. Unfortunately, the destruction of von Ardenne's laboratory and prototype instruments during a 1944 air raid, coupled with the end of World War II, halted further work on the STEM. While elements of von Ardenne's work were incorporated into Ruska's TEM, von Ardenne himself abandoned instrumental development in favour of pursuing research into fissionable isotopes (a most pressing matter in post-War Germany) [4].

Despite the temporary misfortunes of the STEM, the TEM was successfully commercialised by Siemens and interest in transmission electron microscopy continued to grow. Despite only a very limited range of samples being suitable for the microscope (as there were extensive difficulties in preparing sufficiently thin specimens of most materials), more than thirty instruments (with a spatial resolution on the order of 10 nm [5]) were built and installed by 1945 [3]. Rapid developments in instrumentation meant that by the mid-1950s, high-resolution TEM became feasible, with Menter and Bowden being the first to demonstrate lattice resolution imaging [6]. Their work showed the TEM could visualise the 12 Å separation of the $(20\overline{1})$ planes in platinum and copper phthalocyanine, and provided the first direct observations of edge dislocations and

crack propagation.

1.2.2 Scanning Transmission Electron Microscopy

In 1963, Albert Crewe proposed a new instrumental design which aimed to improve the spatial resolution and image contrast in comparison to the TEM [7]. While Crewe had been impressed with the biological TEM images he had seen at reported at a conference, he remained doubtful that the microscope resolution could be improved significantly without what he described in a later publications as "serious and perhaps radical changes" [8]. Crewe's revised experimental configuration was very similar to the STEM described previously by von Ardenne, and based primarily upon a single lens system combined with electromagnetic scan coils to raster the electron probe [8]. The paper called attention to the possibility of performing spatially-resolved chemical imaging using both characteristic x-rays generated by the electron-sample interaction, and by measuring energy lost by a beam electron following an inelastic scattering event (in what are now called energy-dispersive x-ray spectroscopy and electron energy loss spectroscopy respectively, discussed in Chapter 2).

Crewe's motivation to develop the STEM also arose out of the potential capabilities for electron microscopy to visualise single atoms. While Erwin Muller and coworkers had recorded atomic resolution images of tungsten using a field emission microscope (FEM) as early as 1956, such an approach placed exacting constraints on the types of sample which could be examined [9]. In the TEM, several individuals made early arguments that single atoms should in principle be visible [10], [11]. However, in practice such capabilities were not realised until considerably later, and following several decades of improvements in instrumentation.

A major contribution of Crewe and coworkers to the development of the modern STEM was their recognition that a significant limiting factor in achieving single-atom imaging was the brightness of the electron source. In order to achieve the best resolution, the image of the electron source needed to be demagnified by many orders of magnitude. However, each successive demagnification step lead to a loss of electrons from the beam (resulting in fewer electrons incident upon the sample). This meant that to form an image, pixel integration times were so long that sample drift and other instrumental instabilities became prohibitive, no matter the resolution of the microscope.

The solution proposed by Crewe et al. was a new electron gun based on the principles of field emission, capable of producing a stable current on the order of microamperes [12]. One significant benefit of such a configuration was that the current originated from an area of only about 30 $Å^2$, meaning demands on source demagnification (and subsequent loss of electrons from the probe) were vastly reduced [13]. Crewe et al. ultimately achieved their goal of single atom imaging in 1970, using a STEM equipped with a field-emission gun (FEG) to record the first images of isolated single uranium atoms [14]. Following commercialisation of the FEG-STEM (in the form of the VG microscope), the capabilities of the instrument for imaging and microanalysis meant analytical STEM was rapidly adopted within the materials science communities; a thorough review of notable results may be found in Ref. [15].

1.2.3 The Resolution Revolution

Throughout the development of both the TEM and STEM, it was appreciated that the use of electromagnetic lenses in the microscope meant experimental and wavelength-limited resolutions were highly disparate. While this was due in part to imperfections in the lenses themselves, as early as 1936 Scherzer had recognised that the use of round electromagnetic lenses would introduce unavoidable aberrations as a consequence of Maxwell's laws [16]. Scherzer later proposed a number of approaches for correcting such aberrations [17], although these were not realised until many years later.

Zach and Haider were the first to develop a functional aberration corrector, initially for a low-voltage SEM [18] and later for the TEM [19]. Zach and Haider subsequently founded Corrected Electron Optical System (CEOS) GmbH in 1996, producing sextupole TEM correctors for major microscope manufacturers. A thorough review of the early history of aberration correction in the TEM is given by Hawkes in Ref. [20]. At around the same time, the first operational aberration-corrector for the STEM was demonstrated by Krivanek et al. [21]. They achieved an instrumental resolution of 2.3–3.4 Å (dependent on measurement direction relative to the scan) in their 100 kV instrument. Practically this was achieved by countering the inherently positive spherical aberration C_s of the round magnetic lens with a symmetry-breaking combination of quadrupole and octapole lenses. Together, these lenses compensate for the aberration by producing negative C_s. While this approach introduced new aberrations (namely the new lenses' own C_s, and two- and four-fold astigmatism), a semi-automated aberration diagnosis

was sufficient to minimise these effects. A combined user-controlled and computer-moderated process is still in use today.

Even prior to their 1999 paper, Krivanek et al. had stated that their advances in aberration-corrected microscopy would "ultimately lead to an era of lab-sited STEM instruments able to routinely achieve 1 Å or even 0.5 Å resolution" [22]. The sub-1 Å resolution limit was ultimately achieved by Krivanek et al. in 2002 [23], and was followed by successful commercialisation of C_s-corrected STEMs by their company Nion. Nellist and Pennycook (who received one of the very first Nion correctors) were the first to directly image below 1 Å, visualising the 78 pm spacing of Si dumbbells in a corrected 300 kV STEM [24]. This was a notable achievement as previous STEM imaging with sub-1 Å resolution had relied on the appearance of spots in the Fourier transformed image, a more ambiguous metric due to its sensitivity to instrument instabilities.

A thorough and recent review of the remarkable advancements made possible through aberration-corrected STEM is presented by Pennycook in Ref. [25]. In addition to the notable results within materials science enabled by high-resolution STEM, Pennycook highlighted how initial misgivings - mostly concerning dramatic reductions in depth of focus and increases in probe current - ultimately became beneficial. For example, the ability to probe the sample at different depths has ultimately opened up a new field of microscopy, allowed 3D-information about the sample to be recovered [26]. Increased probe currents, rather than causing catastrophic sample damage, have instead enabled the field of analytical STEM (as will be discussed in Chapter 2).

1.3 Instrumentation

As described in the previous Section, several lens systems are combined in the STEM to facilitate high-resolution imaging. While the exact configurations vary between microscopes and manufacturers, the basic principles are similar throughout.

1.3.1 Configuration of the STEM

Most electron microscopes installed in facilities today are not dedicated STEMs (even though they may be operated almost exclusively in this mode). An example of such an instrument may be found in the JEOL ARM200F located in the Department of Materials at the University of Oxford. While this microscope is technically operational in both TEM and STEM modes, it is used considerably more frequently in the latter mode. As this instrument is the one on which the majority of data in this thesis were recorded, a simplified schematic of the STEM mode is shown in Figure 1.1.

For any STEM, the most critical parts of the system (i.e. the ones which limit instrument performance) are the electron source and the condenser-objective system. The aberration corrector also plays a key role. These systems act collectively to form a focused probe of high-energy electrons, which is then raster-scanned across the sample. The image magnification is set by the extent of the scan, and the type of detector situated at the image plane then determines the nature of the image recorded from electrons scattered by the sample. A comprehensive description may be found in *Transmission Electron Microscopy: A Textbook for Materials Science* by Williams and Carter, specifically in Chapters 5, 6 and 9 [27].

1.3.2 The Electron Gun

In hybrid TEM-STEMs the electron source is typically installed at the top of the microscope column, as additional post-specimen electron optics are required for operation in TEM mode (this is not the case in a dedicated STEM, where placing the electron gun at the bottom affords more mechanical stability). In a cold field emission gun (c-FEG) of the type installed on the Oxford instrument, electrons are extracted by field emission from the tip of a tungsten needle under ultra-high vacuum. A second anode positions the first beam cross-over, and is critical in determining the overall system resolution. As demagnification of this cross-over ultimately sets the size of the probe incident on the sample, it is important that the tungsten tip is atomically sharp so that the electron flux is uni-directional [28]. This configuration produces electrons with a small energy spread (down to as little as 0.3 eV), and has high brightness. Cold-FEGs are amongst the brightest objects in the known universe, with typical values around $10^{8-9}\,\mathrm{A\,cm^2/sr}$. This brightness is particularly crucial for analytical spectroscopy, where high probe currents are

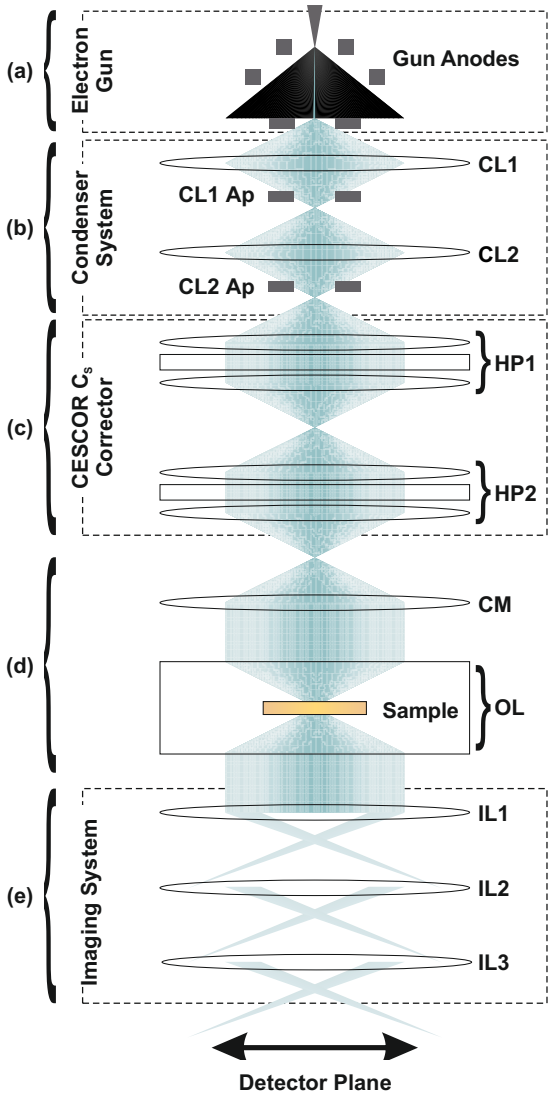


Figure 1.1: Schematic of key lenses of the JEOL ARM-200F scanning transmission electron microscope. (a) Field emission from a tungsten needle provides the electron source; (b) the lenses of the condenser system (CL1 and CL2) act to demagnify the electron source. Apertures CL1Ap and CL2Ap may be used to limit the angular range of electrons ultimately used to form the probe; (c) a two-stage system of round and hexapole lenses (HP1 and HP2) correct C_s and other aberrations up to 3rd order; (d) the condenser mini-lens (CM) and the objective lens (OL) project the demagnified image of the source onto the sample. The second objective lens, OL2, projects the scattered electrons into the imaging system. (e) three intermediary lenses (IL1-3) provide sequential magnification of the transmitted signal. The degree of lens excitation in this system controls the effective distance of the detector from the back focal plane of the sample.

required to produce sufficient signal to noise for quantitative analysis.

1.3.3 The Condenser System

After producing many near-monochromatic electrons, it is then necessary to direct them down (or up) the microscope column and focus them onto the sample. This is achieved by the use of electromagnetic lenses, which are typically composed of an alloyed metal core surrounded by copper wire coils. When a current is passed through the wire, it produces a magnetic field which deflects passing electrons. By altering this current, the Lorentz force experienced by the electron can be varied, causing deflection to a greater or lesser extent [29].

Amongst the most critical lenses of the STEM are those found in the condenser system. The first condenser lens (CL1) demagnifies the first beam crossover from the gun. The second condenser lens (CL2) projects the image of the source crossover to the objective lens or, as in the case of the ARM 200F, the back focal plane of the CESCOR corrector (see Section 1.3.4).

Inserting an aperture into the condenser system allows the highest angle (and therefore most highly aberrated) electrons to be removed from the probe. However, the condenser aperture and the probe are reciprocally related, and therefore larger aperture placed at CL2 produces a smaller probe. For aberration-free imaging at high resolution, the microscope operator must balance the probe size with excluding aberrated waves. This is further complicated for microanalytical experiments, where quantification accuracy depends heavily on retaining sufficient electrons in the probe as discussed in Chapter 2.

1.3.4 Aberration Correction

Aberrations for electrons travelling closest to the optical axis tend to zero, and the most dominant aberrations in most microscopes are those of defocus and spherical aberration (C_s) [29]. Defocus is easily mitigated by increasing or decreasing the strength of the objective lens, but correction of C_s requires an additional dedicated lens system. For high-resolution STEM, where the formation of a small probe relies on collecting electrons relatively farther from the optical axis, higher-order aberrations also become important. If uncorrected, the presence of three-fold astigmatism and axial coma are observed as a reduction in resolution and a degradation in the image quality.

Modern high-resolution instruments contain a dedicated corrector system, which is partially automated.

Aberration correction systems are offered commercially by companies such as CEOS GmbH *(Heidelberg, Germany)* and Nion *(Kirkland, WA, USA)*. The Oxford JEOL ARM 200F is equipped with a CEOS CESCOR-type hexapole corrector, which allows for probe-correction of aberrations up to third order and, as shown in Figure 1.1, is located within the condenser system. Newer systems such as the JEOL *(Akishima, Tokyo, Japan)* ASCOR corrector are capable of correcting aberrations up to 5th order. This is particularly useful at lower accelerating voltages, and allows sub-200 pm resolution at 30 kV.

1.3.5 Other Lens Systems

As shown in Figure 1.1, another condenser lens CM (sometimes called CL3) is positioned after the corrector system. This lens is used in microscopes which operate in both TEM and STEM mode. When strongly excited, it produces another beam cross-over before the OL, which may then project a parallel beam onto the sample for TEM. In STEM, it is only weakly excited, and a focused probe is achieved using the objective lens alone.

The sample sits in a gap between the pole pieces of the objective. The shorter the focal length of these lenses, the higher the spatial resolution of the instrument; indeed, the pre-field of the OL system is critical in setting this parameter. However, a small pole piece gap imposes constraints on the space available to fit e.g. an energy dispersive x-ray spectrometer or a high-tilt tomography sample holder [29].

In the final lens system, three intermediary lenses project the scattered signal to the detector. The degree of magnification here controls the angular range ultimately recorded by the detector, and therefore the type of image contrast as described in the next section.

1.4 Imaging Modes

When a beam electron passes through a sample, a number of outcomes are possible. The first is that the electron is transmitted without interacting at all; this is the direct beam. Another

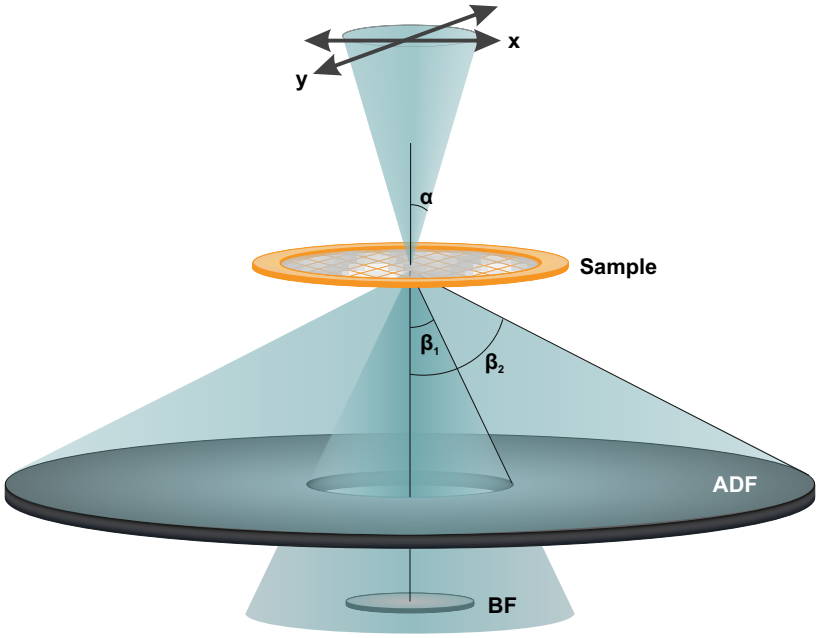


Figure 1.2: A simplified schematic of signal detection in the STEM. The parameter α is the probe semi-convergence angle, and β_1 and β_2 refer to the inner and outer ADF semi-collection angles respectively. An annular detector (ADF) or bright-field (BF) detector may be placed in the far field of the sample. The effective distance between the sample and detector is controlled by the intermediary lenses. The ADF detector collects higher-angle scattering, and the BF detector collects a portion of the low-angle scattering.

possibility is elastic scattering by atomic nuclei (i.e. coherent Rutherford scattering); for periodic samples such as crystals, interference in this scattering can give rise to diffractive effects (e.g. Bragg diffraction). Electrons may also undergo quasi-elastic thermally diffuse scattering from sample lattice vibrations. Alternatively, incident electrons may interact inelastically with the nucleus or the electron cloud [30].

Each of these components may contribute to the image recorded in the microscope, but by judicious choice of collection angles it is possible to "tune" which are included in the final image. As discussed later in Section 1.4.2, this is particularly useful in the case of high angle scattering, as the image contrast can be directly related to the chemical composition of the sample. However, no matter what angles are recorded the configuration of the detectors is similar, and a schematic is shown in Figure 1.2.

Annular detectors, as shown in Figure 1.2, are often used in the STEM. As the probe is scanned across the sample, the whole intensity incident upon the detector is integrated and read out to generate a value for that pixel. Engel [31] and Misell et al. [32] showed that an annular detector is able to transform the phase variation acquired by an electron upon passing through the electromagnetic field of a sample into a variation in amplitude only. Nellist et al. showed that for a sufficiently large detector, the annular geometry will destroy any interference effects and give resulting images which are free from contrast reversal [33]. This means that in an ADF image, the vacuum will always be dark and sample will be bright; this is very different to conventional TEM imaging, where vacuum and atoms can be bright or dark, or change depending on the effects of many factors (thickness, defocus and diffraction to name just a few).

ADF imaging is an incoherent technique, which means that the image intensity can be written as a convolution of wave and probe intensities as shown in Equation 1.1:

$$I(\mathbf{R}_0) = |\psi(\mathbf{R}_0)| \otimes O(\mathbf{R}_0), \tag{1.1}$$

where $\psi(\mathbf{R}_0)$ is the incident probe function (dependent upon scan position $\mathbf{R}_0$), and $O(\mathbf{R}_0)$ is an object function encapsulating information about the sample.

In comparison, TEM records the intensity of a convolution between $\psi(\mathbf{R}_0)$ and the transmittance function $\phi(\mathbf{R}_0)$ (i.e. $|\psi(\mathbf{R}_0) \otimes \phi(\mathbf{R}_0)|^2$), which results in interference between waves affecting image intensity in a complex manner. This has significant implications for image interpretation, particularly when compared with the camera-like behaviour of the ADF detector. There are further consequences for spatial resolution; in conventional TEM imaging, interference between electrons from spatially separated sample regions may degrade the image resolution. These interference effects are not present in incoherent techniques such as ADF [33].

In the STEM, α is typically between 10-30 milliradians. Approximate criteria for the different "flavours" of ADF imaging are shown in Table 1.4. In practice, the detector collection angles for low-, medium- and high-angle ADF (LAADF, MAADF and HAADF respectively) imaging are set by the microscope and sample and the values presented in Table 1.4 are therefore only a guide. In addition, as the angular range which reaches the detector is controlled by the intermediary lenses, a single annular detector can be used for multiple imaging modes.

ADF Type	Experimental Setup	Dominant Contrast Mechanism
LAADF	$\beta_1 \gtrsim \alpha$	Diffraction
MAADF	$\beta_1 \gtrsim 2\alpha$	Mixed
HAADF	$\beta_1 \gtrsim 3\alpha$	Thermal Diffuse Scattering

Table 1.1: Approximate criteria to categorise LAADF, MAADF and HAADF STEM imaging, where α is the probe semi-convergence angle and β_1 is the inner angle of the ADF detector. The value of the outer detector angle β_2 is less important as the amount of scattering falls off rapidly with angle, but is typically well in excess of 100 mrad.

1.4.1 LAADF & MAADF

At lower scattering angles, a greater degree of the electrons have undergone diffraction by the sample and therefore for both LAADF and MAADF images, a varying amount of of diffraction contrast is recorded. At the lowest collection angles (LAADF), this contrast mechanism is dominant over all others. Unsurprisingly, it is particularly useful for imaging sample features which diffract strongly, such as dislocations (e.g. in $SrTiO_3$ [34]), or crystalline precipitates on amorphous films (e.g. [35]). LAADF imaging is also useful for imaging specimens with low atomic number (e.g. as in organic molecular crystals [36]). In these samples, very few electrons will be scattered to angles above α, and so signal-to-noise can be maximised by limiting the angular range of electrons from which the image is formed.

As the inner collection angle is increased to around 2α, the effects of diffraction are felt less strongly, and the contributions of the thermal diffuse scattering become comparable. Experimentally MAADF has been used to perform electron tomography on dislocations [37], [38]. This is achieved more successfully with MAADF than LAADF, as the ADF detector captures information from multiple diffracted beams (as opposed to just one or two in low-angle case).

1.4.2 HAADF

High-angle ADF refers to a set of imaging conditions which are fully incoherent, and whereby image contrast is unambiguously related only to atomic number. In this case, the inner collection angle of the detector is sufficiently high that diffracted beams are not collected, and only the

diffuse high-angle scattering contributes to the image. HAADF images are therefore often said to contain only mass-thickness or Z-contrast, because the amount of high-angle scattering which occurs is directly related to either a) the atomic species present (i.e. Z), or b) the amount of atoms present (i.e. thickness).

Rutherford scattering of electrons by an sample nucleus would suggest that the degree of scattering goes as Z^2. However, Hartel et al. described how experimentally the exponent of this dependence is reduced to around 1.6-1.9, due to the partial shielding of the atomic nucleus by the atomic electron cloud [39]. The effects of probe electron-sample electron interactions, and also thermal diffuse scattering (from the collective vibration or phonon of sample atoms), therefore act to reduce the amount of scattering reaching the detector. The exponent is also modified in the case of dynamical scattering within atomic columns. In this case, the ADF intensity becomes rapidly non-linear with thickness as the transmitted electron is repeatedly deflected within the periodic potential of the crystal nuclei (i.e. due to electron channelling).

1.4.3 HAADF Quantification

An important consequence of ADF as an incoherent technique is that the image interpretation is considerably simpler than in conventional TEM. While single atom images were recorded in TEM at around the same time as in the STEM [40], the use of an annular detector in the latter case meant the atoms were significantly more distinguishable against the amorphous carbon support.

The predictable image contrast of ADF also simplifies quantification. The earliest attempts are from Isaacson et al., who published ADF micrographs of highly dispersed U, Au, Cd, In, and Ag samples [41]. By comparing the intensities of the bright spots in each image, they showed that the intensity of each small cluster was a multiple of the intensity of a single atom of that species. The authors also used an 80%Pt:20%Pd sample, and found that while they were unable to distinguish between the two atomic species (due to relatively large errors in intensity measurement), the spot intensities were in agreement with those expected stoichiometrically. In all cases, the scattering angle was approximately 2α, but as only small non-crystalline clusters of atoms were examined no diffraction contrast would have been recorded, and any coherent effects would have been outweighed by other errors.

More sophisticated approaches to image quantification involved comparison with image simulation. In 1957, Cowley and Moodie had suggested a theoretical framework for TEM image simulation which, unlike previous attempts, could cope with challenges posed by dynamical scattering in thick, strongly-diffracting samples [42]. They proposed that a three-dimensional sample could be approximated as a stack of two-dimensional potential fields, and that by propagating the incident electron beam (including probe aberrations) between each slice the resulting exit wave function could be retrieved. This approach has come to be known as a multislice simulation, and was first implemented computationally by Allpress et al. for lattice-resolution brightfield TEM imaging of $W_4Nb_{26}O_{77}$ at different thicknesses [43], [44].

Multislice simulation was extended to include STEM by Kirkland et al. [45]. However, it was rapidly realised that a full HAADF STEM simulation would need to accurately encapsulate the thermal diffuse scattering which, for most samples, dominates the image contrast in this regimen [46]. These effects were incorporated into the multislice calculation by Ishizuka, who showed that an absorptive potential could be used to successfully model the effects of atomic number and specimen thickness [47]. However, in the present day, the effects of TDS are usually modelled using the "frozen-phonon" method. As the period of phonon oscillation is much greater than the time an incident electron spends in the sample, the electron "sees" atoms frozen in place. By summing the results of many phonon configurations, the inelastic TDS may somewhat paradoxically be accurately modelled by the inherently elastic multislice calculation [48], [49]. A large number of softwares to simulate STEM images are now available based on such an approach, with many packages also incorporating options to simulate conventional TEM images. These include (amongst others) QSTEM [50], DrProbe [51] and MULTEM [52]. The variation between simulation output in each of these is small, and primarily related to minor differences in potential parameterisation and user interface.

For completeness, it should be noted that other approaches to image simulation are available. Bloch wave simulation may be used to model electron microscopy imaging of all types, and has some advantages over a multislice approach. Pennycook noted that multislice simulations provide no physical insight into electron scattering within the crystal [46], while Bloch wave analysis allows information about the nature of the scattering to be accessed - not just the resultant exit function. However, for a real sample Bloch wave analysis becomes rapidly impractical due to computational requirements. For a simulation with N Fourier components, the memory

requirements increase as N^2, and simulation time as N^3. In comparison, multislice simulation memory requirements scale as N, and simulation time as $N \log_2 N$ [53].

1.4.4 BF and Other Techniques

In addition to annular techniques, the axial transmitted signal within a STEM may also be collected by a brightfield detector as shown in Figure 1.2. Due the principle of reciprocity, BF-STEM images can be shown to be identical to those recorded by BF-TEM [54]. However, such images have a significantly lower signal-to-noise ratio relative to their TEM counterparts, and literature examples of BF-STEM performed in isolation are therefore limited. More commonly, BF-STEM is used to complement ADF imaging, by providing information on low-Z, weakly scattering atomic columns. Kotaka showed how HAADF and BF imaging could be performed simultaneously for $SrTiO_3$, GaAs and $LiCoO_2$ crystals [55]. In his experiment, the HAADF detector recorded intensity from strongly scattering atomic columns of Sr, Ti, Ga and Co, while complementary (but not quantitative) images of O, N and Li columns were recorded simultaneously. Combining both images yielded more comprehensive information about crystal structure than use of either method in isolation.

It is also possible for both low- and high-Z elements in some samples to be imaged simultaneously using only one detector. Annular Bright Field (ABF) imaging uses electrons recorded from the edges of the brightfield disc to form an image. For low-Z elements, most of the scattering falls within the hole in the ABF detector, and for high-Z elements the electrons scatter to angles higher than those subtended by the ABF detector. This results in all atoms in the image appearing dark, as the detector is recording an absence of scattered electrons. This method has been used to image elements from across the periodic table, including hydrogen columns within YH_2 [56]. However, ABF is only suitable for a subset of materials samples and requires careful tuning of experimental parameters; as described by Findlay et al. for their simulated investigations of Li-containing battery materials, the influences of sample thickness, microscope parameters and local sample structure all affect what is ultimately recorded [57]. The complex nature of the ABF intensity recorded means simulation (and ultimately interpretation) can be challenging.

1.4.5 Other Detectors and Next Generation Microscopy

The detectors used to record ADF, BF and ABF signals are all examples of indirect detectors, which rely on collected electrons being converted to photons which are then recorded via a photomultiplier device [58]. However, the detection quantum efficiency of such a detector is compromised by use of a scintillator, where signal is lost and noise gained through use of the optics required to measure the signal.

A new class of direct detectors eliminate the need for a scintillator intermediary, and are instead exposed directly to the electron beam. The resulting detector is both more sensitive and less noisy than its conventional counterpart, and allows for the full scattering to be recorded [59]. The data can then be post-processed to retrieve any of annular or bright-field signals described previously or used to retrieve phase information encoded in diffraction patterns [60]. Direct-detection methods are also used extensively for very low electron dose imaging [61]. Direct detectors are now commercially available from a number of companies, including JEOL, Gatan *(Pleasanton, CA, USA)*, Quantum Detectors *(Harwell, UK)*, and Direct Electron *(San Diego, CA, USA)*.

1.5 Summary

The development of the modern STEM scanning transmission electron microscope occurred primarily in the 1960s, and the advent of the field emission gun and capabilities for aberration correction mean modern instruments are powerful tools for characterising materials at very high resolution. The flexibility afforded by minimal post-specimen optics means there is a significant degree of control over which angular ranges (and therefore which physical processes) contribute to the final image. One of the most important imaging modes in the STEM is HAADF, where only mass-thickness contributes to the image contrast. This simplifies the quantification process significantly, and allows for chemical identification from the image alone. New direct detectors afford opportunities for future work.

Chapter 2

Spectroscopic Methods

2.1 Aims & Scope

In addition to the elastically scattered electrons which may be used to form e.g. a HAADF image, the result of inelastic processes may also be recorded in the STEM. In this Chapter, the two complementary methods of energy dispersive x-ray and electron energy-loss spectroscopy (EDX and EELS) are discussed. Details of the signal origin, instrumentation and quantification procedures are reviewed in turn for both techniques. EDX and EELS are compared in terms of their key benefits and limitations, alongside considerations for minimum detectable mass fraction and relative errors.

2.2 Inelastic Interactions

As discussed in the Chapter 1, when a beam electron interacts with an sample atom, one likely outcome is that it will scatter elastically. However, another possibility is that the incident electron will interact inelastically, losing energy by exciting the sample plasmon or causing an ionisation event. In the latter case, the resulting electronic configuration of the ionised sample atom is unstable. De-excitation of the ion returns it to its ground state by filling a core hole with an outer-shell electron. This is accompanied by the emission of an x-ray photon or an Auger electron. In the (S)TEM, only the former of these is detected routinely. A schematic of this process is shown in Figure 2.1.

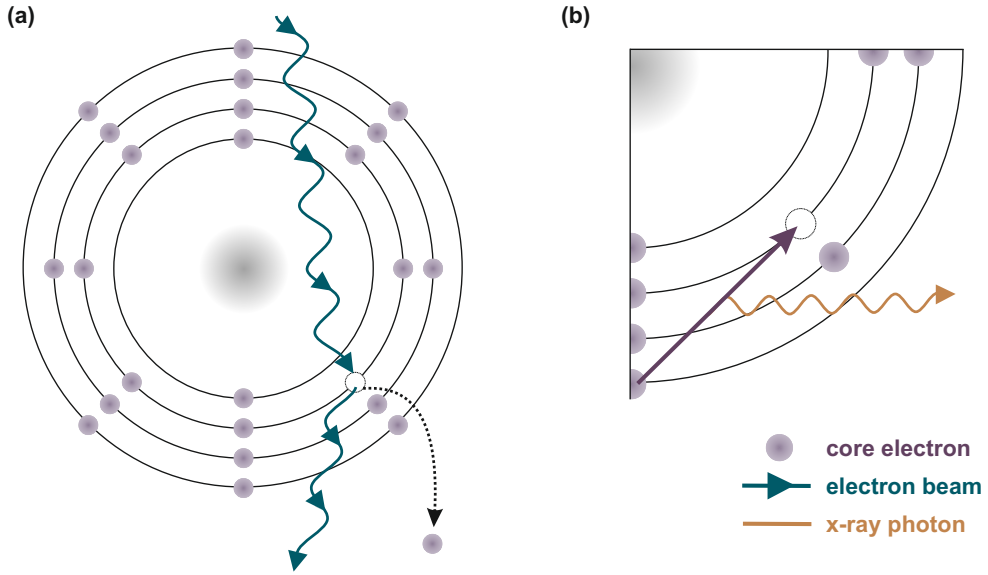


Figure 2.1: Schematic of an inelastic electron-sample interaction. (a) A core-shell electron in an atom may be displaced by the incident beam, resulting in an unstable electronic configuration. The incident electron loses energy. (b) Almost instantaneously, an outer-shell electron will fill the hole in the core. To do this, energy must be radiated as an photon (in this case, an Fe Lβ x-ray at 0.718 kV).

The collection of x-rays which result from this process is referred to as energy-dispersive x-ray spectroscopy (EDX), while energy analysis of the transmitted electron beam by a dedicated spectrometer is known as electron energy-loss spectroscopy (EELS).

EDX and EELS are often described as complementary techniques as the signal arises from the same ionisation event. The energies of the x-ray produced and the loss by the beam electron depend on the energy levels of the atom, and are therefore characteristic of the atomic species present. Both techniques are therefore able to provide information about the chemical nature of the sample at the position of the STEM probe. They may also be used simultaneously and alongside ADF imaging as shown in Figure 2.2. While generally EELS is regarded as being more suitable for the characterisation of lighter elements, and EDX more appropriate for heavier species, in practice the suitability of each method is sample-dependent.

2.3 Energy Dispersive X-ray Spectroscopy

The history of chemical analysis using x-rays is many decades older than that of TEM. In the early 1900s, Moseley published two papers concerning the energies of x-rays emitted by different elements following bombardment with electrons [62], [63]. In addition to relating the x-ray energy to the element's "atomic number" (a term he coined), Moseley also noted that his supposedly pure elemental standards were, in fact, anything but. His recognition of the presence of unexpected lines in the spectra, with wavelengths matching exactly with those of other elements, meant Moseley had inadvertently performed the first electron-induced x-ray analysis.

Dedicated instruments for spectroscopy emerged in the late 1940s, borrowing components from the developing TEM and SEM. The result was the electron probe microanalyser (EPMA), which combined basic TEM optics with an optical microscope, and could analyse sample areas of around $1\,\mu m^2$ [64]. Castaing and Guinier were among the first to use the EPMA to measure x-ray production, and to introduce a means of discriminating between different wavelengths. The use of a quartz crystal in the pre-field of the Geiger counter used for x-ray detection allowed Cu Kα x-rays to be separated from those of Sn and Sb, forming a chemical image of precipitates within the alloy [65]. Coslett and Duncumb were the first to modify their EPMA to allow the electron probe to be scanned across a sample [66]. Their first results were simple maps of Ag

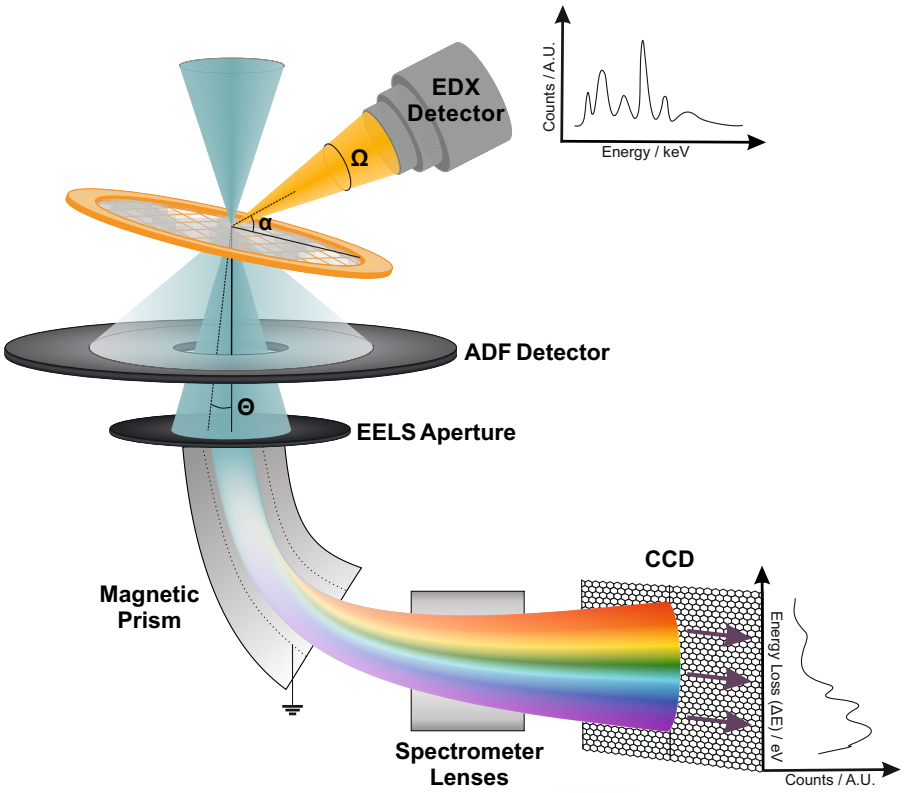


Figure 2.2: Geometry for acquisition of simultaneous EDX, EELS and ADF data. Typically the sample grid is tilted towards the EDX detector to increase the take-off angle α. This reduces the amount of x-rays blocked by the edges of the sample grid. The EDX detector is characterised by its solid angle Ω; typical values are in the range of 0.1–1 sr. Below the ADF detector, an aperture limits the angular range Θ of transmitted electrons coupled into the energy-loss spectrometer. A magnetic prism deflects the electrons through 90° and disperses them in energy. A series of spectrometer lenses focuses the spectrum onto the CCD to be read out.

and Cu grids recorded using a gas proportional detector [67]. While the energy resolution of 1keV was insufficient for more complex analyses, it was sufficient to separate Ag and Cu x-rays for the formation of the first compositional images. Soon afterwards, wavelength dispersive spectrometers (WDS) were employed to enhance the energy resolution available and extend the applications of x-ray microanalysis [68].

At around the same time, semiconductor-based x-ray detectors were developed for use by the nuclear industry to measure radioactivity. Bowman et al. suggested that a detector of this type could be employed in an EPMA, and while it would have slightly lower energy resolution than a WDS, parallel acquisition of x-rays across a broad energy range could be advantageous [69]. Fitzgerald et al. were the first to incorporate a detector of this type into their EPMA, and were able to distinguish characteristic x-rays from all elements between Ca (Z=7) and Zn (Z=12) [70]. The transmission electron microscope and the energy-dispersive x-ray spectrometer were combined for the first time commercially into a single instrument, the "electron-microscope with microanalyser" (EMMA-4), in 1970 [71].

As the sample volume which generates x-rays is set by the size of the electron probe, incorporation of the EDX detector into the STEM means that the spatial resolution is approximately that achievable for imaging. Qualitative chemical imaging of $SrTiO_3$ at atomic resolution was reported by D'Alfonso et al. in 2010 [72], and quantitatively (i.e. with supporting theoretical simulation) by Kothleitner et al. in 2014 [73]. EDX has also been used to locate single heteroatoms; this was shown by Lovejoy et al., who detected single Si and Pt adatoms on monolayer graphene [74]. In modern materials laboratories, EDX is now used routinely alongside ADF imaging to provide complementary compositional information.

2.3.1 The EDX Detector

The fundamental design of a modern spectrometer is largely unchanged from that described by Fitzgerald et al. As shown in Figure 2.2, the window of the EDX detector is positioned as close to the sample as afforded by the microscope configuration. A collimating assembly blocks extraneous electrons and x-rays generated elsewhere within the microscope column, as well as setting the detector solid angle Ω. The value of Ω is dependent on the physical size of the detector aperture, and the distance from the sample; larger and closer mean Ω, and

therefore the recorded counts, are increased. However, as discussed in Section 1.3.5, detector size and proximity are limited by the microscope geometry. A common approach to increase the collection efficiency of the EDX system is to introduce a second detector (or in the case of the FEI *(Hillsboro, OR, USA)* ChemiSTEM, an additional 3 detectors) into the same plane.

Early EDX detectors used a beryllium window to isolate the detector vacuum from the (relatively dirty) microscope column and prevent contaminant build-up on the detector crystal. However, even 8–10 µm of Be film is sufficient to absorb low-energy x-rays, and therefore such detectors could not be used to identify any element with an atomic numbers below that of sodium (Z=11) [75]. As modern (S)TEMs maintain very high vacuum, newer EDX detectors instead use very thin polymer windows (which transmit x-rays with energies above about 0.1 keV), or expose the semiconductor directly to the microscope vacuum. Both allow the detection of very light elements, down to Li (Z=3) in the case of a windowless detector [76].

The final part of the detector is the semiconductor crystal, which converts the energy of an incident x-ray into electron-hole pairs. The number of pairs generated depends on the energy deposited into the semiconductor. Therefore, when a bias is applied to separate the charge carriers, the signal read out is proportional to the x-ray energy (neglecting electrical noise, which may be reduced by cooling the EDX detector). Most detectors use a lithium-doped silicon (Si(Li)) crystal, but inherent challenges in fabricating such materials compromise detector efficiency. The most modern EDX systems use silicon drift arrays, which are supplanting Si(Li) systems due to their reduced noise and minimal requirements for cooling [77].

2.3.2 EDX Spectra

An example of a typical EDX spectrum is shown in Figure 2.3. The energy resolution of such a spectrum depends on the noise introduced by the detector, but is typically about 140 eV for both Si(Li) and SDD systems; this limitation means that even qualitative peak identification can be challenging in samples containing elements with peaks at similar energies [77].

The equation for the detected intensity I_A of a characteristic x-ray for element A is given by Equation 2.1,

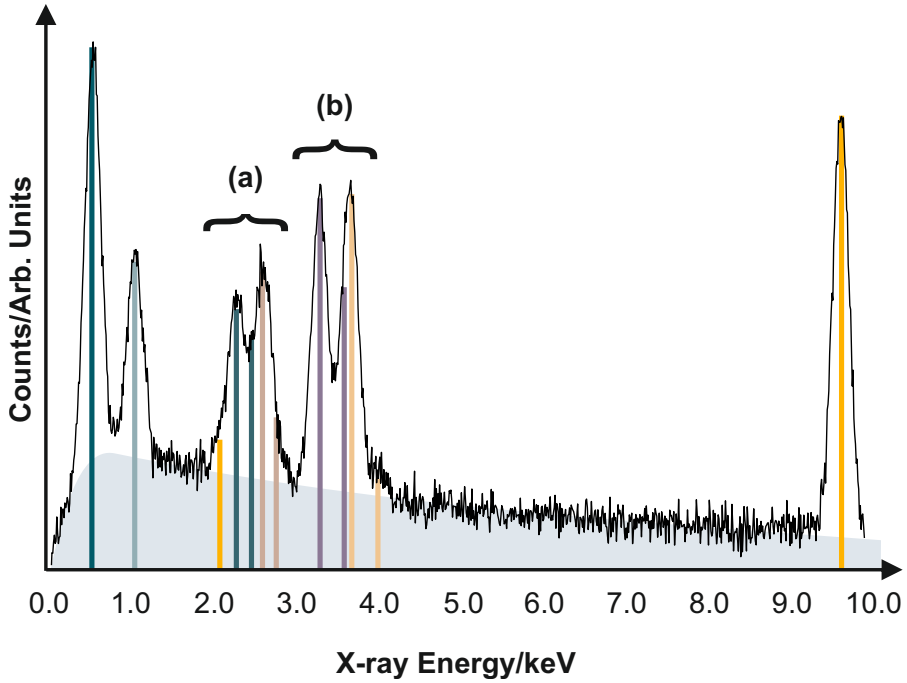


Figure 2.3: Example EDX data for a hypothetical sample containing O, Na, S, Cl, K and Ca on an Au grid. The spectrum is a superposition of background bremsstrahlung intensity (shown here in light blue), and characteristic peaks (indicated by vertical lines). The bremsstrahlung intensity goes approximately as $I_b \propto \frac{E_0 - E}{E}$ (where E_0 is the beam energy, and E is the x-ray energy), but is heavily modified at low energies by self-absorption within the sample. (a) and (b) indicate regions where peak identification is challenging. Region (a) contains the Au M, S Kα and Kβ, and Cl Kα and Kβ peaks (with energies of 2.120, 2.307, 2.465, 2.621 and 2.812 keV respectively), and (b) the K Kα and Kβ, and the Ca Kα and Kβ peaks (energies of 3.312, 3.590, 3.690 and 4.013 keV respectively). The data in this Figure was produced by superimposing Gaussian peaks on the bremsstrahlung background and adding Poissonian noise.

$$I_A = D_e \rho t C_A \frac{N_v}{M_A} \sigma_A \omega_A \alpha_A \frac{\Omega}{4\pi} \epsilon_A, \tag{2.1}$$

where D_e is the electron dose, ρt is the mass thickness, $\frac{\Omega}{4\pi}$ is the detector solid angle, and N_v is Avagadro's number. The concentration of a given element C_A is a property of the sample. The atomic mass number M_A is constant for a particular element, and fluorescence yield ω_A and transition probability α_A are constants for a particular electronic transition within that element. Ionisation cross section σ_A is weakly dependent on the microscope accelerating voltage, and detector efficiency ϵ_A depends on the x-ray energy [78].

An EDX spectrum is a superposition of these characteristic x-ray peaks (with instrumental broadening) and an unavoidable background contribution of bremsstrahlung radiation. These x-rays arise due to the deflection of incident beam electrons within the sample, and have a continuum of energies between zero and the beam energy. Their intensity depends on the sample composition, thickness, density and geometry. As the bremsstrahlung is strongly directional, it can be suppressed to some extent in the microscope; as shown in Figure 2.2, by tilting the sample towards the EDX detector, the take-off angle α is increased, and the bremsstrahlung detected reduced. Tilting also has the advantage of increasing the amount of characteristic x-rays which reach the detector, as shadowing effects from the sample grid are removed [79].

The notation for an EDX peak is formed from two letters. The first letter (K, L, M or N) refers to the shell from which the core electron is displaced. The second character (α, β, γ) describes from which shell the electron filling the hole originates from (one, two or three shells higher than the hole respectively). For example, an Lα x-ray means the hole was created in the second shell, and filled by an electron in the 3rd. The K and L families are the most often recorded in EDX for low-Z elements, and the L and M families for elements with Z>45 (the K family are typically above the range of the detector). The relative intensities of K, L and M lines and α, β, γ transitions are set by quantum mechanical probabilities. Relative line weights have been tabulated by Richie et al., and are maintained in the Electron Probe Quantification library for the US National Institute for Standards and Technology [80]. They are shown to decrease by approximately one and two orders of magnitude for each of β and γ transitions respectively, measured relative to the α. Less variation in intensity is seen between the families of K, L and M edges, although these also decrease for less tightly bound shells.

2.3.3 Quantification of EDX Spectra

"Quantification" of an EDX spectrum generally refers to relating x-ray intensities to elemental concentrations. This was first reported for bulk specimens by Castaing [65]. His approach relied on acquiring spectra from similar samples with known compositions, and determining the elemental concentrations of the unknown sample by linear interpolation.

Equation 2.2 shows this relationship between the ratios of concentration and detected x-ray intensity is moderated by a corrective factor κ:

$$\frac{C_i}{C_{(i)}} = \kappa \frac{I_i}{I_{(i)}}, \tag{2.2}$$

where C_i and $C_{(i)}$ refer to the concentrations of the element i in an unknown and a standard sample respectively, and I_i and $I_{(i)}$ refer to the recorded counts for a given peak in the spectrum. As κ is heavily dependent on x-ray absorption, fluorescence and chemical composition of the sample, the correction is complex to calculate and therefore accurate only for unknown samples with similar properties to the standards.

Cliff-Lorimer k-factors

In 1975 Cliff and Lorimer showed that for a thin film sample of the type suitable for use in the (S)TEM, it was possible to perform quantitative analysis without such stringent requirements on the composition of the standard [81]. By making use of the capability of EDX to simultaneously collect x-rays from all peaks (as opposed to using a wavelength-selecting spectrometer), they showed that the detected x-ray intensities and the concentrations of elements A and B in a given sample were related by Equation 2.3:

$$\frac{I_A}{I_B} = k_{A,B} \frac{C_A}{C_B}, \tag{2.3}$$

where I_A and I_B refer to peak intensities, C_A and C_B to their concentrations, and the constant of proportionality $k_{A,B}$ is a function of the detector and element under investigation.

By taking a ratio of intensities, dependencies on electron dose, detector size and mass

thickness are removed, and values of $k_{A,B}$ may therefore be directly applied for quantification of other samples containing elements A and B (provided they are measured on the same system). Experimentally, the value of $k_{A,B}$ is calculated using intensities I_A and I_B measured from spectra recorded from a standard with known C_A and C_B; Cliff and Lorimer achieved this by using powdered mineral samples to produce a library of $k_{A,\mathrm{Si}}$ values for different elements relative to silicon, but in principle any element pair may be used.

The accuracy of the calculated k-factors depends heavily upon the quality of the standard samples used as references. The challenges posed in producing suitable reference standards for measuring k-factors for other element pairs were swiftly appreciated, and discussed extensively in the literature published shortly after Cliff and Lorimer's original paper [82]–[84]. In brief, the first obstacle is that the sample must remain stable under the electron beam, so that the concentrations of each element remains constant. A further complication is that the requirement for thin films (to reduce absorption effects) means that the number of x-rays generated is inherently small, and the corresponding error on I_A and I_B is therefore increased; as shown by Zaluzec and Fraser, this problem is not wholly solved by longer experimental acquisition, as contaminant build-up may result in x-ray absorption effects [85].

In addition, the standard sample must be homogeneous not just at the relatively large length scales probed by e.g. x-ray diffraction or mass-spectrometry, but also at the nanoscale [78]. Even if the EDX standard is produced from a bulk specimen, retaining this homogeneity may be problematic; Doig and Flewitt reported extensive compositional variation in their Fe-5%Ni alloy as a result of their preparation methods, concluding that "each case of micro-analysis must be treated on its merits" [86]. It is also possible to calculate k-factors from first principles. These calculations require good knowledge of the EDX detector efficiency as a function of energy, and of the cross-section for a particular ionisation event and the fluorescent yield for a particular electron transition. The use of theoretical k-factors is generally sufficient for quantification of elements with Z>16 [87]. However at lower energies, where inaccuracies in these parameters are felt more keenly, theoretical values may increase the error of the measured concentration to more than 20%, depending on which elements and which families of x-rays are measured [88]. In cases where k-factors are measured by the user, despite the emergence of new nanofabrication techniques for making standards (e.g. by focused ion beam milling [89]), unfortunately the accuracy of the concentration measurement is ultimately still limited to ±5-10% in the best

	k-factor	ζ-factors
Key Equation:	$\frac{C_A}{C_B} = k_{A,B}\frac{I_A}{I_B}$	$\rho t = \zeta_A \frac{I_A}{C_A D_e}$
Experimental Factor Determination:	$k_{A,B} = \frac{C_A/C_B}{I_A/I_B}$	$\zeta_A = \frac{\rho t I_A}{C_A D_e}$
Factor Calculation:	$k_{A,B} = \frac{M_B}{M_A}\frac{(\sigma\omega\alpha\epsilon)_A}{(\sigma\omega\alpha\epsilon)_B}$	$\zeta_A = \frac{M_A}{N_v \frac{\Omega}{4\pi}(\sigma\omega\alpha\epsilon)_A}$

Table 2.1: Comparison between the key equations of Cliff-Lorimer k-factor EDX quantification, and Watanabe and Williams's ζ-factor method. The values of $k_{A,B}$ and ζ_A may be measured experimentally, or from first principles.

case [88].

Watanabe-Williams ζ-factors

A more recent method for quantifying EDX spectra using "ζ-factors" has been developed by Watanabe and Williams [88]. Their method does not depend on ratio measurements; instead, a ζ-factor is calculated just once for a particular element. This is arguably a more straightforward approach, as the Cliff-Lorimer method requires calculation of $k_{A,B}$ pairs for all elements present within the sample. The requirements for the standard sample are also reduced for calculation of ζ-factors; pure element references (with no error on concentration) may be used, either as thin films or more recently as nanoparticles [90].

The ζ-factor method relates the concentration of a given element A to the measured x-ray intensity using mass-thickness. The thickness of the sample t may be measured using e.g. electron energy loss spectroscopy (see Section 2.4.3), and the electron dose may be measured in-situ at the time of the experiment. A comparison of the key equations for both Cliff-Lorimer and the ζ-factor method is shown in Table 2.1.

The ζ-factor method may also be more trivially extended to incorporate the effects of absorption [91]. Watanabe and Williams noted the profound effects of absorption on low-energy

x-rays (i.e. light elements), and the challenges of applying such a correction to Cliff-Lorimer (namely the requirement to know density and thickness of the sample). In the ζ-factor approach, absorption may be corrected iteratively and without this prior knowledge, resulting in decreased errors in final composition measurements. Watanabe and Williams were also able to show how measurements of ζ-factors for just a few elements may be used to estimate ζ-factors for the remainder of the periodic table, lessening the experimental demands of the method.

However, relatively few examples of quantification using Watanabe and Williams's approach appear in the literature. Published results are mainly limited to inorganic samples (e.g. [92], [93]) and no presently available commercial analysis software utilises this method. In comparison, the Cliff-Lorimer or k-factor method is still widely used today, and is one of the most commonly included analysis routines on commercial EDX software. Manufacturers may require the software to be calibrated using a standard sample (e.g. Aztec from Oxford Instruments *(Abingdon, UK)*), or may rely on theoretical calculations (e.g. GMS3 from Gatan *(Pleasanton, CA, USA)*).

2.4 Electron Energy Loss Spectroscopy

Electron energy loss spectroscopy of transmitted electrons was first performed by Hillier and Baker in 1944. They observed energy-losses from interactions with the K-, L- and M-shells for elements between Be and Zn, by coupling their EPMA to a dispersive spectrometer [64]. A thorough review of the different approaches for translating energy-loss spectroscopy into the TEM is given by Egerton in Ref. [94].

Spectrometers for EELS became commercially available in the early 1980s in the form of the Gatan 607, which formed a spectrum by electrostatically sweeping energy-dispersed electrons across a slit [95]. Krivanek et al. were the first to report parallel collection across a broad range of energy losses by incorporation of additional lenses and a photodiode array [96]. This greatly enhanced the spectrometer collection efficiency relative to serial systems, which required the spectrum to be measured channel-by-channel, and the time required to measure a single spectrum was reduced from c.100 s [97] to under 1 s for the same number of energy channels [96].

As a result of the reduced acquisition time, challenges surrounding beam damage and sample drift were reduced, and pixel-by-pixel chemical analysis became feasible. In 1989,

Jeanguillaume and Colliex presented the first discussions of spectrum-imaging as enabled by parallel collection [98]. This was achieved experimentally by Hunt and Williams, who recorded EEL spectrum images for CuBeCo samples and for freeze-dried beta cells [99].

Owing to the enhanced collection efficiency of signal (relative to EDX) for low-Z elements, many early applications of EELS were to biological samples; this will be discussed further in Chapter 3. However, many modern results have been concentrated around inorganic materials; improvements in microscope spatial resolution and energy resolution of the spectrometer mean that atomic-resolution EELS [100] and single atom detection [101] are possible. In addition, the nature of the electron-sample interaction means that EELS is capable of providing not just compositional information, but also details concerning chemical bonding and surface properties of the sample [102], [103]. A recent review by Krivanek et al describes how improvements in electron beam monochromation and spectrometer energy resolution have enabled new techniques such as aloof-EELS and vibrational spectroscopy [104]. Together with providing chemical information, such methods therefore render EELS a powerful complementary technique to imaging in the STEM.

2.4.1 The EEL Spectrometer

At the time of writing only a handful of companies manufacture spectrometers for EELS. In addition to in-column spectrometers produced available from JEOL *(Akishima, Tokyo, Japan)*, post-column spectrometers (which may be attached to almost any (S)TEM) are produced by Gatan, CEOS GmbH *(Heidelberg, Germany)* and Thermofisher *(Waltham, MA, USA)*. Nion *(Kirkland, WA, USA)* also produce dedicated spectrometers for their own microscopes, with a strong concentration on monochromatic application. Regardless of the exact model, the spectrometer design is similar to the original proposed by Krivanek et al [105]. The spectrometer installed on the Oxford JEOL ARM-200F is a Gatan Imaging Filter (GIF) Quantum, and in this section the term 'GIF' will be used interchangeably with spectrometer.

As shown in Figure 2.2, transmitted electrons enter the GIF through an aperture which controls the acceptance angle of the spectrometer. These electrons are subsequently deflected through 90° by a magnetic prism, which causes electrons with differing kinetic energies (i.e. which have different energy losses) to disperse spatially. The magnetic prism also provides first-order

focusing onto the back focal plane of the spectrometer. A combination of deflectors, quadrupole and sextupole lenses act together to optimise the projection of the dispersed electrons onto the recording device (typically a CCD or CMOS sensor) [106]. The prism and these additional lenses introduce aberrations related to those discussed previously for the microscope lenses, and are countered by a combination of automated and manual aberration tuning to optimise the focusing of the dispersed beam onto the CCD/CMOS.

In the most modern EEL spectrometers, the CCD/CMOS may be replaced by a direct-detection camera which eliminates some of the noise effects and allows for greater sensitivity to low count rates [107]. Gatan Imaging Filters also retain the capability to perform energy-filtered TEM (where an image is formed only from electrons which have lost a energies within a given range), and direct detectors are particularly suitable for these applications.

2.4.2 Electron Energy Loss Spectra

A typical electron energy loss spectrum is shown in Figure 2.4. The spectrum may be broadly divided into two parts; the low-loss region with energy loss $\Delta E = 0 \sim 50\text{eV}$ and the core-loss region with $\Delta E = 50+\text{eV}$. Each of these regions is further subdivided as described by Egerton [94], and briefly discussed below.

Low Loss Region: $\Delta E = 0 \sim 50\text{eV}$

The main features of the low-loss region are the zero-loss peak (ZLP) and the plasmon. The ZLP contains electrons which have not interacted with the sample, and those which have undergone elastic or quasi-elastic scattering. The full-width-half-maximum (FWHM) of the ZLP limits the spectral energy resolution, and is around 0.5–1 eV in a typical analytical electron microscope. Instruments with monochromatic electron sources may reach energy resolutions of sub-10 meV [109], which may then be used to measure energy losses in the $\Delta E \sim$10–100 meV region which associated with collective sample excitations (phonons).

The plasmon region is mostly contained between 1$\sim$50 eV. The signal in this region originates from collective excitations of valance electrons, and may therefore be used to probe local band structure. This region may also be used to calculate sample thickness and to deconvolve the

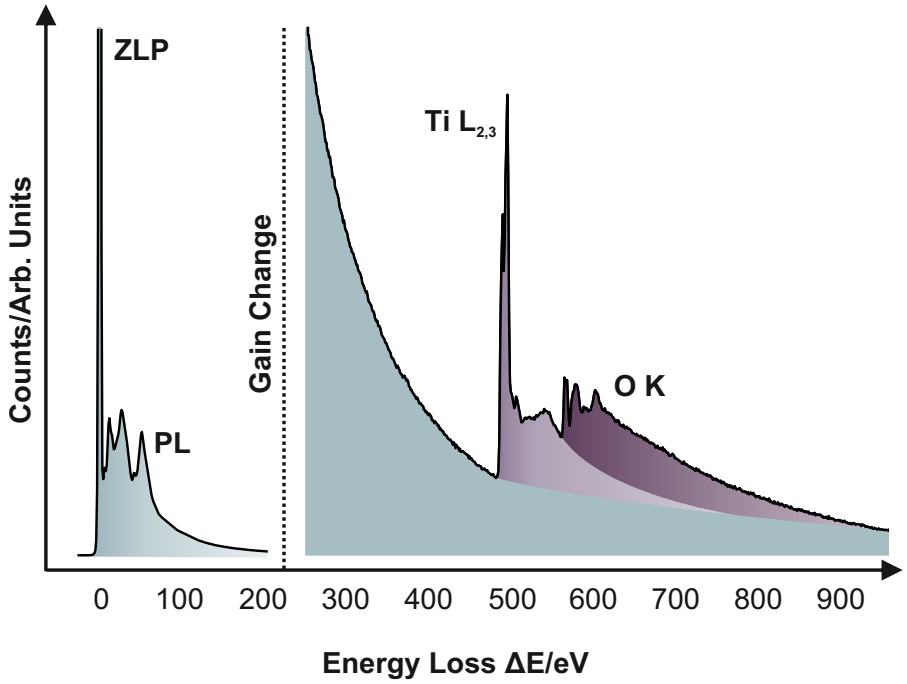


Figure 2.4: Example spectrum of thin-film TiO_2 from Gatan's EELS Atlas [108]. The most intense feature is the zero-loss peak (ZLP), which contains electrons which have passed through the sample without interacting. The plasmon region (PL) is mostly contained in the 0–50 eV region; however, the tail of the plasmon extends for many hundreds of eV and provides a significant background contribution to core-loss measurements. At higher energy losses, the Ti $L_{2,3}$ and O K edges are seen at ΔE of $\sim$ 460 eV and 532 eV respectively.

effects of plural scattering in thicker samples (see Section 2.4.3) [110]. In addition, the plasmon tail extends for many hundreds of eV, and provides a significant background contribution even at higher energies.

Core Loss Region: $\Delta E = 50$+eV

The core-loss region contains ionisation edges which are characteristic of the elements contained in the sample. As discussed in Section 2.2, when an incident beam electron undergoes an inelastic interaction with a localised core-shell orbital in the sample, it loses an amount of energy equal to or greater than the binding energy. This is recorded in EELS as signal which extends over many eV, and is proportional to the amount of element present at that probe position.

The notation used to describe core-loss edges reflects that EELS is able to directly measure the effects of interactions with specific subshells. The letters K, L, M, N, O and P have the same meaning as in EDX. However, as EELS has significantly higher energy resolution and is therefore able to measure much smaller energy differences, a number subscript is used to distinguish between suborbitals where relevant. For example, the O K edge in Figure 2.4 arises due to a perturbation of the 1s orbital, and the Ti $L_{2,3}$ edge from the 2p states.

As the exact energy losses experienced by a beam electron depend on the local bonding environment, it is also possible to use the edge shape to retrieve structural information about the sample (e.g. [111]). Edge shapes change significantly for different orbital interactions (see e.g. the difference between the "white lines" of Ti $L_{2,3}$ and the shape of the O K edges in Figure 2.4); this can complicate the quantification procedure, particularly for trace elements.

2.4.3 EELS Quantification

Quantification of EELS data may refer to a number of processes. In the context of this thesis, 'quantification' means making a measurement of elemental concentrations using core-loss edges. This requires a multi-step procedure, and is generally more complex than the equivalent calculation for EDX spectra. In a broader context, quantification may also refer to extraction of parameters such as the sample band gap and phonon behaviour. Details on approaches for analysis of the low-loss regimen and the edge fine structure may be found in Ref. [112].

Measurement of sample thickness

One of the first parameters which may be measured using EELS is sample thickness, t. As t increases, so too does the probability of an incident electron undergoing an inelastic scattering event. It can be shown that

$$t = \lambda \ln \frac{I_T}{I_{ZL}} \approx \lambda \ln \frac{I_{LL}}{I_{ZL}}, \tag{2.4}$$

where λ is the inelastic mean free path, I_T is the total intensity for the spectrum, and I_{ZL} is the intensity under the elastic zero-loss region [113]. As the most probable inelastic interaction is a plasmon excitation, I_T may also effectively be re-written as the sum of the zero-loss and plasmon intensities I_{LL}.

This approach is generally suitable for samples with $0.1\lambda < t < 4\lambda$. A significant contribution to error in thickness measurement arises from difficulties in ascertaining the inelastic mean free path. λ is a function of the sample composition (which is itself not necessarily constant), and therefore the error on a measurement of t is approximately $\pm 10\%$ [113].

EELS Background Parameterisation

The first consideration for elemental quantification is the nature of the EELS background. Core edges are superimposed on the decaying tails of the plasmon excitation and any preceding edges (in contrast with EDX, which has a single source of background radiation). In cases where the background is sufficiently 'well-behaved' (i.e. the core-loss edge of interest is sufficiently separated from the plasmon and any other core edges), the background intensity I_b at an energy loss ΔE may be modelled with a power-law:

$$I_b = A(\Delta E)^{-r}, \tag{2.5}$$

where A and r are constants. However, such this background is only valid for a small energy range around ΔE, as A and r are themselves functions of energy loss. For more complex background behaviour, the power law model may fail and window methods or fits to reference spectra may be required to accurately remove contributions from I_b [114].

Deconvolution

Another consideration for edge quantification is the effect of plural scattering, which acts to blur the spectrum and ultimately decreases the energy resolution. A number of methods are available to decouple these effects from the single scattering behaviour, but the most commonly used techniques are based on Fourier deconvolution.

The Fourier-Log method may be performed before the background subtraction step described above, and requires the whole spectrum (including the ZLP, the plasmon and any ionisation edges) to be recorded as a continuum.This is challenging for spectra with features at high energy-losses, as the low-loss region may saturate the CCD before any considerable signal can be measured for the ionisation edge. The Fourier-Ratio method allows the low-loss and core-loss regions to be acquired separately (i.e. using DualEELS). However, the edge background must be removed before the calculation can be applied, and additional noise may be introduced by this step. Full details for both calculations may be found in Ref. [115], and both approaches are built-in to many tools for EELS analysis (including Gatan's GMS3 and the open-source Python library Hyperspy [116]).

Deconvolution is particularly useful for cases where the sample thickness exceeds about 0.3-0.5λ, and for improving the signal-to-background ratio of weak signals, such as those generated by trace elements, by removing the edge broadening induced by plural scattering [117].

Element Concentration Measurement

Following appropriate background subtraction and deconvolution, the remaining edge intensity results purely from the inelastic interaction with the sample. For quantification, this intensity is integrated over an energy window, the size of which must be chosen carefully. A small integration window will contain a low number of counts, but a window which extends far from the edge onset will have a more poorly-modelled background. The integrated intensity I_X is a function of probe semi-convergence angle α, spectrometer collection angle Θ, integration window R_{E2-E1} and microscope accelerating voltage E_0. It is related to the areal density $n_X t$ of element X by Equation 2.6:

$$n_X t = \frac{I_X(\alpha, \Theta, \mathrm{R_{E2-E1}}, \mathrm{E_0})}{I_{LL}(\alpha, \Theta, \mathrm{R_{E2-E1}}, \mathrm{E_0})\sigma(\alpha, \Theta, \mathrm{R_{E2-E1}}, \mathrm{E_0})}, \tag{2.6}$$

where σ is the partial ionisation cross-section, and describes the detection probability for a given ionisation event. The value of σ may be calculated from first principles (matching the values of α, Θ, R_{E2-E1} and E_0 from the experiment) by either a hydrogenic model or by the Hartree-Slater method [115]. Provided the integration window R_{E2-E1} is sufficiently wide, σ is accurate to within 5% [118].

Due to the complexities in deconvolution of multiple scattering, modelling the EELS background, choice of the correct integration region, and calculation of the partial ionisation cross-section, core-loss EELS quantification can be very challenging. Other approaches, such as those based on statistical modelling (e.g. EELSModel [119]), still rely on many of the same inputs and are therefore also not straightforward.

2.5 Comparison of EDX and EELS

As discussed extensively in this chapter, both EDX and EELS are established techniques to perform chemical analysis in the STEM. As both arise from the same inelastic interaction within the sample, it is appropriate to compare them in terms of their quantification accuracy and detection sensitivities. These factors, alongside other considerations which affect elemental detection using EDX and/or EELS, are summarised in Table 2.2.

Accuracy

For core-loss EELS, the accuracy of the quantification which can be achieved is limited by inherent effects from the sample (particularly multiple scattering requiring deconvolution), and the accuracy of the calculated cross-sections and extrapolated background fitting. For most experiments, the accuracy is estimated to be between 5-15%, depending on the edge used [94], [120]. For EDX, the accuracy typically ranges between ±10-20%, but can be as high as 50% for low-Z elements [79].

	EDX	EELS
Accuracy	5-50%	5-15%
MMF	10^{-19}–10^{-22} g	10^{-18}–10^{-22} g
Energy Range	10–20 keV	∼2 keV
Energy Resolution	∼120 eV	<1 eV
Spatial Resolution	May be poorer than limit of microscope	∼Limit of microscope
Other Considerations	• Thicker samples OK • More affected by mass loss • Peak overlaps problematic • More user-friendly	• Thinnest samples required • More efficient signal collection • High background problematic • More user-intensive

Table 2.2: Comparison between factors influencing quantitative elemental measurement in EDX and EELS.

Detection Sensitivity

Another consideration is the detection sensitivity, which describes the minimum detectable amount of an element within a particular sample volume. It may be stated as the minimum mass fraction (MMF) in wt% or parts-per-million, or alternatively as the minimum detectable mass (MDM) in absolute units (e.g. atoms, moles etc).

For EDX, the MMF is defined by Equation 2.7:

$$MMF \propto \frac{1}{\sqrt{P(P/B)\tau}}, \tag{2.7}$$

where P is the characteristic peak counts, $P{:}B$ is the peak-to-background ratio, and τ is the total measurement time at that probe position [121].

The value of P is increased for thicker sample areas and higher probe currents, and the value of $P{:}B$ is increased by use of higher accelerating voltages (as less Bremsstrahlung is produced by faster electrons). However, higher accelerating voltages also reduce the ionisation cross-section, so the dependence is not linear. The value of τ is described by Williams and Carter as "a direct

function of your patience" [122]; it is also a function of how robust the sample is under the electron beam.

Values of MMF for EDX reported in the literature are varied. Shuman and Somlyo report 0.9×10^{-19} g for Fe, measured under cryogenic conditions to suppress the background [123]. This is in agreement with the theoretical work of Joy and Maher who calculated that the MDM for elements between Z=10 (Ne) and Z=40 (Zr) would be of the order of 10^{-20} g [82]. However, in both cases these values were calculated for thermionic emission sources and detector solid-angles of less than 0.005 sr; modern cold-FEG electron sources and larger EDX detectors may therefore improve these values further [124].

When detection sensitivity is quoted as an MDM, values range between 0.1-1% [122]. While relatively poor in comparison to other techniques (e.g. EPMA with 0.01% sensitivity), as the analysis volume is so small this value corresponds to sensitivity to a very small numbers of atoms. A modern STEM with a C-FEG may have probe current densities many orders of magnitude higher, and an EDX detector with 20× greater solid angle, and the MMF/MDF is therefore correspondingly lower [125].

In contrast to EDX, where the peak-to-background ratio $P : B$ dominates the MMF and MDF values, for EELS it can be shown that the detection sensitivities instead depend on the signal-to-noise ratio (SNR) [113]. This in turn depends on the spectrometer collection angle, the energy window chosen for signal integration, and the edge ionisation cross-section. Maigne showed how the signal-to-noise ratio may be maximised by setting the spectrometer collection angle to around $3\theta_c$ [126], where θ_c is the characteristic angle and given (non-relativistically) by:

$$\theta_c = \frac{\Delta E}{2E_0}. \tag{2.8}$$

Unlike in EDX, the background cannot be suppressed by tuning the experimental parameters. The signals which contribute to a high background count (and therefore lower the SNR) are largely determined by the sample and are therefore unavoidable.

Isaacson and Johnson, and Krivanek et al, made early reports of EELS MMF and MDM values of 10^{-18}–10^{-22} g and 0.1 atomic% for elements 5<Z<15 and Z=Th respectively [127], [128]. Unlike for EDX, where the sensitivity is relatively constant for elements with Z>10, as

the shape and extent of the EELS edge is highly variable this has a corresponding impact on the detectable MMF [129].

Leapman and Hunt showed that the analytical sensitivity of EELS (as measured for $L_{2,3}$ lines) is between 1.4 to 10 times greater than that of EDX, and that the improvement is strongly dependent on the edge chosen [130]. However, it should be noted that this comparison was made using EDX data recorded from a Si(Li) detector. As discussed by Zaluzec, windowless SDD detectors may reduce this gap significantly [125].

Other Considerations

As shown in Table 2.2, neither EDX nor EELS is fully able to chemically analyse a sample with equal accuracy and sensitivity for all components. What is not easily captured in discussions concerning quantification accuracy and limits on MDF/MMF are more general considerations relating to the nature of the sample under investigation. For example, EDX measures x-rays across a broad energy range, meaning all elements in the sample are captured in the data simultaneously. In comparison, the energy range of an EELS dataset is determined by the user's choice of energy dispersion, but is at most 2 keV. The energy resolution of EELS is significantly higher than that of EDX, which means edge overlaps (and resulting challenges for quantification) may be reduced; however, background effects and the influence of plural scattering means the data is less directly interpretable than EDX.

In samples which contain elements with both low and high atomic numbers, neither EDX or EELS alone are sufficient to fully characterise the sample. Low detection efficiencies and low fluorescent yields compromise EDX detection of low-Z elements, and energy losses above $\sim$2 keV for heavier elements are beyond reach of current EEL spectrometers. In practice, most analytical electron microscopes have both EEL spectrometers and EDX detectors to maximise their applications for elements across the periodic table. Hanssen et al describes this as a "Christmas-tree" TEM which has the best of both worlds, and is able to provide the fullest picture of a complex sample [131].

2.6 Summary

Inelastic interactions in the STEM may be measured using EDX and EELS. EDX measures the characteristic x-rays produced as a result of a dexcitation by an ionised sample atom. The technique suffers from poor counting statistics due to low fluorescent x-ray yields and small detector areas, but is superior to EELS for heavier elements. Spectra are often quantified using the Cliff-Lorimer k-factor method, or Watanabe and Williams's ζ-factors. EELS has a significantly improved collection efficiency relative to EDX, particularly for light elements. However, quantification of core-loss edges requires intensive data processing - namely background subtraction, deconvolution of plural scattering, and careful signal integration - to obtain accurate results.

A number of practical considerations, alongside those of accuracy and minimum detectable limits, determine which approach is best for which sample. Where possible, measurement of both EDX and EELS simultaneously offers the most flexible and comprehensive information.

Chapter 3

STEM in Life Science

3.1 Aims & Scope

As discussed in Chapters 1 and 2, the STEM affords access to a considerable number of image and spectroscopic signals. In this first part of this Chapter, applications of HAADF imaging in biology are discussed, with a particular emphasis on the work which followed shortly after the development of the modern STEM. The latter half of this Chapter will review applications of EDX and EELS in similar samples, with a concentration on the particular challenges of applying these methods in complex chemical environments.

3.2 STEM Imaging Applications in Life Sciences

The use of electrons for imaging biological specimens has a long and distinguished history. Early experiments in the transmission electron microscope led to a number of fundamental discoveries about cellular ultrastructure [132], in large part due to rapid improvements in both TEM resolution and sample preparation techniques. These works resulted in the first observations of organelles such as the ribosome [133] and endoplasmic reticulum [134], along with the providing conclusive evidence of the existence of a cytoskeletal network [135] and sub-structure within mitochondria [136], [137]. In recent years TEM methods have continued to play a key role in biology; nowhere is this more evident than in the critical information provided recently by studies of the SARS-CoV-2 (COVID-19) virus [138].

As discussed in Section 1.2, Albert Crewe's original vision for the STEM was as a tool for biological imaging. In fact, his first discussion of the full instrumental design of the STEM was published in the *Journal of Molecular Biology*, alongside the results of experiments using inelastically scattered electrons in different imaging modes applied to biological samples [139]. Similarly, the first demonstration of Z-contrast in ADF was shown using images recorded from single strands of deoxyribonucleic acid (DNA) stained with low concentrations of uranyl acetate [140]. Many other early results were also concentrated on applications in the life sciences, and are summarised in Ref. [141].

Although conventional TEM imaging achieved single-atom resolution around the same time as the STEM, the contrast produced by the amorphous background posed a significant challenge for image interpretation [40]. While it was hoped that STEM methods would bring considerable improvements for high-resolution biological imaging, it is debatable to what extent Crewe's original vision has been realised. Despite promising early results, the advent of aberration-correction has meant STEM methods have found far more numerous applications in the physical sciences. In parallel, improvements in both TEM techniques and non-EM based methods have largely supplanted the STEM as a tool for biological research.

In this Section, the most significant contributions of the STEM in biology will be explored. These are divided into discussions of STEM-based measurement of macromolecular masses, contributions to structural biology, and finally to labelling applications.

3.2.1 Macromolecular Mass Measurement

Arguably the most significant contribution of STEM imaging in the life sciences is to the measurement of the masses of large biological molecules. While such measurements were initially attempted in the TEM, both variations in the image contrast and the requirement to deduce mass indirectly by analysing the optical transmission through the recorded micrograph, severely limited practical applications of the technique [142].

Upon development of the STEM, and particularly following progress made in "Z-contrast" imaging, mass measurement in the electron microscope became a considerably more feasible goal. Operating out of Crewe's laboratory, Lamvik was amongst the first to demonstrate such measurements by using the inelastic electron scattering to investigate muscle thick filament [143].

Previous efforts using indirect techniques generated inconsistent estimates of the number of myosin molecules per repeat filament unit, and introduced considerable confusion as to the mechanisms of contraction in muscle. By measuring the scattering generated by tobacco mosaic viruses (TMV), which had a well-known mass-per-length of 1.4 Daltons/nm [144], thick filament mass could be measured directly to show conclusively that it contained exactly three myosin molecules per 14.3 nm repeat.

These initial results showed showed the suitability of the STEM for addressing similar biological questions, especially those where mass-per-length (MPL) or mass-per-area (MPA) was a more characteristic parameter than a simple measurement of total mass. Several early publications highlighted the advantages afforded by this approach over other analysis techniques [145]–[147], namely that STEM-based measurement was largely insensitive to molecular size and shape (unlike chemical methods such as liquid chromatography), and could be used to distinguish heterogeneous populations in the sample (unlike bulk-averaging techniques). Comprehensive reviews of STEM mass measurement are available from Wall and Hainfeld [148], Thomas et al. [149] and Muller and Engel [150], and two illustrative examples will be discussed here.

Amyloid Fibrils

STEM-based methods are particularly well-suited to the characterisation of filamentous structures, where high degrees of variation in fibril/fiber length are challenging to address by other methods. A particularly notable application can be found in investigations undertaken on the structure and assembly of amyloid fibrils, which are proteins with atypical conformations whose aggregates are implicated in the development of a number of human diseases [151].

Goldsbury et al. used ADF STEM to examine self-assembly in human amylin, showing that the polymorphic structures observed in their sample had MPL values which were integer multiples of that of the 5 nm protofibril [152]. By combining mass and width measurements, the authors were further able to discern structural information, discriminating between two distinct coiled arrangements of equivalent MPL. While qualitative descriptions of amyloid had previously been generated by TEM studies [153], the results of Goldsbury et al. provided the first quantitative evidence of the structured aggregation and self-assembly behaviours which have since been found to be common to all amyloid fibrils. STEM measurements have subsequently

been used in combination with other techniques to model the full atomic behaviour of fibril association; a detailed review of the role of ADF in this characterisation may be found in Ref. [154].

GroEL & GroES

ADF STEM mass measurement has also been applied successfully to non-fibrous structures, as demonstrated in the study of the GroEL and GroES proteins. Both GroEL and GroES are molecular chaperones which work together to facilitate the correct folding of other proteins in *Escherichi coli* bacteria [155].

While the first demonstration of the seven-fold symmetry of GroEL was first shown using ADF STEM [156], the majority of subsequent studies on the GroEL-GroES complex were performed using TEM techniques. These attempts to understand the interplay between GroES and GroEL had generated conflicting theories about intracellular function, due to radically different observations in the microscope. Chen et al. reported cryo-TEM observations of attachment of GroES at one end of the GroEL cylinder to form a "lid", which supported theories that suggested protein folding occurred inside the cavity complex [157]. In parallel, Azem et al. observed that GroES attached at both ends of GroEL when in the presence of adenosine triphosphate (ATP), and concluded that protein folding therefore likely occurred on the outer surface of the GroEL-$GroES_2$ complex [158].

In both studies only side-on views of complexes were considered, as in the TEM top-down views of GroEL, GroEL-GroES and GroEL-$GroES_2$ were indistinguishable. However, this was not the case in the STEM. Engel et al. made mass measurements from ADF images without orientation bias, showing the differences in the elastic scattering generated by each complex were sufficient to distinguish them individually and when coalesced [159]. Their analysis showed that GroEL-GroES was significantly more likely to be orientated in the beam direction, and that measurements made only from side-on projections alone therefore grossly overestimated the relative abundance of GroEL-$GroES_2$. Later work has confirmed that protein folding occurs inside the GroEL-GroES cavity, while questions concerning the functional role of GroEL-$GroES_2$ remain outstanding [160].

Comparative Mass Measurement vs. First-Principles

The majority of applications of ADF macromolecular mass measurement to date have largely utilised comparative methods similar to those pioneered by Crewe and coworkers. However, as discussed in Chapter 1, it is increasingly common for quantification to be achieved through comparisons with image simulation. Sousa and Leapman demonstrated the applicability of this approach in biological samples, using partial elastic scattering cross-sections to successfully measure the MPL of TMV in a 300 kV STEM [161].

Whilst Sousa and Leapman suggested that this approach may be more beneficial than use of a reference particle, in practice it appears that few others agree. As noted by Wall, the use of an internal calibration standard affords other benefits which may be missed when employing first-principles calculations[162]. Inclusion of standards provides qualitative information about sample quality, as irregularities in their appearance allude to sample preparation issues. An example may be found in Figure 1b of Ref. [163], where dark-field TEM images of TMV particles show enhanced contrast around their perimeter. Inadequate removal of the buffer solution when transferring the TMV would lead to a dried build-up of salt and likely appear similar to these images. In a quantitative experiment, this residue would artificially increase the TMV image intensity and lead to an artificial decrease in the measurement of other unknown masses.

The inclusion of a standard also affords a means to detect electron beam-induced damage, with mass loss being of particular relevance in this case [164]. Mass loss is highly dependent on the individual sample; Wall and Hainfeld have reported losses of up to 100% for lipids and polysaccharides, but as little as 2.5% for proteins at the same electron dose [148]. Muller and Engel have subsequently shown that the effects of mass loss may be corrected to first order through comparison with the standard (provided it is of similar composition to the molecule of interest) [165], or when the damage is dependent upon total electron dose [166].

Future Prospects for ADF Mass Determination

A key benefit of ADF-based mass determination is that measurements can be made simultaneously and across many orders of magnitude. This is shown by the considerable range reported in the literature, with sub-50 kDa masses and 1 GDa macromolecules accurately characterised using

STEM methods [167], [168].

In spite of these successes, there are relatively few contemporary applications detailed in the literature. Modern mass spectrometry (MS) is increasingly able to probe details of macromolecular structure and dynamics, and has thus eliminated many of the prior challenges which motivated the development of STEM-based techniques [169]. Following the publication of several reflective discussions on the contributions of ADF in this area [170]–[172], few (if any) groups remain active in measuring macromolecules in the STEM; a survey of the literature found only a single recent example [173]. However, similar methods to those described here have been successfully adopted for quantification of heavier elements in biological specimens, and these examples will be highlighted throughout the remainder of this Chapter.

3.2.2 Structural Determination and Tomography

In addition to mass determination, STEM methods have also been extensively applied in structural biology. Understanding the organisation and function of biological macromolecules is critical in elucidating fundamental subcellular processes. In many cases, this information may be obtained using techniques such as x-ray crystallography, which has been the dominant method for structural determination for several decades [174]. However, there are a number of historical literature examples where ADF STEM successfully determined aspects of structure and function which were then unobtainable using other methodologies.

Chromatin

An example may be found in the difficulties faced in understanding the of structure in chromatin, a DNA-protein complex found in the chromosomes of eukaryotes [175]). As reviewed by Comings in 1972, much of the contemporary TEM and x-ray diffraction (XRD) data from chromatin was heavily disputed, with even the most basic structural properties contested [176].

A short time later, Langmore and Wooley were able to conclusively determine several key parameters of chromatin using ADF STEM [177]. While considerable uncertainty around fiber diameter had been generated by TEM studies due to the use of heavy metal stains, the image contrast afforded by their high-angle elastic scattering was sufficient to make accurate

measurements of the 30 Å fiber diameter from unstained and unfixed samples. They were further able to utilise the mass-thickness contrast inherent to ADF STEM to determine for the first time that the subunits of chromatin (histones) were non-spherical. Langmore and Wooley proposed a flattened disk shape which was later confirmed by neutron and x-ray scattering experiments on purified crystallised histones [178].

Ferritin

A further example of structural determination using ADF STEM may be found in early examinations of ferritin (a protein for iron storage [179]). X-ray and electron diffraction experiments had showed that a fraction of the iron core was crystalline [180]. However, the diffraction patterns recorded did not match any known crystallographic arrangement, and there was therefore considerable uncertainty about the nature of iron storage within the protein. Massover and Cowley used dark-field TEM to image lattice planes within the ferritin core, and measured spacings which agreed with a model proposed from diffraction data [181]. Ohtsuki et al. later found consistent values using ADF STEM [182], but with the significant benefit that the image signal was sufficient to distinguish for the first time sub-structure within the ferritin core. Such information had not been attainable from previous TEM experiments due to the complex contrast mechanisms which complicated image interpretation.

Future Prospects for STEM in Structural Biology

Despite some early successes, similarly to applications in macromolecular mass measurement, the role of ADF STEM in structural biology has in the present day been largely superseded by other techniques. In particular, developments in cryo-transmission electron microscopy (cryo-TEM) mean that biological structures can be solved to near-atomic resolution in the course of an afternoon. More than 10,000 such structures have been deposited in the Electron Microscopy Data Bank, and at the time of writing, the highest spatial resolution achieved for a single-particle reconstruction is 1.25 Å (reported for human apoferritin) [183].

However, in recent years ADF STEM has to some extent reprised its role for structural determination. This is particularly evident in structures which contain heavier (and therefore more strongly scattering) elements. Benefiting from three decades of improvements in instrumentation,

Pan et al. were able to expand on the original findings of Ohtsuki et al., using HAADF STEM tomography to show that the ferritin core is in fact comprised of eight distinct sub-units [184]. Simultaneous acquisition of EELS data also meant the iron content of each sub-unit could be quantified (although as this was achieved by comparison with reference spectra the error was in excess of $\pm 20\%$). A more accurate measurement has since been made using quantitative HAADF techniques to compare ferrous image intensity with scattering from gold nanoparticles [185], analogous to the comparative mass measurements described in previously.

In other areas, cryo-TEM techniques have facilitated the development of new STEM methodologies. For example, Elad et al. used cryo-STEM and single-particle reconstruction techniques to determine probability densities for the sites of single Fe and Zn atoms in ferritin [186]. Due to limitations on electron dose and image contrast, the full structure of ferritin could not be solved to atomic resolution; however, the averaging of single-atom intensities from ~ 600 proteins was sufficient to capture the most probable locations of heavy single atoms.

Cryo-STEM techniques are also beginning to be applied for electron tomography of vitreous thin sections [187]. Conventional cryo-electron tomography (CET) has been used extensively to examine the structure of macromolecules in the context of the cellular ultrastructure [188]. However, due to the nature of the TEM image, a compromise must be found between spatial resolution and the defocus required to generate contrast. Wolf et al. have shown that cryo-ADF STEM tomography may afford a number of advantages over CET, which include higher spatial resolution and reduced requirements on specimen thickness [189]. Furthermore, unlike CET, the contrast of images acquired using ADF techniques does not change with tilt angle, and thus the tomograph reconstruction is considerably simplified.

3.2.3 Localisation and Imaging

The final application of STEM imaging in biology which will be discussed in this Chapter is to the localisation of biological structures following labelling with heavy metals. As discussed extensively in Chapter 1, HAADF contrast is strongly dependent on atomic number. However, for biological materials containing elemental species with relatively low atomic numbers, the electron dose required to visualise single atoms typically far exceeds that which is tolerated by the sample [190]. One method of overcoming this challenge is by targeted labelling with heavy

elements which are more readily visible under ADF conditions.

DNA Sequencing

An early example of such labelling applications is for DNA sequencing. Around the time the STEM was developed, determining the order nucleobases along a DNA strand posed such a significant challenge that only a handful of successful demonstrations had been shown experimentally, and even then only for short sequences [191]. Following the advent of high resolution conventional TEM, a number of groups developed protocols for labelling DNA with high-Z materials such that it would be visible in the microscope. Di Giamberardino et al. developed a uranium-based stain to selectively label thymine [192], and Moudrianakis and Beer produced a similar agent for labelling guanine [193]. Whiting and Ottensmeyer also demonstrated successful labelling of DNA bases with single Pd, I, Os, Pt and U atoms (identifying them with dark-field TEM) [194].

TEM approaches suffered heavily from the effects of the carbon background support, and no actual sequencing was achieved. Following Crewe's demonstration of visualisation of uranium-labelled DNA in the STEM [140], it was hoped the improvements in image contrast, microscope vacuum and carbon background suppression would afford a reliable sequencing method. However, a number of problems ultimately prohibited STEM methods from being realistically implemented. The sugar-phosphate backbone of DNA is weakly scattering and difficult to image, which presents a challenge for sequencing more than a few base pairs [191]. In addition, a significant degree of electron beam-induced motion inhibits the localisation of single-atom labels to single DNA sites [195].

The development of more sophisticated chemical methods for DNA sequencing meant that electron microscopy based approaches were eventually abandoned [196]. However, there is currently a renewed interest in this field following the first demonstration of partial DNA sequencing in the electron microscope [197]. By labelling individual thymine bases with single mercury atoms, Bell et al. were able to determine the position of each subunit in molecules several thousand base pairs long. Krivanek et al. estimated that developments in this area may ultimately enable sequencing of a full human genome in $\sim$10 h [198].

Immunolabelling Applications Using Undecagold and Nanogold

Another area in which STEM may be used to localise particular molecules is antibody immunolabelling. Antibodies are proteins which bind with high specificity to target molecules called antigens; visualising the sites where antibody-antigen binding occurs (i.e. within a certain cell and/or at a particular organelle) can provide key information about subcellular function. This can be achieved in the electron microscope by labelling antibodies with electron-dense materials such as iron, mercury, uranium, and (most commonly) gold (or combinations thereof [199]). Faulk and Taylor showed that antibody proteins (specifically, purified rabbit anti-salmonella immunoglobulins) could be adsorbed onto the surface of colloidal gold [200]. The resulting immunocolloid was shown to bind to antigens expressed by *Salmonella*, and the antibody-antigen binding sites could be visualised in the TEM. Roth et al. subsequently showed that more non-specific antigen labelling was possible in thin sections of tissue [201]. By first incubating the tissue section with a primary antibody, and then with immunogold, they removed the need to produce different colloidal labels for every antibody, making the technique more readily applied to other samples (see Ref. [202] for a review).

In order to successfully label a sample, the gold particles must be sufficiently small to be able to penetrate the full thickness of the tissue section. Methods for producing very small gold clusters are well established, and in some cases offer further advantages over colloidal gold [203]. For example, Undecagold contains 11 Au atoms and a single covalently-bonded antibody fragment. Each Undecagold particle can therefore bind only a single antigen, which prevents aggregation seen in colloidal gold labels of a similar size. Nanogold contains 67 Au atoms and multiple antibody fragments which are more stably attached than equivalently-sized colloidal gold. The diameters of the gold cores of both Undecagold and Nanogold are well defined (0.8 and 1.4 nm respectively), and have significantly smaller variation than equivalent colloidal particles.

Whether 1.4 nm Nanogold is visible in conventional TEM depends heavily upon sample thickness and the corresponding background image contribution [204]. However, due to the strong scattering from the electron-dense core, a number of applications have been demonstrated in ADF STEM where these dependencies are less problematic. Braig et al. used Nanogold clusters to examine the location of protein folding in the GroEL-GroES complex [205]. As

discussed previously, an ongoing debate concerning this complex meant it was unclear where protein folding occurred. By using ADF STEM, Braig and coworkers were able to provide evidence that these processes occurred inside the cavity, and not on the exterior as previously suggested. A similar application of Nanogold was also shown by Gregori et al., who were able to localise the amyloid β protein to the interior of the proteasome generating further insight into its role in protein degredation [206].

Undecagold is much less visible in the TEM (although as with Nanogold, its visibility may be augmented by further Ag staining [207]), and applications in STEM are more widespread. Yang et al. also used Undecagold to examine the position and flexibility of the mobile regions in the pyruvate dehydrogenase complex [208]. By examining the positions of Undecagold-labelled pyruvate fragments, the authors were able to locate the Undecagold at 75 nm from the center of the core (a distance associated with an interface between two enzymes in the complex). Safer et al. used ADF STEM to visualise biotin-conjugated Undecagold at the binding sites of the protein avidin [209]. Measurement of the separation between gold clusters confirmed that adivin contained four subunits arranged in pairs, which was further supported by STEM mass measurements of the complex. This experiment highlighted another benefit of the use of the smallest metallic clusters; the biotin fragments attached to the Undecagold meant the binding sites could be localised to within 12 Å. Lipka et al. obtained similar results using STEM measurement to localise the position of carbohydrate binding to the haptoglobin-haemoglobin complex [210].

Undecagold and Nanogold as Mass Standards

Another application of Nanogold and Undecagold is as a calibration standard for quantitative ADF STEM, analogous to the use of the tobacco mosaic virus as a mass standard discussed previously. Both have highly monotonic intensity-mass relationships under HAADF conditions [211]. Bhirde et al. used Nanogold clusters to visualise and measure the amount of the platinum-based chemotherapeutic cisplatin attached to single-wall carbon nanotubes (SWNT) designed for targeted drug delivery [212]. Due to the close atomic numbers of gold and platinum, a similar degree of high-angle scattering is generated in the STEM. Similarly to the methods used by Jian et al. to determine the iron content in ferritin [185], by measuring the scattering generated per Au atom from Nanogold, Bhirde et al. could directly apply this value to measure the number

of platinum atoms at each site on the SWNT. In combination with STEM tomography, this showed that larger cisplatin clusters were located inside the SWNT.

Sousa et al. used similar comparative quantification methods to determine whether Nanogold and Undecagold clusters would be visible in conventionally processed osmium-stained tissue samples [213]. Their findings suggest that both should be detectable in lightly-stained tissue, which has important consequences for the detection of antibodies within the context of the cell ultrastructure. Their subsequent development of a larger Au label containing 144 Au atoms (as determined by comparisons with Nanogold) will likely provide further immunolabelling benefits in the STEM, particularly for samples sensitive to beam-induced damage such as vitreous samples [214].

3.2.4 Summary

There are a considerable number of literature examples where STEM methods have made considerable contributions in biology. These applications may be broadly divided into three categories, encompassing structural determination, antibody labelling and mass measurement. The latter of these is arguably the most significant, as STEM measurement is particularly versatile for examining non-homogeneous populations and those containing structures of variable size.

A considerable number of applications discussed in this Section were reported in the years shortly after the instrument's development. As the STEM has become more entrenched in the physical sciences, its original ties to life science fields have become somewhat distant. Despite this, there has been a number of recent examples where STEM techniques have been employed with great success in these areas, particularly for heavier elemental species. In such cases, ADF imaging offers unique capabilities for detection and quantification at extremely high spatial resolution.

3.3 Applications of STEM EDX & EELS in Life Sciences

In addition to imaging applications in biology, STEM spectroscopy has played a key role in elemental identification. As discussed in Chapter 2, EDX and EELS both make use of the

inelastic electron scattering generated by the sample and provide a chemical fingerprint of the atomic species present.

The evolution of these methods in life science has largely mirrored that of imaging. While electron-loss had been used previously in the EPMA, the advent of the STEM and improvement in spectrometer technology brought EELS to the fore both for chemical identification and imaging. Isaacson and Johnson were the first to discuss the use of EELS as a quantitative technique [127], noting that the STEM afforded both superior resolution and faster acquisition times than in the EPMA experiments which had come before. Their initial results showed that the $\sim 5 \times 10^{-19}$ g of iron contained within a single ferritin molecule was detectable in their instrument, even under less than optimal experimental conditions. They were also able to show that measurements of carbon K-edge fine structure were sufficiently sensitive to discriminate between nucleic acid bases.

Around the same time, STEM EDX methods were applied to thin sections of biological tissues prepared under a variety of conditions [215]. While the potential for elemental extraction or redistribution were particularly high in samples prepared for conventional TEM, the contrast generated in ADF was generally found to be sufficient to navigate gross cellular ultrastructure without the need for extensive fixation. This was demonstrated by Leapman and Andrews, who directly compared samples of murine cerebellar cortex prepared by freezing and subsequent freeze-drying, and by conventional freeze-substituted, resin-embedded and stained tissue [216]. These methods were shown to be sufficient to reliably measure concentrations of potassium and calcium in endoplasmic reticulum and mitochondria respectively.

In this remainder of this Section, the biological applications of quantitative EDX and EELS will be reviewed. Due to the breadth of analyses reported in the literature, this discussion will be limited to particularly notable results including the use of new quantitative methods. Comprehensive reviews may be found in articles by Sousa and Leapman [214] and Leapman [217].

3.3.1 EDX

EDX spectroscopy is of particular use in biological samples due to their compositional complexity. Unlike in EELS, x-ray signals from all elements are captured simultaneously. However, this advantage is countered by the fact that the collection efficiency of EDX is relatively poor;

the acquisition of good quantitative data may therefore requires exposure to electron dose incompatible with sample survival. This is particularly evident when compared with cryo-TEM imaging of single biological molecules; such samples often necessitate the use of fluences below 10 electrons per $\mathrm{\AA}^2$, which are far below that required to generate sufficient x-ray signal [218].

Applications to Heavy Species

Despite this, a considerable number of successful STEM-EDX applications have been demonstrated in biological samples. As discussed previously, ADF imaging is particularly suitable for probing heavy elements inside cells, and a natural progression of this work is the simultaneous acquisition of x-ray data. Goode et al. utilised such methods to locate metallic wear debris in tissue retrieved from a failed hip replacement [219]. EDX data showed that in addition to the cobalt and chromium detected in the patient's blood, some aggregation sites also contained molybdenum, also originating from the failed joint. Further investigation with EELS showed such sites were correlated with particular oxidation states of Co and Cr.

STEM EDX techniques also afford a method to examine more esoteric applications, such as the bioaccumulation of uranium in bacteria. Gerber et al. used ADF imaging to identify U in specific cellular compartments of *Rhodosporidium toruloides* recovered from a former mining site [220]. Acquisition of EDX data showed that deposits were correlated with the presence of phosphorous, providing insight into the uranium binding sites in the cellular environment. A number of other studies have also probed biaccumulation and biosynthesis of heavy elements with similar techniques, such as *in vivo* bacterial production of alloyed Au–Ag–Cu nanoparticles [221].

Applications to Low-Z Species

A number of studies have also examined the behaviour of elements more commonly found in biological specimens using (S)TEM-EDX spectroscopy (although due to the particularly poor fluorescent yield of such species, SEM examples are arguably more numerous in the literature). Amongst the first examples of EDX data acquired in parallel with STEM ADF imaging is the work of Somylo et al., who acquired elemental data from *Escherichia coli* [222] and cardiac tissues [223]. Their earlier work had resulted in the development of sample preparation routines which minimised the dissipation of mobile elements in such specimens [224].

Later examples of such work are found in detailed experiments concerning intracellular Na and K concentrations. Work performed by Zierold et al. on unstained and unfixed samples has suggested that a decrease in the intracellular ratio of sodium and potassium concentration is an indicator for apoptosis in cells exposed to heavy metals [225]. Similar work by Arrebola et al. has shown an *increase* in Na:K levels ocurs prior to apoptosis brought about by exposure to UV light [226]. Similar results were also reported in SEM from measurements made on whole cells [227]. While such results may at first glance appear contradictory, the morphological and biochemical changes during cell death are deeply complex and highly dependent upon cell type [228]. As discussed in Fernandez-Segura and Warley, the use of EDX to directly measure concentrations in specific cellular compartments is therefore of great benefit for understanding such processes [229].

Analysis of trace elemental species in biological specimens has also been demonstrated. Andrews et al. measured sub-millimolar concentrations of calcium in various compartments of rat hippocampal tissue, again making use of ADF to navigate tissue ultrastructure [230]. However, their work highlighted a significant challenge of detecting low intracellular concentrations in cases of peak overlap. As shown in their paper, detection of Ca in EDX is significantly complicated by the presence of potassium sue to peak overlaps between the Ca Kα and K Kβ. As in many tissues, potassium is considerably more abundant, acquiring data with sufficient signal-to-noise for quantification can require the use of extremely high electron dose, and ultimately limit the minimum detectable concentration. Similar challenges were also discussed by Somylo et al. for the measurement of sodium in the presence of copper in striated muscle [231].

Quantification of Low-Z Species

As discussed in Chapter 2, the Cliff-Lorimer k-factor approach is now the primary method utilised for the quantification of EDX data, including those recorded from biological specimens. However, a considerable amount of early examples of quantitative EDX in life sciences utilised continuum-normalisation methods developed for thin biological specimens by Hall [232]. In brief, this approach relies on normalisation of the element peak(s) of interest with a peak-free energy window which is in principle proportional to the total sample mass. Through the use of a reference standard, elemental concentration is ultimately extracted in units of mmol/kg of specimen [233].

Continuum-normalisation has a number of advantages over Cliff-Lorimer quantification, the most important of which is that (similar to the ζ-factor approach) only calibration factors for specific elements of interest need be measured. This has considerable consequences for measurement of the complex multi-species samples often found in biology where meticulous determination of tens of k-factor pairs is a highly non-trivial endeavour. Despite this, there has been a significant decline in the use of Hall's methods in the past twenty years. Following withdrawal of commercial software support, Cliff-Lorimer quantification methods are more routine.

However as discussed by Warley [234], incautious application of the Cliff-Lorimer routine can introduce significant error into biological EDX analysis. In particular, extrapolated or theoretical k-factors often significantly underestimate the abundance of elements which produce low-energy x-rays such as carbon and nitrogen. As such species comprise the majority of the biological specimen, inaccurate quantification here can result in huge uncertainties in final elemental composition. It is therefore often insufficient to rely upon the "built-in" k-factors of the spectral acquisition software for anything more than a qualitative analysis.

An example of rigorous biological quantification may be found in the works of Zierold and Arrebola et al. described previously, with both employing Hall continuum-normalisation methods to measure intracellular Na and K. In the case of peak overlaps (as discussed for Andrews et al. and Somlyo et al.), such methods were used following fitting of the EDX data with reference spectra prior to quantification. Particularly successful applications of Cliff-Lorimer methods may be seen in the work of Laquerriere et al. Following diligent measurement of instrumental k-factors and absorption parameters [235], they showed that EDX data recorded from freeze-dried murine neuroglial cells was sufficient to measure elemental ratios of C, O and N with similar success as in EELS [236]. These methods were later also applied successfully to examine intracellular changes in human monocytes as a result of exposure to hydroxyapatite particles [237], and the effects of mercury toxicity in rat hepatocytes [238]. These works, amongst many others, demonstrate that careful EDX analysis does afford a means to probe biological specimens in a quantitative manner in the (S)TEM.

Novel EDX Applications

Similar to the emerging STEM imaging applications described in the previous Section of this review, new developments have also enabled novel biological EDX studies in the STEM [239]. Peckys et al. have recently demonstrated the first acquisition of STEM images and EDX data from live cells, tracking Au nanoparticle uptake for specimens mounted on a liquid cell specimen holder [240]. Similar methods have also been applied to investigate the composition of casein micelles in bovine milk, with EDX used to measure calcium and phosphorous content *in situ* [241].

A number of cryo-STEM-EDX applications are also now well-documented in the literature. Following progress in the development of cryo-STEM tomography described previously, Wolf et al. have further shown that their methods are compatible with the simultaneous acquisition of EDX data. This has been applied to the measurement of phosphorous-rich bodies in *Agrobacterium tumefaciens* [242], and to the measurement of calcium-rich granules in vitreous sections of several murine cell types [243]. While in both cases restrictions on electron dose meant that the EDX data had relatively poor signal-to-noise (quantification was achieved through comparative mass measurements with Nanogold), spectra clearly show characteristic elemental peaks. Subsequent improvements in electron dose distribution, data acquisition techniques and EDX spectrometer design may in such cases allow elemental analysis from such samples frozen in a near-native state.

3.3.2 EELS

The final part of this Chapter will review applications of EELS in biology. As discussed in the preceding section and in Chapter 2, in comparison with x-ray spectroscopy EELS has a higher sensitivity for detecting lighter species and a significantly better collection efficiency. This therefore allows data to be acquired with considerably lower electron dose, which has important implications for beam-sensitive samples [230].

However, the nature of EELS spectral acquisition means that full details of sample composition often cannot be captured simultaneously. Instead, the energy range selected by the operator limits information to just a single (or at most a handful) of elements. The energy of the edge onset, and the edge shape, also affect detection and quantification; elements such as potassium

and sodium are (respectively) close the carbon K-edge and at high energy, and are therefore particularly difficult to examine in a biological context using EELS. For these reasons, it is therefore uncommon for biological samples to be fully characterised using EELS alone.

Calcium & Iron

However, in many cases full characterisation is not required (or indeed even of interest), and there are a considerable number of applications where EELS has been used successfully to measure concentrations of selected elements. This is particularly evident in biological studies of calcium and iron. Both are ideal candidates for EELS, having strongly-peaked $L_{2,3}$ edges at around 346 eV and 708 eV respectively [244], [245].

As discussed previously, EELS studies of iron have been applied to single macromolecules such as ferritin [127], [184]. Ferritin has also been examined *in situ* in murine brain tissue by Zhang et al. [246]. In addition to using ADF STEM to observe morphological changes associated with neuronal degeneration, they used EELS to quantify changes in the distribution of ferritin across different cell types. Their results showed that although ferritin levels increased in tissues obtained from mice with progressive neurodegeneration, ferritin was completely absent in damaged neurons and instead present at much higher concentrations in other cell types.

Calcium quantification in thin sections of cerebellar cortex has also been demonstrated using EELS [129]. Leapman et al. recorded spectra from endoplasmic reticulum and mitochondria, showing that the former contained approximately four times more calcium than the latter. However, while it has been shown that in principle single atoms of both Ca and Fe are detectable with EELS [247], Leapman et al. found that the dose limit tolerated by the sample was in practice much lower than required for such low detection limits. In addition, while the authors were able to measure Ca concentration with an accuracy of ± 0.4 mmol/kg, their analysis relied on summing spectra from several organelles to attain sufficient signal. The concentration measurements obtained from individual compartments have a correspondingly much higher error.

Phosphorous

Leapman and Rizzo have also examined applications of STEM-EELS methods to the mapping of phosphorous in both DNA and TMV [248]. Both specimens were chosen due to their well-known phosphorous content (8 atoms/nm in DNA, and 20 atoms/nm in TMV). Leapman and Rizzo's found that in both cases, EELS could reproduce these values, albeit with high error. This is largely due to both the shape and energy of the P $L_{2,3}$ edge, being both delayed and superimposed on a large plasmon tail due to its onset at 132 eV. In both DNA and TMV, spectrum data required considerable processing to visualise the P edge. A further contribution to the error likely arises due to the use of theoretical partial cross-sections in the quantification; the use of reference spectra as utilised in the measurement of Ca and Fe would typically be more suitable for this application.

H_2O Mapping

In addition to core-loss quantification, several groups have demonstrated the application of low-loss EELS analysis to measure water content in frozen-hydrated specimens. Sun et al. showed that fitting data acquired from sections of hepatic tissue with reference spectra from major biological macromolecules, in addition to vitreous and crystalline ice, allowed the water content of individual cell compartments to be determined with an accuracy of $\pm 2\%$. Such methods have also been employed for epithelium tissue [249]. Following several recent successful demonstrations of STEM-EELS in frozen samples [250], [251] in parallel with the cryo-STEM tomography work of Wolf et al. described previously, such methods may be reprised in the near future.

EFTEM

The closely related technique of energy-filtered transmission electron microscopy (EFTEM) has also recently been applied to measure intracellular elemental distributions. In EFTEM, two sequential images are formed from inelastically scattered electrons within certain energy windows, with the first recorded in the pre-edge region and the second at the edge of interest. Although EFTEM has generally been more suitable for detection of high concentrations, improvements

in spectrometer design mean it is in some cases now possible to detect physiologically-relevant concentrations of elements such as calcium, as demonstrated by Aronova et al. in neuronal tissue [252].

EFTEM techniques have also been utilised to detect lanthanide antibody labels in osmium-stained canine kidney tissue [253]. Such methods are of interest as an extension of immunolabelling; as demonstrated by the work of Adams et al., multiple markers can be used simultaneously in a single sample, and clearly distinguished from their energy-loss signal. While not strictly an application of STEM-based methodology, their EFTEM data suggests that lower concentration of similarly labelled antibodies may be detectable and quantifiable through EELS.

Effects of Specimen Thickness

As discussed in Chapter 2, there are relatively few routes to quantify EEL spectra. The use of partial scattering cross-sections, be they experimentally measured or theoretically calculated, is limited to use in core-loss spectra. Model fitting, or fitting with reference spectra, may be employed for both low- and core-loss data. As described above, both have been applied to biological specimens, and there is relatively little evidence to suggest superiority of either approach.

Instead, the factor which most influences quantification in biological samples (or more accurately, beam sensitive samples) is specimen thickness and electron dose. As discussed by Sousa and Leapman, the use of lower accelerating voltage reduces mass loss from the sample [214]. However, this leads to a corresponding decrease in the inelastic mean free path, from around 185 nm at 300 kV to 100 nm at 100 kV (as estimated using the methods of Iakoubovskii et al. [254]). Correspondingly, the problems of plural scattering - namely enhanced plasmon intensity and loss of energy resolution - are more problematic in relatively thick biological specimens examined at lower voltages [255].

Novel EELS Applications

Similar to the *in situ* EDX experiments described previously, Narayanan et al. have very recently demonstrated the ability to acquire EELS data under similar conditions [256]. They examined

the biomineralisation of ferritin contained within graphene liquid cells, showing sensitivity to the oxidation state at moderate electron dose (10^4 electrons/Å^2). This ability may be of particular interest for the observation of similar macromolecules in live specimens, although such experiments would of course be extremely technically demanding.

Similarly, Hachtel et al. have demonstrated EELS may also be applied to examine isotopically-labeled amino acid molecules using aloof methods [257]. Isotopic labels are often used with conventional mass spectrometry techniques at much lower spatial resolution; however, as shown by Hachtel et al., conditions for measurement with aloof EELS are compatible with those presented by the cell.

3.3.3 Summary

EDX and EELS techniques have been applied extensively in biological specimens, and often in combination with STEM imaging. Both afford the means to measure elemental composition, and their applications are diverse. EDX is particularly useful for the detection of heavier species, but may also be applied to e.g. the measurement of intracellular sodium and potassium ratios. EELS is especially suited to trace elemental measurement of species such as iron and calcium.

Preservation of native elemental distributions is key to ensure EDX and EELS data are representative of the sample's true nature. The use of sample preparation procedures such as freeze drying have often proven sufficient to meet this condition, while preserving sufficient ultrastructural detail to contextualise elemental results.

3.4 Outlook for ADF, EDX & EELS

There are a considerable number of applications of STEM methods in biology, with many of the most significant reported in the years shortly after the instrument's development. As discussed throughout this Chapter, the biological STEM has now been largely superseded by other techniques; structural information, for example, is now acquired routinely in the cryo-TEM or by x-ray crystallography [258]. Mass spectrometry methods, such as matrix-assisted laser desorption/ionization (MALDI-MS [259]) and inductively-coupled plasma mass spectrometry (ICP-MS [260]) are also particularly useful in biology, and often used for the analysis of large

macromolecules and element detection respectively.

Despite this, simultaneous acquisition of quantitative imaging and spectroscopic data, often at very high resolution, is largely unique to the electron microscope; STEM techniques therefore still afford opportunities for biological research. As detailed in this Chapter, there are a number of recent works which have revisited the potential applications of STEM methods - and particularly HAADF/ADF imaging, EDX, and EELS - in this context. This is particularly evident from investigations of heavier elemental species within biological matrices, with STEM applications to elucidate to behaviour of nanoparticles (NPs) in cells particularly well-documented [261]. Both qualitative and quantitative studies of cellular NP ingress and transport have been reported, and examples can be found in the work of Cheng et al. (HAADF imaging and tomography applied to examine cell damage due to multi-walled nanotubes [262]), Muller et al. (EDX and EFTEM to track *in vitro* degradation of ZnO nanowires [263]) and Wills et al. (HAADF and EDX for quantitative investigations of silica NP uptake [264]). The translation of cryo-TEM techniques, for both sample preparation and data acquisition, are likely to bring further improvements for such applications.

In addition, there is increasing evidence to suggest that STEM methods may in some cases afford additional advantages over conventional TEM for imaging beam-sensitive materials (reviewed by Ilett et al. in Ref. [265]). At first glance, this appears counter-intuitive; in an aberration-corrected STEM, even low probe currents are on the order of a few picoamperes, which distributed across a sub-1 $Å^2$ beam area results in a considerably higher electron flux than is typically used in TEM. However, counter to this point is that unlike in TEM, such currents are only applied for a very short time (on the order of a few microseconds). Experiments in several systems have suggested that a scanned probe allows time for the sample to recover and/or cool in between images and thus increase the total electron dose tolerated by the sample [266], [267]. In combination with recently-developed novel approaches for data collection (e.g. low dose [268] and multi-frame imaging [269], multi-frame EDX and EELS [270], Moire scanning methods [271], [272]), it appears likely that STEM methods hold further opportunities for imaging beam-sensitive systems as found in biology.

Chapter 4

Platinum Pharmaceuticals in the STEM

4.1 Aims & Scope

In this chapter, HAADF STEM imaging is used to visualise dried samples of the platinum-based chemotherapeutics cisplatin and oxaliplatin. Both drug molecules contain a single central Pt atom, which binds to DNA and disrupts cellular activity. However, despite sharing a common action mechanism for inducing cancer cell death, high-resolution imaging shows the platinum in cisplatin and oxaliplatin appears to be in very different forms.

In cisplatin, small metallic platinum nanoparticles are found throughout the sample. Their size appears independent of local drying conditions, and is unchanged by the electron beam. Conversely, in oxaliplatin only small disordered atomic Pt clusters are present. This indicates that, unlike in cisplatin, platinum atoms have not been free to nucleate into nanoparticles. Atom-counting shows the clusters have likely arisen from wetting of the carbon support film.

The results in this chapter contain work from the following peer-reviewed publications:

- Sheader, A.A., Varambhia, A.M., Fleck, R.A., Flatters, S.J.L. and Nellist, P.D. (2018). Observation of metal nanoparticles at atomic resolution in Pt-based cancer chemotherapeutics. *Journal of Microscopy*, 270(1) 2018, pp. 92–97 [273].

4.2 Platinum-based Chemotherapeutics

The family of platinum-based anti-cancer medicines, collectively termed platins, are first-line chemotherapy drugs used in more than 50% of cancer treatments globally [274], [275]. In the UK, three platinum-based drugs (cisplatin, carboplatin and oxaliplatin) are approved for medical use and together they are used to treat more than 180,000 people each year [276], [277].

4.2.1 Cisplatin

Despite now playing an integral role in cancer treatment, the first platinum-based drug arose due to a serendipitous discovery. In 1965, Rosenburg et al. were attempting to examine the influence of electric fields on the growth of *Escherichia coli* (*E. coli*) [278]. Initially, the poor growth and abnormal shapes of the *E. coli* were thought to result from the influence of the magnetic field. However, further experiments showed that they were caused by an unforeseen reaction between the "well-known chemically inert" Pt electrodes and the chloride buffer solution in the growth chamber, resulting in the production of a number of toxic platinum complexes.

It was quickly realised that compounds with such profound effects on dividing cells could have potential in anti-cancer treatment. Just four years later, Rosenburg et al. showed that cis-diamminedichloroplatinum(II) ($Pt(II)(NH_3)_2Cl_2$) (which would later become known as cisplatin) was effective at reducing, and in some cases eliminating, sarcomas in mice [279]. The structure of cisplatin is shown in Figure 4.1a. Cisplatin was ultimately licensed for clinical use just thirteen years after Rosenburg et al.'s initial experiments [275]. Cisplatin is now used in the treatment of ovarian, bladder, head and neck, lung and cervical cancers [280]. Cisplatin has also been particularly instrumental in the treatment of testicular cancer; prior to its discovery, only 5% of patients were cured of their disease while today this figure is in excess of 90% [281].

4.2.2 Oxaliplatin

Following the successful demonstration of the anti-cancer properties of cisplatin, a number of derivatives were also investigated for use as chemotherapeutics. These efforts were primarily focused at finding similarly effective treatments with less severe side effects; amongst other deleterious effects, cisplatin is particularly nephrotoxic and ototoxic.

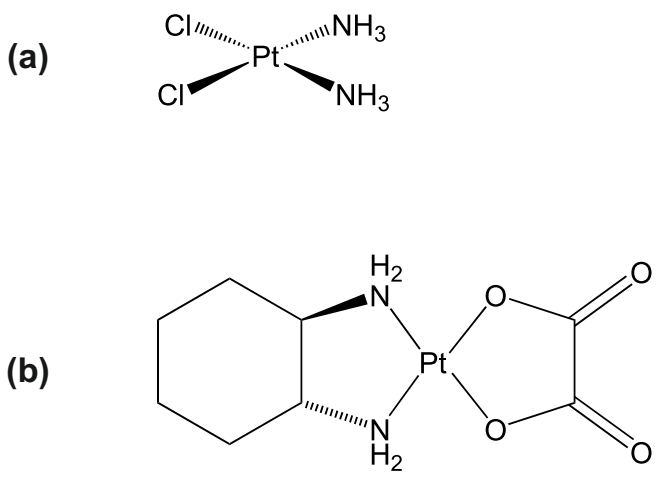


Figure 4.1: Chemical structure of (a) cisplatin and (b) oxaliplatin.

Other platinum-based drugs were also sought to treat tumours which acquired resistance or were intrinsically unresponsive to cisplatin. Oxaliplatin ($C_8H_14N_2O_4Pt$ (oxalato(trans-l-1,2-cyclohexanediamine)Pt(II))) was borne from this latter case as a treatment for colorectal cancer (against which cisplatin had no effect). When administered with other non-Pt based medicines, it improves the outcomes of surgery, and increases rates of progression-free survival in patients with advanced disease [282]. The structure of oxaliplatin is shown in Figure 4.1b.

4.2.3 Mechanisms of Action and Toxicity

Both cisplatin and oxaliplatin are thought to disrupt cellular activity in a similar way. Aquation of the respective chloride and oxalate leaving groups occurs in the cell cytoplasm, and the hydrolysed products of this reaction form intrastrand crosslinks in DNA [282], [283]. Crosslinkage prevents transcription and replication of DNA, ultimately leading to cell death [284].

A number of other platinum complexes have been proposed for use in cancer treatment. However, despite being based on similar principles (i.e. disruption of DNA replication), very few have been successfully implemented in the clinic [285]. A number of fundamental questions, such as how platinum-based compounds enter cells, and how they induce such broad spectra of

side-effects, still remain to be answered.

Electron microscopy-based techniques are emerging as a key tools in structural determination of macromolecular drug targets [286], and as direct methods for drug discovery [271]. HAADF STEM may potentially provide complementary information for medicines containing strongly scattering elements, such as the family of platinum-based chemotherapeutics.

4.3 Sample Preparation

Clinical formulations of 1 mg/ml cisplatin and 5 mg/ml oxaliplatin infusion solutions (both Accord Healthcare Ltd. *(Harrow, UK)*) were prepared for STEM investigation from spent vials from the pharmacy at Guy's Hospital *(London, UK)*. In addition to water, the cisplatin solution contained a mixture of sodium chloride, sodium hydroxide, and hydrochloric acid. The oxaliplatin solution contained water and lactose monohydrate.

3 µl droplets of cisplatin and oxaliplatin were pipetted directly onto lacey carbon support films on 300-mesh copper support grids (TAAB Laboratories Equipment Ltd. *(Aldermaston, UK)*). Wet grids were allowed to rest for approximately 120 s with a droplet of solution on top of the carbon film. The excess solution was then removed using the capillary action of filter paper placed alongside the grid, and the grids left to dry at room temperature.

4.4 Cisplatin

4.4.1 Low Magnification Observation

Low-magnification HAADF images of a cisplatin sample on the TEM grid are shown in Figure 4.2. Local drying conditions vary even within a single sample. For example, in some regions the solution has dried in discrete pieces of varying size and thickness. In others, the solution has wetted the support film and appears well-dispersed.

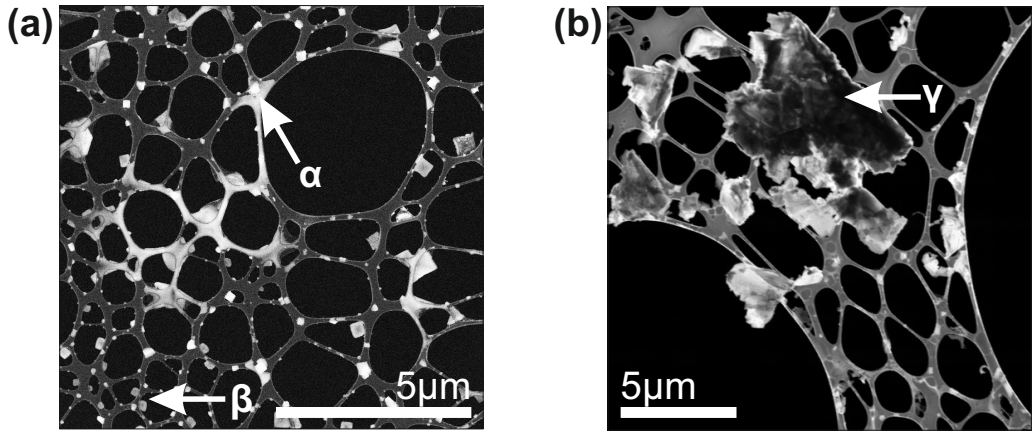


Figure 4.2: Low magnification images of cisplatin. A single grid contains multiple regions where the drying conditions have resulted in significantly different gross morphology. Regions of wetting (α) and sub-0.5 µm discrete pieces (β) are shown in (a), and large, electron-opaque areas (γ) in (b).

4.4.2 High Magnification Observations and Measurements

At higher magnifications, small metallic nanoparticles (NPs) were observed, as shown in Figure 4.3. The presence of NPs was not dependent on local drying conditions. The average nanoparticle diameter is measured at 1.83 nm (for $n = 80$ NPs, and with standard deviation $s = 0.20$ nm), with no dependence on local nanoparticle density (Figure 4.3c).

The platinum-based nature of the nanoparticles is confirmed by measurement of the lattice spacing. As shown in Figure 4.4, some nanoparticles are orientated along the beam direction and may be overlaid with a <110> direction face-centered cubic projected structure. The unit cell is measured to be 3.98±0.15 Å, which is consistent with the literature value of 3.91 Å for bulk Pt [287].

The data presented in Figure 4.3 were recorded using multiframe acquisition, and the SmartAlign (HREMresearch *(Higashimastuyama, Japan)*) image acquisition tool for Digital Micrograph 2.3 (Gatan *(Pleasanton, CA, USA)*) [269]. The resulting image stacks were realigned to correct sample drift during the experiment.

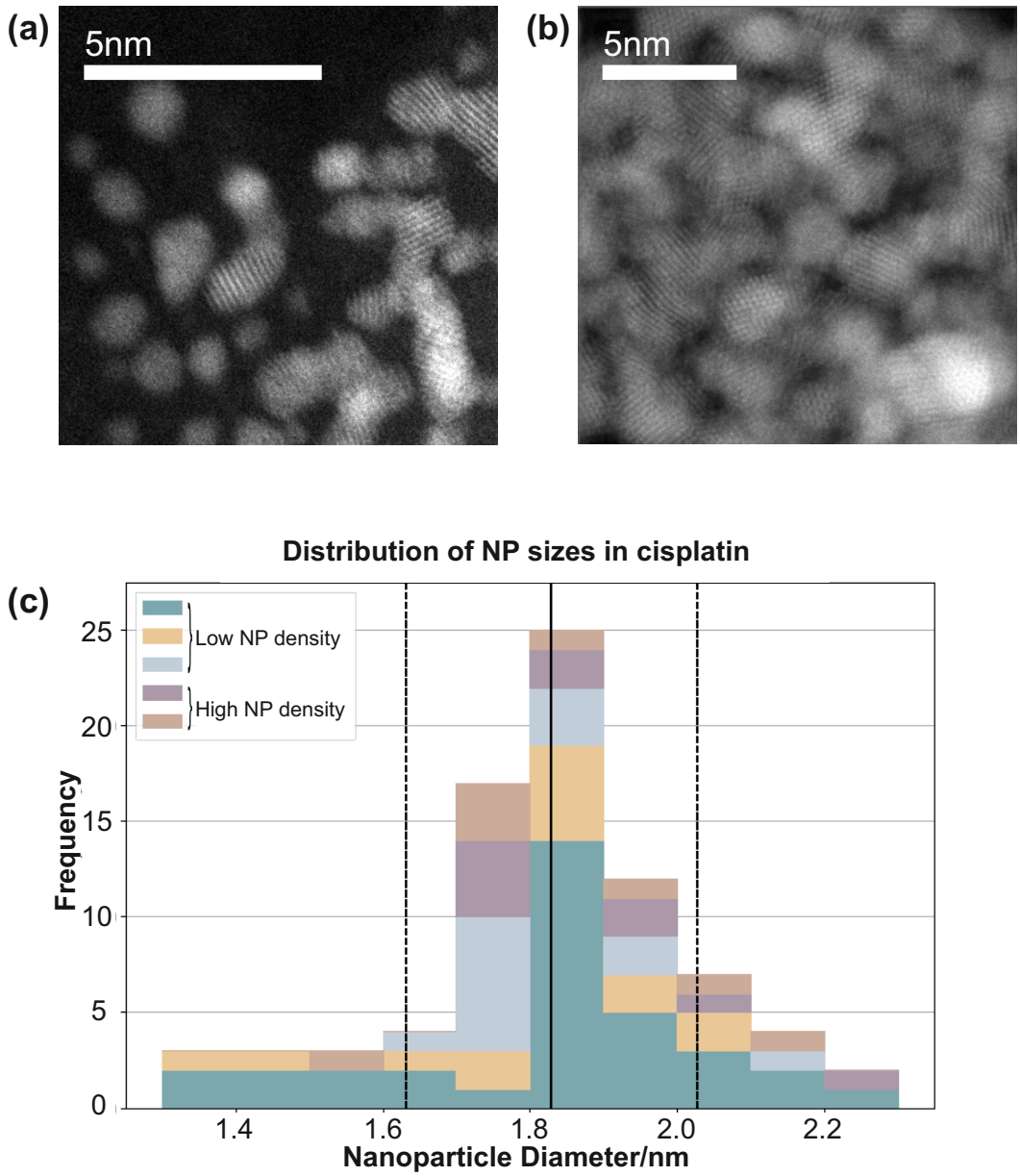


Figure 4.3: Nanoparticles are observed in cisplatin in regions of (a) low density (where individual nanoparticles are largely well-separated from their neighbours) and (b) high density (where the majority of nanoparticles overlap). In some NPs, atomic columns can be clearly resolved; the remainder are either not aligned to the beam direction, or are outwith the focal plane of the STEM probe. A histogram of NP diameters measured from regions with different NP densities is shown in (c). No NP-density dependence of size on concentration is observed. The solid vertical line indicates the mean NP diameter, and the dashed lines one standard deviation.

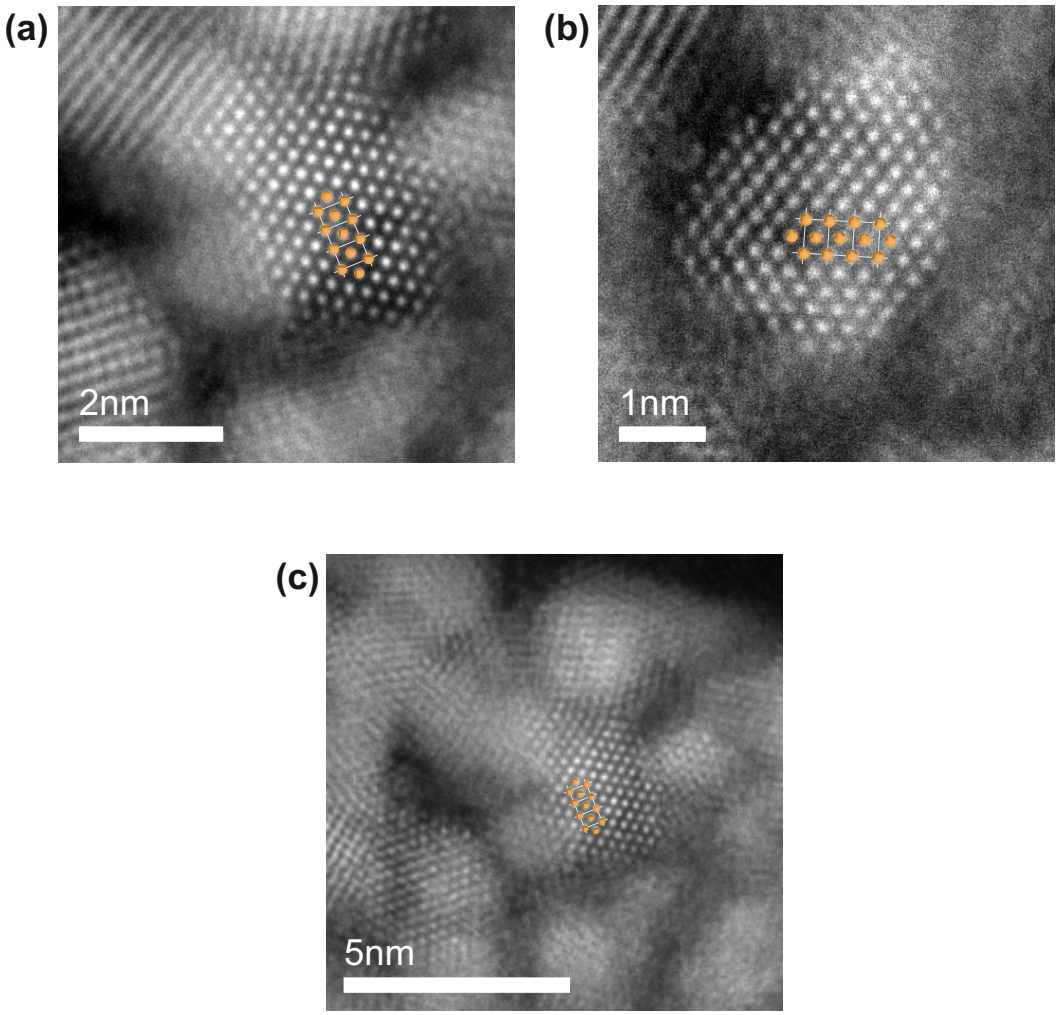


Figure 4.4: Some nanoparticles are orientated in the beam direction, and may be overlaid with a <110> face-centered cubic structure. Measurement of the unit cell is consistent with the literature value for bulk platinum.

Effects of the Electron Beam

As the presence of platinum nanoparticles in cisplatin solution had not been anticipated, it was important to examine whether NPs could have formed as a result of the electron beam. Other experiments have shown that in some cases, interactions with high-energy electrons induce spontaneous formation of metallic nanoparticles in the microscope [288]. This could only occur in this case if cisplatin molecules were sufficiently damaged to the extent that the single central Pt atoms were freed to nucleate and grow into metallic nanoparticles ("ripening").

Multi-frame image stacks were examined for evidence of beam-induced growth; frames from two such image series are shown in Figure 4.5. Twenty sequential images were acquired using a total electron dose of 3.6×10^4 electrons/Å^2 (equivalent to a dose per frame of 1.8×10^3 el/Å^2). Analysis of these series confirms no growth with time, and therefore no growth with accumulating electron dose. As the size of beam-induced nanoparticles is known to be dose dependent [289], this finding suggests that it is unlikely the Pt nanoparticles observed in these experiments are a result of beam-induced effects.

Local Drying Conditions

As concentration-dependent growth has been observed for other nanoparticles (e.g. for iron oxide [290]), local drying conditions were also considered as a potential influence resulting in nanoparticle formation. Effective concentration at a particular site on the TEM grid would vary depending on how quickly the carrier solution evaporated, which could in theory lead to different NP sizes. However, in the experiments described here it was found that local drying conditions only affected the density of nanoparticles and not their size (as shown in Figure 4.3c). Pt nanoparticles have been reported between 1-100+nm [291], [292], and there is therefore no particular underlying physical reason for the formation of c.1.8 nm NPs over any other diameter.

In addition, the standard deviation of diameters measured in these experiments is much narrower than reported for other similarly-sized NPs in the literature (e.g. standard deviation $s = 1.2$ nm for 3.5 nm Pt particles described by Aarons et al. [293] and $s = 1.1$ nm for 2.6 nm Au-Pd particles from Hutchings and Kiely [294]). It would be reasonable to expect nanoparticles arising due drying processes to have at least as similarly large spread, given the pronounced

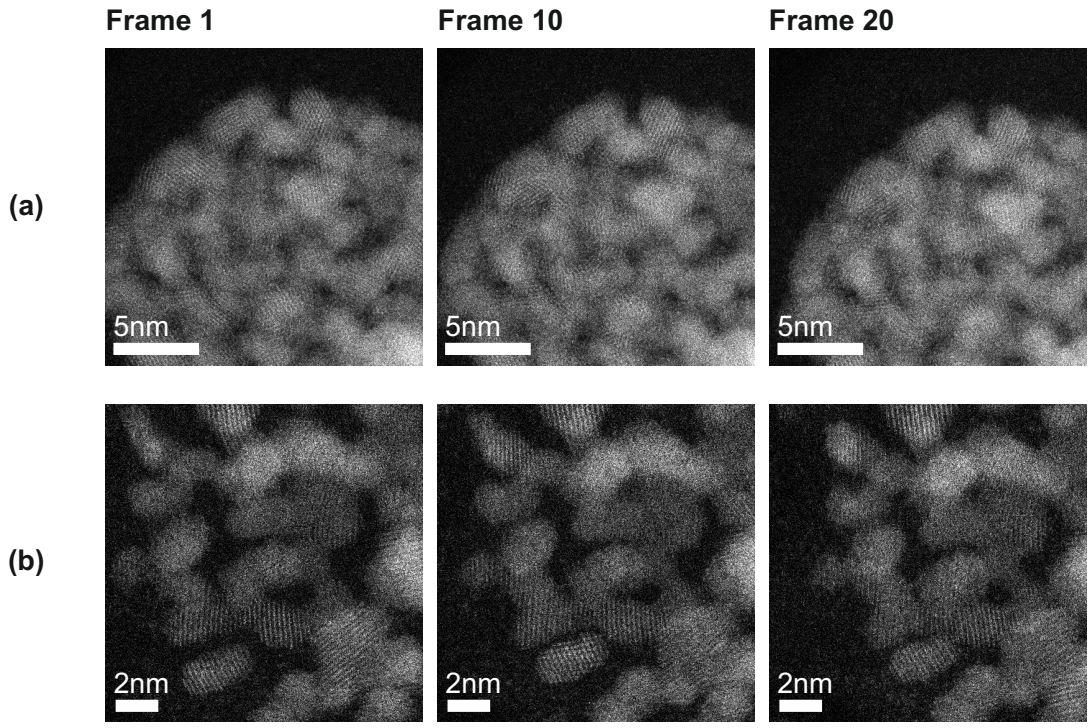


Figure 4.5: Multiframe acquisition of Pt nanoparticles in cisplatin. In (a), the majority of the motion is sample drift towards the lower right corner of the field of view. As the particle density is high, individual NPs do not move significantly. In (b), a small amount of collective drift is observed towards the right. However, as the particles are less coalesced, some NPs are able to move more independently. In both cases, the particle size does not change throughout the acquisition.

differences in apparent Pt concentration at different locations on the TEM grid.

4.4.3 Discussion

Having eliminated beam-induced nanoparticle formation and the effects of local drying conditions as potential origins of Pt NPs, the literature was examined for evidence confirming or excluding NP presence in cisplatin infusion solution. However, while many techniques are able to characterise larger nanoparticles [295], detection of sub-2 nm NPs is challenging and generally limited to just a handful of specialised methods. Cisplatin has been extensively characterised, both shortly after its discovery [296] and using newer methods [297]. However, unsurprisingly there is limited overlap between the approaches used to assess the stability of cisplatin solution in the clinic, and those specifically targeted at detection of ultrasmall NPs.

For example, Gharibshahi et al. have recently shown that UV-visible spectroscopy (UV-vis) can be used to determine the size of Pt nanoparticles as small as 2.8 nm; the same methods have been used extensively to assess aquation rates for cisplatin solution [298], [299]. Unfortunately, extrapolating from Gharibshahi et al. indicates the characteristic absorbance minimum for sub-2 nm NPs would be practically indistinguishable from the regular minimum for Pt(II) and Pt(IV) complexes found in cisplatin solution [296].

High-resolution microscopy-based methods probably afford the most straightforward way of visualising small nanoparticles. Following publication of this work (Ref. [273]), Englert et al. have also reported metallic nanoparticles in cisplatin supplied by Sigma Aldrich *(Burlington, MA, USA)*, of similar diameter (1.81 nm) and standard deviation (0.26 nm) [300]. They report the formation of nanoparticles is reduced in the presence of DNA, and is increased when the amount of Pt presents exceeds the available nucleobase binding sites. Furthermore, while a concentration dependence of NP diameter is observed in the presence of DNA, this is not found for cisplatin solution in isolation.

A number of others have also used electron microscopy to investigate cisplatin. Bhirde et al. used HAADF STEM to image cisplatin tethered to single-wall carbon nanotubes (SWNT) [212]. They observed small 1–2 nm clusters of platinum inside the SWNT, which were estimated (through comparison with nanogold clusters) to contain 10-20 platinum atoms. While this is considerably fewer than a equivalently-sized metallic nanoparticles, 1–2 nm clusters for have

also been observed (but not quantified) by Ajima et al. for single-wall carbon nanohorns [301]. In both studies, the microscope resolution was insufficient to resolve single atoms within the clusters. More recently, Zeng et al. have reported the spontaneous formation of very small Pt NPs in the blood of patients treated with cisplatin, using TEM. however, the authors did not examine the clinical cisplatin solution in isolation, only in combination with different constituents of blood [302].

As platinum-chloride complexes similar to cisplatin are established methods for preparing Pt nanoparticles [291], [303], it is not implausible that small NPs form in cisplatin solution. Very small Pt nanoparticles have been shown to induce nephrotoxicity following *in vivo* exposure in mice [304], and acute kidney injury is a common side effect in patients treated with cisplatin [305]. The presence of Pt NPs in infusion solutions administered to patients, and their fate *in vivo*, therefore merits further examination. A number of cisplatin-derivatives have also been abandoned as potential drug candidates due to particularly severe nephrotoxicity [306], and these findings may therefore have additional implications for Pt-drug development.

4.5 Oxaliplatin

4.5.1 HAADF Observations of Oxaliplatin

Figure 4.6 shows the microscale morphology of dried oxaliplatin solution on a TEM grid. The solution has wetted the lacey carbon support film, and has more amorphous gross morphology than observed in the cisplatin samples. This is likely attributable to different excipients in the two solutions. At higher magnifications small disordered clusters of atoms can be observed, as shown in Figure 4.7. The average size of these clusters is 1.18 nm ($n = 3800$, $s = 0.32$ nm).

4.5.2 Cluster Calculations

Images of the kind shown in Figure 4.7 were recorded using a STEM probe semi-convergence angle of 22.4 mrad, and inner and outer ADF detector semi-angles of 72.8 mrad and ∼271 mrad respectively. On the Oxford JEOL ARM200F, these conditions correspond to use of aperture CL2(3) and camera length of 8 cm for the upper ADF detector [307]

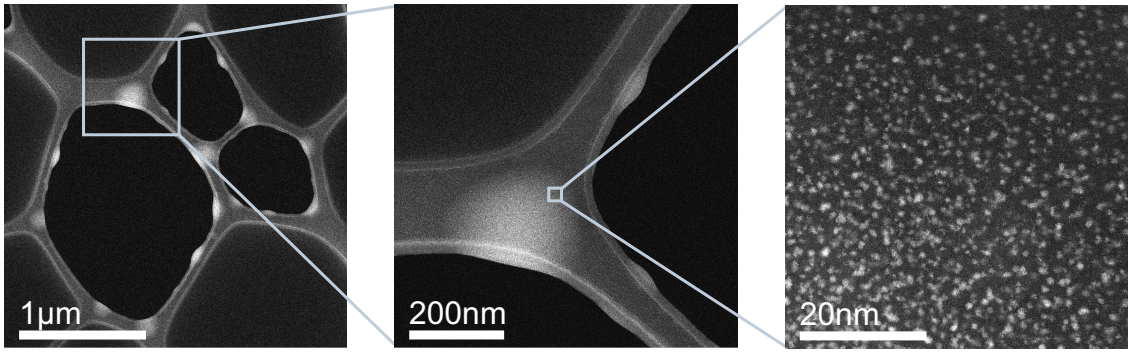


Figure 4.6: HAADF images of oxaliplatin on TEM grid. (L-R) Low magnification shows the oxaliplatin solution has dried amorphously on the carbon film; increased magnification shows structure inside the sample-containing regions.

As discussed in Chapter 1, these values are well into the HAADF regimen, where the image contrast is overwhelmingly dominated by high-angle Rutherford-like scattering. As a consequence of this, the high-resolution images contained within this section may be regarded as having directly-interpretable contrast. In the case of the oxaliplatin clusters shown in Figure 4.7, this means that the intensity of a Pt cluster is linearly related to the number of atoms within it. By comparing the partial scattering cross-section of a single Pt atom with the intensity of a cluster, it is possible to perform atom counting (similar to the early approach used by Isaacson et al., as discussed in Section 1.4.3).

A schematic of the quantification procedure is shown in Figure 4.8. To accurately calculate the scattering of a single platinum atom, it is necessary to remove the influence of the surrounding materials and the out-of-focus material in the background. High-intensity features (single atoms and clusters) were masked, and the background contribution estimated from the remaining pixels and subtracted from the image. A watershed transform was used to separate overlapping or near-neighbour clusters. Single atoms were identified, and used to calculate the average total image counts generated by one Pt atom. The number of HAADF counts per cluster was then converted into number of atoms ($N_{\mathrm{atoms/cluster}}$) by simple linear scaling of the single-atom value.

As the nanoclusters are not regular in shape, making a measurement of diameter in one dimension is not a meaningful quantity for this analysis. Instead, “equivalent diameters” were calculated by redistributing the pixels of each cluster into a circular arrangement and measuring

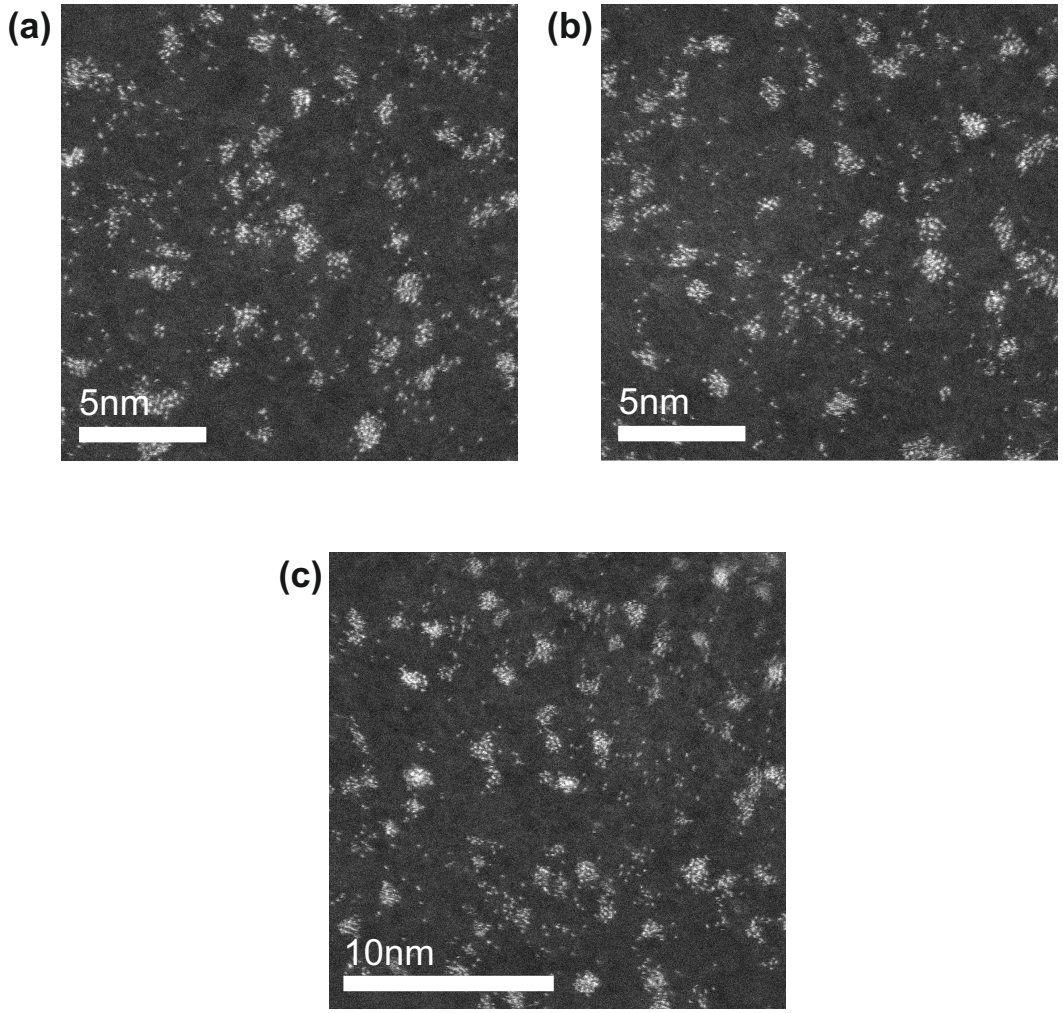


Figure 4.7: (a-c) Small atomic clusters and many single atoms are readily visible at high magnifications and throughout the sample. Unlike the platinum nanoparticles observed in cisplatin, no evidence of crystallinity was found in oxaliplatin.

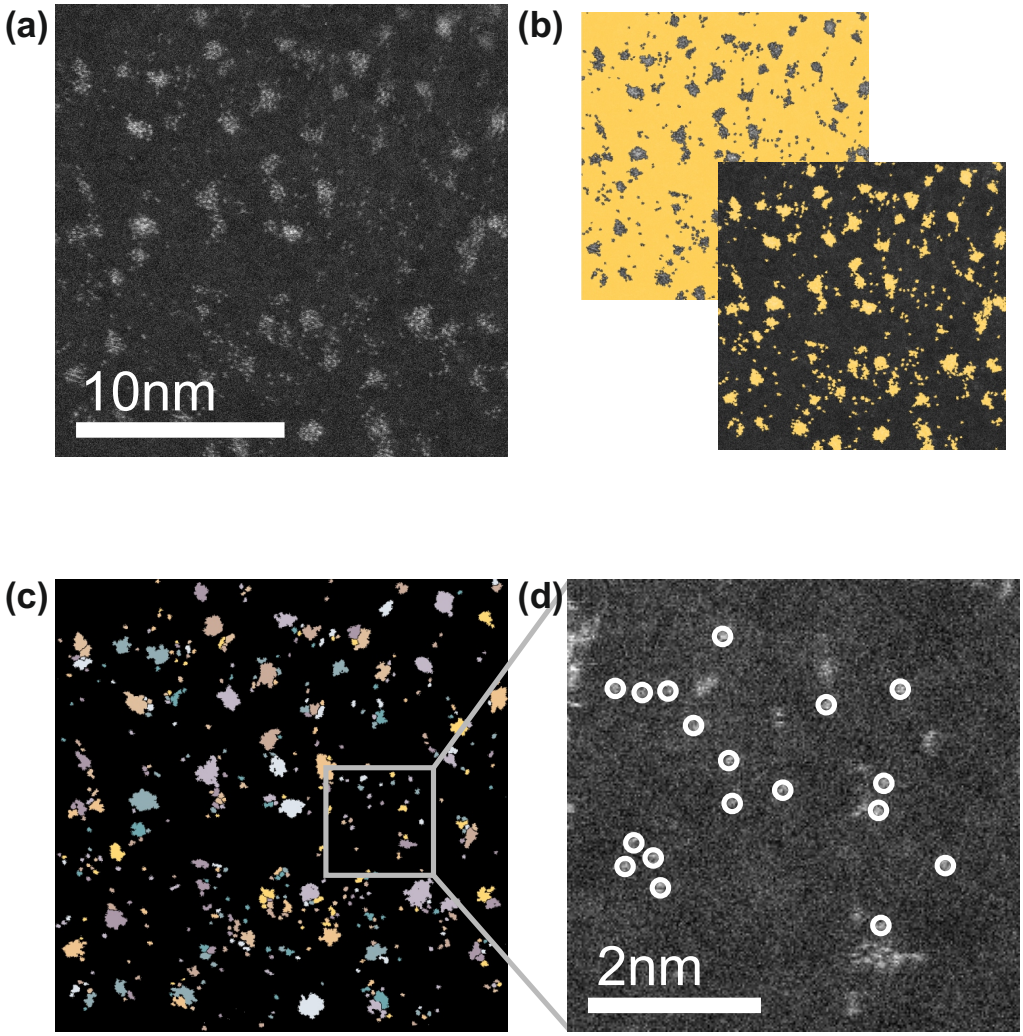


Figure 4.8: Oxaliplatin cluster quantification procedure steps. (a) An experimental HAADF image of atomic clusters in oxaliplatin. (b) Regions of high image intensity, including single atoms and clusters, are identified. The image is segregated into a low-intensity background, and a high-intensity foreground for quantification. (c) The background contribution (calculated using the mask) is subtracted from the whole image. A watershed transformation is used to separate adjacent clusters. (d) The background-subtracted intensity of suitable single atoms is used to determine the number of atoms in each cluster shown in (c).

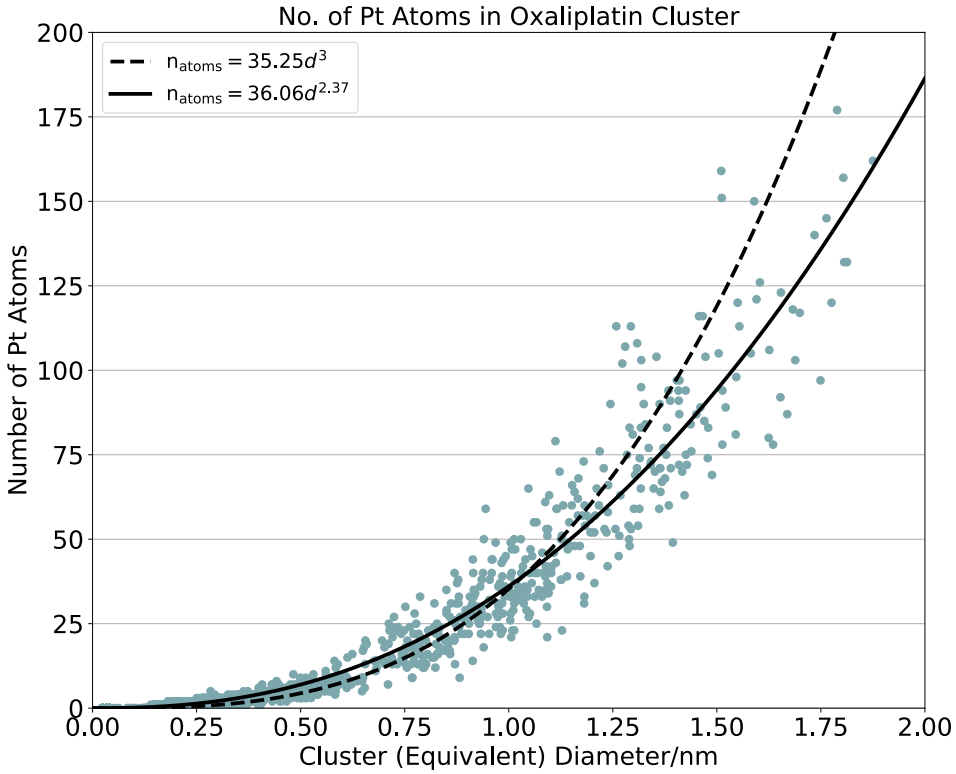


Figure 4.9: Pt atoms per cluster against equivalent diameter. Fitting the data shows the clusters are flattened along the beam direction (with goodness of fit R^2 =0.79). The number of atoms expected for a spherical nanoparticle is also shown, but fits the data more poorly (R^2 = 0.64).

the diameter from this. This is valid as it effectively averages the diameter of the cluster in all x-y directions. A graph of $N_{\text{atoms/cluster}}$ against equivalent diameter is shown in Figure 4.9. Those clusters not wholly within the frame were excluded from the analysis.

Figure 4.9 also shows the result of fitting $N_{\text{atoms/cluster}}$ and equivalent diameter, relative to the number of atoms expected in a metallic nanoparticle of the same size N_{NP}. The value of N_{NP} is given by

$$N_{\text{NP}} = 35.25d^3, \tag{4.1}$$

where d is the particle diameter in nanometers. The prefactor in Equation 4.1 may be found by dividing the spherical nanoparticle volume by the volume of a single Pt unit cell, and multiplying by four (i.e. the number of atoms per face-centered cubic unit cell).

In comparison, fitting the experimental data shows each cluster contains

$$N_{\text{atoms/cluster}} = 36.06d^{2.37}, \tag{4.2}$$

indicating that the clusters are not three-dimensional but instead flattened in the beam direction. This likely arises as a result of the drying process when preparing the sample.

4.5.3 Discussion

While HAADF images cannot detect the other atomic species present in the oxaliplatin molecule, it is likely that the platinum atoms observed in the experiments described here remain within the complex, or are otherwise kept separated by organic molecules formed from decomposition of oxaliplatin. Free Pt atoms would be very likely to form nanoparticles; that they remain separated indicates there is a barrier to this thermodynamically-driven process. Similar behaviour has been reported elsewhere in the literature, e.g. for supported ruthenium catalysts [308]. Quantification of the atomic clusters by a linear scaling of the single-atom intensity is valid for disordered clusters in oxaliplatin, but not for metallic NPs in cisplatin (where chanelling effects may be important). In the former case, where atoms in a particular cluster may be individually resolved, it is very unlikely that an incident beam electron would experience multiple scattering.

High-resolution images (e.g. as shown in Figure 4.7) were recorded using the same imaging conditions and electron dose as for cisplatin. As both drugs have similar chemical structures, the pronounced differences in their nanoscale appearance to provide further evidence against beam-induced NP formation in cisplatin. These differences could contribute to the different toxicity profiles of oxaliplatin and cisplatin; as discussed in Section 4.4.3, Pt nanoparticles are known to cause kidney damage, but this is comparatively rare in patients treated with oxaliplatin.

A potential extension of this work may be to directly visualise the bonding sites of oxaliplatin and other Pt-based drugs in DNA. Differences in the intrastrand crosslinks formed by oxaliplatin are thought to explain why oxaliplatin has some activity against cisplatin-resistant tumours [309]. However, a number of questions about the nanoscale disruption to DNA replication remain to be answered. Atomic force microscopy (AFM) has been used to visualise cisplatin-DNA adducts [310], and direct visualisation using high-resolution HAADF STEM could offer further

advantages over structural determination using e.g. nuclear magnetic resonance (NMR) or x-ray techniques.

4.6 Summary

Cisplatin and oxaliplatin are two chemically similar platinum-based chemotherapeutics. However, high-resolution HAADF imaging shows distinct differences in the nanoscale distributions of platinum. Cisplatin is found to contain sub-2 nm nanoparticles; analysis of multi-frame images shows that these do not arise due to the influence of the electron beam. In oxaliplatin, platinum atoms are observed in small disordered clusters, with no evidence of metallic nanoparticle formation. Atom-counting the small Pt clusters in oxaliplatin shows they are flattened in the beam direction, and likely form only through natural agglomeration during the drying process. As imaging of cisplatin and oxaliplatin was achieved using the same electron dose, this provides further evidence against beam-induced NP formation in cisplatin. The different nanoscale behaviour of platinum in each drug may potentially have implications for *in-vivo* toxicity.

Chapter 5

Quantification of Platinum in DRG

5.1 Aims & Scope

Following successful imaging and quantification of cisplatin and oxaliplatin solution using HAADF STEM, similar methods were applied to examine to what extent platinum-based drugs are visible in sectioned tissue. The dorsal root ganglia (DRG) are known sites of platinum accumulation in patients treated with Pt-based medicines, and following *in vivo* oxaliplatin administration, rat DRG were harvested, frozen, and cryosectioned for imaging in the microscope.

Due to the high atomic number of platinum, sites of oxaliplatin accumulation were readily visible under HAADF conditions in the cytosol of neuronal cell bodies. High-magnification imaging showed these accumulations contained many small atomic clusters. The elemental species of the atoms contained in these clusters was identified as platinum through comparison of experimentally-measured elastic scattering cross-sections with those predicted from image simulation. Cluster masses were further determined by comparison with single-atom HAADF intensities.

5.2 Oxaliplatin in Dorsal Root Ganglia

Chemotherapy-induced peripheral neuropathy (CIPN) arises from treatment with a number of common anti-cancer drugs. Damage to different parts of the peripheral nervous system can

result in a spectrum of painful and debilitating side-effects, which can significantly impact a patient's quality of life both during and after cancer [311].

The platinum-based family of chemotherapeutics are particularly neurotoxic. Nearly all patients treated with these drugs develop some degree of sensory nerve dysfunction, resulting in pain, numbness and loss of coordination in the extremities [312]. CIPN which results from treatment with Pt-containing drugs is currently not predictable or preventable, and is unresponsive to analgesics. As the severity of the condition often increases with cumulative platinum dose, CIPN is often dose-limiting and can therefore impact on survival [313].

Mass spectrometry studies on homogenised whole tissues have shown that dorsal root ganglia (DRG), which contain the cell bodies of sensory neurons (Figure 5.1), are sites of preferential platinum accumulation following treatment with oxaliplatin [314], [315]. *In vitro* studies have suggested that formation of Pt-DNA adducts leads to ultrastructural changes in neuronal cell bodies, and ultimately apoptosis [316]. However, many key questions about how CIPN arises following Pt-based treatment still remain to be answered [317]. In particular, differences in the extent, duration and acute and/or chronic nature of cisplatin-, carboplatin- and oxaliplatin-induced peripheral neuropathy are still relatively unexplained [318], [319].

Following the successful application of high-resolution electron microscopy to observe profound differences in the nanoscale appearance of cisplatin and oxaliplatin solution (Chapter 4 and Ref. [273]), similar methods were applied to examine to what extent platinum-based medicines could be visualised in the DRG.

5.3 Sample Preparation

In this Section, the author wishes to acknowledge Dr Sarah Flatters, who carried out the experimental animal work and dissections to recover DRG. The author also wishes to acknowledge Dr Gema Vizcay-Barrena, who produced some of the cryosections.

Adult male Sprague-Dawley rats with starting weights of 180–220 g (Harlan UK Ltd. *(Blackthorne, UK)*) were kept in a climate-controlled room containing rats only. Rats were housed in plastic cages with sawdust bedding and environmental enrichment materials. Bedding/cages were changed twice a week. Artificial light was provided on a 12 h light-dark cycle (lights on at

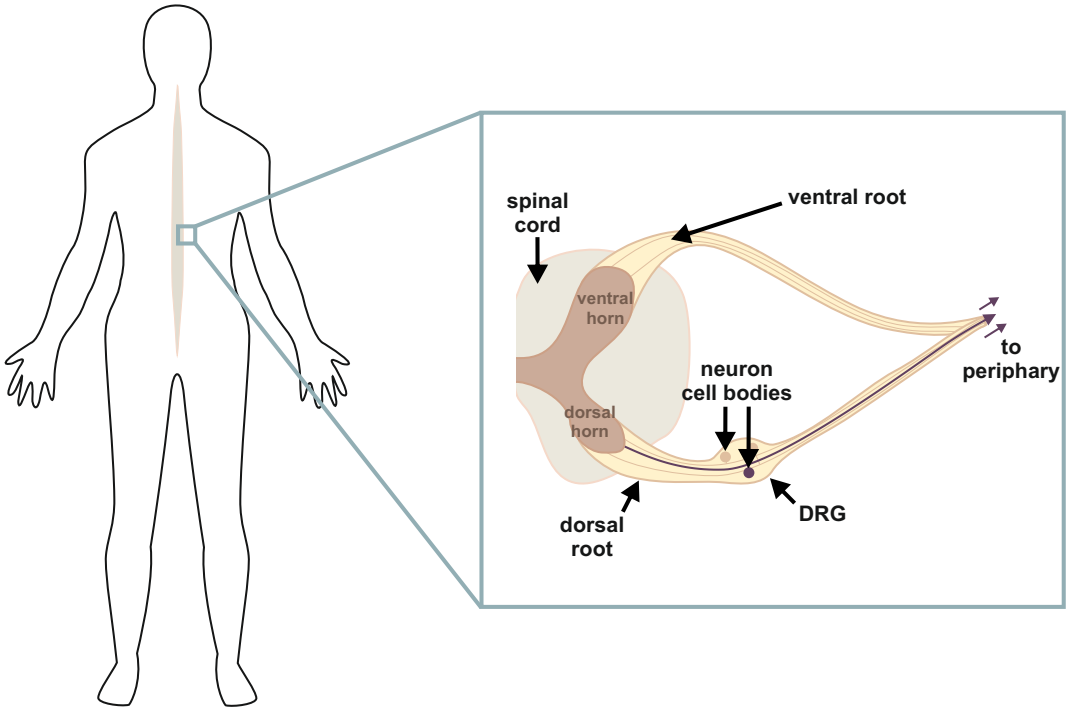


Figure 5.1: Schematic of the Dorsal Root Ganglion (DRG). The neuronal cells of the DRG are pseudo-unipolar; a short process connects the DRG to the spinal cord, and a much larger axonal process (up to 1 m in length in humans [320]) links it to the periphery of the organism. In addition to sensory cell bodies, the DRG also contains a number of non-neuronal cells [320], [321]. The particular vulnerability of the DRG to platinum accumulation is consistent with CIPN as a predominantly sensory neuropathy; motor neurons, and the autonomic system, are relatively unaffected by platinum treatment [312].

7am) with standard food/water ad libitum.

Oxaliplatin was prepared from clinically formulated solution (Oxaliplatin Concentrate for Solution for Injection; 5 mg/mL, Accord Healthcare Ltd. *(Harrow, UK)*). Rats received systemic intraperitoneal intermittent administration of oxaliplatin over a 14-day period, resulting in a cumulative dose of 25 mg/kg oxaliplatin. Rats were routinely visually checked and weighed to ensure good health. All studies were carried out in accordance with the UK Animals (Scientific Procedures) Act, 1986. Protocols were approved by the Ethical Review Panel of King's College London and conducted under the UK Home Office project license 70/8015.

Whole rat DRG were recovered following prolonged *in vivo* oxaliplatin administration. Five hours after the last administration of oxaliplatin, rats received an overdose of pentobarbital. L3-L5 DRG were then dissected bilaterally, with care taken to remove the ventral root. At room temperature, DRG were initially placed into phosphate-buffered solution. This was followed by exposure to 0.5% formaldehyde fixative solution overnight at 4°C. Following this step, the DRG were placed in a 2.3 M sucrose solution and before being plunge frozen and stored in liquid nitrogen.

Ultrathin cryosections were cut using the Leica EM UC7 with FC7 cryo-chamber (Leica *(Wetzlar, Germany)*) and a 35° DiATOME Cryo Immuno Diamond Knife (DiATOME Ltd. *(Biel, Switzerland)*). The cryoultramicrotome was set to a cutting thicknesses of 70–100 nm and cutting speed of 3–5 mm/s. Sections were transferred to pioloform-coated copper TEM grids using a 50:50 1% methylcellulose-2.3 M sucrose solution. The sections were then floated on distilled water droplets, before being washed for a total of 10 min per grid in fresh water droplets, changed every two minutes. The samples were then stored in low vacuum in a manually-pumped storage container until examined in the STEM. This sample preparation protocol was developed to minimise the extraction and redistribution of platinum, while also preserving sufficient tissue morphology to enable ultrastructural contextualisation of Pt aggregations.

5.4 Low- and Medium-Magnification Imaging

Low-magnification ADF imaging as shown in Figure 5.2 allowed rapid identification of regions containing DRG neuronal cell bodies. These images provide comparable information to a high-

magnification conventional light microscope. At low magnification, it is possible to discriminate between cell types; sensory neuronal cell bodies, myelinated axons and other non- neuronal cells are visible within a single section.

At intermediary magnifications (Figure 5.3), nuclear membrane, nucleolus and individual organelles, such as mitochondria, are readily distinguishable. The samples show normal tissue morphology, indicating good ultrastructural preservation during the sample preparation process. Importantly, these images also enabled Pt to be located in the context of the cell. Features with higher average atomic number appear in the image with higher intensity, and were therefore considered as potential sites of Pt accumulation; Figure 5.3(c) shows an example of a feature located on the exterior of the nuclear membrane, which was subsequently shown to contain Pt aggregations.

5.5 Single Atom Visualisation

Once potential sites of Pt accumulation had been identified from the low- and intermediate-magnification images, each feature was examined in more detail. Figure 5.4 is a typical example of typical high-magnification imaging at these sites and shows small atomic clusters with diameter of between about 1–5 nm. Further imaging showed that the clusters contained many single atoms, identifiable as ∼1 Å intensity peaks.

The electron dose used to record images of single atoms was approximately 1×10^6 el /Å^2. Due to the relatively large numerical aperture required to achieve single atom imaging, the depth of focus was restricted to ∼9 nm. As this is significantly smaller than the thickness of the sample, in order to locate single atoms the focal point of the electron probe was repeatedly swept through the full depth of the section. The total dose received by the sample is therefore likely several times the imaging dose, and many orders of magnitude higher than typically used for e.g. single-particle cryo-electron microscopy. However, by restricting the use of high probe currents for imaging only within small areas inside features of interest, single atom detection could be achieved without compromising the ultrastructure observable at lower magnifications.

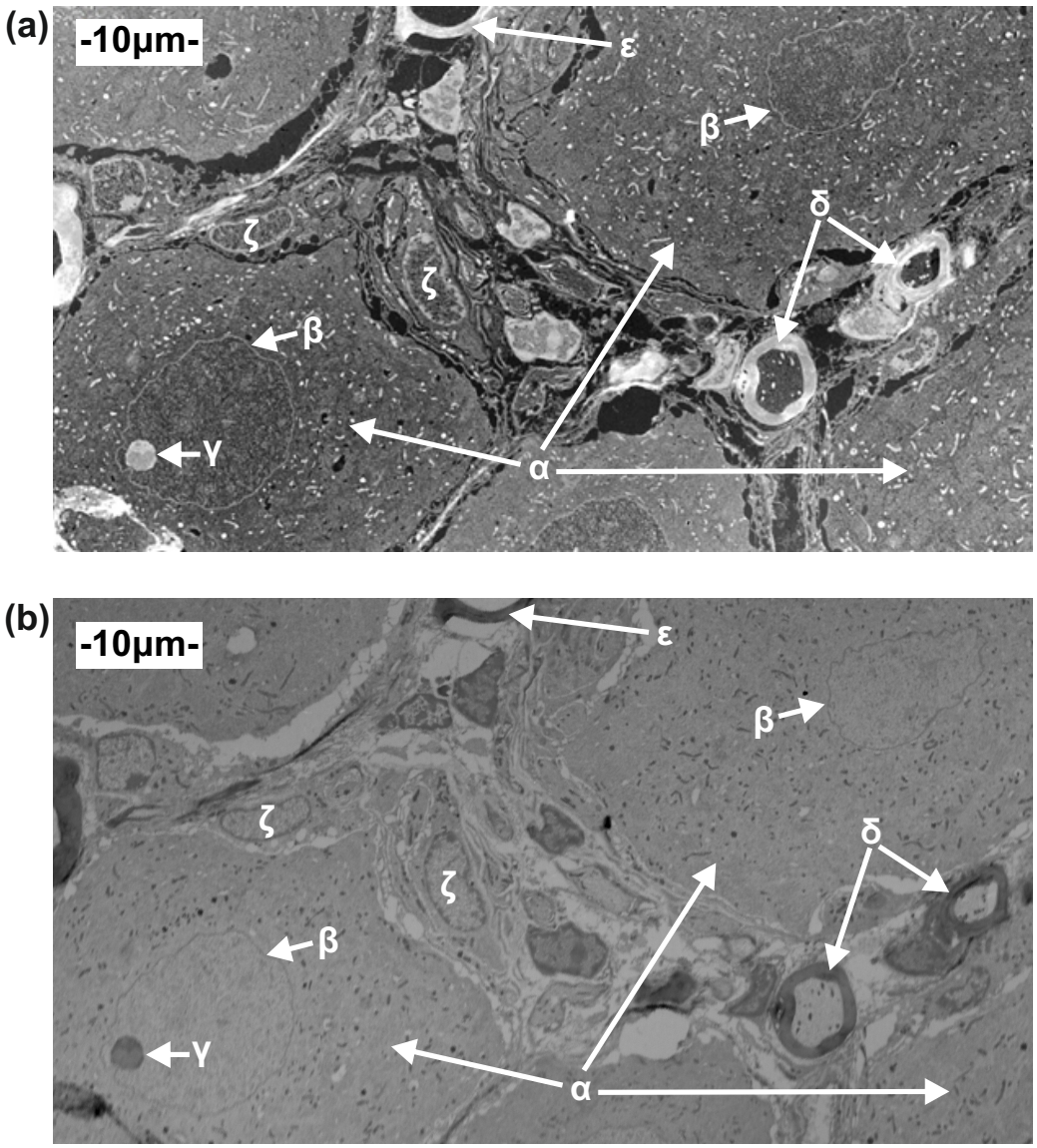


Figure 5.2: Low-magnification images of thin sections of DRG recorded using the (a) upper and (b) lower ADF detectors in "Low-Mag" mode on the Oxford JEOL ARM-200F. While (a) appears to be a true dark-field image (i.e. with contrast arising due to sample mass-thickness), (b) appears more similar to a bright-field STEM image, likely due to a degree of misalignment between the two ADF detectors. Image contrast in these images is therefore somewhat ambiguous. However, these images are sufficient to identify various features of the DRG. For example, neuronal cell bodies (α) (with nuclear membranes (β) and nucleolus (γ), myelinated axons (δ), capillaries (ε), and other non-neuronal (possible Schwann) cells (ζ) are readily visible and help to target high-magnification imaging. While the sectioning process introduces some intercellular disruption, the cell interiors remain intact with identifiable ultrastructure allowing contextualisation of Pt accumulation.

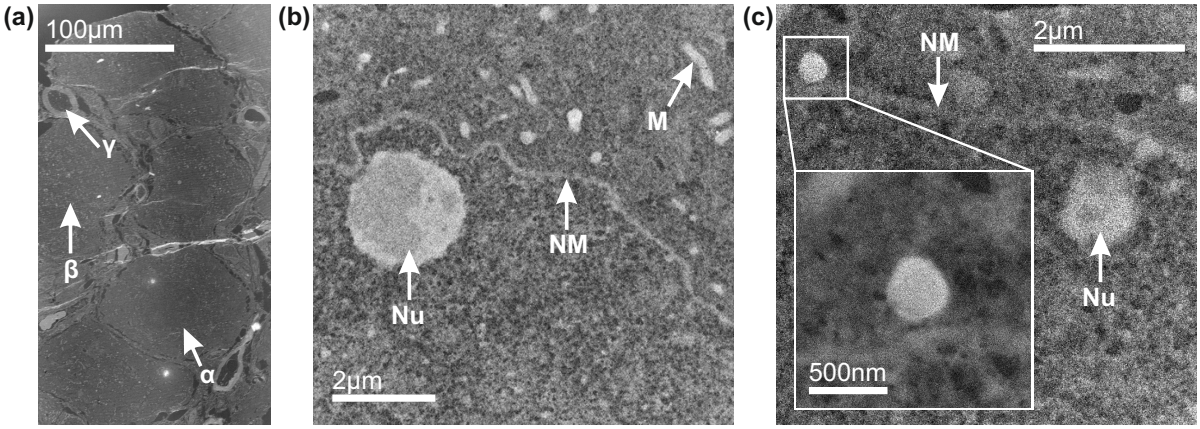


Figure 5.3: ADF imaging in the DRG. (a) A low-magnification overview of DRG allows for identification of regions of interest. Sensory neuronal cell bodies (α, β) and myelinated axons (γ) are indicated. (b) Sections showed good ultrastructural preservation, with identifiable subcellular features such as mitochondria (M), the nucleolus (Nu) and nuclear membrane (NM) visible at higher magnifications. (c) Some regions in the DRG cytosol exhibit increased image contrast, correlating to higher average atomic number or density in that region (inset). The dose used to acquire images of the type displayed in Figure 5.3(b) and (c) was on the order of 20–200 electrons/Å^2.

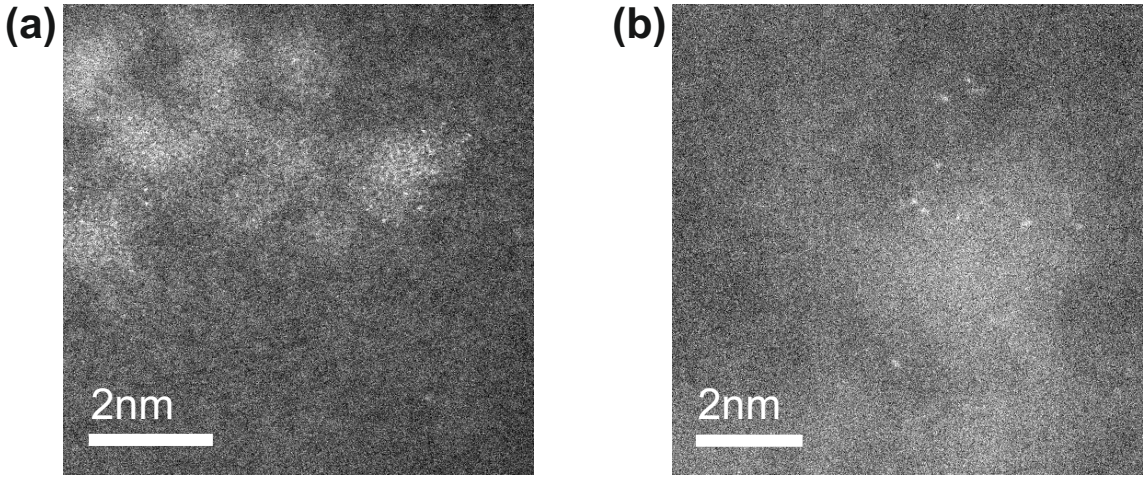


Figure 5.4: HAADF images of atomic clusters in DRG. Measurement of cluster diameter is challenging, as the clusters are highly mobile under the electron beam. The probe convergence semi-angle used in this experiment was 22.4 mrad, and the inner and outer detector convergence semi-angles are 72.4 mrad and 271.0 mrad respectively (i.e. well into the HAADF regimen).

5.6 Species Identification Using Probe-Integrated Scattering Cross-Sections

While atoms observed in images of the type shown in Figure 5.4 clearly scatter more strongly than the surrounding matrix, their elemental species cannot be unambiguously determined without further analysis, as described in this Section.

5.6.1 Theory

As discussed in Chapter 1, the intensity in a HAADF image may be written as a convolution of probe and object wavefunctions. E et al. extended this to show that integrating the fractional intensity for a given feature (e.g. atomic column) a with area A yields a "probe-integrated cross section" (PICS) σ^{HAADF} [322],

$$\int_A I_a(\mathbf{R})d\mathbf{R} = \frac{4\pi}{h\nu}\int_A \bar{V}_a(\mathbf{r}_\perp)d\mathbf{r}_\perp \equiv \sigma^{\mathrm{HAADF}}. \tag{5.1}$$

$\mathbf{R}$ is the vector between the center of the atomic column and the probe position, and $\mathbf{r}_\perp$ is centered on a and orthogonal to the beam. E et al. also showed that, for a HAADF image where each image pixel measures the fraction of the probe scattered at that location, σ^{HAADF} may equivalently be written as a discrete sum (over j pixels which contain the feature), of fractional intensities I_{aj} multiplied by the pixel area a_j:

$$\sigma^{\mathrm{HAADF}} = \sum_j I_{aj}a_j, \tag{5.2}$$

The probe-integrated cross-section is robust to imaging parameters such as defocus and other aberrations. As the PICS is linear with scattered electron intensity, which is itself approximately linear with number of atoms under the probe and highly dependent upon atomic number, it is a very suitable method for comparing experimental and simulated images.

5.6.2 Experimental PICS calculation

The PICS method was then used to compare the cross-sections of the atoms shown in images of the type shown in Figure 5.4 with those calculated from simulation. First, the image was converted from arbitrary intensity units to fractional intensity I_{frac} by using the AbsoluteIntegrator v1.6.4 code [323]. I_{frac} is calculated using

$$I_{frac}(\mathbf{R}) = \frac{I_{exp}(\mathbf{R}) - I_{vac}}{I_{det} - I_{vac}}, \tag{5.3}$$

where I_{exp} is the intensity in the pixel from the experiment, I_{vac} is the background electronic noise intensity level recorded in vacuum, and I_{det} is a radially averaged value of detector response when illuminated by the full unscattered beam. $\boldsymbol{R}$ denotes a dependence upon probe position.

The values of I_{vac} and I_{det} were obtained by recording an ADF detector response sensitivity "map", i.e. by scanning the electron probe across the full ADF detector and recording the detector response at each scan position. This is necessary as the detector response is not uniform, and thus greater and lesser degrees of sensitivity at different points on the detector must be accounted for in order to very accurately quantify ADF images [324], [325]. Figure 5.5 shows an example ADF detector map, along with the result of image fractionation using Equation 5.3.

Total fractional intensity generated by the single atom was calculated by integrating over the relevant image pixels, and subtracting the local background contribution. This background arises due to the presence of other atoms (mostly carbon and platinum) outside the focal plane of the STEM probe. Their contributions to the image were obtained by averaging the surrounding halo of pixels outside the extent of the atom. Experimental cross-sections were then calculated (as per Equation 5.2) by simply multiplying the background-subtracted total fractional intensity by the pixel area (set by the magnification of the microscope). The average cross-section of a single atom $\sigma_{\text{atom}}^{\text{HAADF}}$ was calculated as 1.15 Mbarns (for $n = 13$ single atoms, and standard deviation $s = 0.03$ Mbarns), where 1 barn $= 10^{-28}\,\text{m}^2$

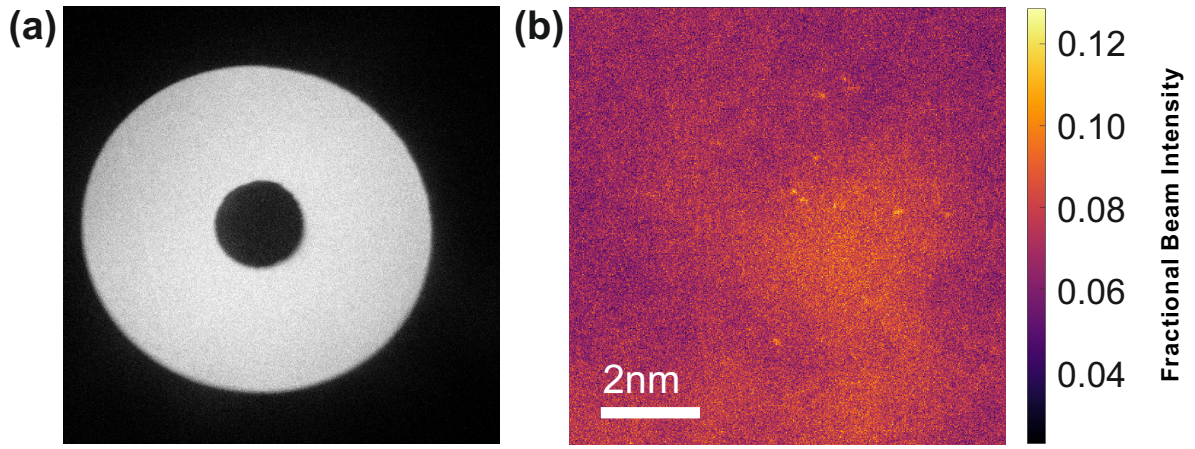


Figure 5.5: (a) Response map of the upper ADF detector in the Oxford JEOL ARM-200F. Non-uniform intensity indicates the response is not homogeneous across the detector. (b) Atomic cluster image converted to units of fractional beam intensity. The most intense areas indicate as much as 12% of the beam is scattered to the HAADF detector at some probe positions.

5.6.3 Simulated PICS

Experimental values were then compared with simulated cross-sections. Single atom STEM multislice image simulations were performed with the MULTEM v2.2.1 code, using the frozen phonon model (10 phonon configurations) and the Lobato potential parameterisation optimized for high-angle scattering [326]. The simulation parameters of probe convergence semi-angle α, ADF inner and outer detector semi-angles (β_1, β_2), and microscope accelerating voltage E_0 were matched with the experiment ($E_0 = 200\,\mathrm{kV}$). A single atom of each elemental species between Z=1 and Z=86 was placed at the center of the 30×30 nm simulation grid, which was subsequently sampled at 0.029 nm. This sampling was sufficient to capture the full high-angle scattering within the simulation. Figure 5.6 shows the resulting calculated cross-section $\sigma_{\mathrm{atom}}^{\mathrm{HAADF}}$ for each species. As indicated, the simulated cross-section for a single Pt atom is 1.13 Mbarns, more than an order of magnitude greater than the cross-sections of more biologically abundant elements. The excellent agreement between this value and that measured experimentally confirms that the strongly-scattering atoms observed aggregating within the cell cytosol are indeed platinum.

5.7 Cluster Weighing

Following successful use of ADF STEM scattering cross-sections to positively identify single platinum atoms within the DRG, it was then possible to use a similar approach to count the total number of Pt atoms in small clusters of the type shown in Figure 5.4. Following the same approach as for obtaining the single atom cross-sections, local background subtraction and image analysis in accordance with Equations 5.2 and 5.3 generates a "cross-section per cluster" value $\sigma_{\mathrm{cluster}}^{\mathrm{HAADF}}$. As HAADF STEM is an incoherent measurement, this cross-section may be regarded simply as

$$\sigma_{\mathrm{cluster}}^{\mathrm{HAADF}} = N_{atoms} \times \sigma_{\mathrm{atom}}^{\mathrm{HAADF}}, \tag{5.4}$$

i.e. as the single Pt atom cross section $\sigma_{\mathrm{atom}}^{\mathrm{HAADF}}$ multiplied by the number of atoms N_{atoms} present in the cluster. Figure 5.7 shows Pt mass as a function of cluster diameter d. Most cluster diameters were found to range between 3–5 nm, and thus contained around 800-2000 platinum atoms (equivalent to 260-650 zeptograms of Pt). It is reasonable to assume the atomic clusters

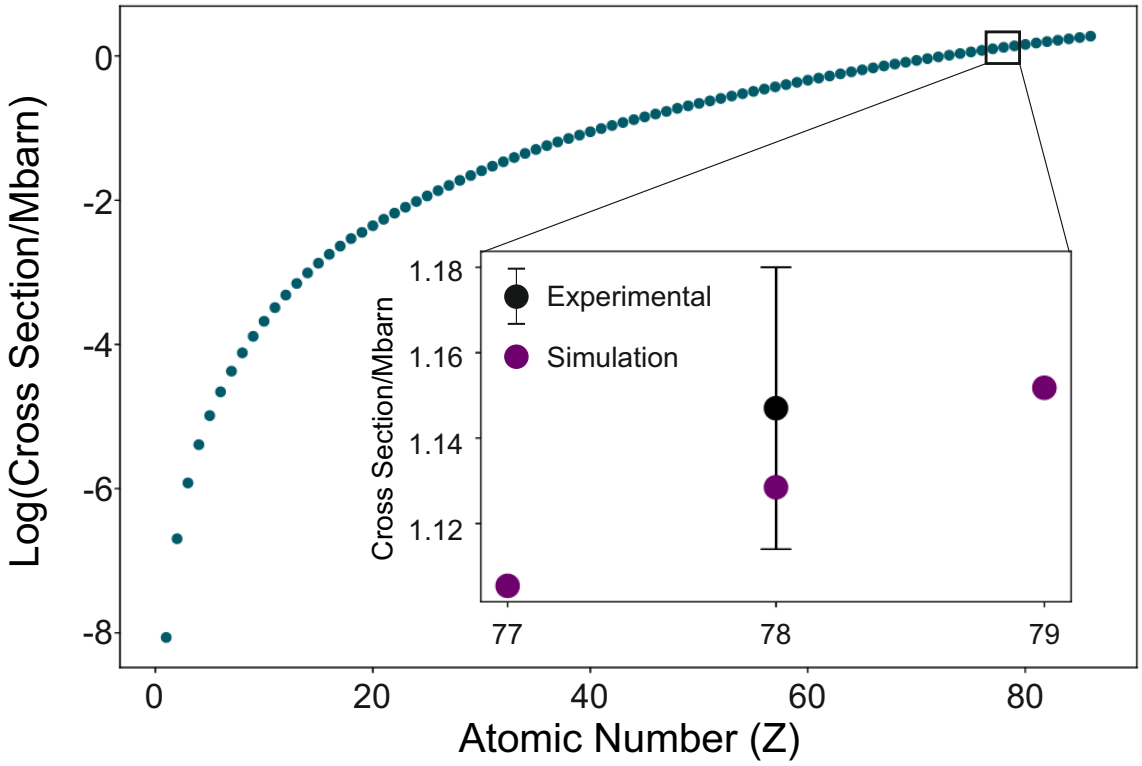


Figure 5.6: Simulated single-atom cross sections for α=22.4 mrad, (β_1, β_2)=(72.4,271.0)mrad at E_0=200 kV. The inset graph shows expected cross-sections for iridium (Z=77), platinum (Z=78) and gold (Z=79). Experimental data with an error bar of 1 standard deviation are is shown in black.

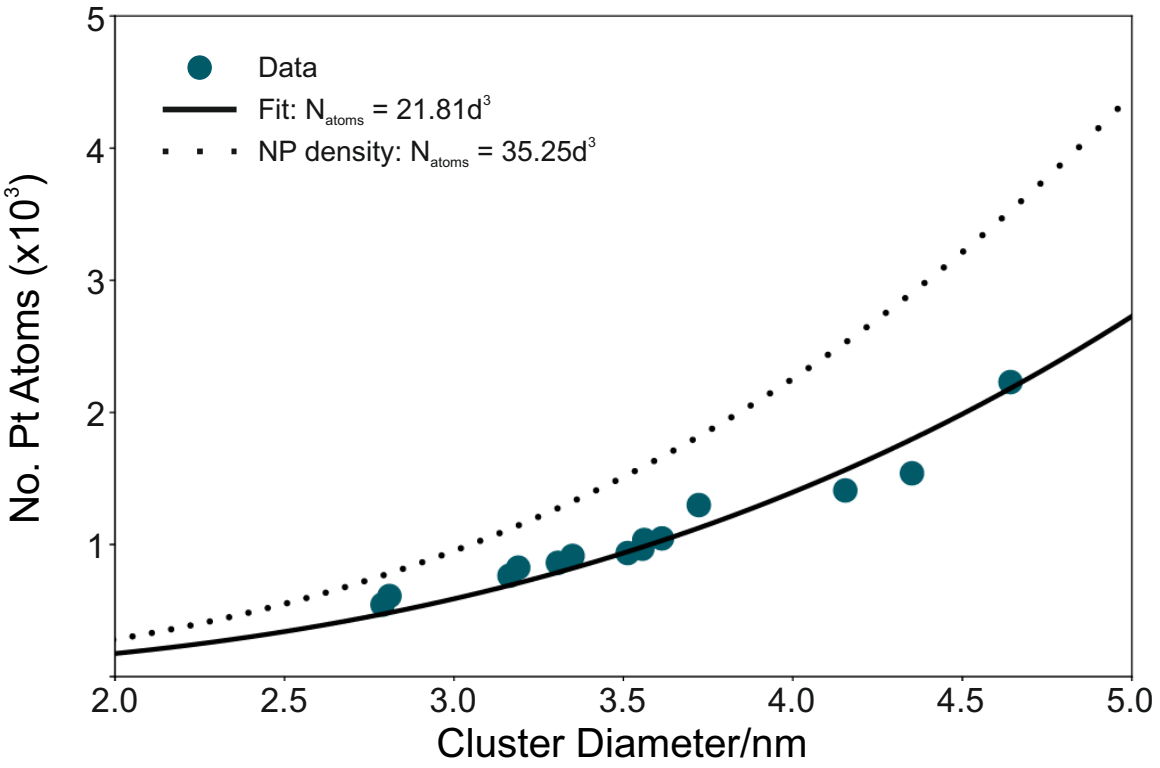


Figure 5.7: Atomic cluster weighing in the DRG. Experimental data are fitted with a cubic dependence upon cluster diameter d, showing they contain approximately 40% fewer atoms per cubic nanometer when compared with metallic nanoparticles. The R^2 value for this fit is 0.87.

observed in the DRG are spherical, and therefore have a cubic dependence on cluster diameter. A fit of the experimental data shows that the density of these clusters is approximately 60% that of metallic platinum nanoparticles, containing around 40 atoms per cubic nanometer. Similarly to the observations described in Chapter 4 made on dried oxaliplatin solution, this lower density implies central platinum atoms within the drug molecules are at no point free to nucleate into nanoparticles.

5.8 Visibility of Other Species

In an ADF STEM image, whether a single atom of a particular elemental species x is visible in a matrix of element y, and to what extent it may then be quantified, is informed by two calculations. The first of these concerns whether the peak associated with a heavy atom is above

the total noise, such that it can be located in a HAADF image.

When the electron probe is directly over a single atom of element x, the number of electrons $n_{el,x}$ it scatters to the ADF detector is given by

$$n_{el,x} = N_e \frac{\sigma_x^{\mathrm{HAADF}}}{A_{beam}}, \tag{5.5}$$

where N_e is the total electrons delivered during the illumination (in this experiment, defined by the probe current i and pixel dwell time τ), and $\sigma_{\mathrm{x}}^{\mathrm{HAADF}}$ is the ADF cross-section of a single atom of element x. Equivalently, the number of electrons $n_{el,matrix}$ scattered to the detector by the background matrix of element y is given by

$$n_{el,matrix} = N_e \rho_y t \sigma_y^{\mathrm{HAADF}}, \tag{5.6}$$

where ρ_y is number density, t is the matrix thickness along the beam direction, and $\sigma_{\mathrm{y}}^{\mathrm{HAADF}}$ is the single atom cross section for element y. Equations 5.5 and 5.6 may be considered as the total number of incident electrons multiplied by an area ratio of the single atom or matrix atoms with the beam area respectively.

In the STEM, the noise (ψ_{el}) generated by both the atom and the background matrix limits whether a single atom of element x may be detected. ψ_{el} obeys Poissonian statistics [327], [328] such that

$$\psi_{el} = \sqrt{n_{el,matrix} + n_{el,x}}. \tag{5.7}$$

To detect a single atom peak, it is required that $n_{el,x} > a\psi_{el}$, with the value of the constant a usually taken to be 3 to ensure near-certainty of detection.

5.8.1 Implications for Integration

However, when integrating image pixels (as implemented in Section 5.6.2), additional considerations apply. The atom signal may equivalently be given by

$$n_{el,x} = D_e \sigma_x^{\mathrm{HAADF}}, \tag{5.8}$$

where the electron fluence D_e is given by $\frac{N_e}{A_{px}}$ for a pixel area A_{px}. Similarly to Equation 5.7, the integrated noise $\psi_{el,total}$ is given by

$$\psi_{el,total} = \sqrt{D_e \sigma_y^{\mathrm{HAADF}} A_{int} \rho_y t + D_e \sigma_x^{\mathrm{HAADF}}}. \tag{5.9}$$

Again, $n_{el,x} > 3\psi_{el,total}$ is imposed to successfully measure the cross section of a single atom of x in a matrix of y.

From Equations 5.7 and 5.9, it is clear that there are subtle but important differences which influence the *detectability* limit, i.e. the ability to distinguish the peak of single atom relative to the surrounding matrix, and the *measurability* limit imposed to measure scattering cross-sections experimentally. In practice, this is because measuring $\sigma_{\mathrm{atom}}^{\mathrm{HAADF}}$ from a HAADF image requires integration of sufficient image pixels to capture the full scattering of that atom, but summation of additional pixels beyond this serve only to add additional noise. Both limits depend on the total electrons incident on the sample, the atomic species x and y, and the areal density $\rho_y t$ of the matrix.

5.8.2 Applications to Thin Sections

The feasibility of detecting and measuring single atoms of element x in samples similar to those produced from the DRG through consideration of Equations 5.5 through 5.9, in combination with values of $\sigma_{\mathrm{atom}}^{\mathrm{HAADF}}$ calculated for the HAADF imaging conditions described in Section 5.5. Following a similar approach to Moran et al., a hydrated sample density of $1\,\mathrm{g/cm^3}$ and a 70% water content by mass is assumed [329]. A "worst-case" scenario occurs when all the dry weight is carbon (in reality this likely overestimates the background contribution to the electron scattering). This means that each cubic nanometer of dehydrated sample contains approximately 15 carbon atoms. In an aberration-corrected C-FEG STEM, the electron probe has a full width at half maximum of 80 pm, such that A_{beam} is approximately $0.5\,\mathrm{\AA}^2$.

The noise generated by this carbon is shown in Figure 5.8, along with the noise generated by

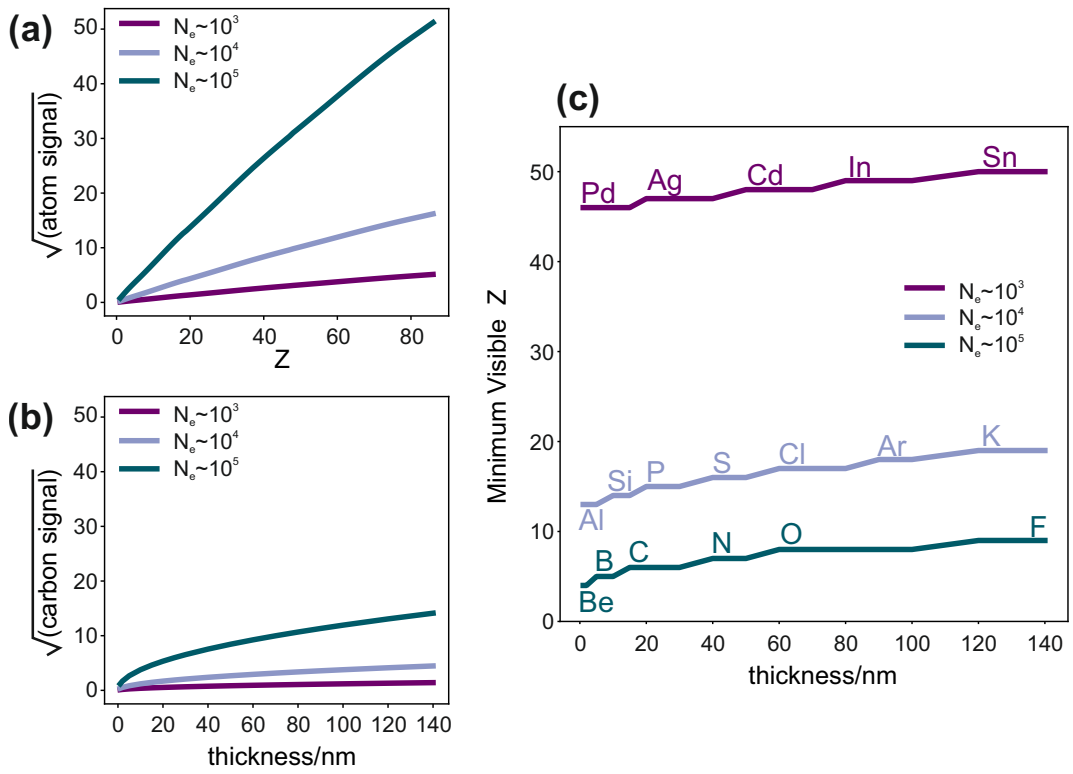


Figure 5.8: Single atom visibility limits in HAADF STEM. (a) and (b) show that the noise generated by the atom and low-density carbon background respectively depends heavily upon the number of total incident electrons. (c) shows which elemental species would be visible under these experimental conditions.

single atoms of each species. The dominant noise contribution is shown to depend on the carbon thickness, and the species of x. For example, detection of a heavy atom in 1 nm of carbon is limited by noise from the atom, but detection of the same atom in 150 nm of carbon is limited by a considerable contribution from the background carbon matrix, with this balance shifting for different numbers of incident electrons. Figure 5.8 also shows the atomic species which may reasonably be expected to be detectable in a certain sample thickness.

Figure 5.9 shows the dependence of the *measurability* limit (for measuring single-atom cross-sections) upon the number of pixels included in the integration. As expected, this limit is degraded for increased integration area. However, noise generated by the single atom itself remains the most significant influence on measurability.

Figures 5.8 and 5.9 indicate that under similar experimental conditions to those used to measure single Pt atoms in the DRG - i.e., a sample with nominal cryosectioning thickness of

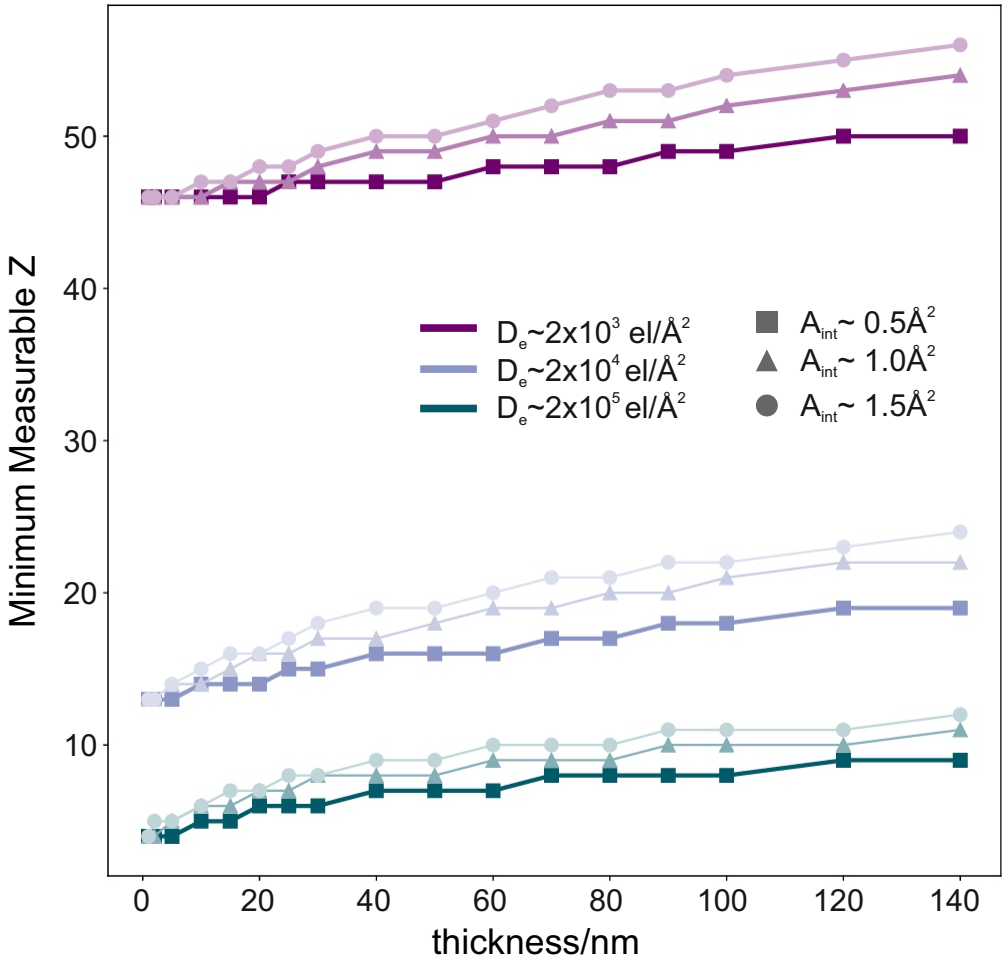


Figure 5.9: Single atom measurability limits in HAADF STEM. Similarly to the HAADF visibility limit, there is a considerable dependence upon electron dose. However, a further limit is imposed by integration, with additional pixels contributing extra noise and degrading the measurability.

about 70 nm, and with D_e $\sim 10^6$ electrons/Å^2, atomic species heavier than sodium should be measurable. However, this limit may be degraded in reality. Firstly, beam-induced motion is likely to be greater for low-Z species. The consequences of this may be that a larger integration area is required to capture the full high-angle scattering, or that the cross-section may have a much larger error bar (and thus be less distinguishable from neighbouring elemental species).

A second challenge would be posed for single-atom detection in regions with enhanced density, or higher concentrations of heavier background species (as, for example, is the case in an organelle). This consideration, in combination with the limited electron dose tolerance of the sample, also indicates that it is unlikely other atomic species present in the oxaliplatin would be directly measurable in drug aggregations under these experimental conditions.

5.9 Limitations of EDX

Platinum Mα and Lα x-rays have energies of 2.05 keV and 9.44 keV respectively. Both are well within the measurable energy range of an energy-dispersive x-ray (EDX) detector. EDX spectroscopy was therefore initially attempted to screen features of the type shown in Figure 5.3(c) for Pt at low magnifications before examining them for single atoms.

Conventionally this would be achieved by acquiring a spectrum image (SI), i.e. recording EDX spectra pixel-by-pixel in the same manner as STEM imaging. However, due to limitations of the acquisition software, the shortest pixel dwell time available on the instrument was 1000 µs (approximately two orders of magnitude longer than the fastest imaging speed). Unfortunately, it was found that even the fastest SI acquisition at significantly reduced electron dose still resulted in substantial damage to the sample.

As shown in Figure 5.10, limited and spatially unresolved x-ray data could be acquired by continuously summing the EDX signal while scanning the probe at imaging speeds. However, the resulting spectra highlight two particular issues with identifying Pt in this manner. Firstly, the Mα line is indistinguishable from the (larger) phosphorous Kα x-ray peak at 2.013 keV. As the spectrometer resolution is only around 100 eV, the platinum signal appears at best as a small shoulder on the primary peak. Secondly, low x-ray yield (about two orders of magnitude lower than the elastic interactions measured by ADF [330]) and poor detection statistics (a few percent,

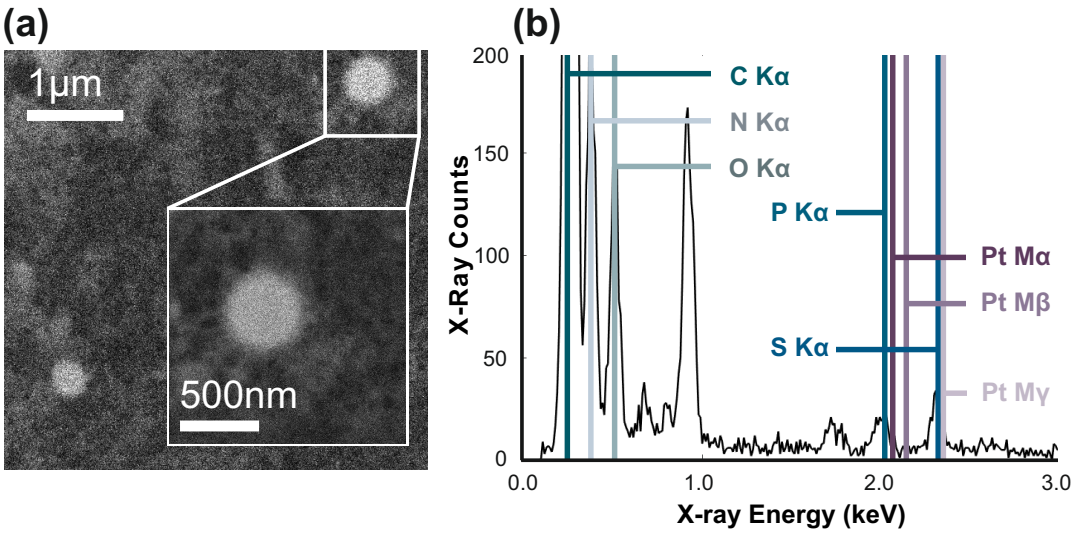


Figure 5.10: EDX of Pt-containing clusters in DRG. (a) Features similar to those in Figure 5.3 are visible throughout the DRG. (b) EDX acquired from continuously scanning over the region indicated in (a) shows characteristic Pt x-rays appear as shoulders on the nearby P Kα and S Kα peaks, and are at most only slightly above the noise level. Qualitatively, the spectrum shows the sample is mostly comprised of carbon, nitrogen, oxygen, with trace amounts of other elements.

compared to nearly all high-angle electrons) result in a very poor counting statistics. Similar challenges exist with measuring the Pt $M_{4,5}$ in electron energy loss spectroscopy (EELS); again, detection and quantification is inhibited by limited signal, which cannot be improved simply be increasing the electron dose without catastrophic damage to the sample. In combination these factors mean measurement of inelastic signals cannot reliably distinguish platinum in the DRG.

5.10 Discussion

As discussed at the beginning of this Chapter, conventional mass spectrometry has shown that the DRG preferentially accumulate platinum following oxaliplatin treatment. However, these methods are not able to localise platinum aggregations inside the cell, and other techniques must be employed to ascertain the fate of oxaliplatin inside the neuronal cell bodies. Accessing this information is particularly important for understanding the mechanisms by which chemotherapy-

induced peripheral neuropathy arises following platinum-based treatment, which are still poorly understood [319].

It is outside the scope of this thesis to make meaningful biological observations concerning platinum accumulation by the DRG. However, research into the intracellular behaviour of platinum agents is a highly active field [331], and the results discussed here will be examined in the context of other existing literature results.

5.10.1 Other Techniques for Pt Localisation

Heterogeneous elemental distributions inside cells drive fundamental biological processes. Quantity, local chemistry and location of each distribution are tightly controlled to regulate cell function; characterisation in the context of the cell ultrastructure can therefore answer fundamental questions concerning subcellular activity [332]. Many techniques may be employed to access this information, each with differing limits on spatial resolution, detection sensitivity, and elemental specificity. In addition, each approach varies as to what extent data are quantifiable [333]–[336].

The intracellular distribution of platinum-containing drugs have been examined extensively and using a broad range of techniques. A number of examples have been shown based upon the measurement of characteristic x-rays following irradiation with high-energy particles (exactly as is invoked to record EDX data in the electron microscope). For example, microbeam particle-induced x-ray emission (microPIXE)) has been used to localise platinum in samples of kidney [337] and liver [338], and in a number of cancer cell lines [339]. Synchotron x-ray fluorescence (SXRF) has also proved suitable to locate platinum-based drugs (and other anti-cancer metal compounds [340]) within cells, with measurements made on samples of human rectal cancer tissue [341] and in platinum-treated cell lines [342], [343].

However, as discussed in Section 5.9, overlapping characteristic x-ray peaks pose a particular problem for quantifying platinum in the context of the cell. While the fundamental detection sensitivities of microPIXE and SXRF are on the order of 1-10 parts per million [335], [336], [344] detecting such small signals above the (more abundant) phosphorous and zinc x-ray peaks presents a significant challenge. This is illustrated in Jeynes et al., who examined platinum content in two ovarian cancer cell lines following incubation with cis- and carboplatin [345].

They were unable to measure a statistically significant difference in platinum accumulation by Pt-sensitive and Pt-resistant cells due to the degree of of overlap between the P Kα and Pt Mα(as observed in the EDX data presented in this Chapter), and the Pt Lα and Zn Kβ x-ray peaks. In addition, despite exposing cells to highly concentrated carboplatin solution, they were also unable to detect any platinum signal in either cell line. Carboplatin has been shown to accumulate in cells at much lower levels than other Pt-based drugs; any Pt x-ray signal generated is therefore significantly more challenging to measure when occluded by other elements. Similar problems have also been encountered in synchotron x-ray fluorescence experiments. Ilinkski et al. report detection of as few as 6×10^4 atoms of platinum in ovarian cancer cells treated with an cisplatin derivative [346]; however, their measurements relied upon extrapolating Zn Kβ counts from the Zn Kα peak, itself convolved with the Cu Kβ. The low x-ray counts would introduce a considerable amount of uncertainty, and make accurately quantifying low platinum concentrations very challenging.

Intracellular metal distributions have also been examined extensively using methods based of measurement of mass-to-charge ratios (m/z) [347]. Samples are fragmented using a high-energy source, and the resulting ions, molecules and/or molecule fragments identified by their characteristic m/z values [348]. Techniques such as laser ablation inductively-coupled plasma mass spectrometry (LA-ICP-MS) and nanoscale secondary-ion mass spectrometry (nanoSIMS) have been applied to measure accumulation of platinum-based drugs in a number of cell lines and tumour samples [349], [350]. For example, Lee et al. observed "hotspots" of Pt aggregation in cisplatin-sensitive human ovarian carcinoma cells using nanoSIMS [351]. However, while elemental maps could be achieved with a spatial resolution of about 70 nm, Pt accumulations had to be correlated with ultrastructure from conventional TEM images, introducing additional uncertainty in correlating Pt with particular organelles. A further complication was that due to the trace Pt concentrations in their sample and the low secondary ion Pt yield, map acquisition times were on the order of ∼20 h. More rapid data acquisition has been reported in other nanoSIMS studies, but only in samples exposed to considerably higher concentrations of platinum far beyond those experienced by cells in vivo [352]. A very thorough review of the applications of mass spectrometry imaging to the localisation of platinum-based drugs, including using other techniques such as time-of-flight SIMS and matrix assisted laser desorption ionization, is given by Lee et al. in Ref. [353].

5.10.2 Electron Microscopy for Pt Localisation

As with other techniques used to characterise elemental distributions, the method described in this chapter also has its own advantages and limitations. A key example of the latter, and a commonality shared with nanoSIMS and microPIXE, is the extensive sample preparation required to produce thin and vacuum-robust samples from whole tissues. Often these procedures are similar to those employed in conventional TEM preparation; however, chemical fixation, serial dehydration and/or resin infiltration pose a considerable risk of elemental extraction and/or redistribution [354], with clear consequences for reliable chemical mapping. The sample preparation methods used to produce the DRG samples shown in this Chapter are based upon those used in Tokuyasu immunolabelling [355]. Mild fixation using 0.5% formaldehyde solution (as opposed to the 10-20+% solution routinely used for such samples) appears to be sufficient to prevent ultrastructural changes caused by osmotic pressures during cryoprotection with 2.3 M sucrose. As indicated by Figure 5.2, this procedure reliably preserved ultrastructural features including cell membranes and other organelles.

Observations of platinum in discrete accumulations has been reported elsewhere in the literature. Legin et al., using nanoSIMS and LA-ICP-MS, observed co-localisation of platinum with sulphur-rich organelles in kidney and tumour tissue following in-vivo administration of two novel platinum complexes [356]. Similar correlations with sulphur were also reported by Lee et al. following *in vitro* cisplatin treatment, with additional observations of accumulation in mitochondria, autophagosomes and the nucleolus [351]. It is therefore likely that the platinum-containing features reported in this work (as shown in e.g. Figures 5.3 and 5.10) do not arise due to artefacts of the sample preparation procedure, and are instead related to the intracellular transport of oxaliplatin in neuronal cell bodies.

As discussed in Chapter 3, HAADF STEM has been used extensively to detect clusters of atoms, usually in the context of molecular labelling. However, thus far the use of electron microscopy in directly visualising intracellular distributions of platinum-containing chemotherapeutic drugs [357], [358] (and other metals [240], [359]) has largely been restricted to qualitative and semi-quantitative observations. Techniques commonly employed for chemical analysis in the electron microscope (such as EDX and EELS) have relatively poor detection limits in such complex samples, largely due to low inelastic scattering strengths and collection efficiencies,

overlapping signals, and limitations placed on electron dose. Other (non-EM) methods without these constraints have therefore proven more favourable for extracting elemental information in these samples. However, as shown in this Chapter, by making use of the much stronger elastic scattering signal and the high collection efficiency of the ADF detector, it is possible to detect and measure extremely small atomic platinum clusters, containing just a few tens of atoms, inside biological specimens. This is possible because the elastic scattering measured by the ADF detector is several orders of magnitude higher than for EDX and EELS.

As HAADF STEM is not easily able to identify every elemental species present at a certain site, other techniques are probably more suitable for routine elemental analysis. However, the spatial resolution of the STEM is several orders of magnitude higher than any comparable method, and may therefore ultimately be useful in providing complementary and quantitative information. A natural extension of this work would be to examine samples from cisplatin-treated animals for evidence of metallic Pt nanoparticles as detailed in Chapter 4, but there are further opportunities for this work to be extended to fields such as nanotoxicology and pharmacology. Metal and metal oxide nanoparticles are now widely used in many industries, but have been shown to have potentially deleterious effects to both human health and the environment [360]. Work by Maher et al. has highlighted the potential neurodegenerative role of pollutant iron-rich nanoparticulates in brain tissue [361], and Moore et al. have shown evidence of potentially toxic sequestration of elements such as arsenic following exposure to contaminated water [362]. As informed by the visibility and measurability calculations in Section 5.8, it would be reasonable to expect Fe and As to be readily visible in thin tissue sections as produced for the DRG. Furthermore, as shown in Figure 5.9, heavier single atoms may be in fact be measurable at electron doses comparable to those used in cryo-TEM. High-resolution STEM imaging may therefore provide additional, quantitative, information about cellular and organelle accumulation.

5.11 Summary

The aims of this work were to examine to what extent STEM techniques could be used to locate platinum in the dorsal root ganglia. Neuronal cell bodies were targeted for imaging due to their established affinity for accumulating platinum during oxaliplatin administration, and ultimately shown to contain discrete sites of Pt aggregation. Literature evidence supports these

observations, which suggest the sample preparation procedure used in this experiment strikes an appropriate balance between the competing challenges of preserving native cell ultrastructure and intracellular Pt distribution.

While it is well-established that elements with high atomic numbers are readily visible using HAADF STEM, the work discussed in this Chapter represents the first demonstration of high-Z single atoms visualised and identified in sample of this kind. This environment poses a particular challenge for quantification, due primarily to the high mobility of single atoms under the electron probe, and limitations on electron dose imposed by the beam-sensitivity of the surrounding low-density carbon matrix. Nevertheless, experimental measurement of the HAADF scattering cross-sections from single atoms were shown to match well with those predicted using multislice simulation, allowing the atoms to be identified as platinum.

Chapter 6

Measurement of EDX and EELS Partial Cross-Sections

6.1 Aims & Scope

An emerging technique for quantifying EDX spectra is based upon measurement of partial cross-sections. Similar to the methods employed for quantifying EELS data, x-ray counts per atom may be converted to partial cross sections through considerations of electron dose and scan area. Thus far, EDX partial cross-sections have only been measured from samples containing only one element, and with well-defined geometry. However, many elements are either not readily available as isolated materials, or cannot be fashioned into configurations suitable for use in the STEM.

In this Chapter, it is shown that the partial cross-section approach for EDX quantification may be extended to incorporate measurements made from multi-element standards. Key to this method is accurate quantification of HAADF images, which allows number of atoms of each species present to be estimated from stochiometric standards independently of spectral data. Partial scattering cross-sections are measured from both an an aberration-corrected and an uncorrected (S)TEM, and for several low atomic number elements of biological significance.

6.2 Partial Scattering Cross-Sections in EDX and EELS

In Chapter 2, two existing methods for quantifying EDX data were reviewed. The Cliff-Lorimer method links elemental concentrations with EDX peak counts, via generation of a library of k-factors from standards of known composition. However, even fastidious measurement of k-factors can still result in significant errors in concentration measurement.

The Watanabe-Williams ζ-factor method can provide absolute measurements of a given element, in atoms per volume, by linking peak counts with mass-thickness. Quantitative results depend on measuring this sample thickness t, usually by analysis of the low-loss EEL spectrum. However, many (S)TEMs (especially those dedicated for biological electron microscopy) are not equipped with an EEL spectrometer. Inability to measure sample thickness then limits acquisition of quantitative spectral data on these instruments. While some efforts have been made to parameterise t from EDX data (e.g. using the Hall continuum-normalisation method), in practice applying these methods is challenging. Low signal-to-noise ratios, the limited electron dose tolerance of the sample, and a lack of commercial or open-source data analysis routines mean such methods are largely unused.

Recently, another route to absolute quantification has been found through consideration of partial scattering cross-sections. This approach has been demonstrated experimentally for EELS by Craven et al. [363], who showed that EELS partial cross-sections for element x may be calculated by

$$\sigma_x^{\mathrm{EELS}} = \frac{I_x}{I_0 n_x t}, \tag{6.1}$$

where I_x is the background-subtracted spectrum counts in a given integration window, I_0 is the intensity in the low-loss regimen, n_x is the number density of x, t is the sample thickness. MacArthur et al. have shown equivalently that the EDX partial cross-section σ_x^{EDX} is given by

$$\sigma_x^{\mathrm{EDX}} = \frac{I_x}{N_e n_x t} \equiv \frac{I_x}{D_e n_x t A_{px}}, \tag{6.2}$$

where I_x is the x-ray peak intensity, and N_e is the total number of electrons incident on the sample at a given probe position. Similarly to the calculations shown in Chapter 5, this

equation may also be recast in terms of electron dose D_e and pixel area A_{px} [364]. Both EDX and EELS cross-sections are "partial", as they are a function of numerous microscope-dependent parameters, including detector geometries and efficiencies.

MacArthur et al. measured EDX counts as a function of distance from the edge of Pt and Co wedges. By considering the wedge geometry, this distance could be converted into numbers of Pt and Co atoms, and subsequently used to calculate $\sigma_{\mathrm{Pt}}^{\mathrm{EDX}}$ and $\sigma_{\mathrm{Co}}^{\mathrm{EDX}}$ respectively. While some modulations in x-ray intensity were observed due to electron channelling effects, these were sufficiently small that the general trend could still be observed. Measured partial cross-sections were then applied to determine the number of Pt and Co atoms in a bimetallic nanoparticle, and were shown to give comparable results with HAADF image quantification. One significant source of error in this approach was in measurement of wedge thickness. The nominal wedge thickness calculated from the focused-ion beam (FIB) milling procedure, and those measured using different parameterisations of the low-loss EEL spectra, varied significantly. Varambhia et al. showed that single-element nanoparticles and needle-shaped samples are both also suitable geometries to determine EDX partial cross-sections, but afford some advantages for thickness determination [365]. For nanoparticles, thickness may be determined by measuring diameter directly from the HAADF image (or using high-tilt tomography, as shown by Zanaga et al. in their application of the ζ-method [90]). Alternatively, needle-shaped samples may be placed in high-tilt sample holders and their thickness measured directly from a 90° image.

Thus far, partial EDX cross-sections have only been measured from single-element standards. However, while materials such as platinum and cobalt readily form nanoparticles, or may otherwise be thinned from bulk samples using FIB, not all elements are suitable for this approach. Many elements which are abundant in biological samples, such as calcium and sodium, are air-sensitive in their pure form. Examination of single-element samples for these materials would necessitate the whole sample preparation process and transfer to the microscope occurring under vacuum. This is a significant barrier to implementing a cross-section based quantification approach in many life-science research facilities. While EDX cross-sections may be calculated from first principles [366], [367], in practice this approach encounters many of the same challenges faced by theoretical k- and ζ-factor calculations - namely that the physical properties of the EDX detector are highly influential on the cross-section, but are very difficult to measure accurately.

The work discussed in this Chapter demonstrates a new methodology for acquiring spec-

Material	APS (nm)	Grid Material	Dispersal Medium
$CaSO_4$	80-100	Cu	ethanol
BK_3O_3	80-100	Cu	chloroform
$NaCO_3$	80-100	Au	ethanol
NaCl	40-60	Au	chloroform

Table 6.1: Table of standards used for EDX quantification. Average particle size (APS) determined by Nanoshel LLS is indicated in the second column. Samples of each material were dispersed in ethanol or chloroform, and pipetted onto TEM grids. As the Na Kα line at 1.041 keV is at a similar energy to the 0.9295 keV Cu Kα peak, Au grids were used in place of Cu grids for sodium-containing samples.

troscopic cross-sections based on stochiometric mixed-element standards. By using HAADF STEM mass measurement and simulated scattering cross-sections, it is possible to estimate the number of atoms of each species present at a given site. These values are then correlated with simultaneously-acquired spectral data to measure EELS and EDX partial cross-sections on both the aberration-corrected JEOL ARM-200F in Oxford, and on the uncorrected JEOL F200 at the Centre for Ultrastructural Imaging (CUI) at King's College London.

6.3 Sample Preparation

Nanopowders of $CaSO_4$, BK_3O_3, NaCl and $NaCO_3$ were obtained from Nanoshel LLC *(Wilmington, DE, USA)*. A small quantity of each sample was ground by hand in an agate pestle and mortar, before being dispersed in approximately 3 ml of either ethanol or chloroform (see Table 6.1). 300 µl droplets of solution were then pipetted onto gold or copper lacey carbon grids (EM Resolutions *(Sheffield, UK)*), with the excess liquid wicked away using filter paper. The grids were then left to dry at room temperature.

Low-magnification images of $CaSO_4$, BK_3O_3, NaCl and $NaCO_3$ are shown in Figure 6.1. The samples are well-dispersed, albeit not necessarily in nanoparticulate form as expected. All samples were mounted on the JEOL Be double-tilt holder, and tilted by 15° in the +x direction on the ARM200F, and 20° on the F200, to reduce shadowing effects from the specimen grid.

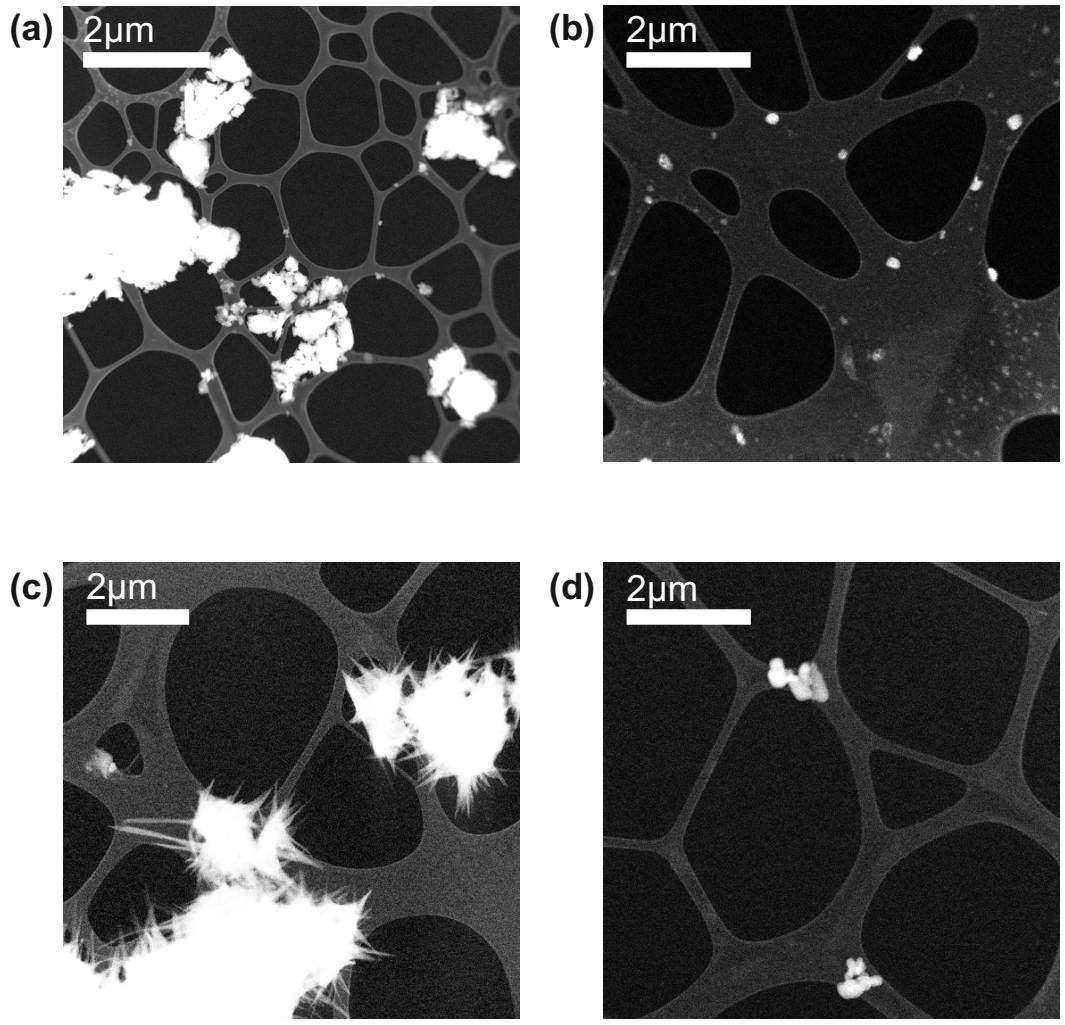


Figure 6.1: Low-magnification overviews of (a) $CaSO_4$, (b) BK_3O_3, (c) $NaCO_3$ and (d) NaCl.

6.4 Partial Cross-Sections Measured for the Oxford ARM

6.4.1 Calculation of $\sigma_{\mathbf{Ca}}^{\mathbf{EDX}}$ and $\sigma_{\mathbf{Ca}}^{\mathbf{EELS}}$

HAADF images of $CaSO_4$ nanoclusters were recorded immediately before acquiring simultaneous EDX and EELS data. EDX and EELS were recorded as 16×16 pixel spectrum images, with further sub-pixel scanning (64×64px) to ensure spectra were representative of the whole pixel area. A representative dataset, showing examples of EDX and low- and core-loss EELS spectra, is shown in Figure 6.2.

A summary of experimental conditions is presented in Table 6.2. The indicated probe current corresponds to spot size 8C at a gun emission current of 14 µA; however, as emission current from a cold-FEG reduces with time, this value was monitored throughout the data acquisition. As not all images and spectrum images were recorded at the same magnification, the electron dose was variable. Imaging doses were between 0.5–3 $\times 10^3$ electrons/Å^2, and for spectral data between 3–20 $\times 10^3$ electrons/Å^2. Thicker particles were excluded from the analysis, as the effects of multiple scattering and/or x-ray absorption complicate image simulation and interpretation of spectroscopic data.

Image Processing

HAADF images of $CaSO_4$ nanoclusters were converted to units of fractional beam current using the procedure described in Section 5.6.2. Total particle cross-sections $\sigma_{\text{cluster}}^{\text{HAADF}}$ were then calculated by integrating all pixels in the nanocluster, and estimating the background contribution from a 20-pixel edge region surrounding the cluster.

In order to estimate the number of calcium atoms in each cluster, further single-atom multislice simulations (as per Chapter 5) were performed using the modified HAADF experimental conditions given in Table 6.2. These cross-sections are approximately 50% of the value calculated for the experimental conditions of Chapter 5, due to the increased detector collection semi-angle used in these experiments.

A combined HAADF cross-section for a stochiometric compound unit may be obtained by a simple linear sum of its constituent atoms, as unlike for metallic nanoparticles, needles or

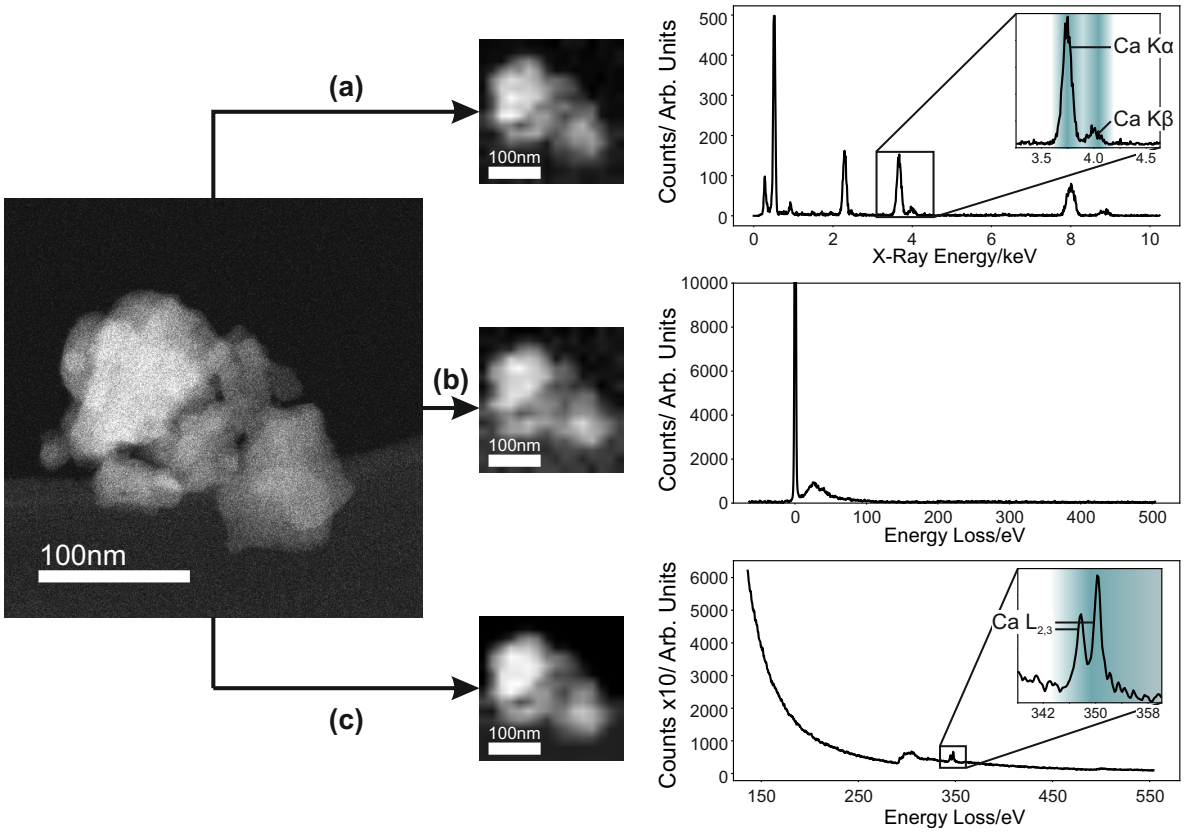


Figure 6.2: Schematic of data acquired for measuring $\sigma_{\mathrm{Ca}}^{\mathrm{EDX}}$ and $\sigma_{\mathrm{Ca}}^{\mathrm{EELS}}$ on ARM200F. A HAADF image of a nanocluster may be simultaneously acquired with (a) EDX, (b) low-loss EELS and (c) core-loss EELS spectral images. The insets of (a) and (c) show the Ca Kα and Kβ x-ray peaks and the $L_{2,3}$ EELS edge respectively.

Whole Experiment	Accelerating Voltage	200 kV
	Probe Current	∼25 pA
	Probe Convergence Semi-Angle	22.48 mrad [307]
	Camera Length	4 cm
HAADF	Detector	ADF2
	Pixel Dwell Time	12 µs
	Image Dimensions	512×512px
	Inner Collection Semi-Angle	77.4 mrad [307]
	Outer Collection Semi-Angle	∼271 mrad [307]
EDX	Tilt	+15°
	Pixel Dwell Time	1 s
	SI Dimensions	16×16px
EELS	Collection Angle	37.94 mrad [307]
	Dispersion	0.25 eV/channel
	Low-Loss Pixel Dwell Time	5×10^{-4} s
	Core-Loss Pixel Dwell Time	1 s
	SI Dimensions	16×16px

Table 6.2: Experimental parameters for measuring $\sigma_{\mathrm{Ca}}^{\mathrm{EDX}}$ and $\sigma_{\mathrm{Ca}}^{\mathrm{EELS}}$.

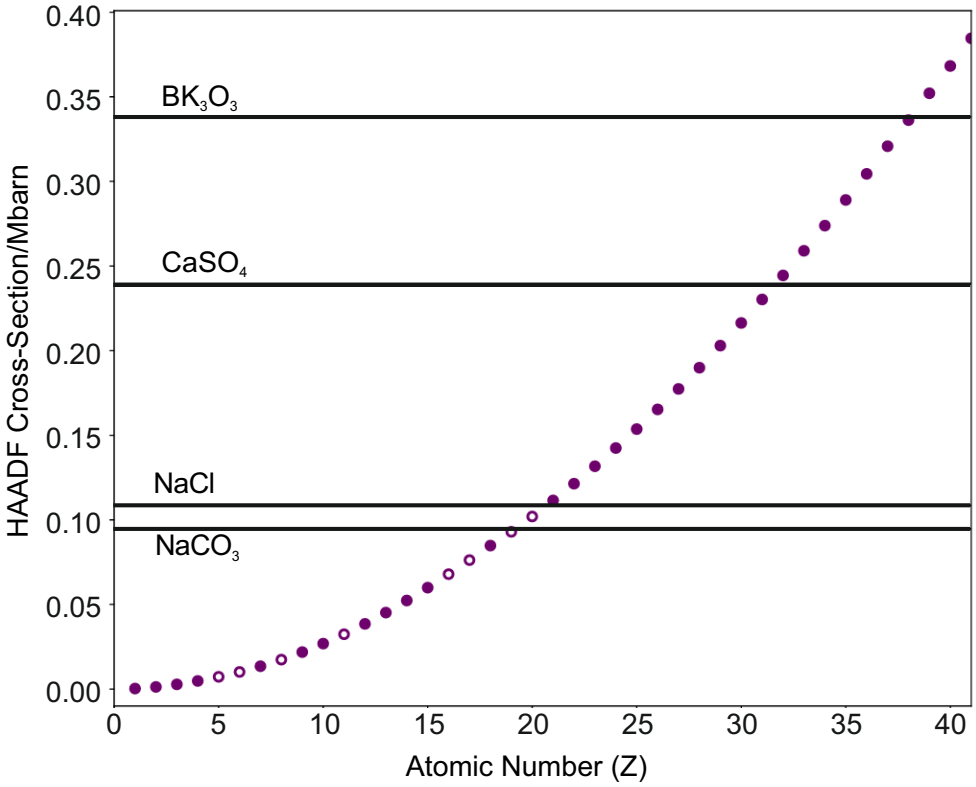


Figure 6.3: Simulated HAADF cross-sections for single atoms, with detector inner and outer semi-collection angles (β_1, β_2) of (77.4, 271)mrad. Cross-sections for stochiometric units of BK_3O_3 (0.34 Mbarn), $CaSO_4$ (0.24 Mbarn), $NaCO_3$ (0.10 Mbarn) and NaCl (0.11 Mbarn) are also indicated.

wedges, there is no need to consider the effects of electron channelling. The total cross-section of one $CaSO_4$ molecule $\sigma^{\mathrm{HAADF}}_{\mathrm{CaSO_4}}$ is estimated to be 0.24 Mbarn, as shown in Figure 6.3. Values of $\sigma^{\mathrm{HAADF}}_{\mathrm{cluster}}$ were then converted to equivalent numbers of Ca, S and O atoms (N_{Ca}, N_{S} and N_{O}) per Equations 6.3 and 6.4 by assuming the clusters were stochiometric mixtures of their constituent elements.

$$N_{\mathrm{Ca}} = N_{\mathrm{S}} = \frac{\sigma^{\mathrm{HAADF}}_{\mathrm{cluster}}}{\sigma^{\mathrm{HAADF}}_{\mathrm{CaSO_4}}}; \qquad (6.3) \qquad\qquad N_{\mathrm{O}} = 4\frac{\sigma^{\mathrm{HAADF}}_{\mathrm{cluster}}}{\sigma^{\mathrm{HAADF}}_{\mathrm{CaSO_4}}}. \qquad (6.4)$$

EDX Processing

EDX spectra were processed using Hyperspy, an open-source Python library for analysis of multi-dimensional data [116]. Spectral images were integrated across all pixels to produce a single EDX spectrum; this approach is valid as the background EDX contribution from the carbon film is negligible (<1%) compared with counts recorded from the $CaSO_4$ nanoclusters. In addition, the EDX detector read-out noise is very low; summing additional near-empty pixels therefore has little effect on the signal-to-noise ratio. Integrated EDX spectra were realigned using the Cu Kα or Au Lα system peaks, to correct for a slight energy offset introduced by Digital Micrograph.

The total number of counts in the Ca Kα, Ca Kβ, S Kα, S Kβ and O Kαpeaks were then calculated. The peak backgrounds were estimated using a two-window method; integrated counts were then calculated for energy windows centered on the peak maxima. These parameters are summarised in Appendix A (Table A.1).

Each intensity was then converted to an EDX partial cross-section using Equation 6.5,

$$\sigma^{\mathrm{EDX:\{line(s)\}}}_{i,\mathrm{cluster}} = \frac{I_T}{D_e}, \qquad (6.5)$$

where for $CaSO_4$ nanoclusters, element i is calcium or sulphur. The notation {line(s)} refers to quantification using the Kα, Kβ or both lines combined, and I_T is the total background-subtracted EDX counts in the respective peak(s). As before, D_e is given by $\frac{N_e}{A_{px}}$. This equation is analogous to Equation 5.2 for measuring the HAADF probe-integrated cross-section; here, the dose-normalised EDX counts is equivalent to the fractional HAADF intensity.

Element, i	$\sigma_i^{\text{EDX: K}\alpha}$ **(b)**	$\sigma_i^{\text{EDX: K}\beta}$ **(b)**	$\sigma_i^{\text{EDX: K}\alpha+\text{ K}\beta}$ **(b)**
Calcium	1.38±0.15	0.07±0.02	1.56±0.16
Sulphur	1.15±0.03	0.200±0.03	1.26±0.17

Table 6.3: Values of $\sigma_{\text{Ca}}^{\text{EDX}}$ and $\sigma_{\text{S}}^{\text{EDX}}$, calculated from the data shown in Figure 6.4 for the Kα, Kβ, and combined x-ray peaks. Partial cross-sections are stated in units of barns, where 1 barn $= 10^{-28}\text{m}^2$

Quantification using Equation 6.5 may be used to measure partial EDX cross-sections for individual peaks (such as the Kα or Kβ), or for the combination of multiple lines (e.g. Kα + Kβ). For the constituent elements of $CaSO_4$, it could reasonably be expected that it would be possible to discriminate between the Ca Kα at 3.691 keV and Ca Kβ (4.012 keV), and the S Kα (2.307 keV) and S Kβ (2.464 keV).

Figure 6.4 shows a plot of $\sigma_{\text{Ca, cluster}}^{\text{EDX}}$ and $\sigma_{\text{S, cluster}}^{\text{EDX}}$ against N_{Ca} and N_{S} respectively. As expected, by judicious choice of sufficiently thin sample areas, the effects of electron channelling and x-ray absorption are minimal even for large numbers of atoms. The total EDX partial cross-section grows linearly with number of atoms, and the gradient of this curve may be interpreted as an EDX cross-section per atom; values of $\sigma_{\text{Ca}}^{\text{EDX: K}\alpha}$, $\sigma_{\text{Ca}}^{\text{EDX: K}\beta}$, $\sigma_{\text{Ca}}^{\text{EDX: K}\alpha+\text{ K}\beta}$, $\sigma_{\text{S}}^{\text{EDX: K}\alpha}$, $\sigma_{\text{S}}^{\text{EDX: K}\beta}$ and $\sigma_{\text{S}}^{\text{EDX: K}\alpha+\text{ K}\beta}$ are given in Table 6.3. Propagation of errors in these calculations is discussed in Section 6.6.

Calculation of $\sigma_{\text{O}}^{\text{EDX}}$

The electronic configuration of oxygen means that the only possible x-ray is the O Kα (0.524 keV), and thus only one partial cross-section value may be calculated. In principle, it should be possible to measure this value of $\sigma_{\text{O}}^{\text{EDX}}$ using the same approach as taken for Ca and S. However, this poses a significant experimental challenge for several reasons. Firstly, oxygen Kα x-rays have relatively low energies, and are therefore more susceptible to absorption (either within the sample, or by the EDX detector). Secondly, x-rays generated by the residual dispersal medium and/or from contaminants on the TEM grid, cannot be uncoupled from those produced by the nanocluster.

In addition, it is likely that oxygen atoms are more vulnerable to redistribution by the

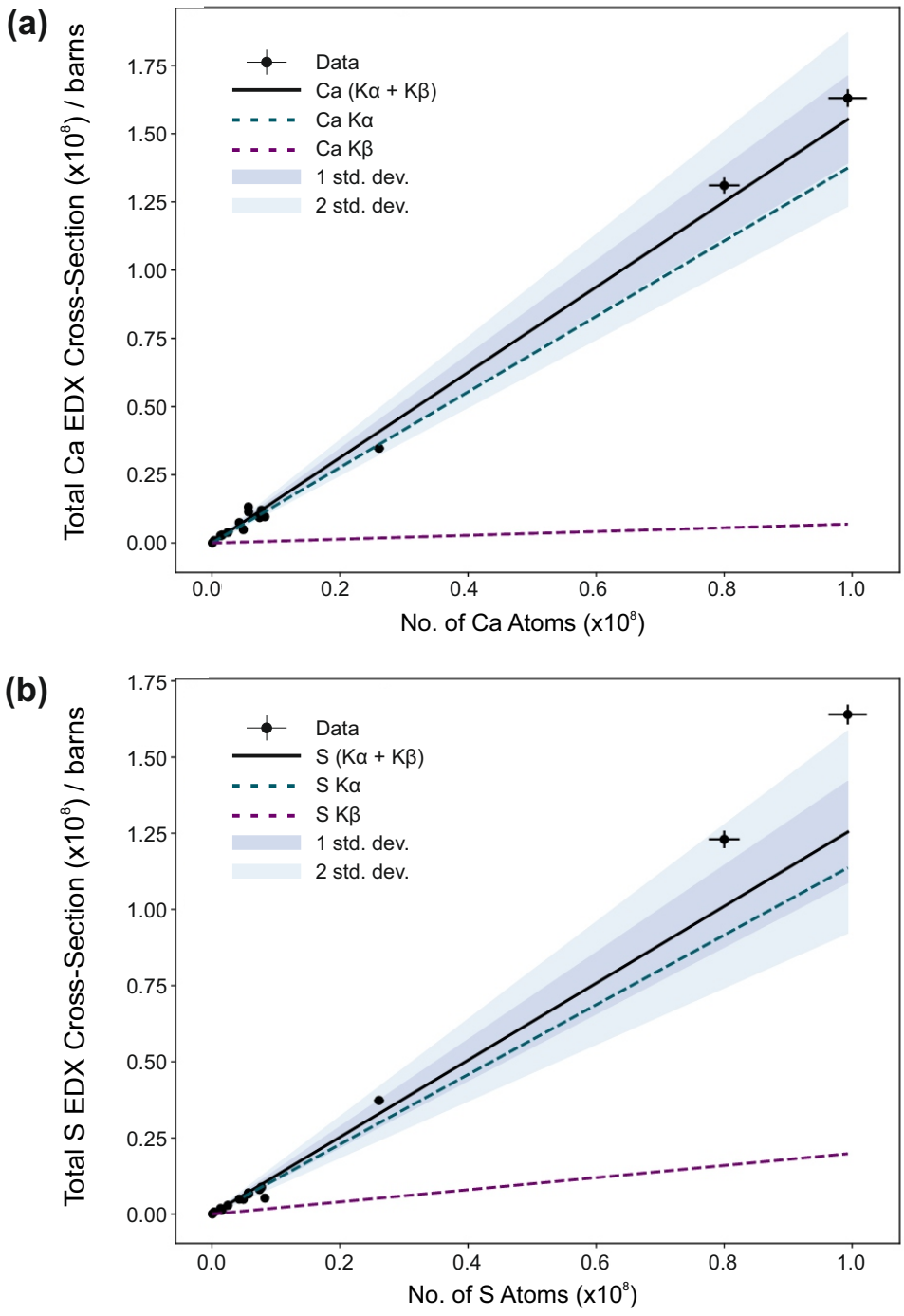


Figure 6.4: Graphs of $\sigma_{\mathrm{Ca}}^{\mathrm{EDX}}$ and $\sigma_{\mathrm{S}}^{\mathrm{EDX}}$. Part (a) shows experimental $\sigma_{\mathrm{Ca,\ cluster}}^{\mathrm{EDX:\ K\alpha+\ K\beta}}$ datapoints plotted against N_{Ca}. The solid black line is the result of linear fitting; dashed lines correspond to measurement of $\sigma_{\mathrm{Ca,\ cluster}}^{\mathrm{EDX:\ K\alpha}}$ and $\sigma_{\mathrm{Ca,\ cluster}}^{\mathrm{EDX:\ K\beta}}$. Part (b) shows the same procedure applied to the measurement of $\sigma_{\mathrm{S,\ cluster}}^{\mathrm{EDX:\ K\alpha}}$.

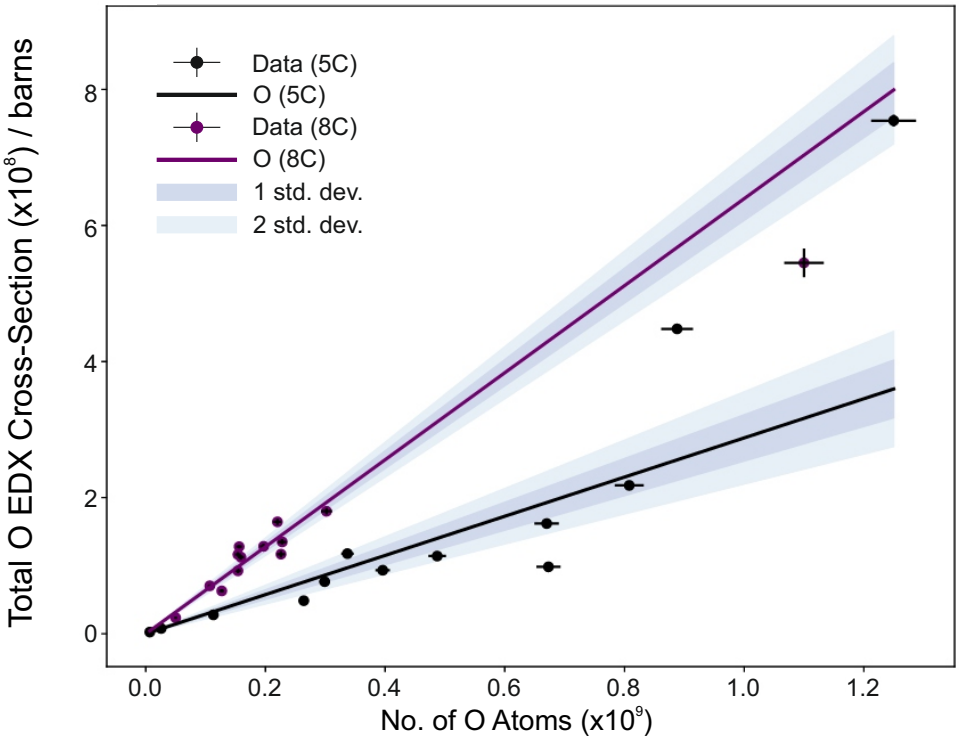


Figure 6.5: Graph of $\sigma_{\mathrm{O}}^{\mathrm{EDX}}$ against N_{O}. Probes 5C and 8C correspond to incident electron currents of approximately ∼150 pA and ∼25 pA respectively. At higher probe current the gradient is significantly reduced; $\sigma_{\mathrm{O}}^{\mathrm{EDX}}$= 0.64±0.06 barns at 8C, but only 0.29±0.03 barns at 5C.

electron beam relative to heavier species. This vulnerability has been reported in the literature; for example, Aranova et al. found that oxygen mass-loss occurred in plastic embedded tissue sections at doses as low as 10^4 electrons/nm^2, while phosphorous (Z=15) remained stable at doses as high as 10^8 electrons/nm^2 [368]. A number of studies have also observed increased dose-rate dependent mass loss of oxygen relative to heavier species [164], [266].

Figure 6.5 shows $\sigma_{\mathrm{O,\,cluster}}^{\mathrm{EDX}}$ plotted against N_{O}, at two different probe currents. While the graphs are linear, the gradient (i.e., the value of $\sigma_{\mathrm{O}}^{\mathrm{EDX}}$ for a single atom) is significantly reduced at higher electron dose. This likely difference likely occurs due to preferential mass loss of oxygen from the $CaSO_4$ nanoclusters, which in turn impacts both HAADF image intensity and x-ray acquisition. Critically for measurements of other elements, this effect is *not* observed when measuring $\sigma_{\mathrm{Ca}}^{\mathrm{EDX}}$ and $\sigma_{\mathrm{S}}^{\mathrm{EDX}}$.

EELS Processing

EELS spectra were also processed using Hyperspy, to extract counts corresponding to the Ca $L_{2,3}$ edge at ~347 eV. The low-loss spectrum image was used to realign the zero-loss peak and plasmon, and the core-loss SI, on a pixel-by-pixel basis. The pre-edge background was modelled using an inverse power-law background and integrated in an 18 eV window between 347–365 eV (Appendix A, Table A.2). As the nanoclusters selected for analysis were relatively thin, and no analysis of the edge fine structure was required, core-loss data were not deconvolved with the low-loss SIs.

Total number of Ca counts was then calculated by integrating pixels containing more than 10% of the maximum count value in the HAADF image for a given cluster. In practice, this means that pixels corresponding to the carbon background were excluded from the integration, unlike for the EDX data. Counts were then converted to Ca $L_{2,3}$ EELS cluster partial cross-sections, ($\sigma_{\mathrm{Ca}}^{\mathrm{EELS:\ L_{2,3}}}$), using Equation 6.6:

$$\sigma_{\mathrm{Ca,cluster}}^{\mathrm{EELS:L_{2,3}}} = \sum_{pixels} \frac{I_T}{I_0} \times A_{px}, \tag{6.6}$$

where I_T is now the total background subtracted counts in the 347–365 eV integration window (i.e. corresponding to the $L_{2,3}$ edge), and I_0 is the counts in the zero-loss and plasmon regions measured using the same sized energy window (i.e. effectively a dose-normalisation). A_{px} is the spectrum image pixel area, and cluster partial cross-sections $\sigma_{\mathrm{Ca}}^{\mathrm{EELS:\ L_{2,3}}}$ are produced by summing over the relevant SI pixels as described above.

The gradient of the graph shown in Figure 6.6 may be interpreted as a Ca $L_{2,3}$ cross-section per atom, $\sigma_{\mathrm{Ca}}^{\mathrm{EELS}}$, and is measured at 5.58±0.66 kbarns. This value may be compared with EELS partial cross-sections calculated using Egerton's SIGMAL3 and SIGPAR2 codes, based upon hydrogenic and Hartree-Slater atomic models respectively [112]. As shown in Table 6.4, there is relatively good agreement with both theoretical values.

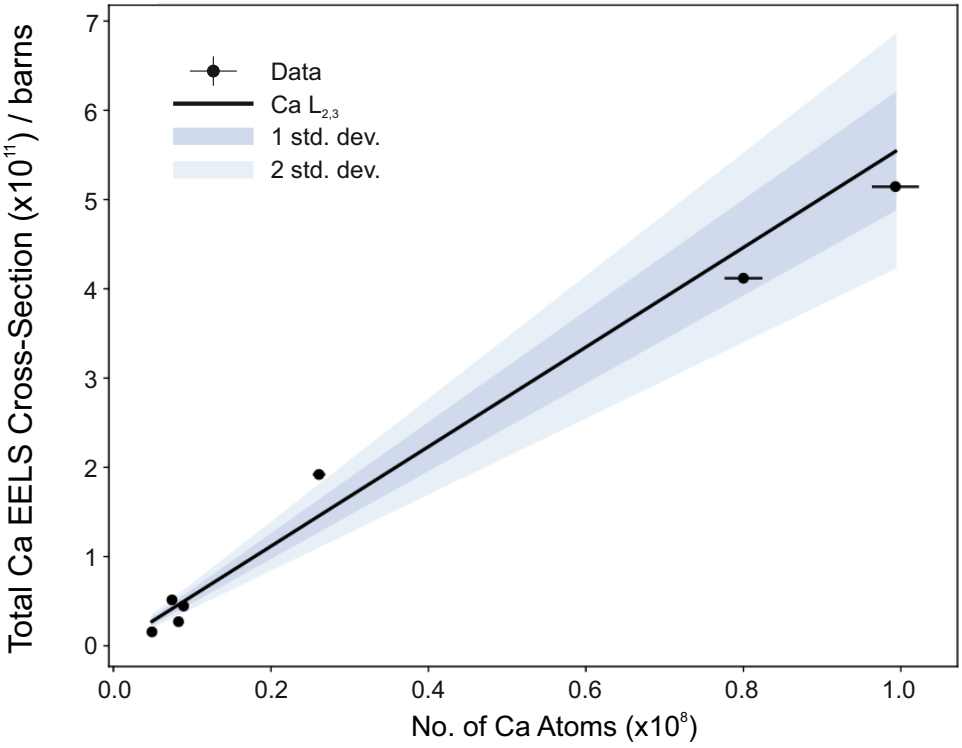


Figure 6.6: Graph of $\sigma_{\mathrm{Ca}}^{\mathrm{EELS}}$ measured using the Ca $L_{2,3}$ edge.

Method	$\sigma_{\mathbf{Ca}}^{\mathbf{EELS}}$ **(kbarns)**
Experiment	5.58±0.66
SIGMAL3	5.22
SIGPAR2	5.44

Table 6.4: Experimental and theoretical values of $\sigma_{\mathrm{Ca}}^{\mathrm{EELS}}$ using hydrogenic and Hartree-Slater atomic models implemented in SIGMAL3 and SIGPAR2 [112].

Element, i	$\sigma_i^{\text{EDX: K}\alpha}$ **(b)**	$\sigma_i^{\text{EDX: K}\beta}$ **(b)**	$\sigma_i^{\text{EDX: K}\alpha+\text{ K}\beta}$ **(b)**
Chlorine	1.36± 0.09	0.13±0.03	1.48±0.10
Potassium	0.95±0.11	0.09±0.01	1.07±0.12

Table 6.5: Values of $\sigma_{\text{Cl}}^{\text{EDX}}$ and $\sigma_{\text{K}}^{\text{EDX}}$, calculated from the data shown in Figure 6.7 for the Kα, Kβ, and combined x-ray peaks.

6.4.2 Calculation of $\sigma_{\text{Na}}^{\text{EDX}}$, $\sigma_{\text{Cl}}^{\text{EDX}}$ and $\sigma_{\text{K}}^{\text{EDX}}$.

HAADF images and EDX spectra were acquired under identical experimental conditions for samples of BK_3O_3, NaCl and $NaCO_3$. EDX SIs were processed as in Section 6.4.1, using the processing parameters in Appendix A (Table A.3). The number of atoms of each species within a cluster was calculated using Equations 6.7 and 6.8 to measure the number of potassium and chlorine atoms (N_{K} and N_{Cl}) from BK_3O_3 and NaCl, and Equations 6.9 and 6.10 to estimate the number of sodium atoms present (N_{Na}) in nanoclusters of $NaCO_3$ and NaCl respectively.

$$N_{\text{K}} = 3\frac{\sigma_{\text{cluster}}^{\text{HAADF}}}{\sigma_{\text{BK}_3\text{O}_3}^{\text{HAADF}}}; \qquad (6.7) \qquad\qquad N_{\text{Cl}} = \frac{\sigma_{\text{cluster}}^{\text{HAADF}}}{\sigma_{\text{NaCl}}^{\text{HAADF}}}; \qquad (6.8)$$

$$N_{\text{Na}} = \frac{\sigma_{\text{cluster}}^{\text{HAADF}}}{\sigma_{\text{NaCO}_3}^{\text{HAADF}}}; \qquad (6.9) \qquad\qquad N_{\text{Na}} = \frac{\sigma_{\text{cluster}}^{\text{HAADF}}}{\sigma_{\text{NaCl}}^{\text{HAADF}}}; \qquad (6.10)$$

Figure 6.7 shows whole-cluster partial cross-sections measured for potassium and chlorine from samples of BK_3O_3 and NaCl respectively. As for calcium and sulphur, K and Cl have both Kα and Kβ peaks which are sufficiently separated to resolve independently. Values of $\sigma_{\text{K}}^{\text{EDX: K}\alpha}$, $\sigma_{\text{K}}^{\text{EDX: K}\beta}$, $\sigma_{\text{K}}^{\text{EDX: K}\alpha+\text{ K}\beta}$, $\sigma_{\text{Cl}}^{\text{EDX: K}\alpha}$, $\sigma_{\text{Cl}}^{\text{EDX: K}\beta}$ and $\sigma_{\text{Cl}}^{\text{EDX: K}\alpha+\text{ K}\beta}$ were therefore calculated, as shown in Table 6.5.

As with oxygen, sodium has only a single Kα line available for quantification. Figure 6.8 shows measurements of $\sigma_{\text{Na, cluster}}^{\text{EDX: K}\alpha}$ recorded from samples of NaCl and $NaCO_3$. As shown in Table 6.6, $\sigma_{\text{Na}}^{\text{EDX}}$ values from both samples are not consistent within the bounds of their errors; this may be due to differing degrees of beam damage between the two samples, and also due to the limited number of datapoints acquired.

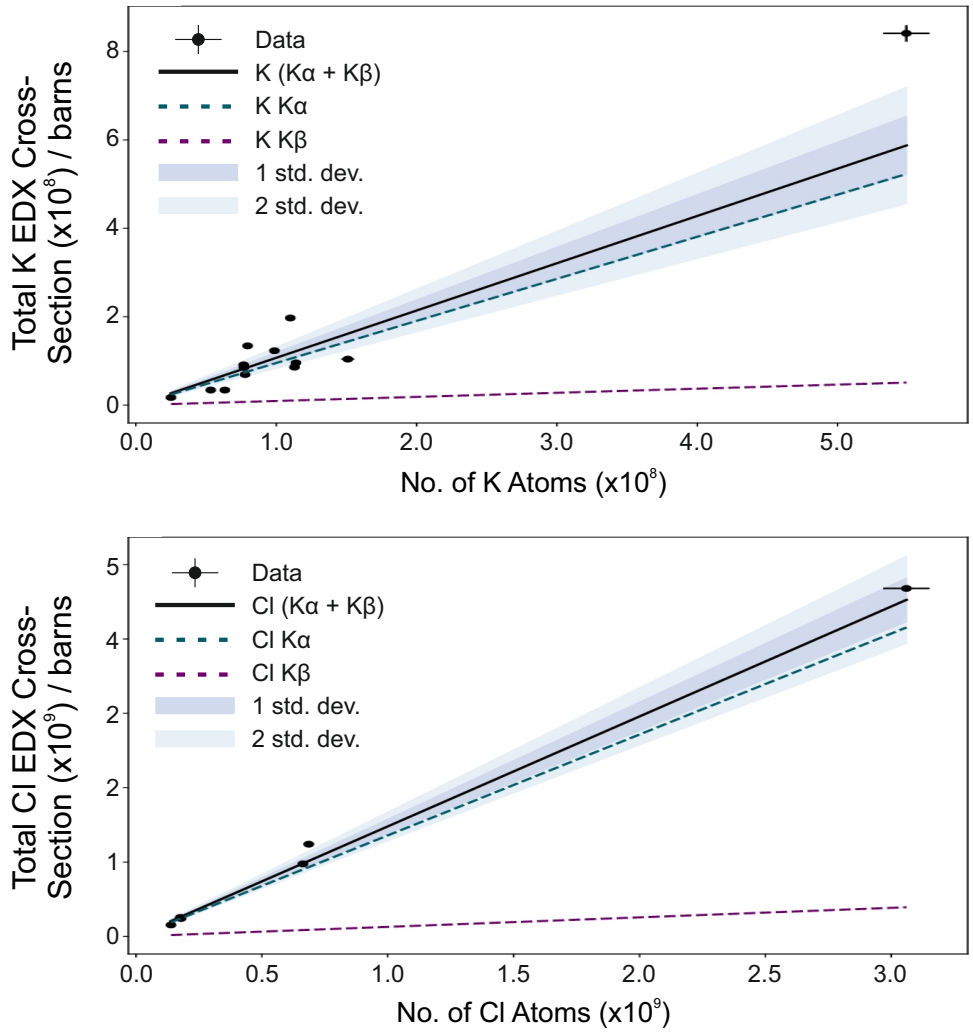


Figure 6.7: Measurement of $\sigma_{\mathrm{K}}^{\mathrm{EDX}}$ and $\sigma_{\mathrm{Cl}}^{\mathrm{EDX}}$. Part (a) shows experimental $\sigma_{\mathrm{K,\ cluster}}^{\mathrm{EDX:\ K\alpha+\ K\beta}}$ data-points plotted against N_{K} measured from nanoclusters of BK_3O_3. The solid black line is the result of linear fitting; dashed lines correspond to measurement of $\sigma_{\mathrm{K,\ cluster}}^{\mathrm{EDX:\ K\alpha}}$ and $\sigma_{\mathrm{K,\ cluster}}^{\mathrm{EDX:\ K\beta}}$. Part (b) shows the same procedure applied to the measurement of $\sigma_{\mathrm{Cl,\ cluster}}^{\mathrm{EDX:\ K\alpha}}$ in NaCl.

Sample	**NaCl:** $\sigma_{\mathbf{Na}}^{\mathbf{EDX:\ K\alpha}}$ **(b)**	**$NaCO_3$:** $\sigma_{\mathbf{Na}}^{\mathbf{EDX:\ K\alpha}}$ **(b)**	**Averaged:** $\sigma_{\mathbf{Na}}^{\mathbf{EDX:\ K\alpha}}$ **(b)**
Sodium	1.01±0.06	0.85±0.09	0.93±0.06

Table 6.6: Values of $\sigma_{\mathrm{Na}}^{\mathrm{EDX}}$, calculated from samples of $NaCO_3$ and NaCl as shown Figure 6.8 using the Kα x-ray peak.

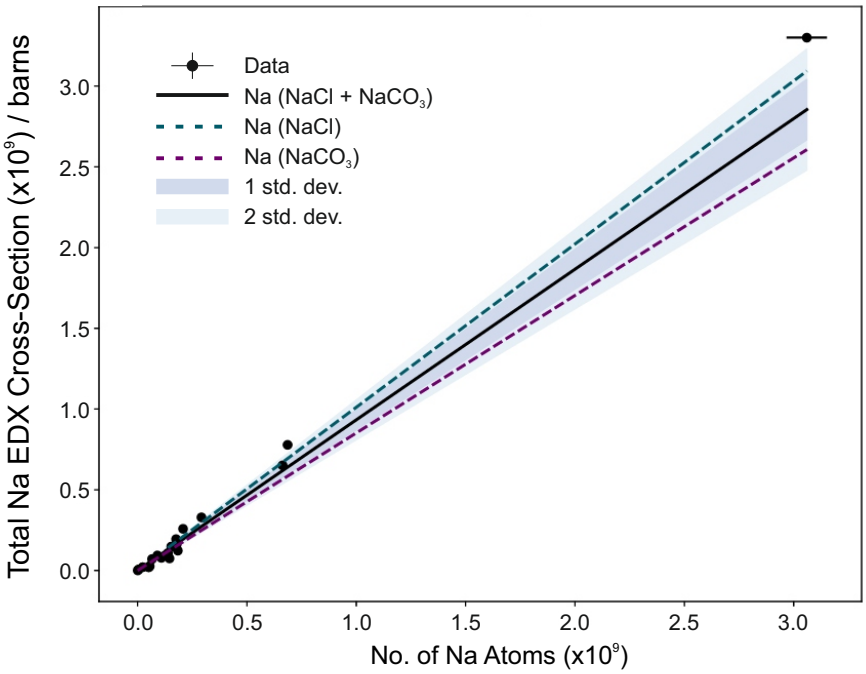


Figure 6.8: Graph of $\sigma_{\mathrm{Na}}^{\mathrm{EDX}}$. The purple dashed line is the result of measurement from samples of $NaCO_3$, and the blue dashed line from NaCl. The solid black line is the result of fitting Na data from both samples.

6.5 Partial Cross-Sections Measured for the CUI F200

As discussed at the beginning of this chapter, hybrid (S)TEMs found in life-science facilities are typically equipped for EDX but not EELS. One example of such an instrument is the JEOL JEM-F200 "F2" located in the Centre for Ultrastructural Imaging (CUI) at King's College London. The CUI's F200 is a non-aberration corrected Schottky FEG (S)TEM, and is used for both research and diagnostic purposes. While the microscope does not have a post-column spectrometer, it is equipped with an Oxford Instruments Ultim Max TLE for acquiring EDX data. The solid angle of this detector is nominally 1-3 times that of the Oxford ARM200F, and thus partial scattering cross-sections would likely also be increased relative to those reported in Section 6.4.

6.5.1 Calculation of $\sigma^{\mathbf{EDX}}_{\mathbf{Na}}$, $\sigma^{\mathbf{EDX}}_{\mathbf{Cl}}$ and $\sigma^{\mathbf{EDX}}_{\mathbf{K}}$.

Firstly, the F200 condenser aperture and ADF detector angles were calibrated, using a modification of the procedure implemented by Jones et al. for the Oxford ARM200F [307] and described in Appendix B. Samples of BK_3O_3 and NaCl were mounted in a JEOL Be double-tilt holder, and tilted by 20° in the +x direction. HAADF images were recorded using the JEOL scan system, and EDX spectra directly afterwards using AZtec (Oxford Instruments). Full experimental details are shown in Table 6.7. Data were processed as per Section 6.4.1, with additional compound cross-sections generated using the appropriate semi-convergence and ADF detector collection angles. EDX spectra were analysed as per Section 6.4.1. Similar plots to those shown for the Oxford ARM200F are presented in Figure 6.9, for data recorded on the CUI JEOL F200. EDX partial cross-sections for Na, Cl and K are shown in Table 6.8

All	Accelerating Voltage	200 kV
	Probe Current	∼17 pA
	Probe Convergence Semi-Angle	13.2 mrad
	Camera Length	200 mm
HAADF	Detector	ADF
	Pixel Dwell Time	6 µs
	Image Dimensions	512×512px
	Inner Collection Semi-Angle	46.99 mrad
	Outer Collection Semi-Angle	∼172 mrad†
EDX	Tilt	+15°
	Pixel Dwell Time	6 µs
	SI Dimensions	variable

Table 6.7: Experimental parameters for measuring $\sigma_{\mathrm{Na}}^{\mathrm{EDX}}$, $\sigma_{\mathrm{Cl}}^{\mathrm{EDX}}$ and $\sigma_{\mathrm{K}}^{\mathrm{EDX}}$ on the CUI F200.
† Extrapolated from nominal values in Operational Manual.

Element, i	$\sigma_i^{\mathbf{EDX:\ K\alpha}}$ **(b)**	$\sigma_i^{\mathbf{EDX:\ K\beta}}$ **(b)**	$\sigma_i^{\mathbf{EDX:\ K\alpha+K\beta}}$ **(b)**
Sodium	-	-	0.66±0.08
Chlorine	3.98±0.47	0.32±0.03	4.32±0.51
Potassium	5.16±0.64	0.05±0.01	5.32±0.65

Table 6.8: Values of $\sigma_{\mathrm{Na}}^{\mathrm{EDX}}$, $\sigma_{\mathrm{Cl}}^{\mathrm{EDX}}$ and $\sigma_{\mathrm{K}}^{\mathrm{EDX}}$ measured for the CUI F200.

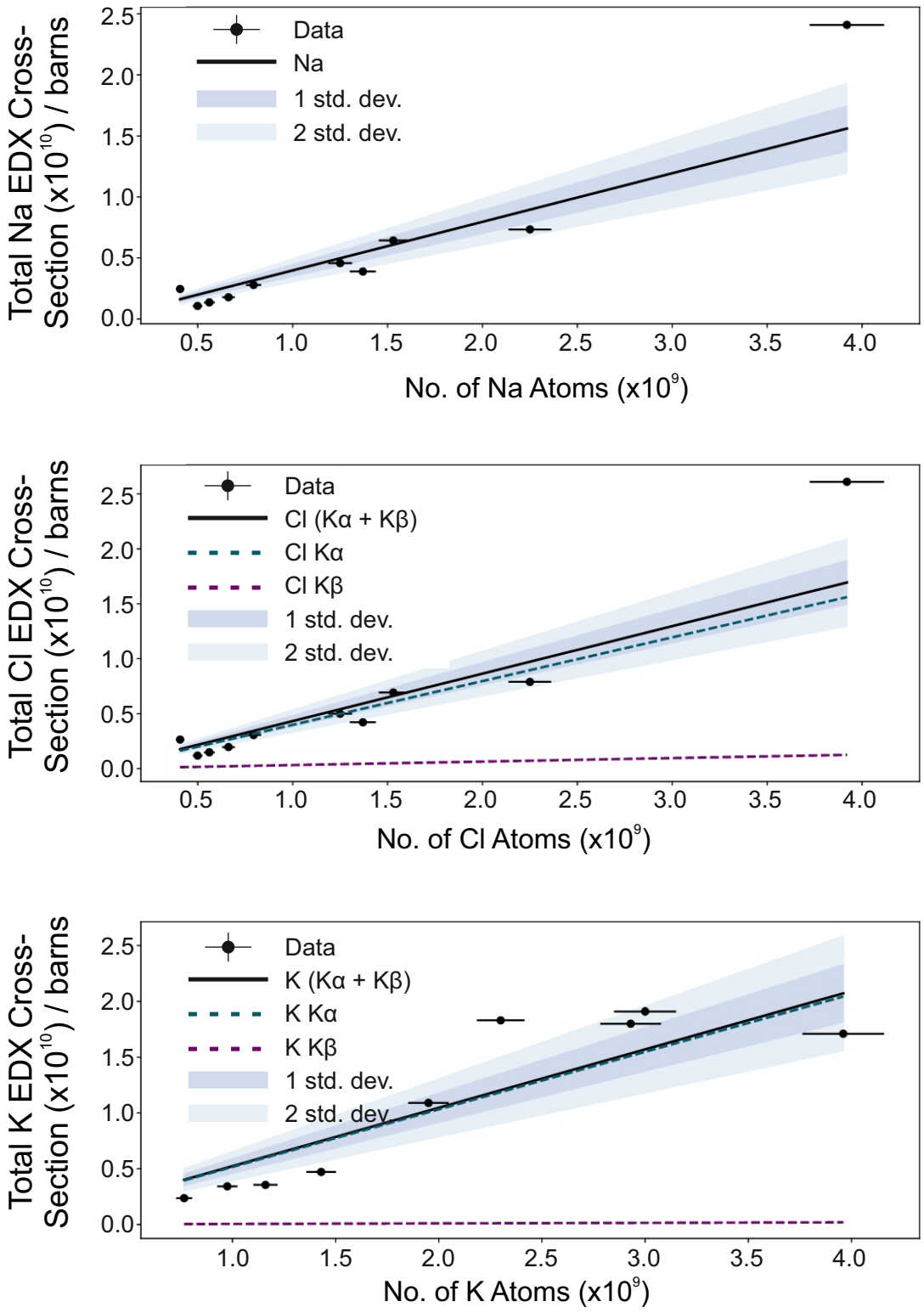


Figure 6.9: Plot of $\sigma^{\mathrm{EDX}}_{\mathrm{Na,\ cluster}}$, $\sigma^{\mathrm{EDX}}_{\mathrm{Cl,\ cluster}}$ and $\sigma^{\mathrm{EDX}}_{\mathrm{K,\ cluster}}$ against N_{Na}, N_{Cl} and N_{K} respectively, recorded on the CUI F200.

6.6 Error Propagation

6.6.1 EDX Error

The error on the measurement of a cluster EDX partial cross-section is given by

$$\Delta\sigma^{\mathrm{EDX}}_{\mathrm{cluster}} = \sigma^{\mathrm{EDX}}_{i,\mathrm{cluster}}\sqrt{\sum^{n}\left(\frac{\Delta i}{i}\right)^{2}}, \tag{6.11}$$

for n independent parameters i each with error Δi [365]. The parameters in this calculation of Equation 6.5 are: probe current (i.e. electron dose), SI pixel area, and error on the integrated peak counts. The first two are small, and on the order of a few percent in a well-calibrated instrument. The most significant error on $\sigma^{\mathrm{EDX}}_{i,\ \mathrm{cluster}}$ arises due to the limited x-ray counts recorded during the spectrum acquisition. As EDX spectra obey Poissonian statistics [88], Equation 6.11 may, to a first approximation, be reduced to

$$\Delta\sigma^{\mathrm{EDX}}_{\mathrm{cluster}} = \sigma^{\mathrm{EDX}}_{i,\mathrm{cluster}}\frac{1}{\sqrt{\mathrm{I_T}}}, \tag{6.12}$$

where $\mathrm{I_T}$ is the total integrated counts for a given x-ray peak or peaks.

However, to calculate $\sigma^{\mathrm{EDX}}_{i}$ for a single atoms, it is also necessary to consider the error on N_{atoms}. Again, this value may acquire error from a number of sources. However, if those arising from inaccuracies in the electron dose and pixel size are neglected, along with those from error on ADF detector collection angles in the simulation, the largest contributing factor is error on the HAADF image thresholding. This is on the order of 3-5%, depending on the particular nanocluster.

In order to calculate the error on $\sigma^{\mathrm{EDX}}_{i}$, graphs of cluster partial cross-section against N_{atoms} were fitted using the orthogonal distance regression (ODR) function in SciPy [369], [370]. Unlike ordinary least-squares fitting, ODR also accounts for possible error in the "independent" variable N_{atoms}. Errors in the gradient of fitted data therefore encapsulate errors arising from HAADF image quantification and EDX counting statistics.

6.6.2 EELS Error

Error propagation for EELS partial cross-sections is considerably more challenging than for EDX data. In addition to errors on probe current, pixel area, and Poissonian noise from the data itself, there is additional error (in the form of read-out noise, and from the effects of a poor factory gain and dark reference correction) introduced at the point spectra are read out from the GIF. The acquisition software applies an internal correction to attempt to minimise this contribution; however, this correction is unlikely to be valid for all GIF operating conditions. Attempts were made to minimise this error by acquiring EEL spectra at the same energy dispersion.

Another considerable source of error arises due to challenges of fitting and subtracting the inverse power-law background. As discussed in Section 2.4.3, the background fit is increasingly inaccurate with distance from the background window. Depending on a given spectrum's signal-to-noise ratio, this error may be well in excess of 10% [115] and highly variable even within a single SI. For the calculation performed in Section 6.4.1, only error on N_{Ca} from the HAADF quantification was considered; further work is required to parameterise the error on the EELS data itself.

6.7 Discussion

6.7.1 EDX

EDX partial cross-sections measured from experiments on the Oxford ARM200F are summarised in Table 6.9. The combined-line partial cross-sections are around $6{\times}10^4$ times smaller than the corresponding single-atom HAADF cross-sections. This is primarily due to the low fluorescent yield and low detection efficiency of EDX relative to ADF. These measurements also reflect the lower probability of electronic transition from M-shells relative to L- when a K-shell electron is displaced; partial cross-sections arising from Kβ x-rays are between 5-15% of the corresponding Kα partial cross-section.

Figure 6.10 shows combined-line EDX partial cross-sections plotted against x-ray energy. This primarily reflects the rise in detection probability with increasing energy; higher energy x-rays are less easily absorbed (either within the sample itself, or by the EDX detector). Varambhia et

Element, i	$\sigma_i^{\text{EDX: K}\alpha}$ **(b)**	$\sigma_i^{\text{EDX: K}\beta}$ **(b)**	$\sigma_i^{\text{EDX: K}\alpha+\text{ K}\beta}$ **(b)**
Oxygen*	-	-	0.64±0.06
Sodium†	-	-	0.93±0.06
Sulphur	1.15±0.03	0.20±0.03	1.26±0.17
Chlorine	1.36± 0.09	0.13±0.03	1.48±0.10
Potassium	0.95±0.11	0.09±0.01	1.07±0.12
Calcium	1.38±0.15	0.07±0.02	1.56±0.16

Table 6.9: All partial EDX cross-sections measured on the Oxford ARM200F.

* From data recorded at spot size 8C. † Combined value from NaCl and $NaCO_3$ samples.

al. used the same microscope, and similar experimental conditions, to measure $\sigma_{\text{Co}}^{\text{EDX: K}\alpha+\text{ K}\beta}$ for cobalt [365]; while this value is not consistent with the results of the experiments described here for lower-Z elements, the error bar of the cobalt datapoint is very large due to the difficulties in measuring the Co wedge thickness. While the data shown in Figure 6.10 are not fitted with an energy-dependent function, it is clear that with further measurements of K-shell partial EDX cross-sections it would be feasible to produce a library of $\sigma_{\text{v}}^{\text{EDX}}$alues, analogous to those used in the Cliff-Lorimer quantification routine.

The sodium EDX partial cross-section measured on the CUI F200 instrument (Table 6.8) is smaller than that measured for the Oxford ARM200F. However, the values of $\sigma_{\text{Cl}}^{\text{EDX}}$ and $\sigma_{\text{K}}^{\text{EDX}}$ are between three and five times greater than for the Oxford instrument. This indicates the EDX detector installed on the CUI's F200 instrument has a reduced efficiency for detecting low-energy x-rays, but an increased solid angle such that higher energy x-rays are detected with greater probability.

It is notable that data used to obtain $\sigma_{\text{K}}^{\text{EDX}}$ has greater spread than for other elements; this may arise due to contaminants introduced in the manufacturing of the BK_3O3 nanopowder. Many spectra recorded from BK_3O_3 nanoclusters contained small additional x-ray peaks corresponding to other elements (primarily sodium and sulphur). This would mean that there is a significantly larger error bar on the value of N_{K} than measured from the HAADF uncertainty alone. The value of $\sigma_{\text{K}}^{\text{EDX}}$ measured using the ARM200F also appears reduced relative to what would be expected for neighbouring elements.

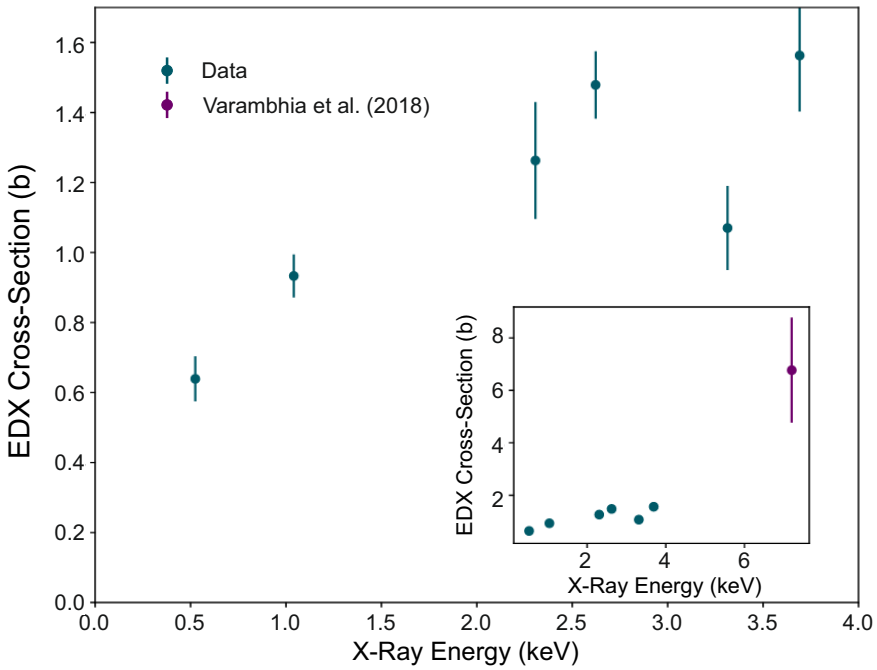


Figure 6.10: All σ^{EDX} measured on the ARM200F, plotted alongside the value of $\sigma_{\mathrm{Co}}^{\mathrm{EDX:\ K\alpha+\ K\beta}}$ obtained by Varambhia et al. [365]

.

This highlights a particular disadvantage of the approach to partial cross-sectional measurement described in this chapter. Previous measurements of partial EDX cross-sections have used single-element standards with well-defined geometry; the opportunity for contaminants to be introduced during the sample preparation process for these is very minimal, or physically impossible. Synthesis of mixed-element references is significantly more susceptible to generating non-stochiometric "standards". HAADF imaging alone is unable to identify nanoclusters with unexpected contents; only when the EDX spectra are analysed are impurities in the sample detected.

However, the approach discussed in the Chapter also offers some advantages over single-element measurements. The most obvious is in the experimental burden required to measure σ^{EDX}. The sample preparation procedure is more straightforward than that required to generate a needle or wedge sample. That the standards used are multi-element is in itself an advantage too; x-ray peaks are measured for all elements in a particular material simultaneously, and therefore mean measurements of σ_i^{EDX} can be obtained for as many elements i as are present in the compound. As these element-specific values should be consistent between different

materials, mixed-element standards allow us to verify the partial cross-section values from different, independent, measurements (as achieved in this Chapter for $\sigma_{\mathrm{Na}}^{\mathrm{EDX}}$).

While considerable efforts have been expended to calibrate the HAADF detector collection angles for both the Oxford and CUI instruments, it is likely this is not strictly necessary in most instruments. As discussed in Chapter 3, a number of laboratories have demonstrated quantitative mass measurements based on mass calibration from standards such as the tobacco mosaic virus. This would afford other laboratories the ability to quantify their EDX spectra in the manner described here. As shown from Figure 6.10, many elements may be measured using just three or four samples; in comparison, many $k_{A,B}$ for different element pairs must be measured to quantify spectra using the Cliff-Lorimer method, necessitating the use of many different standards. Furthermore, σ_i^{EDX} are related to Watanabe-Williams ζ-factors, ζ_i, by

$$\sigma_i^{EDX} = \frac{A_r}{N_A \zeta_i}, \tag{6.13}$$

where A_r is the relative atomic mass, and N_A is Avogadro's constant. It may therefore be possible to apply the absorption correction algorithms developed for ζ-factor quantification on instruments without a GIF.

6.7.2 EELS

The partial EELS cross-section calculated for the Ca $L_{2,3}$ edge may also be compared with the simulated single-atom HAADF cross-section; $\sigma_{\mathrm{Ca}}^{\mathrm{EELS}}$ is estimated to be approximately twenty times lower than $\sigma_{\mathrm{Ca}}^{\mathrm{HAADF}}$. Varambhia et al. measured the cobalt $L_{2,3}$ partial cross-section as 0.85 kbarns, a factor of 10^3 lower than their ADF value [365]; however, the detector collection inner semi-angle in this case was significantly smaller than used in this work.

While EEL spectra were not recorded for elements other than calcium, in principle a number of other element edges would be accessible experimentally. The boron, oxygen and sodium K edges are of favourable energies and shapes to permit quantification, while the sulphur K and chlorine K and $L_{2,3}$ edges would be more challenging. Measurement of the potassium $L_{2,3}$ would also be difficult in these samples, owing to its proximity to the carbon K edge.

Element, *i*	**Energy (eV)**	$\sigma_{\mathbf{i}}^{\mathbf{EELS:\ K}}$ **(kbarns)**
Boron	188	4.92
Oxygen	532	5.80
Sodium	1072	0.12
Sulphur	2472	-*
Chlorine	2822	-*
Potassium	3607	-*
Element, *i*	**Energy (eV)**	$\sigma_{\mathbf{i}}^{\mathbf{EELS:\ L_{2,3}}}$ **(kbarns)**
Sulphur	165	15.0
Chlorine	200	11.9
Potassium	294	8.0

Table 6.10: Theoretical values of $\sigma_{\mathrm{f}}^{\mathrm{EELS}}$or other elements, calculated using the SIGPAR3 code [112] using a 20 eV integration window.

* These lines are note deigned viable lines for measurement and therefore are not included in SIGPAR3.

6.8 Summary

The measurement of partial scattering cross-sections in EDX and EELS affords another route to quantification of spectral data acquired in the STEM. However, thus far these cross-sections have been measured only using single-element standards, and from sample geometries unattainable for many other species.

In this Chapter, it is shown that mixed-element standards are suitable choices for cross-section measurement. Provided standard samples are stochiometric mixes of their constituent elements, and sufficiently thin, quantitative HAADF imaging can be used to recover the number of atoms present for each species. This number may be correlated with the background-subtracted peak and/or edge counts in EDX and EELS respectively to generate element-specific partial scattering cross-sections. Measurements for a number of elements are made on the Oxford JEOL ARM-200F and CUI JEOL JEM-F200.

Chapter 7

Applications of EDX and EELS Partial Cross-Sections

7.1 Aims & Scope

As shown in Chapter 6, it was possible to measure EDX and EELS partial scattering cross-sections for a number of elements with biological significance. In this Chapter, these experimental values are applied to quantify intracellular elemental distributions at two sites within axons of the peripheral nerve. In the first example, $\sigma_{\mathrm{Ca}}^{\mathrm{EELS}}$ and $\sigma_{\mathrm{Ca}}^{\mathrm{EDX}}$ measured on the Oxford JEOL ARM-200F are used to atom-count calcium in suspected mitochondrial storage granules. Estimates of calcium number density made using both EDX and EELS are in agreement, validating the use of partial scattering cross-sections in this context. In a second case study, $\sigma_{\mathrm{Na}}^{\mathrm{EDX}}$ and $\sigma_{\mathrm{K}}^{\mathrm{EDX}}$ measured using the JEOL JEM-F200 at the Center for Ultrastructural Imaging at King's College London are applied to the measurement of intra-axonal levels of sodium and potassium. The results confirm previous observations that administration of the chemotherapeutic paclitaxel affects intracellular Na:K ratios, and that these changes are detectable both prior to and at the time-point associated with the peak of pain-like behaviour.

7.2 Intracellular Elemental Distributions and the Effects of Paclitaxel

Paclitaxel is a chemotherapeutic agent used to a number of cancers, including those of the ovaries, breast and lung [371]. As with the platinum-containing drugs discussed in Chapters 4 and 5, treatment with paclitaxel leads to the development of peripheral neuropathy in as many as 100% of patients [372]. There are currently no pharmaceutical methods for preventing or alleviating paclitaxel-induced peripheral neuropathy (PIPN) [373]. In addition, due to its poor solubility in water, paclitaxel is usually formulated in a vehicle solution of ethanol and Cremophore EL. Cremophore EL is a polyethoxylated castor oil which can itself induce a number of deleterious effects after administration, including peripheral neuropathy [374].

While the mechanisms by which PIPN arises are still poorly understood, links between PIPN and intracellular changes in levels of sodium and potassium are well-established [375], [376]. Concentration gradients of ions, particularly Na^+ and K^+, drive the generation of the action potentials which transmit information through the body [377]. Evidence suggests that disruption of these gradients in patients treated with paclitaxel is a key step in development of PIPN [378]–[380].

Unpublished data from Flatters et al. indicated that changes in intra-axonal Na and K were detectable in peripheral nerve sections using EDX (full details may be found in Appendix C). However, their work was considerably limited by the sample preparation methods used to prepare tissue sections, and the EDX detector itself. The work presented in this Chapter was performed following several years of improvements in sample preparation methods, and therefore aimed to examine whether EDX partial scattering cross-sections measured in Chapter 6 could substantiate these changes, and quantify other intracellular elemental distributions.

7.3 Sample Preparation

In this section the author wishes to acknowledge Dr Sarah Flatters and Dr Christina Ferguson, who carried out the experimental animal work and dissections. Dr Christina Ferguson also performed the cryosectioning and freeze-drying.

Adult Sprague-Dawley rats (Harlan UK Ltd. *(Blackthorne, UK)*) with starting weighs of >200 g were maintained as per the description in Chapter 5. Rats received intraperitoneal injections on days 0, 2, 4 and 6 with either 2 mg/kg paclitaxel solution (TEVA UK *(Castleford, UK)*) or 1:1 solution of ethanol (Sigma *(Gillingham, UK)*) and Cremophor EL (Sigma *(Gillingham, UK)*) diluted with 0.9% sterile saline. Saphenous nerves were harvested under terminal anaesthesia at two timepoints. The first group were collected on Day 7 (the "D7" timepoint), prior to the onset of pain-like behaviour. The second group were collected at the peak of pain-like behaviour (as assessed by mechanical hypersensitivity per Ref. [378]) at days 25-30 (the peak-pain or "PP" timepoint).

A ∼2 mm length of saphenous nerve was placed in a copper sample carrier (Leica Microsystems *(Wetzlar, Germany)*) and immersed in 20% dextran dissolved in phosphate-buffered saline (both Sigma *(Gillingham, UK)*). Carriers were transferred to the Leica EM ICE (Leica Microsystems *(Wetzlar, Germany)*) and high-pressure frozen before storing in liquid nitrogen. The time between cutting the nerve and the sample being fully frozen was on the order of one minute.

Ultrathin cryosections were cut using the Leica Ultracut 6 (Leica *(Wetzlar, Germany)*) and a 45° DiATOME Ultra Diamond Knife (DiATOME Ltd. *(Biel, Switzerland)*). The cryoultramicrotome was set to a cutting thicknesses of 70 nm and cutting speed of 50 mm/s. Care was taken to orientate the carrier to ensure sections were cut transverse to the axons. Sections were transferred to gold TEM grids in the chamber and transferred to the Leica EM CPD300 for overnight freeze drying. This sample preparation protocol was developed to minimise the diffusion and extraction of highly mobile elements such as calcium, sodium and potassium, while preserving good cell ultrastructure and producing a sample stable at room temperature.

In both the Oxford ARM200F and the CUI JEOL JEM-F200, samples were mounted in a JEOL Be double-tilt holder. Images and spectra were recorded with 15° (ARM200F) and 20° (F200) tilt in the +x direction to maximise x-ray counts. Figure 7.1 shows a typical nerve sample produced using this procedure. As for the DRG, one sample contains many distinct features, which are easily recognisable from a low-magnification HAADF STEM image.

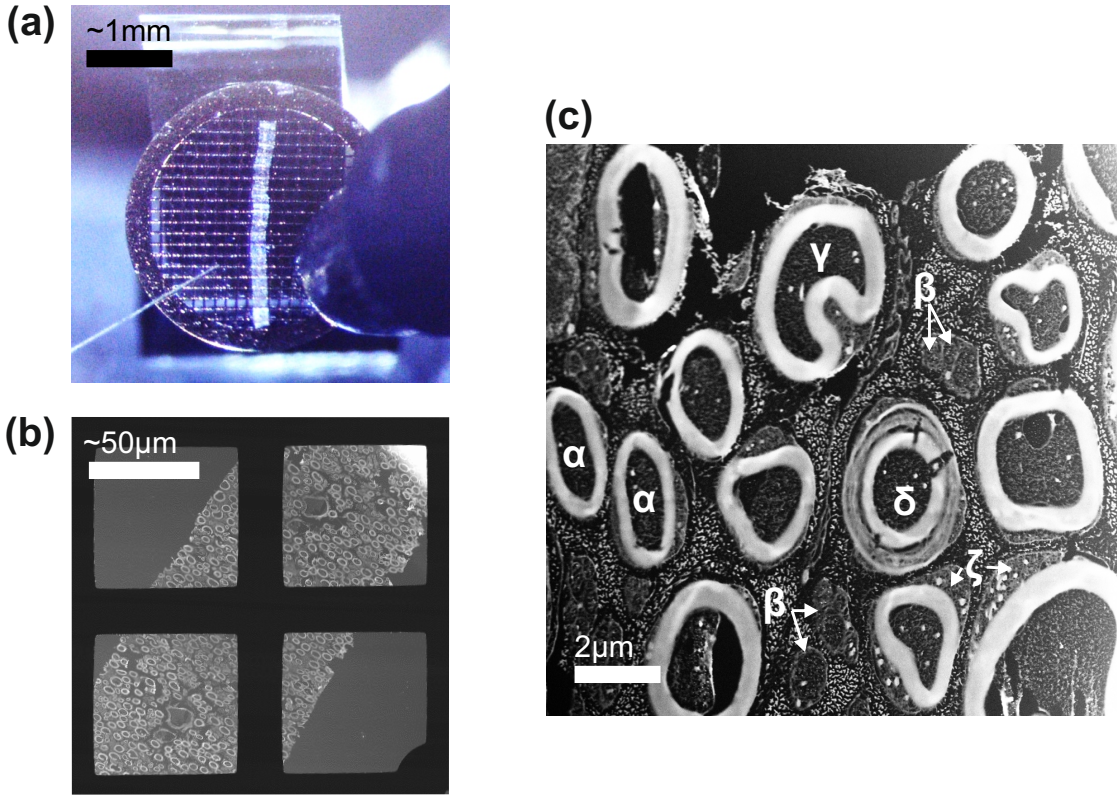


Figure 7.1: Low-magnification overview images of peripheral nerve samples. (a) shows the frozen cryosection being transferred to the TEM grid. (b) Ultra-low magnification images show the section has survived both the transfer and freeze-drying process. (c) Identifiable regions in this image are myelinated axons (α), bundles of unmyelinated axons (β), mylinated axons proximal to a node of Ranvier (γ), possible demyelination (δ) and Schwann cells (ζ).

7.3.1 Discussion

As discussed in Chapter 5, extensive sample preparation is required to produce suitable samples from bulk tissue. To preserve the native elemental distributions within the nerve, an approach was developed based on that used for cryo-electron microscopy of vitreous sections (CEMOVIS) [381]. Dextran:PBS solution was used as a cryoprotectant to support uniform freezing throughout the nerve. Freezing under high pressure minimises the formation of crystalline ice, and instead (provided the sample is sufficiently thin) results in a vitrified sample with minimal disruption to the sample ultrastructure and intracellular compartments.

Freeze drying removes water from the frozen sample without the use of fixatives and/or solvents (as used in freeze-substitution). By careful control of the temperature and pressure, water sublimates into the vacuum, rather than forming crystalline ice. Slow removal of the water in this way means that the shrinkage of biological specimens may be limited to around 10%, as opposed to more than 70% in conventional TEM preparation [354].

7.4 Application 1: Mitochondrial Calcium Stores

Prior to examination of intra-axonal sodium and potassium levels, peripheral nerve samples were examined under HAADF STEM conditions on the Oxford ARM200F. The aim of these experiments was to independently validate the partial scattering cross-sections measured in Cahpter 6 using a biological specimen.

7.4.1 Data Acquisition

As shown in Figure 7.2, a number of strongly scattering aggregates were observed inside both myelinated and unmyelinated axons recovered from vehicle-treated animals at Day 7. Figure 7.3 shows simultaneous spectral data recorded from one of these sites. The calcium $L_{2,3}$ edge and Ca K x-ray peaks are clearly observable in the EELS and EDX spectra respectively. Data were recorded using the parameters given in Table 7.1. The electron dose used to record spectral data varied between 3.4–7.1 $\times 10^5$ electrons/Å^2.

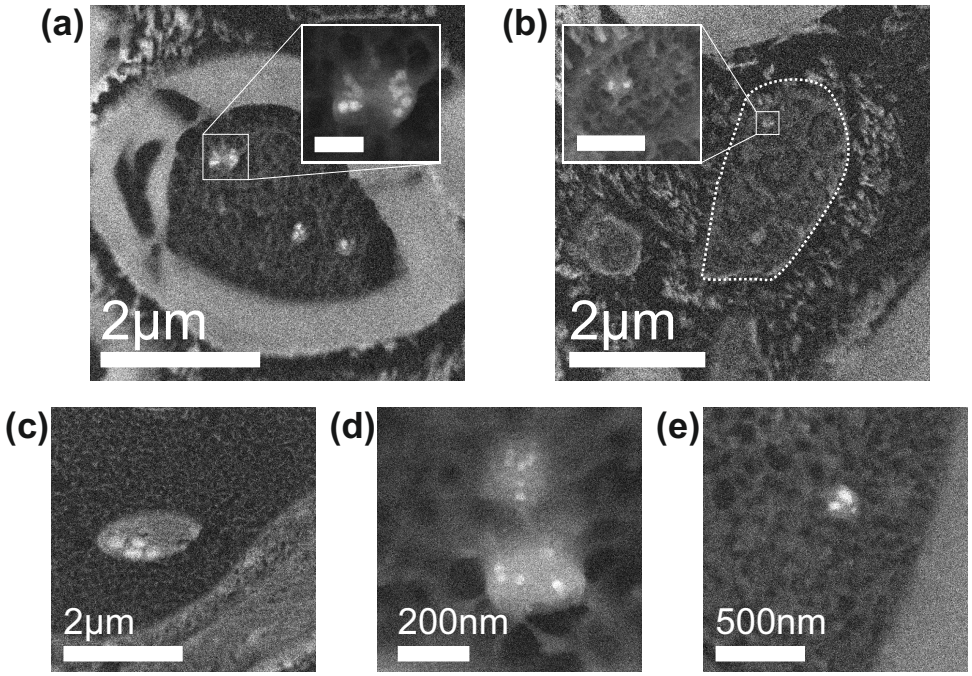


Figure 7.2: Strongly scattering granules were observed in (a) myelinated and (b) unmyelinated peripheral nerve axons. Inset scalebars are both 200 nm. (c)-(e) show other examples of dense clusters in the axon interior.

Whole Experiment	Accelerating Voltage	200 kV
	Probe Current	∼150 pA
	Probe Convergence Semi-Angle	22.48 mrad [307]
	Camera Length	4 cm
EDX	Tilt	+15°
	Pixel Dwell Time	0.05–1 s
	SI Dimensions	64×64px
EELS	Collection Angle	37.94 mrad [307]
	Dispersion	0.25 eV/channel
	Low-Loss Pixel Dwell Time	$1–5 \times 10^{-4}$ s
	Core-Loss Pixel Dwell Time	0.05–1 s
	SI Dimensions	64×64px

Table 7.1: Experimental parameters used to acquire data in calcium-containing clusters.

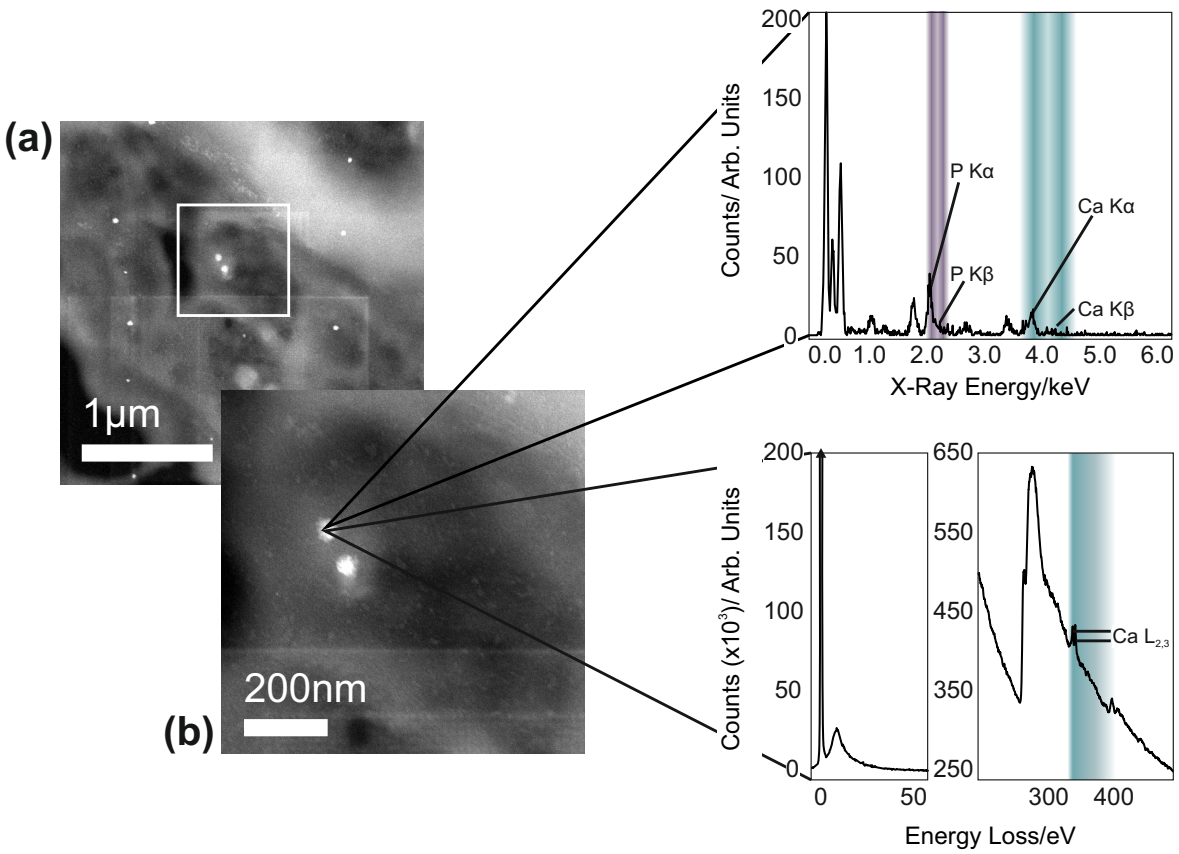


Figure 7.3: A bundle of unmyelinated axons is shown in (a), and higher magnification reveals two distinct electron-dense clusters as shown in (b). EDX and EELS data recorded from these regions show a clear Ca $L_{2,3}$ edge at ∼347 eV in the EEL spectrum, and a distinct calcium Kα peak in the EDX. Due to the low x-ray counts, the weaker Kβ is not visible in the single-pixel data. Carbon contamination from previous SI acquisitions is visible in (a) and (b). Atom counting granules using HAADF intensity is not possible in this case as the image is overexposed and therefore not suitable for mass measurement using the techniques from Chapters 5 and 6.

7.4.2 Spectral Processing

As per Chapter 6, spectral data was processed using Hyperspy [116]. EELS low- and core-loss data were realigned using the zero-loss peak. The energy regions used to model the inverse power-law background and for integration were kept the same as for measurement of $\sigma_{\mathrm{Ca}}^{\mathrm{EELS}}$. Ca $L_{2,3}$ counts were extracted for each pixel, and summed those containing values greater than the noise introduced from the background removal process.

The EDX data was realigned using the Au Lα system peak and integrated for the same pixels used in obtaining the total EELS counts. Due to the poor signal-to-noise level of the data, the combined Ca Kα and Kβ cross-section $\sigma_{\mathrm{Ca}}^{\mathrm{EDX:\ K\alpha+\ K\beta}}$ was measured, again with counts integrated in the same energy range used in Chapter 6. Using the experimental probe current and the spectrum image pixel size, total EDX and EELS counts were converted to cluster cross-sections. The number of calcium atoms in the cluster N_{Ca} was calculated using the experimental cross-sections measured on the ARM200F, i.e. by

$$N_{\mathrm{Ca}}^{\mathrm{EDX}} = \frac{\sigma_{\mathrm{Ca,cluster}}^{\mathrm{EDX}}}{\sigma_{\mathrm{Ca}}^{\mathrm{EDX}}} = \frac{\sigma_{\mathrm{Ca,cluster}}^{\mathrm{EDX}}}{1.563\mathrm{barns}} \tag{7.1}$$

for the EDX data, and

$$N_{\mathrm{Ca}}^{\mathrm{EELS}} = \frac{\sigma_{\mathrm{Ca,cluster}}^{\mathrm{EELS}}}{\sigma_{\mathrm{Ca}}^{\mathrm{EELS}}} = \frac{\sigma_{\mathrm{Ca,cluster}}^{\mathrm{EELS}}}{5578\mathrm{barns}} \tag{7.2}$$

for the processed EELS counts.

7.4.3 Measurement of N_{atoms} from EDX and EELS

Table 7.2 shows the results of calculations using Equations 7.1 and 7.2. The largest errors on $N_{\mathrm{Ca}}^{\mathrm{EDX}}$ arise due to the poor counting statistics (and therefore large Poissonian noise) of the x-ray data and the error on the measurement of $\sigma_{\mathrm{Ca}}^{\mathrm{EDX}}$. The error on $N_{\mathrm{Ca}}^{\mathrm{EELS}}$ arises primarily due to contributions from $\sigma_{\mathrm{Ca}}^{\mathrm{EELS}}$, and also from difficulties in fitting the spectral background. By modifying the energy region used for fitting, it is estimated that this error contribution is about 10%. Despite this, $N_{\mathrm{Ca}}^{\mathrm{EDX}}$ and $N_{\mathrm{Ca}}^{\mathrm{EELS}}$ show good agreement.

Method	**Upper Cluster** N_{Ca}	**Lower Cluster** N_{Ca}
EDX	$(6.18\pm0.35)\times10^6$	$(3.90\pm0.28)\times10^6$
EELS	$(5.96\pm0.60)\times10^6$	$(3.87\pm0.42)\times10^6$

Table 7.2: Number of calcium atoms measured in samples of vehicle-treated peripheral nerve at Day 7, measured using EDX and EELS. "Upper" and "lower" clusters refer to those shown in Figure 7.3.

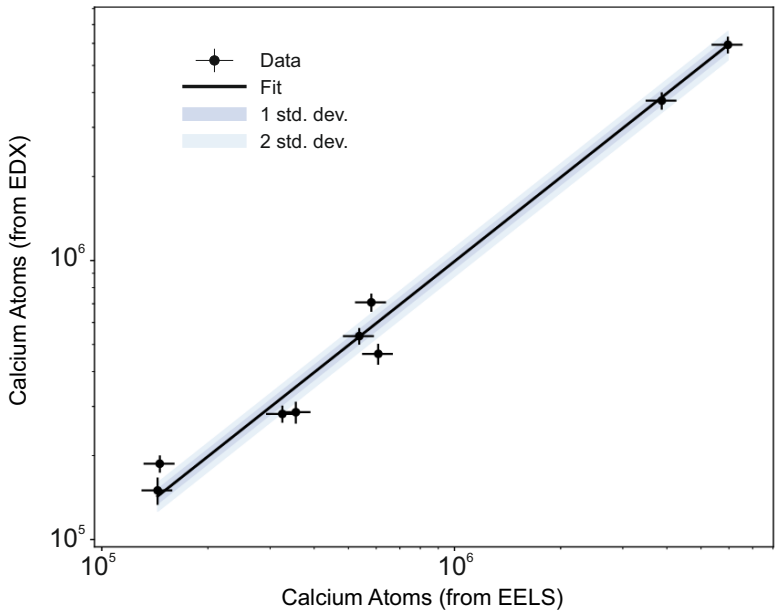


Figure 7.4: $N_{\mathrm{Ca}}^{\mathrm{EDX}}$ against $N_{\mathrm{Ca}}^{\mathrm{EELS}}$ measured for different clusters (log-log scale). The results of the fit show that $N_{\mathrm{Ca}}^{\mathrm{EDX}} = (0.98\pm0.05)N_{\mathrm{Ca}}^{\mathrm{EELS}}$.

Additional data was recorded from other clusters, in both myelinated and unmyelinated axons, under the same experimental conditions described above. A plot of $N_{\mathrm{Ca}}^{\mathrm{EDX}}$ against $N_{\mathrm{Ca}}^{\mathrm{EELS}}$ is shown in Figure 7.4. The number of atoms calculated using either technique agree; the curve gradient measured from $n = 9$ clusters is 0.98, with a standard deviation of 0.05.

7.4.4 Discussion

Dense, calcium-containing clusters were observed in multiple vehicle-treated samples and in both myelinated and unmyelinated axons. Excluding the carbon and oxygen EDX peaks, the most intense spectral feature was the phosphorous Kα and Kβ peaks, at 2.01 and 2.14 keV respectively.

In some EELS data, it was possible to observe increased spectrum intensity corresponding to the P $L_{2,3}$ edge (at 132eV). However, due to the edge shape and its delayed onset, plus that it is superimposed on a more intense region of the plasmon tail, it is very difficult to extract and measure reliably.

It is possible the clusters observed are similar to those observed in other cells types by Wolf et al. [243]. Their EDX data was recorded from frozen hydrated samples, and also showed the clusters (termed "storage granules") primarily contain calcium and phosphorous. Due to the use of bright-field tomography, the authors were also able to show the granules were located inside the cell mitochondria; these observations had been reported previously, but only from heavily stained and fixed samples [382]–[384].

The diameter of granules observed in these data were estimated from the HAADF image, and the calcium number density calculated using N_{atoms} measured with spectroscopy. The average value was 26 ± 11 calcium atoms/nm^3 ($n = 9$), where the error is the standard deviation measured from the sample population alone (i.e. not incorporating the significant error on the volume estimate). This value of calcium number density is similar to that of amorphous calcium triphosphate (18 calcium atoms/nm^3, assuming a density of 3.14 g/cm^3 [385]).

The value calculated here is two times greater than that of Wolf et al., who measured density using a comparative HAADF mass measurement approach. However, this discrepancy may be accounted for by a key difference in the definition of granule size. At low magnifications, the granule diameters appeared similar to those of Wolf et al. However, at higher magnifications, internal structure could be seen within individual granules. The estimates of diameter used here were made for the most dense (core-like) regions, which were the only ones to produce EDX and EELS signal. The diameters measured by Wolf et al. appear to have been taken from relatively low-magnification images (likely due to dose limitations imposed by cryo conditions), potentially leading to an overestimation of the true cluster volume and a corresponding underestimate of the calcium number density.

Prospects for Investigation of PIPN

The analysis described in this Section was applied only to data obtained from vehicle-treated animals at the Day 7 timepoint. While calcium-rich granules were also observed in peak-pain and

paclitaxel-treated specimens, as the aim of the work discussed here was to validate methodology, and not to probe physiological differences in mitochondrial calcium content, only the vehicle D7 granules were analysed in depth.

However, several publications have reported correlation between development of paclitaxel-induced peripheral neuropathy and mitochondrial dysfunction [378], [386]. Given the critical role of mitochondria in calcium management within the cell [387], it may be possible to use EDX and EELS partial scattering cross-sections to probe these changes chemically. While the large standard deviation on the calcium number density measured here would likely prohibit the detection of small changes in calcium storage, there are a number of areas where data collection could be optimised (i.e. through the use of multi-frame spectroscopy as described in Chapter 3). The use of direct-detection EELS would also likely have considerable benefits over the indirect system used in this work.

7.4.5 Summary

By measuring calcium-containing granules in samples of peripheral nerve, measurements of $\sigma_{\mathrm{Ca}}^{\mathrm{EDX}}$ and $\sigma_{\mathrm{Ca}}^{\mathrm{EELS}}$ in the Oxford ARM200F have been validated. There is very good agreement between N_{atoms} measured with either EDX or EELS, which would not be the case if there was considerable error in the values of spectroscopic partial cross-sections measured in Chapter 6.

It has also been shown that $\sigma_{\mathrm{Ca}}^{\mathrm{EDX}}$ and $\sigma_{\mathrm{Ca}}^{\mathrm{EELS}}$ may be used to measure calcium with some biological relevance. While it is not possible to definitively identify particular organelles, calcium- and phosphorous-containing granules are observed inside regions of the sample with increased mass-thickness (as shown in Figure 7.2), which may correspond to mitochondria. Future work should examine whether differences in mitochondrial calcium storage are detectable with EELS and EDX techniques.

7.5 Application 2: Intracellular Na and K

Recently, Ferguson et al. have acquired further EDX data from the samples produced per Section 7.3 using the CUI JEM-F200 [388]. Similar to the analysis described in Appendix C, they measured intracellular sodium and potassium content from the lumens of both myelinated

and unmyelinated axons, quantifying their data with theoretical Cliff-Lorimer $k_{A,B}$ factors incorporated in the software package Aztec (Oxford Instruments *(Abingdon, UK)*) used to acquire the EDX data.

At Day 7 (prior to the onset of pain-like behaviour), Ferguson observed no significant changes in the weight percentages (wt%) of Na or K in either myelinated or unmyelinated axons following treatment with paclitaxel (relative to vehicle-treated samples). However, they did report a statistically significant change in the ratio of intracellular Na:K. This apparent contradiction likely arises due to the changes in Na or K alone being small; however, these differences are sufficiently increased upon taking the ratio of the two as to be significant. In samples recovered at the peak-pain time-point, there were no statistically significant differences between intracellular Na wt%, K wt%, or ratios thereof.

7.5.1 Data Acquisition

In this section the author wishes to acknowledge Dr Christina Ferguson, who acquired the EDX data analysed in this Section.

Data from between 15-40 myelinated and 15-30 unmyelinated axons per animal were measured during these experiments. At the D7 timepoint, samples from 5 vehicle-treated and 4 paclitaxel-treated animals were included in the analysis. At the PP timepoint, both vehicle- and paclitaxel-treated groups contained 5 animals. EDX data were recorded from samples prepared as per Section 7.3. In myelinated axons, a $1\,\mu m^2$ region inside the lumen was recorded, with care taken to avoid regions with obvious ultrastructural damage. In the (significantly smaller) unmyelinated axons, a region of $300\times300\,nm$ was selected using the same criteria. Data were acquired with a probe current of approximately 15 nA; however, due to the relatively low magnifications used, this corresponds to an electron dose of between 30–500 electrons/$Å^2$, dependent upon pixel number and step size.

7.5.2 Spectral Processing: Theoretical k-factors

As considerably more data were recorded by Ferguson et al. than were included in their analysis, the current author selected a similar subset of axon lumens at both timepoints, and processed

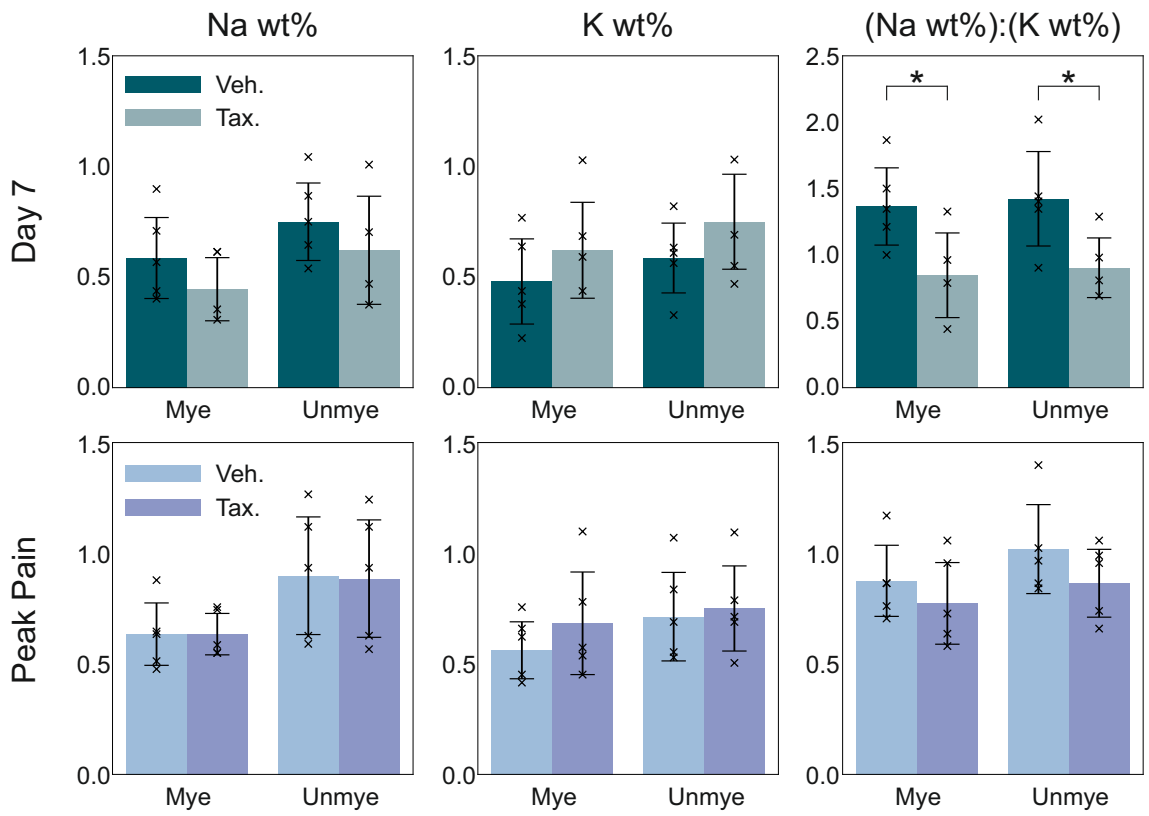


Figure 7.5: Intra-axonal wt% of Na and K measured using theoretical k-factors. Top row: Day 7 values of wt% Na, wt% K and the ratio of wt%Na:wt%K. Bottom row: Peak pain values of wt% Na, wt% K and the ratio of wt%Na:wt%K. As indicated, only the ratio change at D7 is statistically significant. Each cross represents the mean data from one animal, and the error bar is one standard deviation from the pooled data (i.e. all myelinated axons in the group of $n = 5$ vehicle-treated animals at D7 etc.).

the data using the theoretical k-factors available in Aztec. The same analysis procedure was followed, with biologically significant elements such as carbon, oxygen and nitrogen included in the percentage weight analysis. Gold, cobalt and iron x-ray peaks were deliberately excluded, as they likely originate from the microscope column or TEM grid.

For consistency with the methods of Ferguson, statistical significance was assigned for $p < 0.05$, as assessed using two-tailed unpaired Mann-Whitney U-tests, calculated using OriginPro Academic 2017 (OriginLab Corporation *(Northampton, MA, USA)*). As shown in Figure 7.5, analysis using the theoretical Cliff-Lorimer $k_{A,B}$ factors from Aztec reproduced Ferguson's findings for the subset of axons selected by the current author.

7.5.3 Spectral Processing: Partial Scattering Cross-Sections

Following the successful reproduction of Ferguson's results, EDX spectra were reanalysed using the EDX partial cross-sections found previously for the F200. Using Hyperspy [116], these data were processed using the same background and integration energy windows used to measure $\sigma_{\mathrm{Na}}^{\mathrm{EDX}}$ and $\sigma_{\mathrm{K}}^{\mathrm{EDX}}$ in Chapter 6. Peak counts I_x for the Na Kα and combined K Kα and Kβ were extracted and converted to an "areal density" of element x, $n_x t$, using Equation 7.3:

$$n_x t = \frac{I_x}{N_e \sigma_x^{\mathrm{EDX}}}, \tag{7.3}$$

where N_e is the total number of electrons incident on the sample during the spectral acquisition. The units of areal density are therefore average Na or K atoms per area of the sample. While values of $n_x t$ will clearly have a dependence on specimen thickness, all samples were sectioned at the same temperature and using the same cutting thickness. Variation should therefore be minimal, but for the avoidance of doubt the dimensionless number density ratio, $n_{\mathrm{Na}}/n_{\mathrm{K}}$, is also computed.

7.5.4 Measurement of Na and K Areal Densities

The results of these measurements, and calculations of Na:K ratios, are shown in Figure 7.6. At Day 7, in myelinated axons, the differences between sodium and potassium areal densities and the ratio of $n_{\mathrm{Na}}/n_{\mathrm{K}}$ are statistically significant between the paclitaxel- and vehicle-treated samples. Paclitaxel-treated samples show decreased intracellular sodium and increased intracellular potassium, relative to the vehicle-treated samples. Overall, this leads to a reduction in $n_{\mathrm{Na}}/n_{\mathrm{K}}$. At the same time-point, unmyelinated axons in the paclitaxel-treated group show a statistically-significant increase in potassium areal density and decrease in $n_{\mathrm{Na}}/n_{\mathrm{K}}$. The increase in intracellular sodium does not meet the threshold for statistical significance ($p = 0.14$).

In samples recovered at the peak of pain-like behaviour, statistically significant decreases in intracellular Na and $n_{\mathrm{Na}}/n_{\mathrm{K}}$ are observed in myelinated axons. There is no significant change in intracellular potassium. In unmyelinated axons, there are statistically significant decreases in intracellular Na, K and $n_{\mathrm{Na}}/n_{\mathrm{K}}$. These findings are summarised in Table 7.3, and given as percentage differences $\%_{diff}$ where

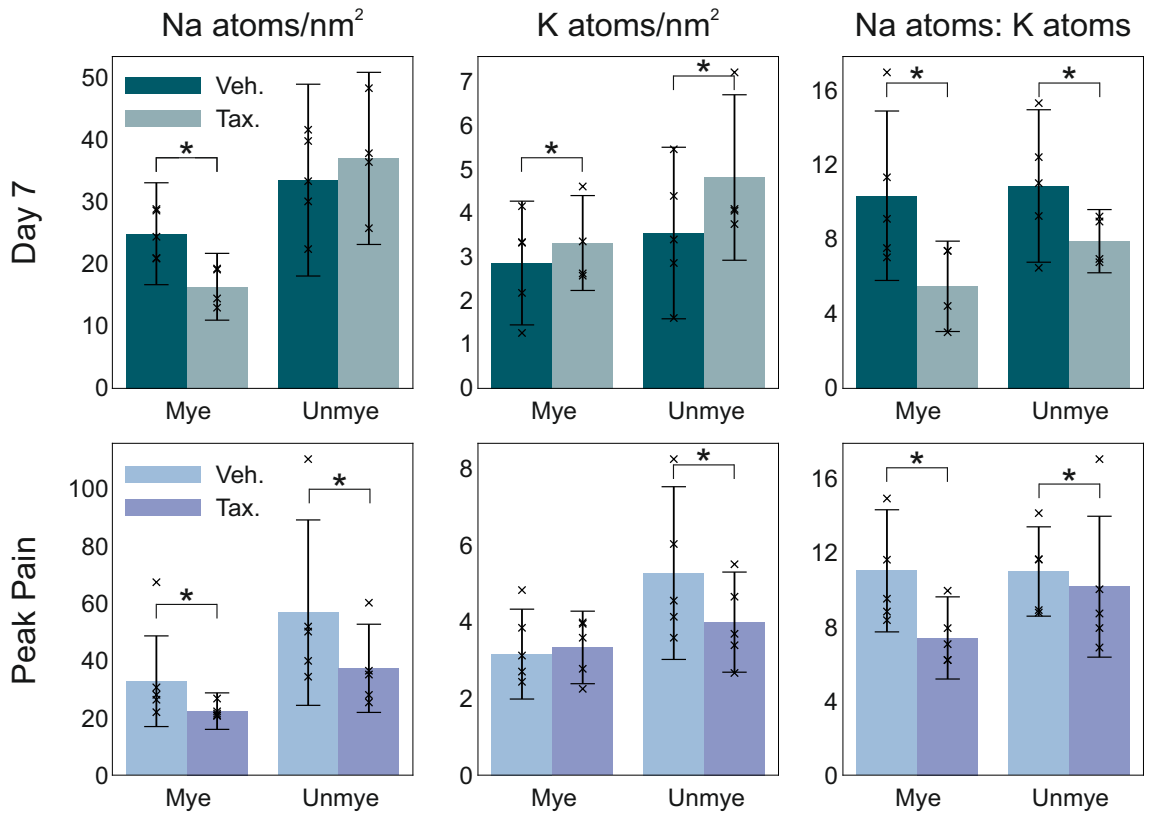


Figure 7.6: Intra-axonal areal density of Na and K measured using partial scattering cross-sections. Top row: Day 7 values of Na areal density (atoms/nm^2), K areal density (atoms/nm^2) and the dimensionless ratio for myelinated and unmyelinated axons. Bottom row: Peak pain values of Na areal density, K areal density and the ratio.As indicated, all changes are statistically significant except in the Na areal density of unmyelinated axons at Day 7, and in the K areal density of myelinated axons at at Peak Pain. Each cross represents the mean data from one animal, and the error bar is one standard deviation from the pooled data (i.e. all myelinated axons in the group of $n = 5$ vehicle-treated animals at D7 etc.).

		Day 7	Peak Pain
Myelinated	$n_{\mathrm{Na}}t$	-41%	-38%
	$n_{\mathrm{K}}t$	+15%	(+5%)
	$n_{\mathrm{Na}}/n_{\mathrm{K}}$	-61%	-39%
Unmyelinated	$n_{\mathrm{Na}}t$	(+9%)	-41%
	$n_{\mathrm{K}}t$	+30%	-28%
	$n_{\mathrm{Na}}/n_{\mathrm{K}}$	-32%	-8%

Table 7.3: Percentage differences in Na and K areal density and their ratio for the data shown in Figure 7.6. Values in parentheses indicate non-statistical significance (i.e. $p > 0.05$).

$$\%_{diff} = 100\% \times \frac{2|V_{veh} - V_{PTx}|}{|V_{veh} + V_{PTx}|}, \tag{7.4}$$

where V_{veh} and V_{PTx} represent a measured value (such as an areal density, or a ratio) at a certain timepoint and for a certain axon type, for vehicle-treated and paclitaxel-treated populations respectively.

7.5.5 Comparison of Experimental and Literature k-factors

In general, the data processed using partial scattering cross-sections appear to demonstrate more sensitivity to changes in intra-axonal sodium and potassium than the theoretical k-factor analysis of Ferguson et al. This may be in part due to considerable errors in values of Cliff-Lorimer $k_{x,\mathrm{Si}}$ (for element x relative to silicon) at low energies. Figure 7.7 shows these values plotted alongside experimentally measured $k_{x,\mathrm{Si}}$ from the literature.

Furthermore, due to the interdependence of k- and ζ-factors, and EDX partial scattering cross-sections, values of $k_{\mathrm{Na,K}}$ may be estimated by evaluating

$$k_{\mathrm{Na,K}} = \frac{k_{\mathrm{Na,Si}}}{k_{\mathrm{K,Si}}}, \tag{7.5}$$

for the data of Cliff and Lorimer [81], Sheridan [389], and the theoretical values incorporated in Aztec, or

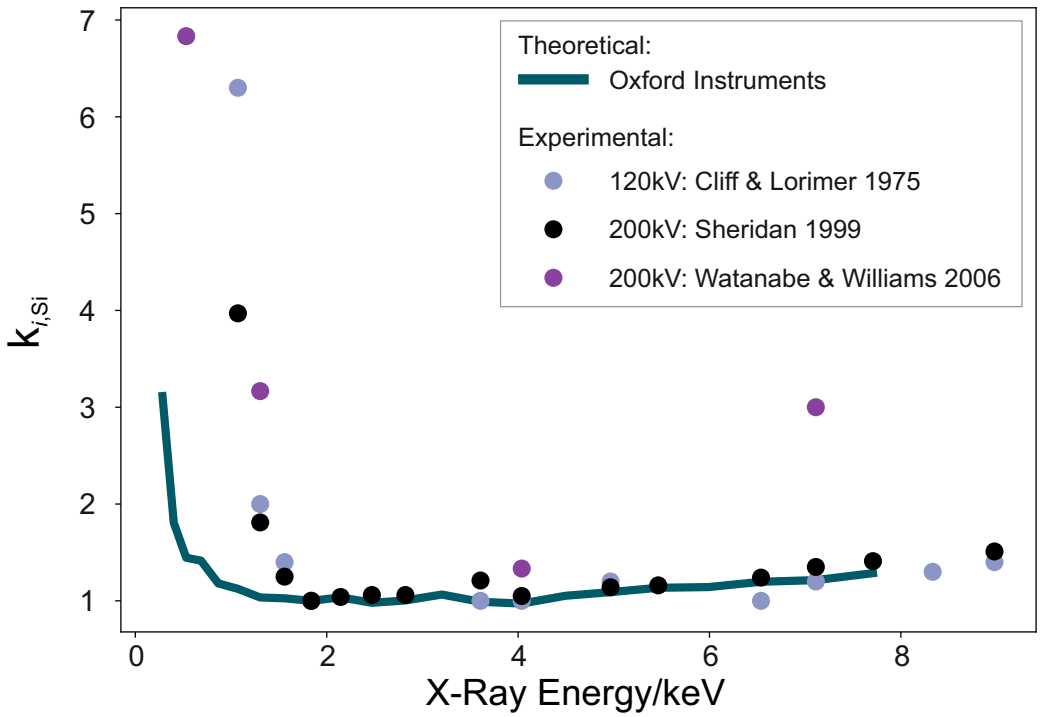


Figure 7.7: Theoretical and literature experimental values of Cliff-Lorimer k-factors $k_{x,\mathrm{Si}}$. The solid line shows the former of these extracted from Aztec, while the individual points are taken from Cliff and Lorimer [81], Sheridan [389] and Watanabe and Williams [88]. While these data are not recorded for the same experimental conditions and cannot be compared directly, there is a clear trend in the experimental measurements of $k_{x,\mathrm{Si}}$ at low energy which is not mirrored by the theoretical values from Aztec.

		$k_{\mathrm{Na,K}}$
Experimental	Cliff & Lorimer [81]	6.2
	Sheridan [389]	3.3
	Watanabe & Williams [88]	2.9
	$\sigma^{\mathrm{EDX}}_{\mathrm{CUI\ F200}}$	4.8
Theoretical	Aztec (OI)	1.1

Table 7.4: Comparison of theoretical and experimental $k_{\mathrm{Na,K}}$, calculated using data presented in Figure 7.7 and from Chapter 6.

$$k_{\mathrm{Na,K}} = \frac{\zeta_{\mathrm{Na}}}{\zeta_{\mathrm{K}}} \tag{7.6}$$

for values taken from Watanabe and Williams [88], and

$$k_{\mathrm{Na,K}} = \frac{M_{\mathrm{Na}}}{M_{\mathrm{K}}} \frac{\sigma^{\mathrm{EDX}}_{\mathrm{K}}}{\sigma^{\mathrm{EDX}}_{\mathrm{Na}}} \tag{7.7}$$

for the EDX partial scattering cross-sections measured in Chapter 6, and where M_{K} and M_{Na} are the molar masses of potassium and sodium respectively. These values are tabulated in Table 7.4. While differences between the EDX detectors used to measure these values mean they cannot be compared directly, it is notable that experimental $k_{\mathrm{Na,K}}$ are consistently much higher than incorporated to the EDX acquisition software. This implies that use of these theoretical values will considerably underestimate the sodium content.

Further error may also be introduced due to similar inaccuracies in the theoretical $\mathrm{k}_{x,\mathrm{Si}}$ of other elements (as shown in Figure 7.7); this is particularly important in analyses similar to Ferguson's, where all elements which make up the sample must be included in the wt% concentration calculations. In samples similar to those used in this work, errors in quantification of abundant elements such as carbon and oxygen would be likely to significantly impact the final result.

The use of EDX partial scattering cross-sections therefore presents an interesting opportunity for quantifying elements in complex samples of this nature. Rather than requiring the measurement of many $\mathrm{k}_{x,y}$, it is already possible to observe some significant changes in e.g. intracellular

sodium and potassium, through measurements of areal density and number density ratio.

7.5.6 Discussion

Following their measurements of intra-axonal Na and K, Ferguson separated axons according to their apparent stage of an action potential generation, as determined by the wt%Na/wt%K ratio. Those with wt%Na/wt%K<1 were classified as hyperpolarised axons, and those with wt%Na/wt%K>1 were considered to be depolarised. These two states correspond to the axon being in the "resting" state or in the process of impulse transmission, as shown in Figure 7.8.

In atomic percent, a sodium to potassium weight ratio of unity is approximately equivalent to at%Na/at%K=$M_{\mathrm{K}}/M_{\mathrm{Na}} \sim 1.7$. However, this ratio is considerably lower than the atomic ratios measured using partial scattering cross-sections (as shown in Figure 7.6). The number density ratios described here indicate that there are many more sodium atoms present in both axon types, at both timepoints, and in axons from both paclitaxel- and vehicle-treated rats. This is likely attributable to errors in Ferguson et al.'s analysis arising due to the use of theoretical k-factors; their subsequent analysis of axons based upon wt%Na/wt%K ratios is therefore of questionable validity.

It is challenging to relate the changes discussed in Section 7.5.4 directly to a particular stage of the action potential. However, the changes between vehicle- and paclitaxel-treated animals indicate that in general, intra-axonal sodium is reduced in the latter group. This may correspond to a reduction in action potential generation, i.e. fewer depolarised axons. At Day 7, this is supported by an elevated level of potassium in the same animals; again this may correspond to more axons captured in the "resting" state.

At the peak of pain-like behaviour, the data are more complex to interpret. A decrease in intracellular sodium may, as at D7, correspond to fewer action potential generation events. However, a decrease in intracellular potassium in paclitaxel treated animals (relative to the vehicle cohort) could also indicate axons remain in the hyperpolarised state for longer periods of time. At both timepoints, these changes may correspond with alterations in impulse amplitude and conduction velocity, and the development of pain associated with chemotherapy treatment (particularly for unmyelinated axons, responsible for the burning/aching pain characteristic of PIPN) [390].

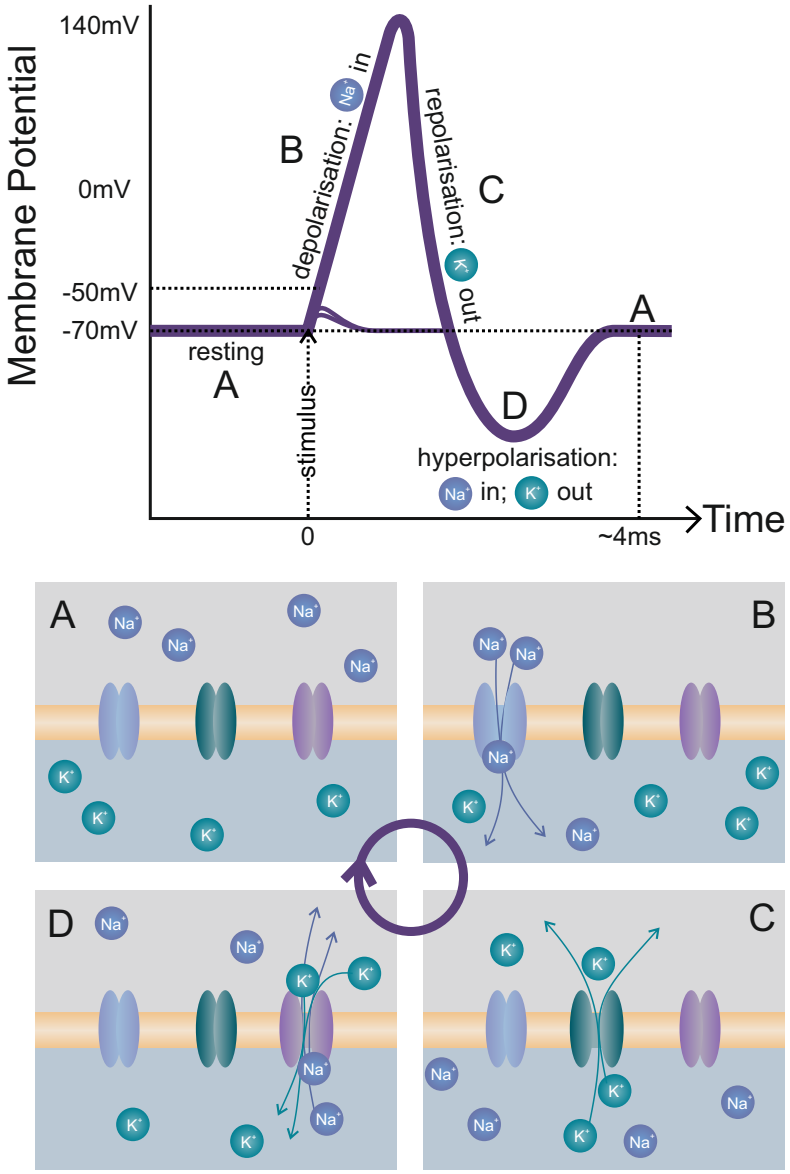


Figure 7.8: Schematic of action potential generation. At rest (A), the axon is relatively impermeable to Na and K influx and efflux, and the potential gradient across the membrane is stable. Upon detection of a stimulus, the cell membrane depolarises (B); voltage-gated sodium channels (shown in blue) open, and Na^+ ions enter the nerve. Upon reaching the maximum positive value, the membrane repolarises (C). Sodium channels close, blocking further Na^+ ions from entering the cell, and voltage gated potassium channels (green) open, with K^+ ions diffusing into the extracellular space. During the refractory hyperpolarised period (D), sodium-potassium pumps actively transport Na^+ and K^+ ions out and into the nerve respectively, returning the nerve to its resting state (A).

Effects of Sample Preparation

Electron probe microanalysis (EPMA) studies have previously shown that, in contrast to the results described in this Section, in healthy tibial and sciatic nerve [391], [392], and optic nerve [393], intracellular sodium levels are much lower than intracellular potassium. However, the sample preparation methods utilised in these studies are considerably different to those employed to produce the specimens investigated here and described in Section 7.3.

For EPMA, samples were obtained by freezing the nerve *in situ* using cooled copper pliers. Samples were then placed directly into liquid nitrogen or melting Freon-12, and later cryosectioned at -55°C. Although *in situ* freezing may minimise movement of species such as Na and K, this benefit is considerably overshadowed by the practicalities of such an approach. In particular, the dimensions of the nerves (around 15 mm in length, and 0.3 mm thick) mean that it is very unlikely samples were homogeneously frozen. Submersion in e.g. liquid nitrogen without a cryoprotectant such as sucrose would introduce similar challenges, particularly for nerve tissue containing structures with variable water content. Given that the formation of crystalline ice is likely to disrupt the native elemental distributions in the tissue, and that there is clear evidence of extensive ice damage in the images contained within Refs. [391]–[393], this casts doubt on the validity of these results.

Even under the high-pressure conditions utilised for this work, the nerve fiber diameter of 300 µm is at the limit of the maximum vitrifiable specimen thickness [394]. However, as seen in Figures 7.1 and 7.2, this procedure was sufficient to preserve the intraaxonal ultrastructure. Samples which showed evidence of poor freezing (from visual inspection in the cryomicrotome), or crystalline ice formation (observed in the microscope) were rejected from the experiment. Furthermore, as the sample preparation procedure for vehicle- and paclitaxel-treated samples was identical, it is unlikely the differences observed in the data shown here result solely from artefacts in this process.

Possible Physiological Implications

The data shown in Figure 7.6 indicate that even prior to the onset of pain-like behaviour (i.e. at Day 7), there are already significant changes to the intracellular levels of sodium and potassium

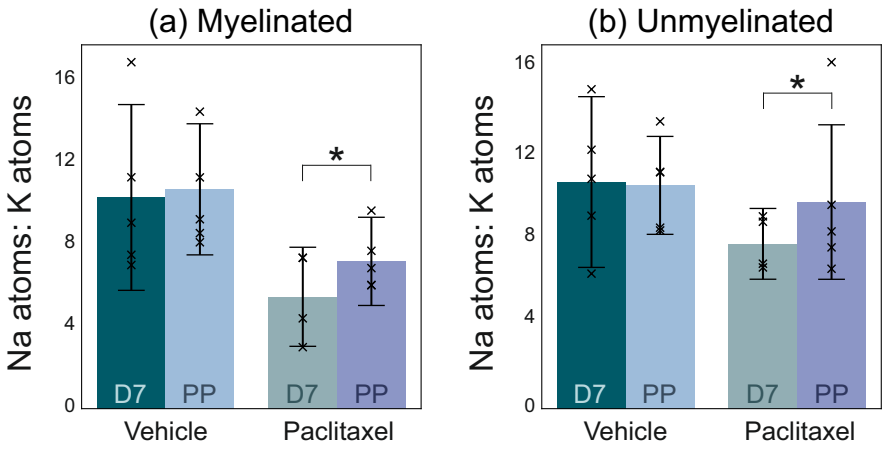


Figure 7.9: Ratio data (measured using EDX partial scattering cross-sections) for myelinated and unmyelinated axons compared at Day 7 and Peak Pain timepoints. In both myelinated and unmyelinated axons, there are no statistical differences between Na:K in the vehicle-treated populations at D7 and PP. However, in those treated with paclitaxel there is a significant change, with Na:K increased at the latter timepoint.

in the axons of vehicle- and paclitaxel-treated animals. These differences are also evident at the peak pain time-point. Furthermore, as shown in Figure 7.9, while there are no statistical differences between the $n_{\mathrm{Na}}/n_{\mathrm{K}}$ levels at Day 7 and peak-pain time-points in vehicle-treated animals, there are significant differences in those treated with paclitaxel.

As discussed at the beginning of this Chapter, the causal mechanisms of paclitaxel-induced peripheral neuropathy are poorly understood. While paclitaxel treatment is associated with changes to the expression of a number of different voltage-gated sodium and potassium ion channels within the peripheral nerve [379], [395], [396], the implications of this on the intracellular elemental distributions of Na and K are unclear and merit further investigation.

Furthermore, a number of other studies have yielded conflicting results concerning the effects of paclitaxel treatment on nerve ultrastructure. For example, some reports suggest paclitaxel is associated with changes to the number and diameter of myelinated axons [397], [398], while others have concluded paclitaxel has no effect on these parameters [378], [386]. Some studies have also observed axonal degeneration and thinning of the myelin sheath in some axons [398], [399]. These changes would also be important for the transport of sodium and potassium ions;

larger fibers typically have more ion channels, but reduced myelination may lead to a loss of ions from the axon [400].

While the physiological implications of these findings are beyond the scope of this thesis, it is of note that statistically significant differences in intracellular sodium and potassium are measurable using EDX partial scattering cross-sections. As discussed in Chapter 3, concentration ratios of sodium and potassium have previously been used as a measure of cytotoxicity in several systems [225], [226]. Absolute concentrations have also been assessed as a function of cell division rate [401]. The latter of these in particular merits further investigation in the context of this work; intracellular levels of Na and K were shown to be lower in slowly-dividing cells, and paclitaxel is known to inhibit cell division. Xiao et al. have shown that paclitaxel is detectable in the peripheral nerve at Day 7, but not at the peak of pain-like behaviour [402]; it is possible that the changes in intracellular sodium and potassium reflect this, particularly given the return of $n_{\mathrm{Na}}/n_{\mathrm{K}}$ to levels more closely reflecting those of the vehicle-treated population at the peak-pain time-point.

7.5.7 Summary

EDX partial scattering cross-sections have been applied to measure intracellular levels of several of sodium and potassium in axons of the peripheral nerve. This approach is sensitive to changes induced by treatment with paclitaxel, with axons showing pronounced differences in elemental composition relative to those recovered from vehicle-treated animals. A σ^{EDX}-based approach appears more sensitive to small changes than one based solely upon theoretical Cliff-Lorimer k-factors.

This work also highlights the potential of σ^{EDX} for complex biological specimens. Accurate measurement of $k_{A,B}$ pairs for all elements present in the sample is essential for successful quantification, but is laborious and technically challenging. Partial scattering cross-sections therefore afford a means of accessing quantitative specimen information for elements of interest alone, without the requirement to fully characterise the EDX detector response.

Conclusions & Outlook

7.6 Summary

The main aim of this thesis has been to establish to what extent quantitative STEM methods may be applied for the measurement of intracellular distributions. As discussed in Chapters 1 and 2, the STEM affords access to a range of signals which can be used independently and collectively to investigate structure and composition with very high spatial resolution. Applications of these techniques in life sciences were reviewed in Chapter 3.

Chapters 4 through 7 contain experimental results pertaining to the measurement and application of scattering cross-sections. In Chapter 4, these are applied indirectly to measure the mass of small disordered platinum clusters observed in the drug oxaliplatin. The very high spatial resolution of the STEM, when used in combination with HAADF imaging, means these clusters may be atom-counted through comparisons with the single-atom intensity. This Chapter also showed the capabilities of the STEM for nanoscale characterisation, as the chemotherapeutic cisplatin was found to contain small metallic platinum nanoparticles. Further work is merited here to ascertain whether these nanoparticles are truly present in solutions of cisplatin administered in the clinic, as this would be likely to have significant implications for *in vivo* toxicity.

Chapter 5 showed that HAADF STEM is also suitable to examine platinum-containing drugs in tissues, again at very high resolution. While such samples usually produced for TEM typically require extensive chemical fixation and staining, this work shows that the contrast of ADF STEM is sufficient to navigate the gross cell ultrastructure without this condition. Due to the high elastic scattering generated by platinum aggregations, these could be located in the cytosol of neuronal cell bodies. These features are likely consistent with accumulation by organelles such as autophagosomes; this could be confirmed by post-staining existent samples to

show the membrane structure in these areas. The increasing interest in in subcellular elemental mapping, particularly in the context of metals in cells, means that access to ultra-high resolution information in this way may be of interest in many research areas.

Chapters 6 and 7 are concerned with the measurement and application of *spectroscopic* partial scattering cross-sections in intracellular measurements. EDX and EELS are both methods used frequently to perform elemental analysis in the STEM. However their interpretation, and particularly their quantification, often pose a considerable challenge due to the low count rates and signal overlaps which are inherent in complex biological samples. Measurement of EDX and EELS partial scattering cross-sections is a relatively recent technique for spectrum quantification, which has thus far been limited to applications only in inorganic specimens. The work shown in these Chapters indicates such methods are also applicable in biology, and are capable of measuring intracellular elemental distributions. Particularly for EDX, cross-section measurement presents a new opportunity for spectral quantification. There is therefore particular scope to examine whether such methods afford more straightforward or accurate route to quantitative results than the Cliff-Lorimer method, and equivalently whether it is possible to develop a corrective procedure for x-ray absorption in the same manner as employed in the ζ-method.

7.7 Emerging Opportunities

The applications of HAADF, EDX and EELS partial scattering cross-sections in the measurement of intracellular elemental distributions are likely to benefit from a number of emerging methods, not least those afforded by improved sample preparation methods, new imaging modes, and other advances to overcome inherent challenges of electron beam-induced damage.

Sample Preparations and Cryo-STEM

The sample preparation procedures utilised in this thesis have aimed to balance preservation of cell ultrastructure with that of native intracellular elemental distributions. The work demonstrated in Chapter 5 shows that sucrose infiltration and plunge freezing is likely sufficient to preserve distributions of heavy elements such as platinum in a biological context. However in order to preserve elements known to be more vulnerable to extraction and redistribution (generally

those with much lower atomic numbers than Pt [354]), more conscientious methods are needed. The preparation techniques used to produce the peripheral nerve samples in Chapter 7 - namely high-pressure freezing, ultra low-temperature cryosectioning, and freeze-drying - already represent a step-change in technical difficulty. Poor freezing (due to, amongst other reasons, poor cryoprotection, high sample water content and inherent density differences in nerve tissue), devitrification (at any stage when frozen tissue samples or cryosections were transferred, and while sectioning in the cryomicrotome) and poor freeze-drying (for reasons as yet unknown) meant production of these samples was incredibly challenging. It may be found in future experiments that the use of e.g. cryoFIB [403] is a more appropriate and controlled method to produce suitably thin and representative samples from bulk tissue.

In addition, following the enormous growth in cryo-TEM techniques, there is now considerable and renewed interest in the development of cryo-STEM. The ability to acquire imaging and spectroscopic data from frozen samples eliminates the risks posed by freeze-drying or other dehydration steps, and would likely enable intracellular elemental distributions to be examined in a more representative manner. A number of recent publications have shown the feasibly of acquiring cryo-EDX and cryo-EELS data [250], [251].

Electron Ptychography

It is also of considerable interest as to how quantitative spectroscopy may be combined with emerging imaging techniques such as electron ptychography. Ptychographic methods have a number of demonstrable advantages in the imaging of beam-sensitive materials, and for those containing both high- and low-Z elements [60]. A recent proof-of-concept study has shown ptychographic reconstruction may be in principle be combined with spectroscopic data [404], with reliable quantitative methods for the treatment of EDX and EELS data becoming increasingly important in this context. Recently, the use of defocussed-probe ptychography has been demonstrated for biological samples at both cryogenic and room temperatures, and for relatively large fields of view [405].

Next-Generation Detectors and Approaches for Dose-Management

As mentioned briefly in Chapter 2, both EDX and EELS are benefiting from improvements spectrometer design. For EDX, the introduction of silicon drift detectors, in combination with larger detector solid angles (and in some cases, simply more detectors) mean it is possible to maximise x-ray collection in the STEM. For EELS, the incorporation of direct detectors (as used in electron ptychography) offers a means to significantly reduce noise and thus maximise sensitivity. Furthermore, progress in multi-frame imaging (as employed for the imaging of platinum nanoparticles in Chapter 4, and in electron ptychography) may also offer advantages in the acquisition of spectral images. There is considerable discussion in the literature about the degrees to which dose, dose rate and fluence influences electron beam-induced damage [406]. It is also clear that these mechanisms are not the same for all samples, with complex dependencies upon composition and structure. Recently, the development of multi-frame spectrum imaging techniques (complementary to those demonstrated for STEM imaging) have shown particular promise in the acquisition of high-resolution elemental maps [270]. It is likely there would also be considerable benefits to the acquisition of spectral images from materials where dose rate is particularly important.

7.8 Wider Applications

The work presented in this thesis has largely concerned the measurement of heavy atomic species (i.e. platinum), and elements with more general biological significance (such as calcium). However, in principle there is no limitation on which species may be investigated with HAADF or spectroscopic cross-sections.

Biomedicine & Molecular Localisation

In addition to the development of novel platinum drugs, other metal-based compounds are also of considerable interest. A number of ruthenium-, osmium- and iridium-containing compounds have been shown to have a different spectrum of activity and a different toxicity profile to Pt-medicines [407]. The methods described in Chapter 5 would be equally applicable to aggregations of these and other such drugs.

In addition, the quantitative imaging methods employed throughout this work would be well-suited to the detection of single atoms localised at particular binding sites (exactly as initially attempted for DNA). This could provide complementary information to that generated using cryo-TEM techniques, similar to the approach employed by Elad et al. [186] detailed in Chapter 3. It is still extremely challenging to solve biological structures to atomic resolution, but advances in STEM instrumentation and quantitative HAADF methods have not yet been truly examined in this context.

General EDX Analysis

In addition, the route for EDX quantification presented in Chapters 6 and 3 may afford additional benefits for quantification more widely. While in this work, measurements of partial scattering cross-section were made on an extensively characterised STEM, in principle there is no reason that the instrument must be calibrated to the same extent. The comparative mass measurements described in Chapter 3 may afford an alternative and more accessible route for other laboratories to measure EDX partial cross-sections, by extrapolating mass (and atomic content) without the need for full quantitative HAADF analysis. This would have particular benefits for the application of the absorption correction routines developed for the ζ-factor method, which may prove of particular importance for the chemical characterisation of fully hydrated biological specimens.

Appendices

Appendix A

A.1 Spectroscopic Processing Parameters

A.1.1 $CaSO_4$ EDX Processing

X-Ray Line	**Peak Maxima (keV)**	**Background Windows (keV)**	**Integration Windows (keV)**
O Kα	0.5249	0.3483-0.4072; 0.6426-0.7015	0.4660-0.5838
S Kα	2.3072	2.0402-2.1292; 2.6466-2.7378	2.2181-2.3962
S Kβ	2.4643	2.0402-2.1292; 2.6466-2.7378	2.3731-2.5555
Ca Kα	3.6917	3.3716-3.4783; 4.2335-4.3439	3.5850-3.7984
Ca Kβ	4.0127	3.3716-3.4783; 4.2335-4.3439	3.9023-4.1231

Table A.1: Data processing parameters for measuring $\sigma_{\mathrm{Ca}}^{\mathrm{EDX}}$.

A.1.2 $CaSO_4$ EELS Processing

Edge	**Edge Onset (eV)**	**Background Window (eV)**	**Integration Window (eV)**
Ca $L_{2,3}$	∼345	333-343	347-365

Table A.2: Data processing parameters for measuring $\sigma_{\mathrm{Ca}}^{\mathrm{EELS}}$.

A.1.3 BK_3O_3, NaCl and $NaCO_3$ EDX Processing

X-Ray Line	**Peak Maxima (keV)**	**Background Windows (keV)**	**Integration Windows (keV)**
Na Kα	1.041	0.9031-0.9720; 1.1416-1.2111	0.9720-1.1100
Cl Kα	2.6224	2.4358-2.5291; 2.9114-3.0074	2.5291-2.7157
Cl Kβ	2.8158	2.4358-2.5291; 2.9114-3.0074	2.7197-2.9115
K Kα	3.3138	3.0073-3.1095; 3.8006-3.9061	3.2116-3.4160
K Kβ	3.5896	3.0073-3.1095; 3.8006-3.9061	3.4841-3.6951

Table A.3: Data processing parameters for measuring $\sigma_{\mathrm{Na}}^{\mathrm{EDX}}$ and $\sigma_{\mathrm{K}}^{\mathrm{EDX}}$.

Appendix B

B.1 CUI F200 Detector Calibration

The JEOL JEM-F200 "F2" located in the Centre for Ultrastructural Imaging at King's College London is an uncorrected hybrid (S)TEM, with a Schottky field-emission electron source. Unlike the JEOL ARM200F located in Oxford, the F2 does not have a GIF, or other suitable post-column detectors suitable for recording a diffraction pattern. In this chapter, we will describe the basic steps taken to calibrate the probe-forming apertures and the inner and outer angles of the F2 ADF detector.

B.1.1 Recording a Diffraction Pattern

We first measured values of milliradians-per-pixel for the phosphor viewing screen camera at different camera lengths (Figure B.1). As per Jones et al., the condenser lens system (specifically the CL3 lens) was dexcited to form a broad "pencil-beam" of electrons at the sample plane. Gold nanoparticles were used to generate diffraction rings on the phosphor screen. We recorded images of these patterns at camera lengths of 1500, 1200, 1000 and 800 mm. Values for mrad-per-pixel for shorter camera lengths were not measured at this point, as the diffraction pattern was too small to measure reliably.

B.1.2 Calibration of Condenser Apertures

We then measured the probe-forming apertures located in the condenser system (Figure B.2) by observing them on the phosphor screen, in an area of sample vacuum. Using the calibrations

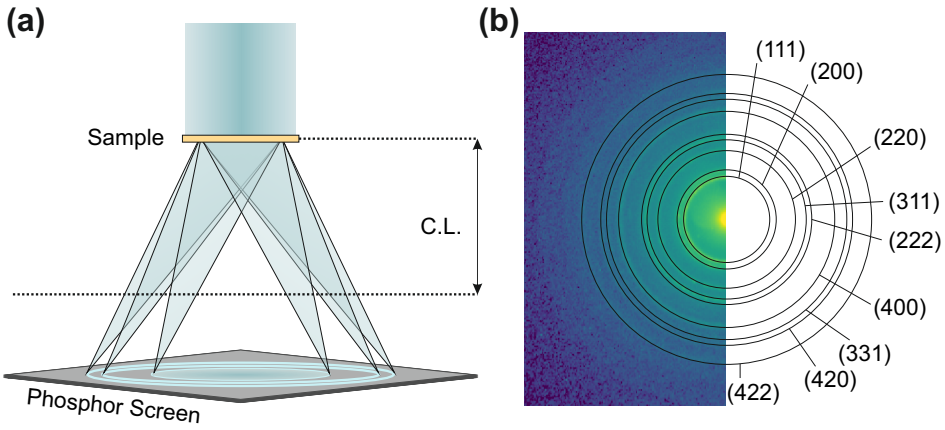


Figure B.1: (a) a broad pencil beam of electrons incident on the sample generates a diffraction pattern at the phosphor screen; "C.L." indicates the nominal camera length between the phosphor screen and the plane of the ADF detector. (b) an indexed Au diffraction pattern.

obtained in the previous section, we could measure the probe semi-convergence angles (α) directly using the radius of the aperture. The 10, 40, 100 and 200 µm apertures form STEM probes with α between 4–66 mrad.

B.1.3 Extension of Camera Calibration

We then imaged the condenser apertures at different camera lengths (Figure B.3). As their angular extent had been measured in the previous section, this allowed us to extend our calibration of "milliradians-per-pixel" for the large phosphor screen to all camera lengths (including those where the Au diffraction patterns were too small and/or intense to measure directly).

B.1.4 Observation of Inner Edge of ADF Detector

Next, we inserted the ADF detector and imaged the detector hole at different camera lengths (Figure B.4). Again, this could be converted to an angle; however, this is not the inner angle of the detector. The ADF detector has an inactive "dead layer" between the inner edge and the

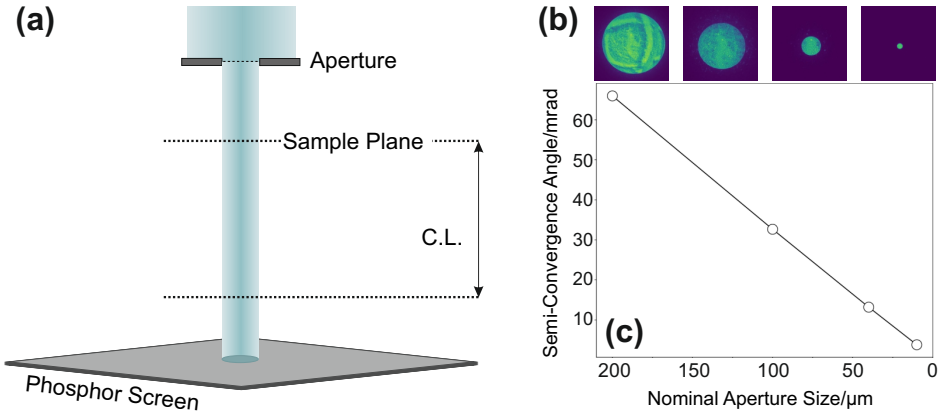


Figure B.2: (a) Probe-forming apertures observed on the phosphor screen. (b) aperture images recorded using the phosphor screen camera. (c) The radius of these apertures was converted to milliradians using the calibration found from the Au diffraction patterns.

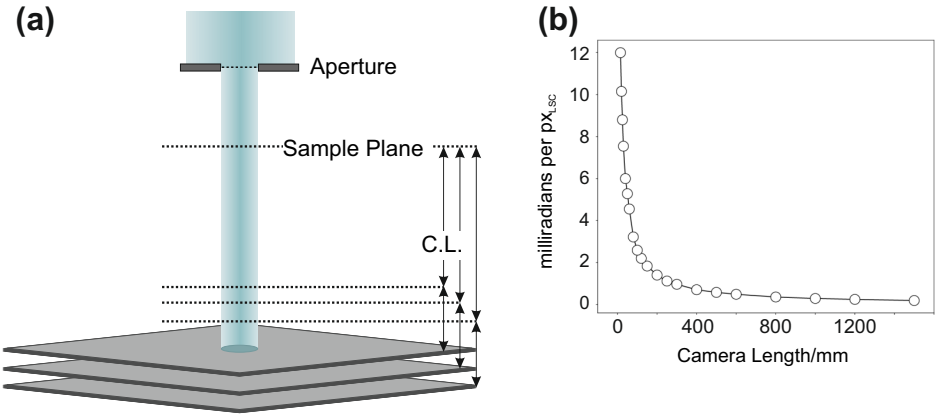


Figure B.3: (a) Measuring condenser apertures at different camera lengths; (b) full angular calibration curve of the large phosphor screen camera at different camera lengths.

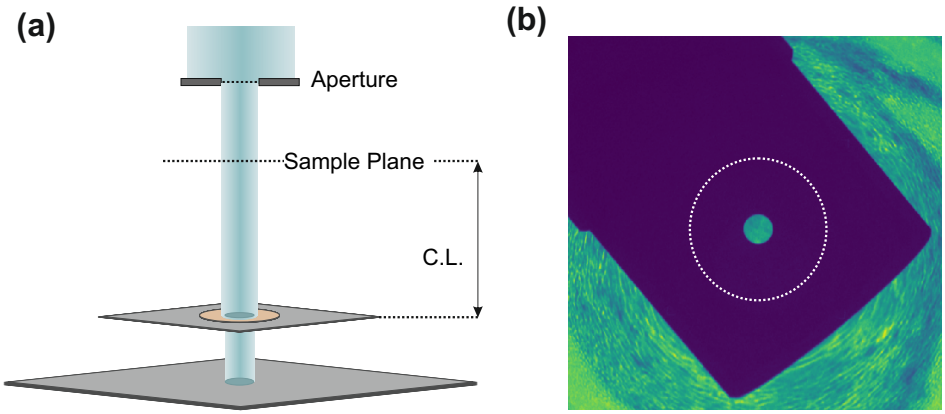


Figure B.4: (a) The ADF detector is inserted before the large phosphor screen. The shadow of the detector hole (b) may be observed. The dashed white line indicates the active annulus of the detector.

start of the active scintillator material.

B.1.5 ADF Detector Scans

Finally, we re-excited CL3 to form a converged probe, and further excited the intermediary lens to form a pencil beam (Figure B.5). The beam was scanned over the ADF detector, with care taken not to saturate the detector, and ADF images recorded at different camera lengths. For each image, we could observe both the detector hole and the start of the active scintillator region. As the former has a known angular extent (measured in the previous step), we could extrapolate to obtain the true inner ADF angle β_1, and the outer detector angle β_2.

B.1.6 Results

Tables B.1 and B.2 show the values for aperture semi-convergence angle α and ADF detector semi-collection angles (β_1, β_2) respectively, along with those indicated in the instrument's operating manual. There is general agreement between our experimentally measured values

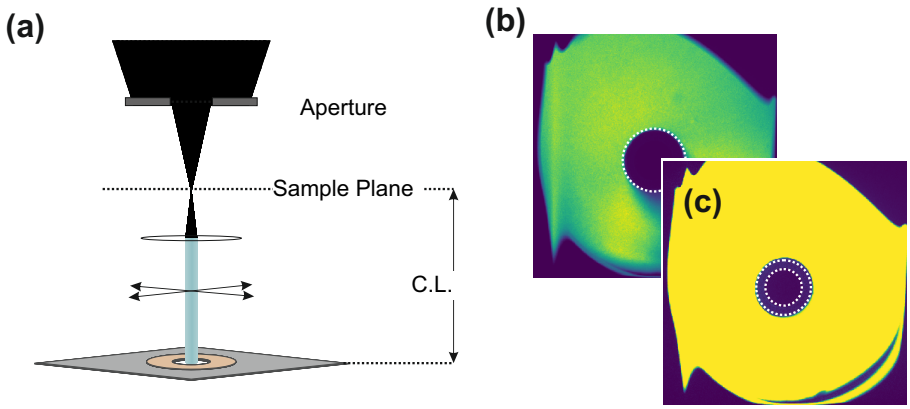


Figure B.5: (a) The pre-specimen microscope lenses are returned to their normal configuration, while the intermediary system is excited to form a pencil beam on the ADF detector. (b) an ADF detector map is produced by scanning the beam across the detector. (c) saturating this image allows us to observe the detector hole and dead layer.

Condenser Aperture	**Size (µm)**	**Nominal Semi-Convergence Angle (mrad)**	**Measured Semi-Convergence Angle (mrad)**
CAp1	200	-	65.98
CAp2	100	34.5-36.0	32.66
CAp3	40	12.0-14.5	13.20
CAp4	10	3.5-4.0	3.81

Table B.1: Nominal and measured probe semi-convergence angles for different camera lengths on the CUI F200. Nominal values are taken from the instrument's Operating Manual.

and those provided by the manufacturer. However, HAADF imaging and simulations are very sensitive to small changes in angle (particularly to β_1), necessitating α and (β_1, β_2) be measured experimentally to produce accurate results. For most camera lengths, the outer detector semi-angle was not attainable directly. However, as shown for camera lengths between 40–60 mm, and from the nominal values in the Operating Manual, the ratio of β_1:β_2 is approximately constant. We may therefore extrapolate β_2 values using this ratio with relatively little impact on quantitative results.

B.2 Probe Currents

We also measured the probe currents for all spot sizes and condenser aperture configurations using the integrated Faraday cup (located on the condenser aperture strip) and a Kiethley 6485/E picoammeter. Unlike a cold field emission gun, probe currents generated by a Schottky emitter remain stable throughout the experiment and therefore only need to be measured once. While nominal probe currents are again provided in the operating manual, they vary considerably with gun lens conditions and therefore must be measured experimentally for each instrument.

Camera Length (mm)	**Nominal (β_1, β_2) (mrad)**	**Measured (β_1, β_2) (mrad)**
1500	(4.3, 15.8)	(6.17, -)
1200	(5.6, 20.7)	(8.33, -)
1000	(6.4, 23.4)	(9.98, -)
800	(8.3, 30.4)	(12.25, -)
600	(10.9, 40.0)	(16.27, -)
500	(12.9, 47.3)	(19.36, -)
400	(16.9, 61.8)	(23.48, -)
300	(20.1, 73.6)	(32.12, -)
250	(24.4, 89.4)	(37.13, -)
200	(33.4, 122)	(46.99, -)
150	(45.0, 165)	(61.40, -)
120	(62.8,230)	(73.35, -)
100	(75.4, 276)	(84.62, -)
80	(94.2,345)	(104.24, -)
60	(125, 460)	(147.72, 580.52)
50	(150, 552)	(168.08, 675.04)
40	(188, 690)	(205.46, 764.94)
30	(250, 921)	(247.48, -)
25	(300, 1105)	(285.94, -)
20	(377, 1381)	(330.07, -)
15	(502, 1842)	(340.34, -)

Table B.2: Nominal and measured ADF detector semi-angles for different camera lengths on the CUI F200. Nominal values are taken from the instrument's Operating Manual.

Spot Size	**ClAp4 Current (nA)**	**ClAp3 Current (nA)**	**ClAp2 Current (nA)**	**ClAp1 Current (nA)**
1C	0.1753	2.1800	13.2667	52.9333
2C	0.0767	0.9093	5.4567	21.5667
3C	0.0390	0.4613	2.7433	11.2000
4C	0.01797	0.2220	1.3067	5.4333
5C	0.0103	0.1220	0.7317	3.0100
6C	0.0065	0.0777	0.4553	1.8767
7C	0.0043	0.05177	0.3053	1.2500
8C	0.0023	0.0271	0.1627	0.6560
9C	0.0018	0.0205	0.1233	0.5073
10C	0.0014	0.0167	0.0982	0.4040

Table B.3: Probe currents measured for the CUI F200.

Appendix C

C.1 EDX Data from Peripheral Nerve

The data displayed in this section are not the work of the author, and are provided for background context only. The experimental animal work and dissections were carried out by Dr Sarah Flatters, and the sample preparation, EDX data acquisition, and data processing were performed by Prof. Alice Warley and other staff at the Centre for Ultrastructural Imaging (CUI) at King's College London.

C.1.1 Sample Preparation

Samples of peripheral nerve were prepared by plunge freezing and cryosectioning. The exact conditions utilised for these experiments are unknown. As shown in Figure C.1, the preservation of intra- and extra-axonal material is very poor. In unmyelinated axons, the majority of the intra-axonal region has been lost during the sample preparation procedure.

C.1.2 EDX Data Collection

EDX data were recorded from regions in myelinated axons which retained some intra-axonal material. An example EDX spectrum is shown in Figure C.2. Data were collected using a 30mm^2 EDAX detector on the FEI Tecnai T12 microscope.

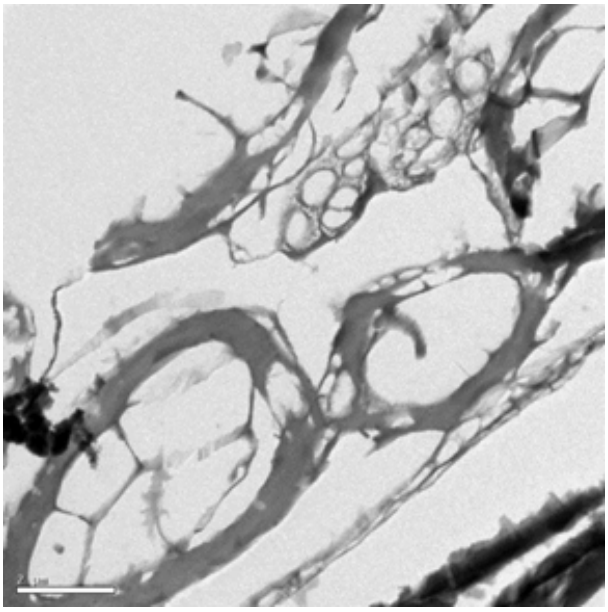


Figure C.1: Bright-field STEM image of peripheral axons from Technai T12. Tissue is poorly preserved in both myelinated and unmyelinated axons, which has considerable implications for intracellular analysis. Scale bar is 2 µm.

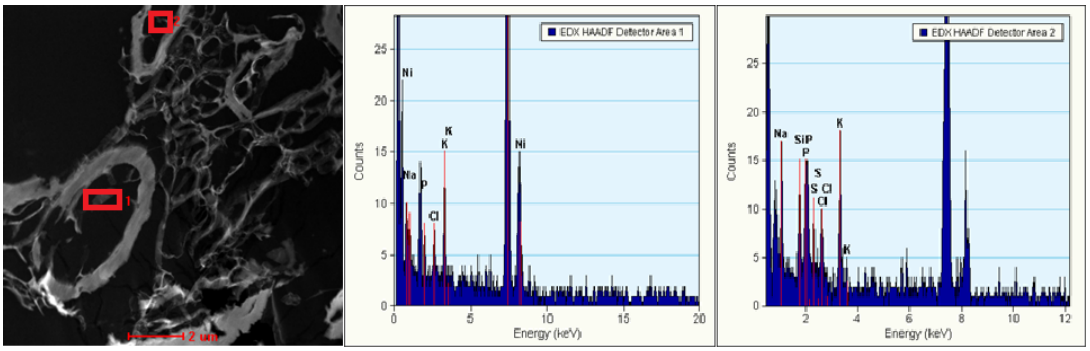


Figure C.2: Example EDX data recorded from Technai T12 with EDAX detector. Left: ADF STEM image of peripheral nerve sample. Middle: EDX data recorded from lower region indicated on (L) image. Right: EDX data recorded from upper region indicated on (L) image. Due to the poor sample preservation and the relatively small solid angle of the EDX detector, data are very noisy.

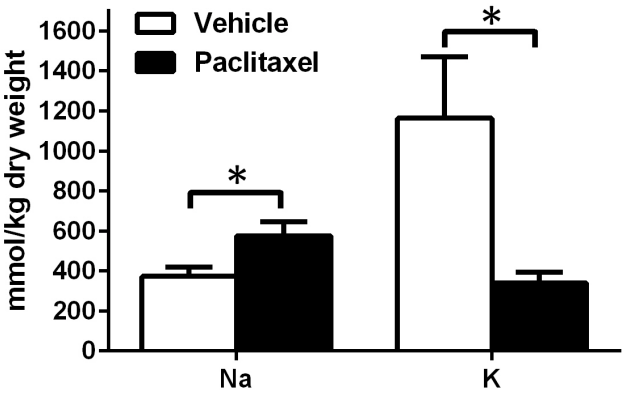


Figure C.3: Statistical analysis of Technai T12/EDAX EDX data, following quantification via the continuum-normalisation methods described in Chapter 3. Data show an increase and decrease in intra-axonal sodium and potassium respectively.

C.1.3 Statistical Analysis

Analysis of these data from vehicle and paclitaxel-treated animals showed statistically significant increases in intracellular sodium, and decreases in intracellular potassium, in the latter group (Figure C.3). The number of animals and the number of axons used to analyse these data are unknown.

Bibliography

[1] E. Ruska, "The emergence of the electron microscope: Connection between realization and first patent application, documents of an invention," *Journal of Ultrastructure and Molecular Structure Research*, vol. 95, no. 1, pp. 3–28, 1986.

[2] M. Knoll and E. Ruska, "Das Elektronenmikroskop (German) [The electron microscope]," *Zeitschrift für Physik*, vol. 78, pp. 318–339, 1932.

[3] E. Ruska, "The development of the electron microscope and electron microscopy," *Nobel Lecture*, 1986.

[4] M. Von Ardenne, "Reminiscences on the origins of the scanning electron microscope and the electron microprobe," *Advances in Imaging and Electron Physics*, vol. 96, pp. 635–652, 1996.

[5] B. V. Borries and E. Ruska, "Versuche, Rechnung und Ergebnisse zur Frage des Auflösungsvermögens beim Übermikroskops (German) [Experiments, calculations and results on the question of the resolving power of the super microscope]," *Zeitschrift für Technische Physik*, vol. 20, pp. 225–235, 1939.

[6] J. W. Menter and F. P. Bowden, "The direct study by electron microscopy of crystal lattices and their imperfections," *Proceedings of the Royal Society of London A*, vol. 236, 1956.

[7] A. V. Crewe, "A new kind of scanning microscope," *Journal de Microscopie*, vol. 2, pp. 369–371, 1963.

[8] A. V. Crewe, "Scanning electron microscopes: Is high resolution possible?" *Science*, vol. 154, no. 3750, pp. 729–738, 1966.

[9] E. W. Müller, "Resolution of the atomic structure of a metal surface by the field ion microscope," *Journal of Applied Physics*, vol. 27, no. 5, pp. 474–476, 1956.

[10] J. Hillier, "A discussion of the fundamental limit of performance of an electron microscope," *Physical Review*, vol. 60, pp. 743–745, 1941.

[11] L. I. Schiff, "Ultimate resolving power of the electron microscope," *Physical Review*, vol. 61, pp. 721–722, 1942.

[12] A. V. Crewe, D. N. Eggenberger, J. S. Wall, and L. M. Welter, "Electron gun using a field emission source," *Review of Scientific Instruments*, vol. 39, no. 4, pp. 576–583, 1968.

[13] A. V. Crewe, J. S. Wall, and L. M. Welter, "A high-resolution scanning transmission electron microscope," *Journal of Applied Physics*, vol. 39, no. 13, pp. 5861–5868, 1968.

[14] A. V. Crewe, J. S. Wall, and J. Langmore, "Visibility of single atoms," *Science*, vol. 168, no. 3937, pp. 1338–1340, 1970.

[15] S. J. Pennycook and P. D. Nellist, *Scanning Transmission Electron Microscopy: Imaging and Analysis*. Springer New York, 2011, ISBN: 9781441972002.

[16] O. Scherzer, "Über einige Fehler von Elektronenlinsen (German) [Some defects of electron lenses]," *Zeitschrift für Physik*, vol. 101, pp. 593–603, 1936.

[17] O. Scherzer, "Sphärische und chromatische Korrektur von Elektronenlinsen (German) [Spherical and chromatic correction of electron lenses]," *Optik*, vol. 2, pp. 114–132, 1936.

[18] J. Zach and M. Haider, "Aberration correction in a low voltage SEM by a multipole corrector," *Nuclear Instruments and Methods in Physics Research Section A: Accelerators, Spectrometers, Detectors and Associated Equipment*, vol. 363, no. 1-2, pp. 316–325, 1995.

[19] M. Haider, S. Uhlemann, E. Schwan, H. Rose, B. Kabius, and K. Urban, "Electron microscopy image enhanced," *Nature*, vol. 392, no. 6678, pp. 768–769, 1998.

[20] P. W. Hawkes, "The correction of electron lens aberrations," *Ultramicroscopy*, vol. 156, A1–A64, 2015.

[21] O. L. Krivanek, N. Dellby, and A. R. Lupini, "Towards sub-Å electron beams," *Ultramicroscopy*, vol. 78, no. 1, pp. 1–11, 1999.

[22] O. L. Krivanek, N. Dellby, A. J. Spence, R. A. Camps, and L. M. Brown, "Aberration correction in the STEM," *Institute of Physics Conference Series*, vol. 153, no. 2, pp. 35–40, 1997.

[23] P. E. Batson, N. Dellby, and O. L. Krivanek, "Sub-Ångstrom resolution using aberration corrected electron optics," *Nature*, vol. 418, no. 6898, pp. 617–620, 2002.

[24] P. D. Nellist, M. F. Chisholm, N. Dellby, O. L. Krivanek, M. F. Murfitt, Z. S. Szilagyi, A. R. Lupini, A. Borisevich, W. H. Sides, and S. J. Pennycook, "Direct sub-ångstrom imaging of a crystal lattice," *Science*, vol. 305, no. 5691, pp. 1741–1741, 2004.

[25] S. J. Pennycook, "The impact of STEM aberration correction on materials science," *Ultramicroscopy*, vol. 180, pp. 22–33, 2017.

[26] A. Y. Borisevich, A. R. Lupini, S. Travaglini, and S. J. Pennycook, "Depth sectioning of aligned crystals with the aberration-corrected scanning transmission electron microscope," *Journal of Electron Microscopy*, vol. 55, no. 1, pp. 7–12, 2006.

[27] D. B. Williams and C. B. Carter, *Transmission Electron Microscopy: A Textbook for Materials Science*, 2nd ed. Boston, MA: Springer US, 2009, ISBN: 978-0-387-76501-3.

[28] D. B. Williams and C. B. Carter, "Chapter 5: Electron sources," in *Transmission Electron Microscopy: A Textbook for Materials Science*. Boston, MA: Springer US, 2009, pp. 73–89, ISBN: 978-0-387-76501-3.

[29] D. B. Williams and C. B. Carter, "Chapter 6: Lenses, apertures, and resolution," in *Transmission Electron Microscopy: A Textbook for Materials Science*. Boston, MA: Springer US, 2009, pp. 91–114, ISBN: 978-0-387-76501-3.

[30] D. B. Williams and C. B. Carter, "Chapter 3: Elastic scattering," in *Transmission Electron Microscopy: A Textbook for Materials Science*. Boston, MA: Springer US, 2009, pp. 39–51, ISBN: 978-0-387-76501-3.

[31] A. Engel, "Principle of reciprocity and its application to conventional and scanning dark field electron microscopy.," *Optik*, vol. 41, pp. 117–126, 1974.

[32] D. L. Misell, G. W. Strokes, and M. Haliou, "Coherent and incoherent imaging in the scanning transmission electron microscope," *Journal of Physics D: Applied Physics*, vol. 7, no. 10, pp. L113–L117, 1974, ISSN: 0022-3727.

[33] P. D. Nellist and S. J. Pennycook, "The principles and interpretation of annular dark-field z-contrast imaging," in, ser. Advances in Imaging and Electron Physics, P. W. Hawkes, Ed., vol. 113, Elsevier, 2000, pp. 147–203.

[34] L. Fitting, S. Thiel, A. Schmehl, J. Mannhart, and D. A. Muller, "Subtleties in ADF imaging and spatially resolved EELS: A case study of low-angle twist boundaries in $SrTiO_3$," *Ultramicroscopy*, vol. 106, no. 11, pp. 1053–1061, 2006.

[35] M. U. Rothmann, J. S. Kim, J. Borchert, K. B. Lohmann, C. M. O'Leary, A. A. Sheader, L. Clark, H. J. Snaith, M. B. Johnston, P. D. Nellist, and L. M. Herz, "Atomic-scale microstructure of metal halide perovskite," *Science*, vol. 370, no. 6516(eabb5940), 2020.

[36] M. Haruta and H. Kurata, "Direct observation of crystal defects in an organic molecular crystals of copper hexachlorophthalocyanine by STEM-EELS," *Scientific Reports*, vol. 2, no. 1, pp. 1–4, 2012.

[37] M. Tanaka, K. Higashida, K. Kaneko, S. Hata, and M. Mitsuhara, "Crack tip dislocations revealed by electron tomography in silicon single crystal," *Scripta Materialia*, vol. 59, no. 8, pp. 901–904, 2008.

[38] J. S. Barnard, A. S. Eggeman, J. Sharp, T. A. White, and P. A. Midgley, "Dislocation electron tomography and precession electron diffraction – minimising the effects of dynamical interactions in real and reciprocal space," *Philosophical Magazine*, vol. 90, no. 35-36, pp. 4711–4730, 2010.

[39] P. Hartel, H. Rose, and C. Dinges, "Conditions and reasons for incoherent imaging in STEM," *Ultramicroscopy*, vol. 63, no. 2, pp. 93–114, 1996, ISSN: 0304-3991.

[40] R. M. Henkelman and F. P. Ottensmyer, "Visualization of single heavy atoms by dark field electron microscopy," *Proceedings of the National Academy of Sciences of the United States of America*, vol. 68, no. 12, pp. 3000–3004, 1971.

[41] M. S. Isaacson, "Seeing single atoms," *Ultramicroscopy*, vol. 123, pp. 3–12, 2012.

[42] J. M. Cowley and A. F. Moodie, "The scattering of electrons by atoms and crystals. I. A new theoretical approach," *Acta Crystallographica*, vol. 10, no. 10, pp. 609–619, 1957.

[43] J. G. Allpress, E. A. Hewat, A. F. Moodie, and J. V. Sanders, "N-beam lattice images. I. Experimental and computed images from $W_4Nb_{26}O_{77}$," *Acta Crystallographica Section A*, vol. 28, no. 6, pp. 528–536, 1972.

[44] D. F. Lynch and M. O'Keefe, "N-beam lattice images. II. Methods of calculation," *Acta Crystallographica Section A*, vol. 28, pp. 536–548, 1972.

[45] E. J. Kirkland, R. F. Loane, and J. Silcox, "Simulation of annular dark field stem images using a modified multislice method," *Ultramicroscopy*, vol. 23, no. 1, pp. 77–96, 1987.

[46] S. Pennycook and D. Jesson, "High-resolution Z-contrast imaging of crystals," *Ultramicroscopy*, vol. 37, no. 1, pp. 14–38, 1991.

[47] K. Ishizuka, "A practical approach for STEM image simulation based on the FFT multislice method," *Ultramicroscopy*, vol. 90, no. 2, pp. 71–83, 2002.

[48] Z. L. Wang, "The 'frozen-lattice' approach for incoherent phonon excitation in electron scattering. How accurate is it?" *Acta Crystallographica Section A*, vol. 54, no. 4, pp. 460–467, 1998.

[49] D. Van Dyck, "Is the frozen phonon model adequate to describe inelastic phonon scattering?" *Ultramicroscopy*, vol. 109, no. 6, pp. 677–682, 2009.

[50] C. T. Koch, "Determination of core structure periodicity and point defect density along dislocations," Ph.D. dissertation, Arizona State University, Jan. 2002.

[51] J. Barthel, "Dr. Probe: A software for high-resolution STEM image simulation," *Ultramicroscopy*, vol. 193, pp. 1–11, 2018.

[52] I. Lobato and D. Van Dyck, "MULTEM: A new multislice program to perform accurate and fast electron diffraction and imaging simulations using graphics processing units with CUDA," *Ultramicroscopy*, vol. 156, pp. 9–17, 2015.

[53] E. J. Kirkland, *Advanced Computing in Electron Microscopy*, 2nd ed. Springer, 2010, ISBN: 978-1-4419-6533-2.

[54] P. D. Nellist, "The principles of STEM imaging," in *Scanning Transmission Electron Microscopy: Imaging and Analysis*, S. J. Pennycook and P. D. Nellist, Eds., New York, NY: Springer New York, 2011, pp. 91–115, ISBN: 9781441972002.

[55] Y. Kotaka, "Direct visualization method of the atomic structure of light and heavy atoms with double-detector C_s-corrected scanning transmission electron microscopy," *Applied Physics Letters*, vol. 101, no. 13, p. 133 107, 2012.

[56] R. Ishikawa, E. Okunishi, H. Sawada, Y. Kondo, F. Hosokawa, and E. Abe, "Direct imaging of hydrogen-atom columns in a crystal by annular bright-field electron microscopy," *Nature Materials*, vol. 10, no. 4, pp. 278–281, 2011.

[57] S. D. Findlay, N. R. Lugg, N. Shibata, L. J. Allen, and Y. Ikuhara, "Prospects for lithium imaging using annular bright field scanning transmission electron microscopy: A theoretical study," *Ultramicroscopy*, vol. 111, no. 8, pp. 1144–1154, 2011.

[58] E. J. Kirkland and M. G. Thomas, "A high efficiency annular dark field detector for STEM," *Ultramicroscopy*, vol. 62, no. 1, pp. 79–88, 1996.

[59] I. MacLaren, T. A. Macgregor, C. S. Allen, and A. I. Kirkland, "Detectors—the ongoing revolution in scanning transmission electron microscopy and why this important to material characterization," *APL Materials*, vol. 8, no. 11, p. 110 901, 2020.

[60] H. Yang, R. Rutte, L. Jones, M. Simson, R. Sagawa, H. Ryll, M. Huth, T. Pennycook, M. Green, H. Soltau, *et al.*, "Simultaneous atomic-resolution electron ptychography and Z-contrast imaging of light and heavy elements in complex nanostructures," *Nature Communications*, vol. 7, no. 1, pp. 1–8, 2016.

[61] J. Song, C. S. Allen, S. Gao, C. Huang, H. Sawada, X. Pan, J. Warner, P. Wang, and A. I. Kirkland, "Atomic resolution defocused electron ptychography at low dose with a fast, direct electron detector," *Scientific Reports*, vol. 9, no. 1, pp. 1–8, 2019.

[62] H. G. J. Moseley, "XCIII. The high-frequency spectra of the elements," *The London, Edinburgh, and Dublin Philosophical Magazine and Journal of Science*, vol. 26, no. 156, pp. 1024–1034, 1913.

[63] H. G. J. Moseley, "LXXX. The high-frequency spectra of the elements. Part II," *The London, Edinburgh, and Dublin Philosophical Magazine and Journal of Science*, vol. 27, no. 160, pp. 703–713, 1914.

[64] J. Hillier and R. F. Baker, "Microanalysis by means of electrons," *Journal of Applied Physics*, vol. 15, no. 9, pp. 663–675, 1944.

[65] R. Castaing, "Application of electron probes to local chemical and crystallographic analysis," Ph.D. dissertation, University of Paris, Jul. 1955.

[66] V. E. Cosslett and P. Duncumb, "Micro-analysis by a flying-spot x-ray method," *Nature*, vol. 177, no. 4521, pp. 1172–1173, 1956.

[67] P. Duncumb and V. E. Cosslett, "A scanning microscope for x-ray emission pictures," *X-ray Microscopy and Microradiography*, pp. 374–380, 1957.

[68] S. J. B. Reed, "Wavelength dispersive spectrometry: A review," in *X-Ray Spectrometry in Electron Beam Instruments*, D. B. Williams, J. I. Goldstein, and D. E. Newbury, Eds. Boston, MA: Springer US, 1995, pp. 221–238, ISBN: 978-1-4615-1825-9.

[69] H. R. Bowman, E. K. Hyde, S. G. Thompson, and R. C. Jared, "Application of high-resolution semiconductor detectors in x-ray emission spectrography," *Science*, vol. 151, no. 3710, pp. 562–568, 1966.

[70] R. Fitzgerald, K. Keil, and K. F. J. Heinrich, "Solid-state energy-dispersion spectrometer for electron-microprobe x-ray analysis," *Science*, vol. 159, no. 3814, pp. 528–530, 1968.

[71] "New instrument combines electron microscopy and x-ray microanalysis," *Electronics & Power*, vol. 16, 102–102(0), 3 1970, retrieved 21.01.2021. [Online]. Available: `https://digital-library.theiet.org/content/journals/10.1049/ep.1970.0109`.

[72] A. J. D'Alfonso, B. Freitag, D. Klenov, and L. J. Allen, "Atomic-resolution chemical mapping using energy-dispersive x-ray spectroscopy," *Physical Review B*, vol. 81, p. 100 101, 10 2010.

[73] G. Kothleitner, M. J. Neish, N. R. Lugg, S. D. Findlay, W. Grogger, F. Hofer, and L. J. Allen, "Quantitative elemental mapping at atomic resolution using x-ray spectroscopy," *Physical Review Letters*, vol. 112, p. 085 501, 8 2014.

[74] T. C. Lovejoy, Q. M. Ramasse, M. Falke, A. Kaeppel, R. Terborg, R. Zan, N. Dellby, and O. L. Krivanek, "Single atom identification by energy dispersive x-ray spectroscopy," *Applied Physics Letters*, vol. 100, no. 15, p. 154 101, 2012.

[75] D. C. Bell and A. J. Garratt-Reed, "Chapter 3: The energy-dispersive x-ray detector," in *Energy Dispersive X-ray Analysis in the Electron Microscope*, ser. Microscopy Handbooks. Taylor & Francis, 2003, pp. 19–45, ISBN: 9780203483428.

[76] P. Hovington, V. Timoshevskii, S. Burgess, H. Demers, P. Statham, R. Gauvin, and K. Zaghib, "Can we detect Li K x-ray in lithium compounds using energy dispersive spectroscopy?" *Scanning*, vol. 38, no. 6, pp. 571–578, 2016.

[77] D. B. Williams and C. B. Carter, "Chapter 32: X-ray spectrometry," in *Transmission Electron Microscopy: A Textbook for Materials Science*. Boston, MA: Springer US, 2009, pp. 581–603, ISBN: 978-0-387-76501-3.

[78] D. Bell and A. Garratt-Reed, "Chapter 6: X-ray microanalysis in the transmission electron microscope," in *Energy Dispersive X-ray Analysis in the Electron Microscope*, ser. Microscopy Handbooks. Taylor & Francis, 2003, pp. 88–116, ISBN: 9780203483428.

[79] R. Brydson and N. Hondow, "Chapter 7: Electron energy loss spectrometry and energy dispersive x-ray analysis," in *Aberration-Corrected Analytical Transmission Electron Microscopy*, R. Brydson, Ed. John Wiley & Sons, Ltd, 2011, pp. 163–210, ISBN: 9781119978848.

[80] N. W. M. Richie, *NIST Github Openmicroanalysis/EPQ*, retrieved 21.02.2021, 2019. [Online]. Available: `https://github.com/openmicroanalysis/EPQ/blob/master/src/gov/nist/microanalysis/EPQLibrary/`.

[81] G. Cliff and G. W. Lorimer, "The quantitative analysis of thin specimens," *Journal of Microscopy*, vol. 103, no. 2, pp. 203–207, 1975.

[82] J. I. Goldstein, "Chapter 3: Principles of thin film x-ray microanalysis," in *Introduction to Analytical Electron Microscopy*, J. J. Hren, J. I. Goldstein, and D. C. Joy, Eds. Boston, MA: Springer US, 1979, pp. 83–120, ISBN: 978-1-4757-5581-7.

[83] N. J. Zaluzec, "Chapter 4: Quantitative x-ray microanalysis: Instrumental considerations and applications to materials science," in *Introduction to Analytical Electron Microscopy*, J. Hren, J. Goldstein, and D. Joy, Eds., Springer, 1979, pp. 129–168, ISBN: 978-1-4757-5581-7.

[84] Z. Horita, T. Sano, and M. Nemoto, "An extrapolation method for the determination of Cliff-Lorimer $k_{A,B}$ factors at zero foil thickness," *Journal of Microscopy*, vol. 143, no. 3, pp. 215–231, 1986.

[85] N. J. Zaluzec, "An analytical electron microscope study of the omega phase transformation in a zirconium-niobium alloy," Ph.D. dissertation, University of Illinois at Urbana-Champaign, 1979.

[86] P. Doig and P. E. J. Flewitt, "Limitations in the x-ray microanalysis of thin foils in a scanning transmission electron microscope," *Journal of Microscopy*, vol. 110, no. 2, pp. 107–112, 1977.

[87] E. Metcalfe and J. Broomfield, "Determination of Cliff-Lorimer k-factors for a Hitachi H700h 200kV scanning transmission electron microscope," *Le Journal de Physique Colloques*, vol. 45, no. C2, pp. C2–407, 1984.

[88] M. Watanabe and D. B. Williams, "The quantitative analysis of thin specimens: A review of progress from the Cliff-Lorimer to the new ζ-factor methods," *Journal of Microscopy*, vol. 221, no. 2, pp. 89–109, 2006.

[89] D. M. Longo, J. M. Howe, and W. C. Johnson, "Experimental method for determining Cliff–Lorimer factors in transmission electron microscopy (TEM) utilizing stepped wedge-shaped specimens prepared by focused ion beam (FIB) thinning," *Ultramicroscopy*, vol. 80, no. 2, pp. 85–97, 1999.

[90] D. Zanaga, T. Altantzis, J. Sanctorum, B. Freitag, and S. Bals, "An alternative approach for ζ-factor measurement using pure element nanoparticles," *Ultramicroscopy*, vol. 164, pp. 11–16, 2016.

[91] M. Watanabe, "Chapter 7: X-ray energy-dispersive spectrometry in scanning transmission electron microscopes," in *Scanning Transmission Electron Microscopy: Imaging and Analysis*, S. J. Pennycook and P. D. Nellist, Eds. New York, NY: Springer New York, 2011, pp. 291–351, ISBN: 9781441972002.

[92] V. Srot, M. Watanabe, C. Scheu, P. van Aken, U. Salzberger, B. Luerßen, J. Janek, and M. Rühle, "Characterization of chemical composition and electronic structure of Pt/YSZ interfaces by analytical transmission electron microscopy," *Solid State Ionics*, vol. 181, no. 35, pp. 1616–1622, 2010.

[93] Q. Yang, C. Hwang, C. J. Marvel, A. Chauhan, V. Domnich, A. U. Khan, J. C. LaSalvia, M. P. Harmer, K. J. Hemker, and R. A. Haber, "Fabrication and characterization of arc melted Si/B co-doped boron carbide," *Journal Of The European Ceramic Society*, vol. 39, no. 16, pp. 5156–5166, 2019.

[94] R. F. Egerton, "Chapter 1: An introduction to EELS," in *Electron Energy-Loss Spectroscopy in the Electron Microscope*. Boston, MA: Springer US, 2011, pp. 1–28, ISBN: 978-1-4419-9583-4.

[95] R. Brydson, "Chapter 2: The EEL spectrum," in *Microscopy Handbooks 48: Electron Energy Loss Spectroscopy*, R. Brydson, Ed. Taylor & Francis, 2001, pp. 27–38, ISBN: 1 85996 134 7.

[96] O. L. Krivanek, C. C. Ahn, and R. B. Keeney, "Parallel detection electron spectrometer using quadrupole lenses," *Ultramicroscopy*, vol. 22, no. 1, pp. 103–115, 1987.

[97] C. Colliex and P. Trebbia, "Performance and applications of electron energy loss spectroscopy in stem," *Ultramicroscopy*, vol. 9, no. 3, pp. 259–266, 1982.

[98] C. Jeanguillaume and C. Colliex, "Spectrum-image: The next step in EELS digital acquisition and processing," *Ultramicroscopy*, vol. 28, no. 1, pp. 252–257, 1989.

[99] J. A. Hunt and D. B. Williams, "Electron energy-loss spectrum-imaging," *Ultramicroscopy*, vol. 38, no. 1, pp. 47–73, 1991.

[100] R. F. Klie, I. Arslan, and N. D. Browning, "Atomic resolution electron energy-loss spectroscopy," *Journal of Electron Spectroscopy and Related Phenomena*, vol. 143, no. 2, pp. 105–115, 2005.

[101] K. Suenaga, M. Tencé, C. Mory, C. Colliex, H. Kato, T. Okazaki, H. Shinohara, K. Hirahara, S. Bandow, and S. Iijima, "Element-selective single atom imaging," *Science*, vol. 290, no. 5500, pp. 2280–2282, 2000.

[102] P. E. Batson, "Simultaneous STEM imaging and electron energy-loss spectroscopy with atomic-column sensitivity," *Nature*, vol. 366, no. 6457, pp. 727–728, 1993.

[103] J. Nelayah, M. Kociak, O. Stéphan, F. J. G. de Abajo, M. Tencé, L. Henrard, D. Taverna, I. Pastoriza-Santos, L. M. Liz-Marzán, and C. Colliex, "Mapping surface plasmons on a single metallic nanoparticle," *Nature Physics*, vol. 3, no. 5, pp. 348–353, 2007.

[104] O. L. Krivanek, N. Dellby, J. A. Hachtel, J.-C. Idrobo, M. Hotz, B. Plotkin-Swing, N. J. Bacon, A. L. Bleloch, G. J. Corbin, M. V. Hoffman, *et al.*, "Progress in ultrahigh energy resolution EELS," *Ultramicroscopy*, vol. 203, pp. 60–67, 2019.

[105] O. L. Krivanek, S. L. Friedman, A. J. Gubbens, and B. Kraus, "An imaging filter for biological applications," *Ultramicroscopy*, vol. 59, no. 1-4, pp. 267–282, 1995.

[106] R. F. Egerton, "Chapter 2: Energy-loss instrumentation," in *Electron Energy-Loss Spectroscopy in the Electron Microscope*. Boston, MA: Springer US, 2011, pp. 29–109, ISBN: 978-1-4419-9583-4.

[107] J. L. Hart, A. C. Lang, A. C. Leff, P. Longo, C. Trevor, R. D. Twesten, and M. L. Taheri, "Direct detection electron energy-loss spectroscopy: A method to push the limits of resolution and sensitivity," *Scientific Reports*, vol. 7, no. 1, pp. 1–14, 2017.

[108] Gatan, *EELS Atlas: Titanium*, retrieved 30.01.2021, 2015. [Online]. Available: `https://eels.info/atlas/titanium`.

[109] J. A. Hachtel, A. R. Lupini, and J. C. Idrobo, "Exploring the capabilities of monochromated electron energy loss spectroscopy in the infrared regime," *Scientific Reports*, vol. 8, no. 1, pp. 1–10, 2018.

[110] D. B. Williams and C. B. Carter, "Chapter 38: Low-loss and no-loss spectra and images," in *Transmission Electron Microscopy: A Textbook for Materials Science*. Boston, MA: Springer US, 2009, pp. 699–713, ISBN: 978-0-387-76501-3.

[111] N. L. McDougall, R. J. Nicholls, J. G. Partridge, and D. G. McCulloch, "The near edge structure of hexagonal boron nitride," *Microscopy and Microanalysis*, vol. 20, no. 4, p. 1053, 2014.

[112] R. F. Egerton, *Electron Energy-Loss Spectroscopy in the Electron Microscope*. Boston, MA: Springer US, 2011, ISBN: 978-1-4419-9583-4.

[113] R. F. Egerton, "Chapter 5: TEM applications of EELS," in *Electron Energy-Loss Spectroscopy in the Electron Microscope*. Boston, MA: Springer US, 2011, pp. 293–397, ISBN: 978-1-4419-9583-4.

[114] D. B. Williams and C. B. Carter, "Chapter 39: High energy-loss spectra and images," in *Transmission Electron Microscopy: A Textbook for Materials Science*. Boston, MA: Springer US, 2009, pp. 715–739, ISBN: 978-0-387-76501-3.

[115] R. F. Egerton, "Chapter 4: Quantitative analysis of energy-loss data," in *Electron Energy-Loss Spectroscopy in the Electron Microscope*. Boston, MA: Springer US, 2011, pp. 231–291, ISBN: 978-1-4419-9583-4.

[116] F. de la Peña et al., *Hyperspy: Release v1.6.1*, version v1.6.1, 2020. [Online]. Available: `https://hyperspy.org/`.

[117] R. Brydson, "Chapter 4: The EEL spectrum," in *Microscopy Handbooks 48: Electron Energy Loss Spectroscopy*, R. Brydson, Ed. Taylor & Francis, 2001, ch. 4, pp. 59–68, ISBN: 1 85996 134 7.

[118] X. Weng and P. Rez, "Solid state effects on core electron cross-sections used in microanalysis," *Ultramicroscopy*, vol. 25, no. 4, pp. 345–348, 1988.

[119] G. Bertoni and J. Verbeeck, "Accuracy and precision in model based EELS quantification," *Ultramicroscopy*, vol. 108, no. 8, pp. 782–790, 2008.

[120] R. Leapman, "Chapter 3: Eels quantitative analysis," in *Transmission Electron Energy Loss Spectrometry in Materials Science and The EELS Atlas*, C. C. Ahn, Ed. John Wiley & Sons, Ltd, 2004, pp. 49–96, ISBN: 9783527605491.

[121] T. O. Ziebold, "Precision and sensitivity in electron microprobe analysis," *Analytical Chemistry*, vol. 39, no. 8, pp. 858–861, 1967.

[122] D. B. Williams and C. B. Carter, "Chapter 36: Spatial resolution and minimum detection," in *Transmission Electron Microscopy: A Textbook for Materials Science*. Boston, MA: Springer US, 2009, pp. 663–677, ISBN: 978-0-387-76501-3.

[123] H. Shuman and A. P. Somlyo, "Electron probe x-ray analysis of single ferritin molecules," *Proceedings of the National Academy of Sciences*, vol. 73, no. 4, pp. 1193–1195, 1976.

[124] M. Watanabe, D. W. Ackland, A. Burrows, C. J. Kiely, D. B. Williams, O. L. Krivanek, N. Dellby, M. F. Murfitt, and Z. Szilagyi, "Improvements in the x-ray analytical capabilities of a scanning transmission electron microscope by spherical-aberration correction," *Microscopy and Microanalysis*, vol. 12, no. 6, pp. 515–526, 2006.

[125] N. J. Zaluzec, "Improving the sensitivity of x-ray microanalysis in the analytical electron microscope," *Ultramicroscopy*, vol. 203, pp. 163–169, 2019.

[126] A. Maigne, "How to optimize your EELS experiments by adjusting the collection angle of your spectrometer," *Gatan*, 2007, retrieved 04.04.2021. [Online]. Available: `https://analyticalscience.wiley.com/do/10.1002/micro.140/full/`.

[127] M. Isaacson and D. Johnson, "The microanalysis of light elements using transmitted energy loss electrons," *Ultramicroscopy*, vol. 1, no. 1, pp. 33–52, 1975.

[128] O. L. Krivanek, C. Mory, M. Tence, and C. Colliex, "EELS quantification near the single-atom detection level," *Microscopy, Microanalysis and Microstructure*, vol. 2, no. 2-3, pp. 257–267, 1991.

[129] R. D. Leapman and D. E. Newbury, "Trace elemental analysis at nanometer spatial resolution by parallel-detection electron energy loss spectroscopy," *Analytical Chemistry*, vol. 65, no. 18, pp. 2409–2414, 1993.

[130] R. D. Leapman and J. A. Hunt, "Comparison of detection limits for EELS and EDXS," *Microscopy, Microanalysis and Microstructure*, vol. 2, no. 2-3, pp. 231–244, 1991.

[131] E. Hanssen, M. P. Watts, E. R. Smith, P. Gosavi, P. A. Gleeson, and J. W. Moreau, "The best of both world, how a 'Christmas tree' TEM can please biologist and material scientists," *Microscopy and Microanalysis*, vol. 21, no. S3, pp. 913–914, 2015.

[132] G. Palade, "Intracellular aspects of the process of protein synthesis," *Science*, vol. 189, no. 4200, pp. 347–358, 1975.

[133] G. E. Palade, "A small particulate component of the cytoplasm," *The Journal of Cell Biology*, vol. 1, no. 1, pp. 59–68, 1955.

[134] K. R. Porter, A. Claude, and E. F. Fullam, "A study of tissue culture cells by electron microscopy: Methods and preliminary observations," *The Journal of Experimental Medicine*, vol. 81, no. 3, p. 233, 1945.

[135] J. J. Wolosewick and K. R. Porter, "Microtrabecular lattice of the cytoplasmic ground substance. Artifact or reality.," *Journal of Cell Biology*, vol. 82, no. 1, pp. 114–139, 1979.

[136] G. E. Palade, "The fine structure of mitochondria," *The Anatomical Record*, vol. 114, no. 3, pp. 427–451, 1952.

[137] F. S. Sjöstrand, "The ultrastructure of cells as revealed by the electron microscope," in, ser. International Review of Cytology, G. Bourne and J. Danielli, Eds., vol. 5, Academic Press, 1956, pp. 455–533.

[138] D. Wrapp, N. Wang, K. S. Corbett, J. A. Goldsmith, C.-L. Hsieh, O. Abiona, B. S. Graham, and J. S. McLellan, "Cryo-EM structure of the 2019-nCoV spike in the prefusion conformation," *Science*, vol. 367, no. 6483, pp. 1260–1263, 2020.

[139] A. V. Crewe and J. S. Wall, "A scanning microscope with 5Å resolution," *Journal of Molecular Biology*, vol. 48, no. 3, pp. 375–393, 1970.

[140] A. V. Crewe, H. E. Huxley, and A. Klug, "High resolution scanning microscopy of biological specimens," *Philosophical Transactions of the Royal Society of London. B, Biological Sciences*, vol. 261, no. 837, pp. 61–70, 1971.

[141] A. V. Crewe and O. H. Kapp, *Electron Microscope Studies - Progress Report [DOE ER60437-7] for Period 1st July 1964 to 1st June 1992, Prepared for the U.S. Dept. of Energy*, 1992.

[142] E. Zeitler and G. F. Bahr, "A photometric procedure for weight determination of submicroscopic particles quantitative electron microscopy," *Journal of Applied Physics*, vol. 33, no. 3, pp. 847–853, 1962.

[143] M. K. Lamvik, "Muscle thick filament mass measured by electron scattering," *Journal of Molecular Biology*, vol. 122, no. 1, pp. 55–68, 1978.

[144] A. Klug and D. L. D. Caspar, "The structure of small viruses," in, ser. Advances in Virus Research, K. M. Smith and M. A. Lauffer, Eds., vol. 7, Academic Press, 1961, pp. 225–325.

[145] A. Engel, J. Dubochet, and E. Kellenberger, "Some progress in the use of a scanning transmission electron microscope for the observation of biomacromolecules," *Journal of Ultrastructure Research*, vol. 57, no. 3, pp. 322–330, 1976.

[146] A. Engel, "Molecular weight determination by scanning transmission electron microscopy," *Ultramicroscopy*, vol. 3, pp. 273–281, 1978.

[147] R. Freeman and K. R. Leonard, "Comparative mass measurement of biological macromolecules by scanning transmission electron microscopy," *Journal of Microscopy*, vol. 122, no. 3, pp. 275–286, 1981.

[148] J. S. Wall and J. F. Hainfeld, "Mass mapping with the scanning transmission electron microscope," *Annual Review of Biophysics and Biophysical Chemistry*, vol. 15, no. 1, pp. 355–376, 1986.

[149] D. Thomas, P. Schultz, A. C. Steven, and J. S. Wall, "Mass analysis of biological macromolecular complexes by STEM," *Biology of the Cell*, vol. 80, no. 2, pp. 181–192, 1994.

[150] S. A. Müller and A. Engel, "Mass measurement in the scanning transmission electron microscope: A powerful tool for studying membrane proteins," *Journal of Structural Biology*, vol. 121, no. 2, pp. 219–230, 1998.

[151] F. Chiti and C. M. Dobson, "Protein misfolding, amyloid formation, and human disease: A summary of progress over the last decade," *Annual Review of Biochemistry*, vol. 86, no. 1, pp. 27–68, 2017.

[152] C. S. Goldsbury, G. J. Cooper, K. N. Goldie, S. A. Müller, E. L. Saafi, W. Gruijters, M. P. Misur, A. Engel, U. Aebi, and J. Kistler, "Polymorphic fibrillar assembly of human amylin," *Journal of Structural Biology*, vol. 119, no. 1, pp. 17–27, 1997.

[153] R. A. Crowther, "Straight and paired helical filaments in Alzheimer disease have a common structural unit," *Proceedings of the National Academy of Sciences*, vol. 88, no. 6, pp. 2288–2292, 1991.

[154] C. Goldsbury, U. Baxa, M. N. Simon, A. C. Steven, A. Engel, J. S. Wall, U. Aebi, and S. A. Müller, "Amyloid structure and assembly: Insights from scanning transmission electron microscopy," *Journal of Structural Biology*, vol. 173, no. 1, pp. 1–13, 2011.

[155] B. Alberts, A. Johnson, J. Lewis, M. Raff, K. Roberts, and P. Walter, "Chapter 6: How cells read the genome: From DNA to protein," in *Molecular Biology of the Cell*, B. Alberts, A. Johnson, J. Lewis, M. Raff, K. Roberts, and P. Walter, Eds., 5th ed. Taylor & Francis, 2008, pp. 329–410, ISBN: 978 0 8153 4105 5.

[156] T. Hohn, B. Hohn, A. Engel, M. Wurtz, and P. R. Smith, "Isolation and characterization of the host protein groE involved in bacteriophage lambda assembly," *Journal of Molecular Biology*, vol. 129, no. 3, pp. 359–373, 1979.

[157] S. Chen, A. M. Roseman, A. S. Hunter, S. P. Wood, S. G. Burston, N. A. Ranson, A. R. Clarke, and H. R. Saibil, "Location of a folding protein and shape changes in GroEL–GroES complexes imaged by cryo-electron microscopy," *Nature*, vol. 371, no. 6494, pp. 261–264, 1994.

[158] A. Azem, M. Kessel, and P. Goloubinoff, "Characterization of a functional $GroEL_{14}(GroES_7)_2$ chaperonin hetero-oligomer," *Science*, vol. 265, no. 5172, pp. 653–656, 1994.

[159] A. Engel, M. K. Hayer-Hartl, K. N. Goldie, G. Pfeifer, R. Hegerl, S. A. Muller, A. C. da Silva, W. Baumeister, and F. U. Hartl, "Functional significance of symmetrical versus asymmetrical GroEL-GroES chaperonin complexes," *Science*, vol. 269, no. 5225, pp. 832–836, 1995.

[160] M. Hayer-Hartl, A. Bracher, and F. U. Hartl, "The GroEL–GroES chaperonin machine: A nano-cage for protein folding," *Trends in Biochemical Sciences*, vol. 41, no. 1, pp. 62–76, 2016.

[161] A. A. Sousa and R. D. Leapman, "Quantitative STEM mass measurement of biological macromolecules in a 300kV TEM," *Journal of Microscopy*, vol. 228, no. 1, pp. 25–33, 2007.

[162] J. S. Wall and M. N. Simon, "Chapter 41: Scanning transmission electron microscopy of DNA-protein complexes," in *DNA-Protein Interactions: Principles and Protocols*, T. Moss, Ed. New York, NY: Springer New York, 2001, pp. 589–601, ISBN: 1592592082.

[163] B. Chen, K. R. Thurber, F. Shewmaker, R. B. Wickner, and R. Tycko, "Measurement of amyloid fibril mass-per-length by tilted-beam transmission electron microscopy," *Proceedings of the National Academy of Sciences*, vol. 106, no. 34, pp. 14 339–14 344, 2009.

[164] R. F. Egerton, "Radiation damage to organic and inorganic specimens in the TEM," *Micron*, vol. 119, pp. 72–87, 2019.

[165] S. A. Müller, K. N. Goldie, R. Bürki, R. Häring, and A. Engel, "Factors influencing the precision of quantitative scanning transmission electron microscopy," *Ultramicroscopy*, vol. 46, no. 1, pp. 317–334, 1992.

[166] S. A. Müller and A. Engel, "Structure and mass analysis by scanning transmission electron microscopy," *Micron*, vol. 32, no. 1, pp. 21–31, 2001.

[167] B. Blechschmidt, W. Jahn, J. F. Hainfeld, M. Sprinzl, and M. Boublik, "Visualization of a ternary complex of the Escherichia coli Phe-tRNA(Phe) and Tu.GTP from Thermus thermophilus by scanning transmission electron microscopy," *Journal of Structural Biology*, vol. 110, no. 1, pp. 84–89, 1993.

[168] X. Chen, L. Vinade, R. D. Leapman, J. D. Petersen, T. Nakagawa, T. M. Phillips, M. Sheng, and T. S. Reese, "Mass of the postsynaptic density and enumeration of three key molecules," *Proceedings of the National Academy of Sciences*, vol. 102, no. 32, pp. 11 551–11 556, 2005.

[169] L. Konermann, S. Vahidi, and M. A. Sowole, "Mass spectrometry methods for studying structure and dynamics of biological macromolecules," *Analytical Chemistry*, vol. 86, no. 1, pp. 213–232, 2014.

[170] J. S. Wall, M. N. Simon, B. Y. Lin, and S. N. Vinogradov, "Mass mapping of large globin complexes by scanning transmission electron microscopy," *Methods in Enzymology*, vol. 436, pp. 487–501, 2008.

[171] A. Engel, "Chapter 9: Scanning transmission electron microscopy: Biological applications," in, ser. Advances in Imaging and Electron Physics, vol. 159, Elsevier, 2009, pp. 357–386.

[172] A. A. Sousa and R. D. Leapman, "Mass mapping of amyloid fibrils in the electron microscope using STEM imaging," in *Nanoimaging: Methods and Protocols*, A. A. Sousa and M. J. Kruhlak, Eds., Springer, 2013, pp. 195–207.

[173] C. Martinez-Torres, F. Burla, C. Alkemade, and G. H. Koenderink, "Revealing the assembly of filamentous proteins with scanning transmission electron microscopy," *PLOS ONE*, vol. 14, no. 12, pp. 1–16, Dec. 2019.

[174] S. Curry, "Structural biology: A century-long journey into an unseen world," *Interdisciplinary Science Reviews*, vol. 40, no. 3, pp. 308–328, 2015.

[175] B. Alberts, A. Johnson, J. Lewis, M. Raff, K. Roberts, and P. Walter, "Chapter 4: DNA, chromosomes, and genomes," in *Molecular Biology of the Cell*, B. Alberts, A. Johnson, J. Lewis, M. Raff, K. Roberts, and P. Walter, Eds., 5th ed. Taylor & Francis, 2008, pp. 195–262, ISBN: 978 0 8153 4105 5.

[176] D. E. Comings, "Chapter 5: The structure and function of chromatin," in *Advances in Human Genetics*, H. Harris, Ed. Springer, 1972, pp. 237–431, ISBN: 978-1-4757-4431-6.

[177] J. P. Langmore and J. C. Wooley, "Chromatin architecture: Investigation of a subunit of chromatin by dark field electron microscopy," *Proceedings of the National Academy of Sciences*, vol. 72, no. 7, pp. 2691–2695, 1975.

[178] G. Felsenfeld, "Chromatin," *Nature*, vol. 271, no. 5641, pp. 115–122, 1978.

[179] A. Liljas, L. Liljas, M.-R. Ash, G. Lindblom, P. Nissen, and M. Kjeldgaard, "Chapter 2: The folding, folds and functions of proteins," in *Textbook of Structural Biology*, A. Liljas, L. Liljas, M.-R. Ash, G. Lindblom, P. Nissen, and M. Kjeldgaard, Eds., 2nd ed. World Scientific Publishing Co. Pte. Ltd, 2017, pp. 37–68, ISBN: 9813142464.

[180] P. M. Harrison, F. A. Fischbach, T. G. Hoy, and G. H. Haggis, "Ferric oxyhydroxide core of ferritin," *Nature*, vol. 216, no. 5121, pp. 1188–1190, 1967.

[181] W. H. Massover and J. M. Cowley, "The ultrastructure of ferritin macromolecules. the lattice structure of the core crystallites," *Proceedings of the National Academy of Sciences*, vol. 70, no. 12, pp. 3847–3851, 1973.

[182] M. Ohtsuki, M. S. Isaacson, and A. V. Crewe, "Dark field imaging of biological macromolecules with the scanning transmission electron microscope," *Proceedings of the National Academy of Sciences*, vol. 76, no. 3, pp. 1228–1232, 1979.

[183] K. M. Yip, N. Fischer, E. Paknia, A. Chari, and H. Stark, "Atomic-resolution protein structure determination by cryo-EM," *Nature*, vol. 587, no. 7832, pp. 157–161, 2020.

[184] Y.-H. Pan, K. Sader, J. J. Powell, A. Bleloch, M. Gass, J. Trinick, A. Warley, A. Li, R. Brydson, and A. Brown, "3D morphology of the human hepatic ferritin mineral core: New evidence for a subunit structure revealed by single particle analysis of HAADF-STEM images," *Journal of Structural Biology*, vol. 166, no. 1, pp. 22–31, 2009.

[185] N. Jian, M. Dowle, R. D. Horniblow, C. Tselepis, and R. E. Palmer, "Morphology of the ferritin iron core by aberration corrected scanning transmission electron microscopy," *Nanotechnology*, vol. 27, no. 46(46LT02), 2016.

[186] N. Elad, G. Bellapadrona, L. Houben, I. Sagi, and M. Elbaum, "Detection of isolated protein-bound metal ions by single-particle cryo-STEM," *Proceedings of the National Academy of Sciences*, vol. 114, no. 42, pp. 11 139–11 144, 2017.

[187] M. Elbaum, "Quantitative cryo-scanning transmission electron microscopy of biological materials," *Advanced Materials*, vol. 30, no. 41, p. 1 706 681, 2018.

[188] M. Beck and W. Baumeister, "Cryo-electron tomography: Can it reveal the molecular sociology of cells in atomic detail?" *Trends in Cell Biology*, vol. 26, no. 11, pp. 825–837, 2016.

[189] S. G. Wolf, L. Houben, and M. Elbaum, "Cryo-scanning transmission electron tomography of vitrified cells," *Nature Methods*, vol. 11, no. 4, p. 423, 2014.

[190] J. S. Wall, "Limits on visibility of single heavy atoms in the scanning transmission electron microscope: An experimental study," *Chimica Scripta*, vol. 14, pp. 271–278, Jan. 1979.

[191] W. A. Salser, "DNA sequencing techniques," *Annual Review of Biochemistry*, vol. 43, no. 1, pp. 923–965, 1974.

[192] L. Di Giamberardino, T. Koller, and M. Beer, "Electron microscopic study of the base sequence in nucleic acids: IX. Absence of fragmentation and of cross-linking during reaction with osmium tetroxide and cyanide," *Biochimica et Biophysica Acta*, vol. 182, no. 2, pp. 523–529, 1969.

[193] E. N. Moudrianakis and M. Beer, "Determination of base sequence in nucleic acids with the electron microscope II. The reaction of a guanine-selective marker with the mononucleotides," *Biochimica et Biophysica Acta*, vol. 95, no. 1, pp. 23–39, 1965.

[194] R. F. Whiting and F. P. Ottensmeyer, "Heavy atoms in model compounds and nucleic acids imaged by dark field transmission electron microscopy," *Journal of Molecular Biology*, vol. 67, no. 2, pp. 173–181, 1972.

[195] M. D. Cole, J. W. Wiggins, and M. Beer, "Molecular microscopy of labeled polynucleotides: Stability of osmium atoms," *Journal of Molecular Biology*, vol. 117, no. 2, pp. 387–400, 1977.

[196] J. M. Heather and B. Chain, "The sequence of sequencers: The history of sequencing DNA," *Genomics*, vol. 107, no. 1, pp. 1–8, 2016.

[197] D. C. Bell, W. K. Thomas, K. M. Murtagh, C. A. Dionne, A. C. Graham, J. E. Anderson, and W. R. Glover, "DNA base identification by electron microscopy," *Microscopy and Microanalysis*, vol. 18, no. 5, pp. 1049–1053, 2012.

[198] O. L. Krivanek, M. F. Chisholm, M. F. Murfitt, and N. Dellby, "Scanning transmission electron microscopy: Albert Crewe's vision and beyond," *Ultramicroscopy*, vol. 123, pp. 90–98, 2012.

[199] K. T. Tokuyasu, A. H. Dutton, B. Geiger, and S. J. Singer, "Ultrastructure of chicken cardiac muscle as studied by double immunolabeling in electron microscopy," *Proceedings of the National Academy of Sciences*, vol. 78, no. 12, pp. 7619–7623, 1981.

[200] W. P. Faulk and G. M. Taylor, "An immunocolloid method for the electron microscope," *Immunochemistry*, vol. 8, no. 11, pp. 1081–1083, 1971.

[201] J. Roth, M. Bendayan, and L. Orci, "Ultrastructural localization of intracellular antigens by the use of protein A-gold complex," *Journal of Histochemistry & Cytochemistry*, vol. 26, no. 12, pp. 1074–1081, 1978.

[202] J. Roth, "The silver anniversary of gold: 25 years of the colloidal gold marker system for immunocytochemistry and histochemistry," *Histochemistry and cell biology*, vol. 106, no. 1, pp. 1–8, 1996.

[203] J. F. Hainfeld and R. D. Powell, "New frontiers in gold labeling," *Journal of Histochemistry & Cytochemistry*, vol. 48, no. 4, pp. 471–480, 2000.

[204] J. F. Hainfeld, "Labeling with nanogold and undecagold: Techniques and results," *Scanning Microscopy*, vol. 1996, no. 10, p. 25, 1996.

[205] K. Braig, M. Simon, F. Furuya, J. F. Hainfeld, and A. L. Horwich, "A polypeptide bound by the chaperonin groEL is localized within a central cavity," *Proceedings of the National Academy of Sciences*, vol. 90, no. 9, pp. 3978–3982, 1993.

[206] L. Gregori, J. F. Hainfeld, M. N. Simon, and D. Goldgaber, "Binding of amyloid β protein to the 20 s proteasome," *Journal of Biological Chemistry*, vol. 272, no. 1, pp. 58–62, 1997.

[207] G. Hacker and J. Gu, *Gold and Silver Staining: Techniques in Molecular Morphology*, ser. Advances in Pathology, Microscopy, & Molecular Morphology. CRC Press, 2002.

[208] Y.-S. Yang, A. Datta, J. F. Hainfeld, F. R. Furuya, J. S. Wall, and P. A. Frey, "Mapping the lipoyl groups of the pyruvate dehydrogenase complex by use of gold cluster labels and scanning transmission electron microscopy," *Biochemistry*, vol. 33, no. 32, pp. 9428–9437, 1994.

[209] D. Safer, J. Hainfeld, J. S. Wall, and J. E. Reardon, "Biospecific labeling with undecagold: Visualization of the biotin-binding site on avidin," *Science*, vol. 218, no. 4569, pp. 290–291, 1982.

[210] J. J. Lipka, J. F. Hainfeld, and J. S. Wall, "Undecagold labeling of a glycoprotein: STEM visualization of an undecagoldphosphine cluster labeling the carbohydrate sites of human haptoglobin—hemoglobin complex," *Journal of Ultrastructure Research*, vol. 84, no. 2, pp. 120–129, 1983.

[211] N. P. Young, Z. Y. Li, Y. Chen, S. Palomba, M. Di Vece, and R. E. Palmer, "Weighing supported nanoparticles: Size-selected clusters as mass standards in nanometrology," *Physical Review Letters*, vol. 101, p. 246 103, 24 Dec. 2008.

[212] A. A. Bhirde, A. A. Sousa, V. Patel, A. A. Azari, J. S. Gutkind, R. D. Leapman, and J. F. Rusling, "Imaging the distribution of individual platinum-based anticancer drug molecules attached to single-wall carbon nanotubes," *Nanomedicine*, vol. 4, no. 7, pp. 763–772, 2009.

[213] A. A. Sousa, M. Hohmann-Marriott, M. A. Aronova, G. Zhang, and R. D. Leapman, "Determination of quantitative distributions of heavy-metal stain in biological specimens by annular dark-field STEM," *Journal of Structural Biology*, vol. 162, no. 1, pp. 14–28, 2008.

[214] A. A. Sousa and R. D. Leapman, "Development and application of STEM for the biological sciences," *Ultramicroscopy*, vol. 123, pp. 38–49, 2012.

[215] T. Hall and B. Gupta, "Chapter 3: EDS quantitation and application to biology," in *Introduction to Analytical Electron Microscopy*, J. J. Hren, J. I. Goldstein, and D. C. Joy, Eds. Boston, MA: Springer US, 1979, pp. 83–120, ISBN: 978-1-4757-5581-7.

[216] R. D. Leapman and S. B. Andrews, "Analysis of directly frozen macromolecules and tissues in the field-emission STEM," *Journal of Microscopy*, vol. 161, no. 1, pp. 3–19, 1991.

[217] R. D. Leapman, "Application of EELS and EFTEM to the life sciences enabled by the contributions of Ondrej Krivanek," *Ultramicroscopy*, vol. 180, pp. 180–187, 2017.

[218] J. E. Evans, C. Hetherington, A. Kirkland, L.-Y. Chang, H. Stahlberg, and N. Browning, "Low-dose aberration corrected cryo-electron microscopy of organic specimens," *Ultramicroscopy*, vol. 108, no. 12, pp. 1636–1644, 2008.

[219] A. E. Goode, J. M. Perkins, A. Sandison, C. Karunakaran, H. Cheng, D. Wall, J. A. Skinner, A. J. Hart, A. E. Porter, D. W. McComb, *et al.*, "Chemical speciation of nanoparticles surrounding metal-on-metal hips," *Chemical Communications*, vol. 48, no. 67, pp. 8335–8337, 2012.

[220] U. Gerber, R. Hübner, A. Rossberg, E. Krawczyk-Bärsch, and M. L. Merroun, "Metabolism-dependent bioaccumulation of uranium by Rhodosporidium toruloides isolated from the flooding water of a former uranium mine," *PLOS ONE*, vol. 13, no. 8, pp. 1–20, Aug. 2018.

[221] R. G. Haverkamp, A. T. Marshall, and D. van Agterveld, "Pick your carats: Nanoparticles of gold–silver–copper alloy produced in vivo," *Journal of Nanoparticle Research*, vol. 9, no. 4, pp. 697–700, 2007.

[222] C. F. Chang, H. Shuman, and A. P. Somlyo, "Electron probe analysis, x-ray mapping, and electron energy-loss spectroscopy of calcium, magnesium, and monovalent ions in log-phase and in dividing Escherichia coli B cells," *Journal of Bacteriology*, vol. 167, no. 3, pp. 935–939, 1986.

[223] A. V. Somlyo, R. Broderick, H. Shuman, E. L. Buhle, and A. P. Somlyo, "Atrial-specific granules in situ have high calcium content, are acidic, and maintain anion gradients," *Proceedings of the National Academy of Sciences*, vol. 85, no. 16, pp. 6222–6226, 1988.

[224] A. V. Somlyo, H. Shuman, and A. P. Somlyo, "Electron probe x-ray microanalysis of Ca^{2+}, Mg^{2+}, and other ions in rapidly frozen cells," in *Biomembranes Part S*, ser. Methods in Enzymology, vol. 172, Academic Press, 1989, pp. 203–229.

[225] K. Zierold, "Heavy metal cytotoxicity studied by electron probe x-ray microanalysis of cultured rat hepatocytes," *Toxicology in vitro*, vol. 14, no. 6, pp. 557–563, 2000.

[226] F. Arrebola, E. Fernández-Segura, A. Campos, P. V. Crespo, J. N. Skepper, and A. Warley, "Changes in intracellular electrolyte concentrations during apoptosis induced by UV irradiation of human myeloblastic cells," *American Journal of Physiology-Cell Physiology*, vol. 290, no. 2, pp. C638–C649, 2006.

[227] F. Arrebola, J. Canizares, M. Cubero, P. Crespo, A. Warley, and E. Fernández-Segura, "Biphasic behavior of changes in elemental composition during staurosporine-induced apoptosis," *Apoptosis*, vol. 10, no. 6, pp. 1317–1331, 2005.

[228] C. V. Remillard and J. X.-J. Yuan, "Activation of K^+ channels: An essential pathway in programmed cell death," *American Journal of Physiology-Lung Cellular and Molecular Physiology*, vol. 286, no. 1, pp. L49–L67, 2004.

[229] E. Fernandez-Segura and A. Warley, "Chapter 2: Electron probe x-ray microanalysis for the study of cell physiology," in *Introduction to Electron Microscopy for Biologists*, ser. Methods in Cell Biology, vol. 88, Academic Press, 2008, pp. 19–43.

[230] S. Andrews, N. Pivovarova, and R. Leapman, "Quantitative imaging and analysis of biological specimens in the field-emission scanning transmission electron microscope: Capabilities and limitations," *Scanning Microscopy*, vol. 13, no. 1, pp. 147–157, 1999.

[231] A. V. Somlyo, H. Shuman, and A. P. Somlyo, "Elemental distribution in striated muscle and the effects of hypertonicity: Electron probe analysis of cryo sections," *Journal of Cell Biology*, vol. 74, no. 3, pp. 828–857, 1977.

[232] T. A. Hall, "Biological x-ray microanalysis," *Journal of Microscopy*, vol. 117, no. 1, pp. 145–163, 1979.

[233] T. A. Hall and B. L. Gupta, "Quantification for the x-ray microanalysis of cryosections," *Journal of Microscopy*, vol. 126, no. 3, pp. 333–345, 1982.

[234] A. Warley, "Development and comparison of the methods for quantitative electron probe x-ray microanalysis analysis of thin specimens and their application to biological material," *Journal of Microscopy*, vol. 261, no. 2, pp. 177–184, 2016.

[235] P. Laquerriere, V. Banchet, J. Michel, K. Zierold, G. Balossier, and P. Bonhomme, "X-ray microanalysis of organic thin sections in TEM using an UTW Si (Li) detector: Comparison of quantification methods," *Microscopy Research and Technique*, vol. 52, no. 2, pp. 231–238, 2001.

[236] P. Laquerriere, J. Michel, G. Balossier, and B. Chénais, "Light elements quantification in stimulated cells cryosections studied by electron probe microanalysis," *Micron*, vol. 33, no. 7, pp. 597–603, 2002, ISSN: 0968-4328.

[237] P. Laquerriere, A. Grandjean-Laquerriere, L. Kilian, A. Beorchia, M. Guenounou, E. Jallot, G. Balossier, and P. Frayssinet, "Influence of hydroxyapatite particle characteristics on the [K]/[Na] ratio: A human monocytes in vitro study," *Colloids and Surfaces B: Biointerfaces*, vol. 33, no. 1, pp. 39–44, 2004.

[238] K. Zierold, J. Michel, C. Terryn, and G. Balossier, "The distribution of light elements in biological cells measured by electron probe x-ray microanalysis of cryosections," *Microscopy and Microanalysis*, vol. 11, no. 2, pp. 138–145, 2005.

[239] J. S. Wu, A. M. Kim, R. Bleher, B. D. Myers, R. G. Marvin, H. Inada, K. Nakamura, X. F. Zhang, E. Roth, S. Y. Li, *et al.*, "Imaging and elemental mapping of biological specimens with a dual-EDS dedicated scanning transmission electron microscope," *Ultramicroscopy*, vol. 128, pp. 24–31, 2013.

[240] D. B. Peckys and N. de Jonge, "Visualizing gold nanoparticle uptake in live cells with liquid scanning transmission electron microscopy," *Nano Letters*, vol. 11, no. 4, pp. 1733–1738, 2011.

[241] B. R. Van Devener, A. H. Vollmer, and N. N. Youssef, "Resolving the calcium and phosphorus distribution in casein micelles in bovine milk: An in situ STEM/EDX study as applied to hydrated materials in food science," *Microscopy and Microanalysis*, vol. 24, no. S1, pp. 1204–1205, 2018.

[242] S. G. Wolf, P. Rez, and M. Elbaum, "Phosphorus detection in vitrified bacteria by cryo-STEM annular dark-field analysis," *Journal of Microscopy*, vol. 260, no. 2, pp. 227–233, 2015.

[243] S. G. Wolf, Y. Mutsafi, T. Dadosh, T. Ilani, Z. Lansky, B. Horowitz, S. Rubin, M. Elbaum, and D. Fass, "3D visualization of mitochondrial solid-phase calcium stores in whole cells," *Elife*, vol. 6, e29929, 2017.

[244] Gatan, *EELS Atlas: Calcium*, retrieved 23.02.2021, 2015. [Online]. Available: `https://eels.info/atlas/calcium`.

[245] Gatan, *EELS Atlas: Iron*, retrieved 22.01.2021, 2015. [Online]. Available: `https://eels.info/atlas/iron`.

[246] P. Zhang, W. Land, S. Lee, J. Juliani, J. Lefman, S. R. Smith, D. Germain, M. Kessel, R. Leapman, T. A. Rouault, and S. Subramaniam, "Electron tomography of degenerating neurons in mice with abnormal regulation of iron metabolism," *Journal of Structural Biology*, vol. 150, no. 2, pp. 144–153, 2005.

[247] R. D. Leapman, "Detecting single atoms of calcium and iron in biological structures by electron energy-loss spectrum-imaging," *Journal of Microscopy*, vol. 210, no. 1, pp. 5–15, 2003.

[248] R. D. Leapman and N. W. Rizzo, "Towards single atom analysis of biological structures," *Ultramicroscopy*, vol. 78, no. 1, pp. 251–268, 1999.

[249] S. Yakovlev, M. Misra, S. Shi, E. Firlar, and M. Libera, "Quantitative nanoscale water mapping in frozen-hydrated skin by low-loss electron energy-loss spectroscopy," *Ultramicroscopy*, vol. 110, no. 7, pp. 866–876, 2010.

[250] M. Ilett, R. Brydson, A. Brown, and N. Hondow, "Cryo-analytical STEM of frozen, aqueous dispersions of nanoparticles," *Micron*, vol. 120, pp. 35–42, 2019.

[251] M. J. Zachman, Z. Tu, S. Choudhury, L. A. Archer, and L. F. Kourkoutis, "Cryo-STEM mapping of solid-liquid interfaces and dendrites in lithium-metal batteries," *Nature*, vol. 560, no. 7718, pp. 345–349, 2018.

[252] M. A. Aronova, Y. C. Kim, N. B. Pivovarova, S. B. Andrews, and R. D. Leapman, "Quantitative EFTEM mapping of near physiological calcium concentrations in biological specimens," *Ultramicroscopy*, vol. 109, no. 3, pp. 201–212, 2009.

[253] S. R. Adams, M. R. Mackey, R. Ramachandra, S. F. P. Lemieux, P. Steinbach, E. A. Bushong, M. T. Butko, B. N. Giepmans, M. H. Ellisman, and R. Y. Tsien, "Multicolor electron microscopy for simultaneous visualization of multiple molecular species," *Cell Chemical Biology*, vol. 23, no. 11, pp. 1417–1427, 2016.

[254] K. Iakoubovskii, K. Mitsuishi, Y. Nakayama, and K. Furuya, "Thickness measurements with electron energy loss spectroscopy," *Microscopy Research and Technique*, vol. 71, no. 8, pp. 626–631, 2008.

[255] C. Colliex and C. Mory, "Scanning transmission electron microscopy of biological structures," *Biology of the Cell*, vol. 80, no. 2-3, pp. 175–180, 1994.

[256] S. Narayanan, R. Shahbazian-Yassar, and T. Shokuhfar, "In situ visualization of ferritin biomineralization via graphene liquid cell-transmission electron microscopy," *ACS Biomaterials Science & Engineering*, vol. 6, no. 5, pp. 3208–3216, 2020.

[257] J. A. Hachtel, J. Huang, I. Popovs, S. Jansone-Popova, J. K. Keum, J. Jakowski, T. C. Lovejoy, N. Dellby, O. L. Krivanek, and J. C. Idrobo, "Identification of site-specific isotopic labels by vibrational spectroscopy in the electron microscope," *Science*, vol. 363, no. 6426, pp. 525–528, 2019.

[258] M. M. Woolfson, "The development of structural x-ray crystallography," *Physica Scripta*, vol. 93, no. 3, p. 032 501, 2018.

[259] T. C. Baker, J. Han, and C. H. Borchers, "Recent advancements in matrix-assisted laser desorption/ionization mass spectrometry imaging," *Current Opinion in Biotechnology*, vol. 43, pp. 62–69, 2017.

[260] D. Pröfrock and A. Prange, "Inductively coupled plasma–mass spectrometry (ICP-MS) for quantitative analysis in environmental and life sciences: A review of challenges, solutions, and trends," *Applied Spectroscopy*, vol. 66, no. 8, pp. 843–868, 2012.

[261] A. Brown and N. Hondow, "Chapter 4: Electron microscopy of nanoparticles in cells," in *Nanomedicine*, ser. Frontiers of Nanoscience, H. Summers, Ed., vol. 5, Elsevier, 2013, pp. 95–120.

[262] C. Cheng, K. H. Müller, K. K. Koziol, J. N. Skepper, P. A. Midgley, M. E. Welland, and A. E. Porter, "Toxicity and imaging of multi-walled carbon nanotubes in human macrophage cells," *Biomaterials*, vol. 30, no. 25, pp. 4152–4160, 2009.

[263] K. H. Müller, J. Kulkarni, M. Motskin, A. Goode, P. Winship, J. N. Skepper, M. P. Ryan, and A. E. Porter, "pH-dependent toxicity of high aspect ratio ZnO nanowires in macrophages due to intracellular dissolution," *ACS Nano*, vol. 4, no. 11, pp. 6767–6779, 2010.

[264] J. W. Wills, N. Hondow, A. D. Thomas, K. E. Chapman, D. Fish, T. G. Maffeis, M. W. Penny, R. A. Brown, G. J. S. Jenkins, A. P. Brown, *et al.*, "Genetic toxicity assessment of engineered nanoparticles using a 3D in vitro skin model (EpiDerm^{TM})," *Particle and Fibre Toxicology*, vol. 13, no. 1, pp. 1–21, 2015.

[265] M. Ilett, M. S'ari, H. Freeman, Z. Aslam, N. Koniuch, M. Afzali, J. Cattle, R. Hooley, T. Roncal-Herrero, S. M. Collins, N. Hondow, A. Brown, and R. Brydson, "Analysis of complex, beam-sensitive materials by transmission electron microscopy and associated techniques," *Philosophical Transactions of the Royal Society A: Mathematical, Physical and Engineering Sciences*, vol. 378, no. 2186, p. 20 190 601, 2020.

[266] R. F. Egerton and I. Rauf, "Dose-rate dependence of electron-induced mass loss from organic specimens," *Ultramicroscopy*, vol. 80, no. 4, pp. 247–254, 1999.

[267] R. Hooley, A. Brown, and R. Brydson, "Factors affecting electron beam damage in calcite nanoparticles," *Micron*, vol. 120, pp. 25–34, 2019, ISSN: 0968-4328.

[268] J. P. Buban, Q. Ramasse, B. Gipson, N. D. Browning, and H. Stahlberg, "High-resolution low-dose scanning transmission electron microscopy," *Journal of Electron Microscopy*, vol. 59, no. 2, pp. 103–112, 2009.

[269] L. Jones, H. Yang, T. J. Pennycook, M. S. Marshall, S. Van Aert, N. D. Browning, M. R. Castell, and P. D. Nellist, "Smart Align-a new tool for robust non-rigid registration of scanning microscope data," *Advanced Structural and Chemical Imaging*, vol. 1, no. 1, pp. 1–16, 2015.

[270] L. Jones, A. M. Varambhia, R. Beanland, D. Kepaptsoglou, I. Griffiths, A. Ishizuka, F. Azough, R. Freer, K. Ishizuka, D. Cherns, Q. M. Ramasse, S. Lozano-Perez, and P. D. Nellist, "Managing dose-, damage- and data-rates in multi-frame spectrum-imaging," *Microscopy*, vol. 67, no. S1, pp. I98–I113, 2018.

[271] M. S'ari, J. Cattle, N. Hondow, R. Brydson, and A. Brown, "Low dose scanning transmission electron microscopy of organic crystals by scanning moiré fringes," *Micron*, vol. 120, pp. 1–9, 2019.

[272] M. S'ari, N. Koniuch, R. Brydson, N. Hondow, and A. Brown, "High-resolution imaging of organic pharmaceutical crystals by transmission electron microscopy and scanning moiré fringes," *Journal of Microscopy*, vol. 279, no. 3, pp. 197–206, 2020.

[273] A. A. Sheader, A. M. Varambhia, R. A. Fleck, S. J. L. Flatters, and P. D. Nellist, "Observation of metal nanoparticles at atomic resolution in pt-based cancer chemotherapeutics," *Journal of Microscopy*, vol. 270, no. 1, pp. 92–97, 2018.

[274] M. Galanski, M. A. Jakupec, and B. K. Keppler, "Update of the preclinical situation of anticancer platinum complexes: Novel design strategies and innovative analytical approaches," *Current Medicinal Chemistry*, vol. 12, no. 18, pp. 2075–2094, 2005.

[275] L. Kelland, "The resurgence of platinum-based cancer chemotherapy," *Nature Reviews Cancer*, vol. 7, no. 8, pp. 573–584, 2007.

[276] National Institute for Health and Care Excellence, *British National Formulary*, Accessed: 2021-03-22. [Online]. Available: `https://bnf.nice.org.uk/drug/`.

[277] Cancer Research UK, *UK Cancer Incidence Summary (2017)*, Accessed: 2021-03-23. [Online]. Available: `https://www.cancerresearchuk.org/health-professional/cancer-statistics/incidence`.

[278] B. Rosenberg, L. Van Camp, and T. Krigas, "Inhibition of cell division in Escherichia coli by electrolysis products from a platinum electrode," *Nature*, vol. 205, no. 4972, pp. 698–699, 1965.

[279] B. Rosenberg, L. Vancamp, J. E. Trosko, and V. H. Mansour, "Platinum compounds: A new class of potent antitumour agents," *Nature*, vol. 222, no. 5191, pp. 385–386, 1969.

[280] National Institute for Health and Care Excellence, *British National Formulary*, Accessed: 2021-03-23. [Online]. Available: `https://bnf.nice.org.uk/drug/cisplatin.html`.

[281] L. H. Einhorn, "Treatment of testicular cancer: A new and improved model.," *Journal of Clinical Oncology*, vol. 8, no. 11, pp. 1777–1781, 1990.

[282] T. Alcindor and N. Beauger, "Oxaliplatin: A review in the era of molecularly targeted therapy," *Current Oncology*, vol. 18, no. 1, pp. 18–25, 2011.

[283] S. Dasari and P. B. Tchounwou, "Cisplatin in cancer therapy: Molecular mechanisms of action," *European Journal of Pharmacology*, vol. 740, pp. 364–378, 2014.

[284] D. M. Noll, T. M. Mason, and P. S. Miller, "Formation and repair of interstrand cross-links in DNA," *Chemical Reviews*, vol. 106, no. 2, pp. 277–301, 2006.

[285] T. C. Johnstone, G. Y. Park, and S. J. Lippard, "Understanding and improving platinum anticancer drugs–phenanthriplatin," *Anticancer Research*, vol. 34, no. 1, pp. 471–476, 2014.

[286] J.-P. Renaud, A. Chari, C. Ciferri, W.-t. Liu, H.-W. Rémigy, H. Stark, and C. Wiesmann, "Cryo-EM in drug discovery: Achievements, limitations and prospects," *Nature Reviews Drug Discovery*, vol. 17, no. 7, pp. 471–492, 2018.

[287] W. P. Davey, "Precision measurements of the lattice constants of twelve common metals," *Phys. Rev.*, vol. 25, pp. 753–761, 6 1925.

[288] J. E. Evans, K. L. Jungjohann, N. D. Browning, and I. Arslan, "Controlled growth of nanoparticles from solution with in situ liquid transmission electron microscopy," *Nano Letters*, vol. 11, no. 7, pp. 2809–2813, 2011.

[289] S. Sepulveda-Guzman, N. Elizondo-Villarreal, D. Ferrer, A. Torres-Castro, X. Gao, J. P. Zhou, and M. Jose-Yacaman, "In situ formation of bismuth nanoparticles through electron-beam irradiation in a transmission electron microscope," *Nanotechnology*, vol. 18, no. 33, p. 335 604, 2007.

[290] H. S. Dehsari, A. H. Ribeiro, B. Ersöz, W. Tremel, G. Jakob, and K. Asadi, "Effect of precursor concentration on size evolution of iron oxide nanoparticles," *CrystEngComm*, vol. 19, no. 44, pp. 6694–6702, 2017.

[291] N. C. Bigall, T. Härtling, M. Klose, P. Simon, L. M. Eng, and A. Eychmüller, "Monodisperse platinum nanospheres with adjustable diameters from 10 to 100 nm: Synthesis and distinct optical properties," *Nano Letters*, vol. 8, no. 12, pp. 4588–4592, 2008.

[292] C. Liu, G. Li, D. R. Kauffman, G. Pang, and R. Jin, "Synthesis of ultrasmall platinum nanoparticles and structural relaxation," *Journal of Colloid and Interface Science*, vol. 423, pp. 123–128, 2014.

[293] J. Aarons, L. Jones, A. M. Varambhia, K. E. MacArthur, D. Ozkaya, M. Sarwar, C.-K. Skylaris, and P. D. Nellist, "Predicting the oxygen-binding properties of platinum nanoparticle ensembles by combining high-precision electron microscopy and density functional theory," *Nano letters*, vol. 17, no. 7, pp. 4003–4012, 2017.

[294] G. J. Hutchings and C. J. Kiely, "Strategies for the synthesis of supported gold palladium nanoparticles with controlled morphology and composition," *Accounts of Chemical Research*, vol. 46, no. 8, pp. 1759–1772, 2013.

[295] S. Mourdikoudis, R. M. Pallares, and N. T. K. Thanh, "Characterization techniques for nanoparticles: Comparison and complementarity upon studying nanoparticle properties," *Nanoscale*, vol. 10, pp. 12 871–12 934, 27 2018.

[296] C. M. Riley and L. A. Sternson, "Cisplatin," in *Analytical Profiles of Drug Substances*, K. Florey, Ed., vol. 14, Academic Press, 1985, pp. 77–105.

[297] M. E. Bosch, A. R. Sánchez, F. S. Rojas, and C. B. Ojeda, "Analytical methodologies for the determination of cisplatin," *Journal of Pharmaceutical and Biomedical Analysis*, vol. 47, no. 3, pp. 451–459, 2008, ISSN: 0731-7085.

[298] R. F. Greene, D. C. Chatterji, P. K. Hiranaka, and J. F. Gallelli, "Stability of cisplatin in aqueous solution," *American Journal of Hospital Pharmacy*, vol. 36, no. 1, pp. 38–43, 1979.

[299] A. A. Hussain, M. Haddadin, and K. Iga, "Reaction of cis-platinum with sodium bisulfite," *Journal of Pharmaceutical Sciences*, vol. 69, no. 3, pp. 364–365, 1980, ISSN: 0022-3549.

[300] K. Englert, R. Hendi, P. H. Robbs, N. V. Rees, A. P. G. Robinson, and J. H. R. Tucker, "Cisplatin adducts of dna as precursors for nanostructured catalyst materials," *Nanoscale Advances*, vol. 2, pp. 4491–4497, 10 2020.

[301] K. Ajima, M. Yudasaka, T. Murakami, A. Maigné, K. Shiba, and S. Iijima, "Carbon nanohorns as anticancer drug carriers," *Molecular pharmaceutics*, vol. 2, no. 6, pp. 475–480, 2005.

[302] X. Zeng, J. Sun, S. Li, J. Shi, H. Gao, W. S. Leong, Y. Wu, M. Li, C. Liu, P. Li, J. Kong, Y.-Z. Wu, G. Nie, Y. Fu, and G. Zhang, "Blood-triggered generation of platinum nanoparticle functions as an anti-cancer agent," *Nature Communications*, vol. 11, no. 1, pp. 1–12, 2020.

[303] G. S. Devi and V. Rao, "Room temperature synthesis of colloidal platinum nanoparticles," *Bulletin of Materials Science*, vol. 23, no. 6, pp. 467–470, 2000.

[304] Y. Yamagishi, A. Watari, Y. Hayata, X. Li, M. Kondoh, Y. Yoshioka, Y. Tsutsumi, and K. Yagi, "Acute and chronic nephrotoxicity of platinum nanoparticles in mice," *Nanoscale Research Letters*, vol. 8, no. 1, pp. 1–7, 2013.

[305] R. P. Miller, R. K. Tadagavadi, G. Ramesh, and W. B. Reeves, "Mechanisms of cisplatin nephrotoxicity," *Toxins*, vol. 2, no. 11, pp. 2490–2518, 2010.

[306] L. M. Pasetto, M. R. D'Andrea, E. Rossi, and S. Monfardini, "Oxaliplatin-related neurotoxicity: How and why?" *Critical Reviews in Oncology/Hematology*, vol. 59, no. 2, pp. 159–168, 2006.

[307] L. Jones, A. M. Varambhia, H. Sawada, and P. D. Nellist, "An optical configuration for fastidious STEM detector calibration and the effect of the objective-lens pre-field," *Journal of Microscopy*, vol. 270, no. 2, pp. 176–187, 2018.

[308] A. M. Varambhia, L. Jones, A. De Backer, V. T. Fauske, S. Van Aert, D. Ozkaya, and P. D. Nellist, "Quantifying a heterogeneous ru catalyst on carbon black using ADF STEM," *Particle & Particle Systems Characterization*, vol. 33, no. 7, pp. 438–444, 2016.

[309] E. Raymond, S. Faivre, S. Chaney, J. Woynarowski, and E. Cvitkovic, "Cellular and molecular pharmacology of oxaliplatin," *Molecular Cancer Therapeutics*, vol. 1, no. 3, pp. 227–235, 2002.

[310] Z. Liu, S. Tan, Y. Zu, Y. Fu, R. Meng, and Z. Xing, "The interactions of cisplatin and DNA studied by atomic force microscopy," *Micron*, vol. 41, no. 7, pp. 833–839, 2010.

[311] S. B. Park, D. Goldstein, A. V. Krishnan, C. S.-Y. Lin, M. L. Friedlander, J. Cassidy, M. Koltzenburg, and M. C. Kiernan, "Chemotherapy-induced peripheral neurotoxicity: A critical analysis," *CA: A Cancer Journal for Clinicians*, vol. 63, no. 6, pp. 419–437, 2013.

[312] H. Starobova and I. Vetter, "Pathophysiology of chemotherapy-induced peripheral neuropathy," *Frontiers in Molecular Neuroscience*, vol. 10, p. 174, 2017.

[313] G. Cavaletti, "Peripheral neurotoxicity of platinum-based chemotherapy," *Nature Reviews Cancer*, vol. 8, no. 1, pp. 72–72, 2008.

[314] J. Holmes, J. Stanko, M. Varchenko, H. Ding, V. J. Madden, C. R. Bagnell, S. D. Wyrick, and S. G. Chaney, "Comparative neurotoxicity of oxaliplatin, cisplatin, and ormaplatin in a Wistar rat model," *Toxicological Sciences*, vol. 46, no. 2, pp. 342–351, 1998.

[315] G. Cavaletti, G. Tredici, M. Petruccioli, E. Donde, P. Tredici, P. Marmiroli, C. Minoia, A. Ronchi, M. Bayssas, and G. G. Etienne, "Effects of different schedules of oxaliplatin treatment on the peripheral nervous system of the rat," *European Journal of Cancer*, vol. 37, no. 18, pp. 2457–2463, 2001.

[316] L. E. Ta, L. Espeset, J. Podratz, and A. J. Windebank, "Neurotoxicity of oxaliplatin and cisplatin for dorsal root ganglion neurons correlates with platinum–DNA binding," *NeuroToxicology*, vol. 27, no. 6, pp. 992–1002, 2006.

[317] G. Cavaletti and P. Marmiroli, "Chemotherapy-induced peripheral neurotoxicity," *Current Opinion in Neurology*, vol. 28, no. 5, pp. 500–507, 2015.

[318] S. R. McWhinney, R. M. Goldberg, and H. L. McLeod, "Platinum neurotoxicity pharmacogenetics," *Molecular Cancer Therapeutics*, vol. 8, no. 1, pp. 10–16, 2009.

[319] A. Lazić, J. Popović, T. Paunesku, G. E. Woloschak, and M. Stevanović, "Insights into platinum-induced peripheral neuropathy–current perspective," *Neural Regeneration Research*, vol. 15, no. 9, p. 1623, 2020.

[320] R. V. Haberberger, C. Barry, N. Dominguez, and D. Matusica, "Human dorsal root ganglia," *Frontiers in Cellular Neuroscience*, vol. 13, p. 271, 2019.

[321] H. K. P. Feirabend and E. Marani, "Dorsal root ganglion," in *Encyclopedia of the Neurological Sciences*, M. J. Aminoff and R. B. Daroff, Eds., New York: Academic Press, 2003, pp. 28–33, ISBN: 978-0-12-226870-0.

[322] H. E, K. E. MacArthur, T. J. Pennycook, E. Okunishi, A. J. D'Alfonso, N. R. Lugg, L. J. Allen, and P. D. Nellist, "Probe integrated scattering cross sections in the analysis of atomic resolution HAADF STEM images," *Ultramicroscopy*, vol. 133, pp. 109–119, 2013.

[323] L. Jones, K. E. MacArthur, V. T. Fauske, A. T. van Helvoort, and P. D. Nellist, "Rapid estimation of catalyst nanoparticle morphology and atomic-coordination by high-resolution Z-contrast electron microscopy," *Nano Letters*, vol. 14, no. 11, pp. 6336–6341, 2014.

[324] S. D. Findlay and J. M. LeBeau, "Detector non-uniformity in scanning transmission electron microscopy," *Ultramicroscopy*, vol. 124, pp. 52–60, 2013.

[325] G. T. Martinez, L. Jones, A. De Backer, A. Béché, J. Verbeeck, S. Van Aert, and P. D. Nellist, "Quantitative STEM normalisation: The importance of the electron flux," *Ultramicroscopy*, vol. 159, pp. 46–58, 2015.

[326] I. Lobato, S. Van Aert, and J. Verbeeck, "Progress and new advances in simulating electron microscopy datasets using MULTEM," *Ultramicroscopy*, vol. 168, pp. 17–27, 2016.

[327] R. F. Loane, E. J. Kirkland, and J. Silcox, "Visibility of single heavy atoms on thin crystalline silicon in simulated annular dark-field STEM images," *Acta Crystallographica Section A*, vol. 44, no. 6, pp. 912–927, 1988.

[328] H. Yang, T. J. Pennycook, and P. D. Nellist, "Efficient phase contrast imaging in STEM using a pixelated detector. Part II: Optimisation of imaging conditions," *Ultramicroscopy*, vol. 151, pp. 232–239, 2015.

[329] U. Moran, R. Phillips, and R. Milo, "Snapshot: Key numbers in biology," *Cell*, vol. 141, no. 7, pp. 1262–1262, 2010.

[330] D. B. Williams and C. B. Carter, "Chapter 4: Inelastic scattering and beam damage," in *Transmission Electron Microscopy: A Textbook for Materials Science*. Boston, MA: Springer US, 2009, pp. 53–71, ISBN: 978-0-387-76501-3.

[331] D. M. Cheff and M. D. Hall, "A drug of such damned nature - challenges and opportunities in translational platinum drug research: Miniperspective," *Journal of Medicinal Chemistry*, vol. 60, no. 11, pp. 4517–4532, 2017.

[332] R. J. P. Williams and J. J. R. Fraústo da Silva, "The distribution of elements in cells," *Coordination Chemistry Reviews*, vol. 200-202, pp. 247–348, 2000.

[333] M. Ralle and S. Lutsenko, "Quantitative imaging of metals in tissues," *Biometals*, vol. 22, no. 1, pp. 197–205, 2009.

[334] R. McRae, P. Bagchi, S. Sumalekshmy, and C. J. Fahrni, "In situ imaging of metals in cells and tissues," *Chemical Reviews*, vol. 109, no. 10, pp. 4780–4827, 2009.

[335] A. van der Ent, W. J. Przybyłowicz, M. D. de Jonge, H. H. Harris, C. G. Ryan, G. Tylko, D. J. Paterson, A. D. Barnabas, P. M. Kopittke, and J. Mesjasz-Przybyłowicz, "X-ray elemental mapping techniques for elucidating the ecophysiology of hyperaccumulator plants," *New Phytologist*, vol. 218, no. 2, pp. 432–452, 2018.

[336] J. Decelle, G. Veronesi, B. Gallet, H. Stryhanyuk, P. Benettoni, M. Schmidt, R. Tucoulou, M. Passarelli, S. Bohic, P. Clode, *et al.*, "Subcellular chemical imaging: New avenues in cell biology," *Trends in Cell Biology*, vol. 30, no. 3, pp. 173–188, 2020.

[337] T. G. M. H. Dikhoff, J. A. Van Der Heide, and J. G. McVie, "Topographic PIXE analysis of platinum levels in kidney slices from cisplatin treated patients," *Nuclear Instruments and Methods in Physics Research Section B: Beam Interactions with Materials and Atoms*, vol. 10-11, pp. 639–642, 1985.

[338] L. Nianqing, Z. Chuannong, Y. Lingna, L. Xuejun, C. Zhiyu, R. Zhigang, and Z. Shijun, "A preliminary study on the positional distribution of cisplatin and other elements in the liver of normal mice," *Nuclear Instruments and Methods in Physics Research Section B: Beam Interactions with Materials and Atoms*, vol. 75, no. 1, pp. 571–575, 1993.

[339] H. Sakurai, M. Okamoto, M. Hasegawa, T. Satoh, M. Oikawa, T. Kamiya, K. Arakawa, and T. Nakano, "Direct visualization and quantification of the anticancer agent, cis-diamminedichloro-platinum (II), in human lung cancer cells using in-air microparticle-induced x-ray emission analysis," *Cancer Science*, vol. 99, no. 5, pp. 901–904, 2008.

[340] A. A. Hummer and A. Rompel, "The use of X-ray absorption and synchrotron based micro-X-ray fluorescence spectroscopy to investigate anti-cancer metal compounds in vivo and in vitro," *Metallomics*, vol. 5, no. 6, pp. 597–614, 2013.

[341] R. Koba, H. Fujita, M. Nishibori, K. Saeki, K. Nagayoshi, Y. Sadakari, S. Nagai, O. Sekizawa, K. Nitta, T. Manabe, T. Ueki, T. Ishida, Y. Oda, and M. Nakamura, "Quantitative evaluation of the intratumoral distribution of platinum in oxaliplatin-treated rectal cancer: In situ visualization of platinum via synchrotron radiation x-ray fluorescence spectrometry," *International Journal of Cancer*, vol. 146, no. 9, pp. 2498–2509, 2020.

[342] M. D. Hall, C. T. Dillon, M. Zhang, P. Beale, Z. Cai, B. Lai, A. P. Stampfl, and T. W. Hambley, "The cellular distribution and oxidation state of platinum (II) and platinum (IV) antitumour complexes in cancer cells," *JBIC Journal of Biological Inorganic Chemistry*, vol. 8, no. 7, pp. 726–732, 2003.

[343] J. Z. Zhang, N. S. Bryce, A. Lanzirotti, C. K. J. Chen, D. Paterson, M. D. de Jonge, D. L. Howard, and T. W. Hambley, "Getting to the core of platinum drug bio-distributions: the penetration of anti-cancer platinum complexes into spheroid tumour models," *Metallomics*, vol. 4, no. 11, pp. 1209–1217, 2012.

[344] E. F. Garman and G. W. Grime, "Elemental analysis of proteins by microPIXE," *Progress in Biophysics and Molecular Biology*, vol. 89, no. 2, pp. 173–205, 2005.

[345] J. C. G. Jeynes, M. J. Bailey, H. Coley, K. J. Kirkby, and C. Jeynes, "Microbeam PIXE analysis of platinum resistant and sensitive ovarian cancer cells," *Nuclear Instruments and Methods in Physics Research Section B: Beam Interactions with Materials and Atoms*, vol. 268, no. 11, pp. 2168–2171, 2010.

[346] P. Ilinski, B. Lai, Z. Cai, W. Yun, D. Legnini, T. Talarico, M. Cholewa, L. K. Webster, G. B. Deacon, S. Rainone, D. R. Phillips, and A. P. J. Stampfl, "The direct mapping of the uptake of platinum anticancer agents in individual human ovarian adenocarcinoma cells using a hard x-ray microprobe," *Cancer Research*, vol. 63, no. 8, pp. 1776–1779, 2003.

[347] K. Wu, F. Jia, W. Zheng, Q. Luo, Y. Zhao, and F. Wang, "Visualization of metallodrugs in single cells by secondary ion mass spectrometry imaging," *JBIC Journal of Biological Inorganic Chemistry*, vol. 22, no. 5, pp. 653–661, 2017.

[348] T. O. Nicolescu, "Interpretation of mass spectra," in *Mass Spectrometry*, M. Aliofkhazraei, Ed., Rijeka: IntechOpen, 2017, ch. 2.

[349] S. Theiner, A. Schweikert, C. Haberler, A. Peyrl, and G. Koellensperger, "Laser ablation-ICP-TOFMS imaging of germ cell tumors of patients undergoing platinum-based chemotherapy," *Metallomics*, vol. 12, no. 8, pp. 1246–1252, 2020.

[350] S. Theiner, A. Schoeberl, A. Schweikert, B. K. Keppler, and G. Koellensperger, "Mass spectrometry techniques for imaging and detection of metallodrugs," *Current Opinion in Chemical Biology*, vol. 61, pp. 123–134, 2021.

[351] R. F. S. Lee, T. Riedel, S. Escrig, C. Maclachlan, G. W. Knott, C. A. Davey, K. Johnsson, A. Meibom, and P. J. Dyson, "Differences in cisplatin distribution in sensitive and resistant ovarian cancer cells: A TEM/NanoSIMS study," *Metallomics*, vol. 9, no. 10, pp. 1413–1420, 2017.

[352] L. E. Wedlock, M. R. Kilburn, R. Liu, J. A. Shaw, S. J. Berners-Price, and N. P. Farrell, "NanoSIMS multi-element imaging reveals internalisation and nucleolar targeting for a highly-charged polynuclear platinum compound," *Chemical Communications*, vol. 49, pp. 6944–6946, 62 2013.

[353] R. F. S. Lee, S. Theiner, A. Meibom, G. Koellensperger, B. K. Keppler, and P. J. Dyson, "Application of imaging mass spectrometry approaches to facilitate metal-based anticancer drug research," *Metallomics*, vol. 9, no. 4, pp. 365–381, 2017.

[354] B. M. Humbel, S. H., E. M. Tranfield, and R. A. Fleck, "Chapter 10: Chemical fixation," in *Biological Field Emission Scanning Electron Microscopy*, R. A. Fleck and B. M. Humbel, Eds., 1st ed., 2019, pp. 191–222.

[355] K. T. Tokuyasu, "A technique for ultracryotomy of cell suspensions and tissues," *The Journal of cell biology*, vol. 57, no. 2, pp. 551–565, 1973.

[356] A. A. Legin, S. Theiner, A. Schintlmeister, S. Reipert, P. Heffeter, M. A. Jakupec, J. Mayr, H. P. Varbanov, C. R. Kowol, M. Galanski, *et al.*, "Multi-scale imaging of anticancer platinum (IV) compounds in murine tumor and kidney," *Chemical Science*, vol. 7, no. 5, pp. 3052–3061, 2016.

[357] C. Meijera, M. J. A. van Luyn, E. F. Nienhuis, N. Blom, N. H. Mulder, and E. G. E. de Vries, "Ultrastructural morphology and localisation of cisplatin-induced platinum–DNA adducts in a cisplatin-sensitive and -resistant human small cell lung cancer cell line using electron microscopy," *Biochemical Pharmacology*, vol. 61, no. 5, pp. 573–578, 2001.

[358] G. L. Beretta, S. C. Righetti, L. Lombardi, F. Zunino, and P. Perego, "Electron microscopy analysis of early localization of cisplatin in ovarian carcinoma cells," *Ultrastructural Pathology*, vol. 26, no. 5, pp. 331–334, 2002.

[359] P. J. Kempen, A. S. Thakor, C. Zavaleta, S. S. Gambhir, and R. Sinclair, "A scanning transmission electron microscopy (STEM) approach to analyzing large volumes of tissue to detect nanoparticles," *Microscopy and Microanalysis*, vol. 19, no. 5, p. 1290, 2013.

[360] A. B. Seabra and N. Durán, "Nanotoxicology of metal oxide nanoparticles," *Metals*, vol. 5, no. 2, pp. 934–975, 2015.

[361] B. A. Maher, I. A. Ahmed, V. Karloukovski, D. A. MacLaren, P. G. Foulds, D. Allsop, D. M. Mann, R. Torres-Jardón, and L. Calderon-Garciduenas, "Magnetite pollution nanoparticles in the human brain," *Proceedings of the National Academy of Sciences*, vol. 113, no. 39, pp. 10 797–10 801, 2016.

[362] K. L. Moore, M. Schröder, Z. Wu, B. G. Martin, C. R. Hawes, S. P. McGrath, M. J. Hawkesford, J. Feng Ma, F.-J. Zhao, and C. R. Grovenor, "High-resolution secondary ion mass spectrometry reveals the contrasting subcellular distribution of arsenic and silicon in rice roots," *Plant Physiology*, vol. 156, no. 2, pp. 913–924, 2011.

[363] A. J. Craven, J. Bobynko, B. Sala, and I. MacLaren, "Accurate measurement of absolute experimental inelastic mean free paths and EELS differential cross-sections," *Ultramicroscopy*, vol. 170, pp. 113–127, 2016.

[364] K. E. MacArthur, T. J. A. Slater, S. J. Haigh, D. Ozkaya, P. D. Nellist, and S. Lozano-Perez, "Quantitative energy-dispersive x-ray analysis of catalyst nanoparticles using a partial cross section approach," *Microscopy and Microanalysis*, vol. 22, no. 1, pp. 71–81, 2016.

[365] A. M. Varambhia, L. Jones, A. London, D. Ozkaya, P. D. Nellist, and S. Lozano-Perez, "Determining EDS and EELS partial cross-sections from multiple calibration standards to accurately quantify bi-metallic nanoparticles using STEM," *Micron*, vol. 113, pp. 69–82, 2018.

[366] Z. Chen, M. Weyland, X. Sang, W. Xu, J. Dycus, J. LeBeau, A. d'Alfonso, L. Allen, and S. Findlay, "Quantitative atomic resolution elemental mapping via absolute-scale energy dispersive x-ray spectroscopy," *Ultramicroscopy*, vol. 168, pp. 7–16, 2016.

[367] S. Findlay, Z. Chen, M. Weyland, X. Sang, W. Xu, J. Dycus, J. LeBeau, and L. Allen, "Absolute-scale comparison with simulation for quantitative energy-dispersive x-ray spectroscopy in atomic-resolution scanning transmission electron microscopy," *Microscopy and Microanalysis*, vol. 23, no. S1, pp. 388–389, 2017.

[368] M. A. Aronova, A. A. Sousa, G. Zhang, and R. D. Leapman, "Limitations of beam damage in electron spectroscopic tomography of embedded cells," *Journal of Microscopy*, vol. 239, no. 3, pp. 223–232, 2010.

[369] P. T. Boggs and J. E. Rogers, "Orthogonal distance regression," *Contemporary Mathematics*, vol. 112, pp. 183–194, 1990.

[370] P. Virtanen, R. Gommers, T. E. Oliphant, M. Haberland, T. Reddy, D. Cournapeau, E. Burovski, P. Peterson, W. Weckesser, J. Bright, *et al.*, "Scipy 1.0: Fundamental algorithms for scientific computing in Python," *Nature Methods*, vol. 17, no. 3, pp. 261–272, 2020.

[371] B. A. Weaver, "How Taxol/paclitaxel kills cancer cells," *Molecular Biology of the Cell*, vol. 25, no. 18, pp. 2677–2681, 2014.

[372] R. C. Polomano, A. J. Mannes, U. S. Clark, and G. J. Bennett, "A painful peripheral neuropathy in the rat produced by the chemotherapeutic drug, paclitaxel," *Pain*, vol. 94, no. 3, pp. 293–304, 2001.

[373] D. L. Hershman, C. Lacchetti, R. H. Dworkin, E. M. Lavoie Smith, J. Bleeker, G. Cavaletti, C. Chauhan, P. Gavin, A. Lavino, M. B. Lustberg, J. Paice, B. Schneider, M. L. Smith, T. Smith, S. Terstriep, N. Wagner-Johnston, K. Bak, and C. L. Loprinzi, "Prevention and management of chemotherapy-induced peripheral neuropathy in survivors of adult cancers: American society of clinical oncology clinical practice guideline," *Journal of Clinical Oncology*, vol. 32, no. 18, pp. 1941–1967, 2014.

[374] H. Gelderblom, J. Verweij, K. Nooter, and A. Sparreboom, "Cremophor EL: the drawbacks and advantages of vehicle selection for drug formulation," *European Journal of Cancer*, vol. 37, no. 13, pp. 1590–1598, 2001.

[375] K. Meacham, A. Shepherd, D. P. Mohapatra, and S. Haroutounian, "Neuropathic pain: Central vs. peripheral mechanisms," *Current Pain and Headache Reports*, vol. 21, no. 6, p. 28, 2017.

[376] N. P. Staff, J. C. Fehrenbacher, M. Caillaud, M. I. Damaj, R. A. Segal, and S. Rieger, "Pathogenesis of paclitaxel-induced peripheral neuropathy: A current review of in vitro and in vivo findings using rodent and human model systems," *Experimental Neurology*, vol. 324, p. 113 121, 2020.

[377] B. Alberts, A. Johnson, J. Lewis, M. Raff, K. Roberts, and P. Walter, "Chapter 11: Membrane transport of small molecules and the electrical properties of membranes," in *Molecular Biology of the Cell*, B. Alberts, A. Johnson, J. Lewis, M. Raff, K. Roberts, and P. Walter, Eds., 5th ed. Taylor & Francis, 2008, pp. 651–694, ISBN: 978 0 8153 4105 5.

[378] S. J. L. Flatters and G. J. Bennett, "Studies of peripheral sensory nerves in paclitaxel-induced painful peripheral neuropathy: Evidence for mitochondrial dysfunction," *Pain*, vol. 122, no. 3, pp. 245–257, 2006.

[379] K. A. Aromolaran and P. A. Goldstein, "Ion channels and neuronal hyperexcitability in chemotherapy-induced peripheral neuropathy: Cause and effect?" *Molecular Pain*, vol. 13, pp. 1–24, 2017.

[380] P. Verma, M. Eaton, A. Kienle, D. Flockerzi, Y. Yang, and D. Ramkrishna, "Examining sodium and potassium channel conductances involved in hyperexcitability of chemotherapy-induced peripheral neuropathy: A mathematical and cell culture-based study," *Frontiers in Computational Neuroscience*, vol. 14, p. 88, 2020.

[381] A. Al-Amoudi, J.-J. Chang, A. Leforestier, A. McDowall, L. M. Salamin, L. P. Norlén, K. Richter, N. S. Blanc, D. Studer, and J. Dubochet, "Cryo-electron microscopy of vitreous sections," *The EMBO Journal*, vol. 23, no. 18, pp. 3583–3588, 2004.

[382] J. W. Greenawalt, C. S. Rossi, and A. L. Lehninger, "Effect of active accumulation of calcium and phosphate ions on the structure of rat liver mitochondria," *The Journal of Cell Biology*, vol. 23, no. 1, pp. 21–38, 1964.

[383] C. Bordat, J.-L. Guerquin-Kern, M. Lieberherr, and G. Cournot, "Direct visualization of intracellular calcium in rat osteoblasts by energy-filtering transmission electron microscopy," *Histochemistry and Cell Biology*, vol. 121, no. 1, pp. 31–38, 2004.

[384] S. Boonrungsiman, E. Gentleman, R. Carzaniga, N. D. Evans, D. W. McComb, A. E. Porter, and M. M. Stevens, "The role of intracellular calcium phosphate in osteoblast-mediated bone apatite formation," *Proceedings of the National Academy of Sciences*, vol. 109, no. 35, pp. 14 170–14 175, 2012.

[385] National Institute of Health, *Calcium phosphate*, accessed 15.05.2021, 2021. [Online]. Available: `https://pubchem.ncbi.nlm.nih.gov/compound/Calcium-phosphate`.

[386] S. J. L. Flatters and G. J. Bennett, "Ethosuximide reverses paclitaxel-and vincristine-induced painful peripheral neuropathy," *Pain*, vol. 109, no. 1-2, pp. 150–161, 2004.

[387] M. R. Duchen, "Mitochondria and calcium: From cell signalling to cell death," *The Journal of Physiology*, vol. 529, no. 1, pp. 57–68, 2000.

[388] C. M. Ferguson, "Investigating the elemental composition of peripheral sensory nerves and their function in paclitaxel-induced peripheral neuropathy," Ph.D. dissertation, King's College London, 2020, p. 252.

[389] P. J. Sheridan, "Determination of experimental and theoretical $k_{A,Si}$ factors for a 200kV analytical electron microscope," *Journal of Electron Microscopy Technique*, vol. 11, no. 1, pp. 41–61, 1989.

[390] C. D. Scripture, W. D. Figg, and A. Sparreboom, "Peripheral neuropathy induced by paclitaxel: Recent insights and future perspectives," *Current Neuropharmacology*, vol. 4, no. 2, pp. 165–172, 2006.

[391] R. M. LoPachin Jr., J. Lowery, J. Eichberg, J. B. Kirkpatrick, J. Cartwright Jr., and A. J. Saubermann, "Distribution of elements in rat peripheral axons and nerve cell bodies determined by x-ray microprobe analysis," *Journal of Neurochemistry*, vol. 51, no. 3, pp. 764–775, 1988.

[392] R. M. LoPachin Jr., V. R. LoPachin, and A. J. Saubermann, "Effects of axotomy on distribution and concentration of elements in rat sciatic nerve," *Journal of Neurochemistry*, vol. 54, no. 1, pp. 320–332, 1990.

[393] R. M. LoPachin and P. K. Stys, "Elemental composition and water content of rat optic nerve myelinated axons and glial cells: Effects of in vitro anoxia and reoxygenation," *Journal of Neuroscience*, vol. 15, no. 10, pp. 6735–6746, 1995.

[394] D. Studer, B. M. Humbel, and M. Chiquet, "Electron microscopy of high pressure frozen samples: Bridging the gap between cellular ultrastructure and atomic resolution," *Histochemistry and cell biology*, vol. 130, no. 5, pp. 877–889, 2008.

[395] L. Bernal, "Insights into the contribution of voltage-gated sodium channel 1.7 to paclitaxel-induced neuropathy," *Journal of Neuroscience*, vol. 38, no. 27, pp. 6025–6027, 2018.

[396] L. Li, J. Li, Y. Zuo, D. Dang, J. A. Frost, and Q. Yang, "Activation of KCNQ channels prevents paclitaxel-induced peripheral neuropathy and associated neuropathic pain," *The Journal of Pain*, vol. 20, no. 5, pp. 528–539, 2019.

[397] G. Cavaletti, G. Tredici, M. Braga, and S. Tazzari, "Experimental peripheral neuropathy induced in adult rats by repeated intraperitoneal administration of taxol," *Experimental Neurology*, vol. 133, no. 1, pp. 64–72, 1995.

[398] K. D. Cliffer, J. A. Siuciak, S. R. Carson, H. E. Radley, J. S. Park, D. R. Lewis, E. Zlotchenko, T. Nguyen, K. Garcia, J. R. Tonra, *et al.*, "Physiological characterization of taxol-induced large-fiber sensory neuropathy in the rat," *Annals of Neurology*, vol. 43, no. 1, pp. 46–55, 1998.

[399] N. Authier, J.-P. Gillet, J. Fialip, A. Eschalier, and F. Coudore, "Description of a short-term Taxol-induced nociceptive neuropathy in rats," *Brain Research*, vol. 887, no. 2, pp. 239–249, 2000.

[400] D. Purves, G. J. Augustine, D. Fitzpatrick, L. C. Katz, A.-S. LaMantia, J. O. McNamara, and S. M. Williams, "Chapter 4: Channels and transporters," in *Neuroscience*, 2nd ed., Sinauer Associates, 2001, ISBN: 0-87893-742-0.

[401] I. L. Cameron, N. K. R. Smith, T. B. Pool, and R. L. Sparks, "Intracellular concentration of sodium and other elements as related to mitogenesis and oncogenesis in vivo," *Cancer Research*, vol. 40, no. 5, pp. 1493–1500, 1980.

[402] W. H. Xiao, H. Zheng, F. Y. Zheng, R. Nuydens, T. F. Meert, and G. J. Bennett, "Mitochondrial abnormality in sensory, but not motor, axons in paclitaxel-evoked painful peripheral neuropathy in the rat," *Neuroscience*, vol. 199, pp. 461–469, 2011.

[403] J. Zhang, G. Ji, X. Huang, W. Xu, and F. Sun, "An improved cryo-FIB method for fabrication of frozen hydrated lamella," *Journal of Structural Biology*, vol. 194, no. 2, pp. 218–223, 2016.

[404] B. Song, Z. Ding, C. S. Allen, H. Sawada, F. Zhang, X. Pan, J. Warner, A. I. Kirkland, and P. Wang, "Hollow electron ptychographic diffractive imaging," *Physical Review Letters*, vol. 121, p. 146 101, 14 Oct. 2018.

[405] L. Zhou, J. Song, J. S. Kim, X. Pei, C. Huang, M. Boyce, L. Mendonça, D. Clare, A. Siebert, C. S. Allen, E. Liberti, D. Stuart, X. Pan, P. D. Nellist, P. Zhang, A. I. Kirkland, and P. Wang, "Low-dose phase retrieval of biological specimens using cryo-electron ptychography," *Nature Communications*, vol. 11, no. 1, pp. 1–9, 2020.

[406] R. F. Egerton, P. Li, and M. Malac, "Radiation damage in the TEM and SEM," *Micron*, vol. 35, no. 6, pp. 399–409, 2004.

[407] R. J. Mcquitty, "Metal-based drugs," *Science Progress*, vol. 97, no. 1, pp. 1–19, 2014.